

COAXIAL EXTRUSION OF FINE DIAMETER TISSUE FILAMENTS

JACK WILLIAM LOGAN

2022

SUBMITTED FOR THE DEGREE OF

**DOCTOR OF ENGINEERING IN
MEDICAL DEVICES**

DEPARTMENT OF BIOMEDICAL
ENGINEERING

UNIVERSITY OF STRATHCLYDE

This thesis is the result of the author's original research. It has been composed by the author and has not been previously submitted for examination which has led to the award of a degree.

The copyright of this thesis belongs to the author under the terms of the United Kingdom Copyright Acts as qualified by University of Strathclyde Regulation 3.50. Due acknowledgement must always be made of the use of any material contained in, or derived from, this thesis.

Signed:

Date:

Abstract

Coaxial extrusion is a promising technology, which employs a coaxial nozzle composed of two concentrically aligned nozzles (an inner core nozzle and an outer shell nozzle) to fabricate transplantable and autologous tissue filaments contained within robust, porous hydrogel scaffolds. These extruded scaffolds are capable of restoring function to various fibrous tissues within the body, such as peripheral nerve and muscle, which have lost the ability to naturally regenerate through irreversible disease or trauma.

The overall aim of this work was to develop a coaxial bio-extrusion platform to create fine diameter extruded stem cell-laden tissue filaments with the capability to retain long-term viability in culture. Further objectives were to develop a hydrogel scaffold material capable of resisting degradation by culture media to maintain tissue filament integrity. It was also desirable to demonstrate extrusion with multiple cell types and to present an initial assessment of the viability of the coaxial extrusion platform for use in drug testing applications, providing the benefit of a more natural in vivo-like environment to study drug-cell interactions in comparison to traditional two-dimensional methods.

By embedding cells within an extracellular matrix material, such as collagen, an extrudable bioink is created, which may be placed within the inner core of a concentrically aligned coaxial nozzle. By simultaneously extruding using alginate within the outer shell nozzle into a crosslinking bath containing divalent cations such as Ca^{2+} , hollow tubular alginate scaffolds containing cell-laden collagen filaments may be produced. By manipulating key extrusion parameters such as flow rate magnitude, core/shell flow rate and collagen concentration, filament diameters were successfully reduced from $> 400 \mu\text{m}$ to sub- $20 \mu\text{m}$, consequently aiding nutrient diffusion and long-term cell survival in culture.

Small diameter (sub- $20 \mu\text{m}$) adipose-derived stem cell-laden collagen filaments have been extruded and matured with high viability ($> 90\%$) over a 21-day period, achieved by modification of the core/shell flow rate ratio and collagen concentration. Combined calcium and barium cross-linking was employed in order to maintain scaffold integrity by tuning alginate cross-linking concentration, time and ion type. The coaxial extrusion platform was also used to extrude and culture human hepatoma HepaRG cells within small diameter filaments (sub- $25 \mu\text{m}$), which sustained viability for 14 days, thus demonstrating extrusion using multiple cell types.

The preliminary viability of the coaxial extruder to be utilised in drug testing applications has been assessed by performing hepatotoxicity tests of HepaRG cells and obtaining LC_{50} values similar to published data for three compounds. An additional assay of CYP450 enzyme activity further validated this platform by demonstrating strong CYP3A4 activity on induction with rifampicin, a known CYP3A4 inducer.

To conclude, a coaxial extrusion platform was created, wherein fine diameter (sub-20 μm) collagen filaments containing adipose-derived stem cells were fabricated and cultured, retaining high viability (> 90%) over multiple days (> 21 days). This achievement was aided by the tuning of material flow rates, alginate shell cross-linking parameters and collagen concentration. Finally, fine diameter collagen filaments containing human hepatoma HepaRG cells (sub-25 μm) were also extruded and cultured at high viability for 14 days. These HepaRG-containing filaments were also exposed to different hepatotoxic compounds at varying concentrations to obtain LC_{50} values comparable to literature, thus providing preliminary validation of the coaxial extrusion system to be used as a drug testing platform.

Acknowledgements

To everyone who has given me help during my studies, whether it has been to recommend new approaches, fabricating new parts or just a chat, I can't thank you enough. This work would have been impossible without you all!

Firstly, I would like to extend my thanks to my project supervisor, Professor Will Shu. His constant support and infectious enthusiasm kept me motivated and driven throughout my doctorate and his teachings will stay with me as I continue my development.

A big thanks to the staff at the Centre for Doctoral Training in Medical Devices and Health Technologies and the Department of Biomedical Engineering for giving me the opportunity to study an EngD and for all of the behind-the-scenes support work. I'd like to extend a special mention to Carol McInnes: thanks for keeping our EngD's on-track with arranging all of our training and conference days, ordering supplies and taking care of any personal issues which occurred. I'd also like to thank Steven Murray and Catherine Henderson for all of the technical help and expertise in quickly solving all of the problems I was faced with.

I'd also like to thank to the Strathclyde Institute of Pharmacy and Biomedical Sciences for giving the lab a home away from home during renovations, everyone was so helpful giving the hapless engineer help with everything biology-related. Big thanks to Graeme MacKenzie and John Nevin for doing their utmost to ensure technical issues were solved quickly. Also thanks to Craig Pine and Richard Pratt in the stores for getting me supplies as quickly as they could.

To all of my lab colleagues, past and present: thanks for all of the help and assistance when I required it, especially all of the incredibly basic questions I would ask D.J Cornelissen and Alan Faulkner-Jones in the early days to the more technical stuff that Ian MacKenzie, Gareth Turnbull and Gregor Skeldon would take care of. It's truly been a rewarding experience and privilege working with people of different backgrounds and cultures. Understanding different approaches to similar problems has given me a broader perspective and has enriched my understanding of the world we live in.

To the EngD guys: Aiden Hannah, Ian Coghill, Ross McWilliam, Sean Donnelly and Vincent Veza, who have since become great friends, it's been an absolute pleasure being on this ride with you guys. It has been very enriching learning and growing with you and I'll really miss the daily laughs, Vinny's rants and the de-stressing during Friday pints.

Last, but certainly not least, to my family and friends: I cannot thank you all enough for your unconditional support and unwavering confidence in me. It has been monumental for me over the years and I massively appreciate every message of positivity and encouragement that's been sent my way. You've all been my shining light during the tough times and I will be forever grateful for the sacrifices that were made to get me here. A big final thank you to Misha for being with me every day to keep me sane during the final push. Completing the final year of a doctorate during a global pandemic was incredibly difficult but you made it so much easier with your daily support and encouragement.

Table of Contents

Abstract	ii
Acknowledgements.....	iv
Table of Contents.....	vi
Nomenclature	x
List of Publications by the Candidate	xiii
1. Introduction	14
1.1. Background	14
1.2. Motivation	14
1.3. Aims and Objectives	15
1.4. Structure of the Thesis	15
1.5. References	17
2. Literature Review	19
2.1. Introduction	19
2.2. Bioprinting	19
2.2.1. Bioprinting modalities	22
2.2.2. The bioink.....	32
2.3. Engineering of tissue fibres	44
2.3.1. Tissue engineering approaches for the fabrication of tissue fibres	50
2.4. Coaxial bio-extrusion	55
2.5. Challenges and limitations of coaxial bio-extrusion	59
2.6. Recent advances in coaxial bio-extrusion for tissue fibre production	59
2.7. Progress in coaxial bio-extrusion of small diameter tissue fibre coaxial bio-extrusion.....	62
2.8. Traditional drug testing methodologies	69
2.8.1. Cell monolayer testing	69
2.8.2. Spheroid culture	70
2.8.3. Tissue-engineered drug testing platforms.....	72
2.8.4. Bioprinting and extrusion for drug testing.....	73
2.9. Conclusions	75
2.10. References	77
3. Materials and Methods.....	103
3.1. Coaxial extrusion	103
3.1.1. Hydrogel preparation	103
3.1.2. Cell culture.....	103
3.1.3. Production of collagen hydrogel	104

3.1.4.	Collagen bioink production	105
3.1.5.	Extrusion process.....	106
3.1.6.	Staining and microscopy	107
3.2.	Drug testing	109
3.2.1.	LC ₅₀ data fitting.....	109
3.2.2.	CYP 3A4 assay.....	110
3.3.	Measuring and statistical analysis	111
3.4.	Hardware and modifications for coaxial extrusion	113
3.4.1.	Introduction.....	113
3.4.2.	Electronics	114
3.4.3.	Firmware.....	116
3.5.	Coaxial extrusion schematics	118
3.5.1.	V1 - Syringe pump and Arduino Micro	118
3.5.2.	V2 - Extruder and Arduino Micro	120
3.5.3.	V3 - Arduino UNO dual-stepper control.....	121
3.5.4.	V4 - StepperUNO	122
3.5.5.	Stepper motor calibration	123
3.6.	Development of nozzle and bed temperature control systems	126
3.6.1.	Background information and theory	126
3.6.2.	Development of a temperature-controlled extruder	130
3.6.3.	Cooling bed configuration	134
3.7.	Initial testing results	135
3.8.	Conclusion.....	138
3.9.	References	139
4.	Collagen Filament Extrusion	141
4.1.	Introduction	141
4.2.	Background information and theory.....	141
4.2.1.	Alginate	141
4.2.2.	Collagen type I	142
4.2.3.	Shear Stress.....	142
4.2.4.	Reynolds number.....	143
4.3.	Deriving parameters affecting filament diameter	144
4.3.1.	Derivation of Navier-Stokes equation.....	144
4.3.2.	Finding flow velocity distribution	146
4.3.3.	Derivation of Poiseuille's law	148
4.3.4.	Equation for coaxial diameters.....	149

4.4.	Process description	152
4.5.	Collagen filament diameter tuning	154
4.5.1.	Shell flow rate and incubation time	154
4.5.2.	Incubation and cross-linking time effects	157
4.5.3.	Core flow rate tuning	159
4.5.4.	Flow rate magnitude effects	161
4.5.5.	Effect of changing collagen concentration	162
4.5.6.	Combining flow rate and collagen concentration effects	163
4.5.7.	Validation of theoretical equation for coaxial diameters	169
4.6.	Alginate shell tuning	171
4.6.1.	Effect of flow rate ratio on alginate shell diameter	171
4.6.2.	Effects of cross-linking time	174
4.6.3.	Effect of cross-linking bath concentration	177
4.6.4.	Effect of cross-linking cation type	179
4.6.5.	Alginate degradation	182
4.7.	Limitations of the coaxial extrusion process	184
4.8.	Conclusion	186
4.9.	References	188
5.	Coaxial Extrusion of Fine Diameter Cell-laden Filaments	193
5.1.	Introduction	193
5.1.1.	Challenges of adding cells	193
5.2.	Process description	193
5.2.1.	Experimental aims	193
5.3.	Extrusion of ADSCs at high-viability	194
5.4.	High cell density study for tissue filament culture	197
5.5.	Extrusion of Schwann cell-like filaments	200
5.6.	Modification of cross-linking parameters for increased stability	204
5.6.1.	Tuning of alginate exposure time to calcium chloride	204
5.6.2.	Implementation of secondary alginate cross-linking using barium	206
5.7.	Further experimentation for small diameter filaments	209
5.7.1.	Extrusion for fine filaments with secondary barium cross-linking	209
5.7.2.	Combining flow effects with collagen concentration effects	211
5.7.3.	Effect of cell seeding density on filament diameter	224
5.8.	Summary	230
5.9.	References	231
6.	Extruded Tissue Filaments as a Mini Organ Platform for Drug Toxicity Testing	232

6.1.	Introduction	232
6.1.1.	Aims	232
6.2.	Drug testing viability analysis	234
6.2.1.	Drug-free HepaRG extrusion	234
6.2.2.	Acetaminophen.....	235
6.2.3.	Azathioprine.....	237
6.2.4.	Amiodarone	239
6.2.5.	Prednisolone.....	241
6.2.6.	Summary of toxicity data	242
6.3.	CYP assay using rifampicin	242
6.4.	Conclusion.....	244
6.5.	References	245
7.	Research Assessment and Recommendations for Future Work	250
7.1.	Research Summary	250
7.2.	Future Work Recommendations	252

Nomenclature

2D	Two-dimensional
2PP	Two-Photon Polymerisation
3D	Three-dimensional
ABS	Acrylonitrile Butadiene Styrene
ADSC	Adipose Derived Stem Cell
AM	Amiodarone
ANOVA	Analysis Of Variance
APAP	Acetaminophen
AZA	Azathioprine
CAD	Computer Aided Design
CES	Centrifugal Electrospinning
CNC	Computer Numerical Control
CS	Centrifugal Spinning
CYP3A4	Cytochrome P450 3A4 Isozyme
CYP450	Cytochrome P450
dADSC	Differentiated Adipose Derived Stem Cell
DBB	Droplet Based Bioprinting
DC	Direct Current
DHT	Dehydrothermal Treatment
DMSO	Dimethyl Sulfoxide
DPBS	Dulbecco's Phosphate Buffered Saline
EBB	Extrusion Based Bioprinting
ECM	Extracellular Matrix
EDTA	Ethylenediaminetetraacetic Acid
ES	Electrospinning
FBS	Fetal Bovine Serum
FDA	Fluorescein Diacetate
FDM	Fused Deposition Modelling
GelMA	Gelatin Methacryloyl
GGF	Glial Growth Factor
GUI	Graphical User Interface
HA	Hyaluronic Acid
HAMA	Methacrylated Hyaluronic Acid

hBFGF	Human Basic Fibroblastic Growth Factor
HUVEC	Human Umbilical Vein Endothelial Cell
ID	Internal Diameter
IPC	Interfacial Polyelectrolyte Complexation
LAB	Laser Assisted Bioprinting
LCD	Liquid Crystal Display
LIFT	Laser-Induced Forward Transfer
MEM	Minimum Essential Medium
MMP	Matrix Metalloproteinase
MRP-2	Multidrug Resistance-Associated Protein 2
MSC	Mesenchymal Stem Cell
NC	Negative Control
NTP	Normal Temperature And Pressure
OD	Outer Diameter
PBS	Phosphate Buffered Saline
PC	Positive Control
PCL	Polycaprolactone
PDGF	Platelet Derived Growth Factor
PDMS	Polydimethylsiloxane
PEG	Polyethylene Glycol
PI	Propidium Iodide
PID	Proportional Integral Derivate
PLA	Polylactic Acid
PRD	Prednisolone
PWM	Pulsed Width Modulation
RAMPS	Reprap Arduino Mega Pololu Shield
RGD	Arginine-Glycine-Aspartate
RIF	Rifampicin
RPM	Revolutions Per Minute
SD	Standard Deviation
SE	Standard Error
SLA	Stereolithography
SLS	Selective Laser Sintering
UV	Ultraviolet Light
XYZ	3D Printer Datum Axes

ZO-1

Zonula Occludens 1 Protein

List of Publications by the Candidate

I. Holland, **J. Logan**, J. Shi, C. McCormick, D. Liu, and W. Shu, “3D biofabrication for tubular tissue engineering.” *Bio-Design Manuf.*, vol. 1, no. 2, pp. 89–100, 2018.

1. Introduction

1.1. Background

In 1983, Charles ‘Chuck’ Hull was working using ultraviolet light (UV) and photo-curable materials in a small lab, aiming to improve the computer design-to-prototype times where he subsequently discovered that by using a computer to control a concentrated beam of UV light directed onto the surface of a vat of liquid photo-curable resin, one could print successive layers of solid material leading to the production of a three-dimensional (3D) object. This was the invention of stereolithography, known nowadays as 3D printing or additive manufacturing, whereby 3D objects are created from computer code [1]. This invention led to the creation of the world’s first 3D printer, the SLA-1 Stereolithography (SLA) printer, in 1987 [2]. Since then, the global 3D printing market has been consistently growing and global management consulting firm McKinsey & Company have predicted that the global market could reach up to \$490 billion by 2025 [3].

In 2003, upon recognising the potentially revolutionary applications of 3D printing, Thomas Boland et al. successfully created the world’s first bioprinter at Clemson University in South Carolina, USA, by modifying a commercial inkjet printer to print and culture bovine aortic endothelial cells suspended within collagen and a synthetic polymer gel. This seminal demonstration of bioprinting paved the way for researchers around the world to explore the platform and its vast array of applications in the health technology sector and thus began the age of bioprinting [4] [5].

1.2. Motivation

There have been many successes within the field of bioprinting, with a wide array of successfully printed structures and tissues, from articular cartilage [6] [7] and skin [8] [9] to heart valve leaflets [10] and blood vessels [11]. The challenge of printing fully vascularised and functional organs remains a distant goal, largely due to difficulties in facilitating unrestricted nutrient diffusion and perfusion [12] [13] and achieving sufficient vascularisation [14] [15].

It therefore appeared more realistic to first demonstrate bioprinting of a more biologically simple structure; it was at this stage that the main goal of this work was to demonstrate bioprinting or extrusion of transplantable tissue fibres (or filaments). By combining hydrogel and various extracellular matrix materials and multipotent autologous adipose-derived stem cells (ADSCs), it was hypothesised that various types of transplantable tissue fibres could be fabricated and cultured.

By directing the differentiation of the ADSCs, distinct terminally-differentiated cell types and fibres may be engineered. These fibres may primarily be used for the surgical repair of damaged tissues in which the body has failed to naturally regenerate through irreversible trauma or disease, to alleviate loss of function with the added benefit of having minimal or no immunogenic or toxicity issues.

Neural fibres may be formed to treat peripheral neuropathies (peripheral nerve damage) caused by trauma, accidents (mainly road traffic incidents) and disease, avoiding the comorbidities caused by the current gold standard nerve autograft, usually taken from the sural nerve [16] [17] [18]. Similarly, muscle fibres may also be formed and surgically implanted to restore muscle function and prevent comorbidities caused by the current standard of care, autologous muscle pedicle flaps from adjacent regions [19].

1.3. Aims and Objectives

The overall aim of this work was to develop a coaxial bio-extrusion platform to create fine diameter extruded stem cell-laden tissue filaments with the capability to retain long-term viability in culture.

Further objectives included:

1. Developing a hydrogel scaffold material capable of resisting degradation by culture media to maintain tissue filament integrity.
2. Demonstration of extrusion with multiple cell types.
3. Presenting an initial assessment of the viability of the coaxial extrusion platform for use in drug testing applications, providing the benefit of a more natural in vivo-like environment to study drug-cell interactions in comparison to traditional two-dimensional methods.

1.4. Structure of the Thesis

Each chapter of this work focusses on different aspects of the thesis, of which will be summarised below.

- Chapter 1 has provided an introduction to the research and has stated the aims and objectives of the thesis.

- Chapter 2 summarises the basics of bioprinting and extrusion, with explanations on extrusion modalities, bioinks and hydrogels, with a particular emphasis on alginate and collagen, the most-utilised materials in the later experimental chapters. Moreover, a review on recent approaches to the creation of cell-laden fibres using tissue engineering and bio-extrusion is subsequently presented in addition to a final section, which specifically introduces coaxial bio-extrusion before discussing multiple recent advances in small diameter coaxial bio-extrusion of cell-laden tissue fibres.
- Chapter 3 lists the experimental methodology and related materials used to complete all experiments, with information given on the extrusion process, subsequent cell staining and characterisation in addition to details on printing and extrusion hardware components. In addition, coverage is provided on the development of the extrusion hardware and software to facilitate coaxial extrusion of small diameter filaments. Aspects such as firmware modification, electronics development and attempts at nozzle tip temperature control are also explained here.
- Chapter 4 opens with background information on the coaxial extrusion process and provides the relevant theoretical information linked to the rationale behind subsequent experiments, which are focused on reducing the diameter of extruded collagen filaments and tuning the alginate shell scaffold in order to balance scaffold porosity and degradation time.
- Chapter 5 builds on the previous chapter by demonstrating extrusion of adipose-derived stem cell-laden collagen filaments at high viability. Further work focuses on alginate shell tuning using calcium and barium cross-linking to provide adequate porosity to sustain cell viability in addition. The chapter concludes by illustrating the effect of core/shell flow rate, collagen concentration and cell seeding density on filament diameter and viability.
- Chapter 6 aims to provide an initial assessment of the viability of the coaxial extrusion platform for drug testing applications by performing cytotoxicity and CYP450 isozyme activity assays and comparing results to the literature.
- Chapter 7 concludes this thesis by providing an assessment of the research and summarises the key findings prior to providing recommendations for future work.

1.5. References

- [1] J. Leijten *et al.*, "Spatially and temporally controlled hydrogels for tissue engineering." *Mater. Sci. Eng. R Reports*, vol 119, pp. 1-35, 2017.
- [2] A. Su and S. J. Al'Aref, "History of 3D printing," in *3D Printing Applications in Cardiovascular Medicine*, Elsevier, 2018, pp. 1–10.
- [3] N. Nikitakos, I. Dagkinis, D. Papachristos, G. Georgantis, and E. Kostidi, "Economics in 3D printing," in *3D Printing: Applications in Medicine and Surgery*, Elsevier, 2020, pp. 85–95.
- [4] W. C. Wilson and T. Boland, "Cell and organ printing 1: Protein and cell printers," *Anat. Rec. - Part A Discov. Mol. Cell. Evol. Biol.*, vol. 272, no. 2, pp. 491–496, Jun. 2003.
- [5] T. Boland, V. Mironov, A. Gutowska, E. A. Roth, and R. R. Markwald, "Cell and organ printing 2: Fusion of cell aggregates in three-dimensional gels," *Anat. Rec. - Part A Discov. Mol. Cell. Evol. Biol.*, vol. 272, no. 2, pp. 497–502, 2003.
- [6] C. Antich *et al.*, "Bio-inspired hydrogel composed of hyaluronic acid and alginate as a potential bioink for 3D bioprinting of articular cartilage engineering constructs," *Acta Biomater.*, vol. 106, pp. 114–123, Apr. 2020.
- [7] Y. Wu *et al.*, "Hybrid Bioprinting of Zonally Stratified Human Articular Cartilage Using Scaffold-Free Tissue Strands as Building Blocks," *Adv. Healthc. Mater.*, vol. 9, no. 22, p. 2001657, Nov. 2020.
- [8] W. L. Ng, J. T. Z. Qi, W. Y. Yeong, and M. W. Naing, "Proof-of-concept: 3D bioprinting of pigmented human skin constructs," *Biofabrication*, vol. 10, p. 025005, Jan. 2018.
- [9] T. Baltazar *et al.*, "Three Dimensional Bioprinting of a Vascularized and Perfusable Skin Graft Using Human Keratinocytes, Fibroblasts, Pericytes, and Endothelial Cells," *Tissue Eng. Part A*, vol. 26, no. 5–6, pp. 227–238, Mar. 2020.
- [10] A. L. Y. Nachlas *et al.*, "A multilayered valve leaflet promotes cell-laden collagen type I production and aortic valve hemodynamics," *Biomaterials*, vol. 240, p. 119838, May 2020.

- [11] L. Xu *et al.*, “Bioprinting small diameter blood vessel constructs with an endothelial and smooth muscle cell bilayer in a single step,” *Biofabrication*, vol. 12, no. 4, p. 045012, Oct. 2020.
- [12] K. A. Deo, K. A. Singh, C. W. Peak, D. L. Alge, and A. K. Gaharwar, “Bioprinting 101: Design, Fabrication, and Evaluation of Cell-Laden 3D Bioprinted Scaffolds,” *Tissue Eng. - Part A*, vol. 26, no. 5–6, pp. 318–338, Mar. 2020.
- [13] C. L. Hedegaard *et al.*, “Hydrodynamically Guided Hierarchical Self-Assembly of Peptide–Protein Bioinks,” *Adv. Funct. Mater.*, vol. 28, no. 16, p. 1703716, Apr. 2018.
- [14] J. Nulty *et al.*, “3D Bioprinting of prevascularised implants for the repair of critically-sized bone defects,” *Acta Biomater.*, vol. In Press, Mar. 2021.
- [15] M. Dey and I. T. Ozbolat, “3D bioprinting of cells, tissues and organs,” *Scientific Reports*, vol. 10, no. 1. Nature Research, p. 14023, 01-Dec-2020.
- [16] E. B. Petcu, R. Midha, E. Mccoll, A. Popa-wagner, T. V Chirila, and P. D. Dalton, “3D printing strategies for peripheral nerve regeneration,” 2018.
- [17] L. Ning *et al.*, “3D bioprinting of scaffolds with living Schwann cells for potential nerve tissue engineering applications,” *Biofabrication*, vol. 10, no. 3, p. 35014, 2018.
- [18] E. Abelseth, L. Abelseth, L. De La Vega, S. T. Beyer, S. J. Wadsworth, and S. M. Willerth, “3D Printing of Neural Tissues Derived from Human Induced Pluripotent Stem Cells Using a Fibrin-Based Bioink,” *ACS Biomater. Sci. Eng.*, vol. 5, no. 1, pp. 234–243, Jan. 2019.
- [19] J. H. Kim *et al.*, “3D Bioprinted Human Skeletal Muscle Constructs for Muscle Function Restoration,” *Sci. Rep.*, vol. 8, no. 1, p. 12307, Dec. 2018.

2. Literature Review

2.1. Introduction

In essence, 3D (three-dimensional) printing (or additive manufacturing) is the creation of a three-dimensional object from a digital model. A 3D printing process can involve the layer-by-layer movement of an extrusion nozzle or light source in three dimensions (top-down or bottom-up), usually by action of electric stepper motors mounted on a portable frame, inducing a phase change in printable filament or substrate located on the print bed (or in a liquid bath) to create a solid 3D object with successive layers or slices. Through the use of computer-aided design (CAD) software or medical imaging data, 3D models are generated and subsequently converted into G-code files which can be transferred to the printer hardware through storage media, such as secure digital (SD) cards and USB flash drives to initiate printing. G-code is the world's most common numerical control programming language and is used to control CNC (Computer Numerical Control) machines for rapid manufacturing. G-code contains the instructions on printer movement and activation of tools, such as stepper motors or heaters. A letter is assigned to each axis, each of which is controlled by one or two stepper motors, whereby each thin layer is printed before moving a fixed distance in the z-direction to print subsequent layers until the model is complete.

There are many different types of 3D printing technology today, with one of the most popular being fused deposition modelling (FDM) [1] [2], whereby thermoplastics are heated to their melting points and subsequently extruded through a nozzle onto a flat build plate in a bottom-up layer-by-layer fashion. Selective laser sintering (SLS) is another popular modality in which a moving laser solidifies various powdered materials, such as plastics and ceramics, to create 3D objects [3]. In addition, the range of printable materials has grown exponentially, ranging from common thermoplastics such as polylactic acid (PLA) and acrylonitrile butadiene styrene (ABS) and flexible filaments (thermoplastic elastomers) to more exotic materials, such as metals [4], carbon fibre [5] and even chocolate [6].

2.2. Bioprinting

Bioprinting may facilitate the creation of transplantable tissues and organs [7] [8], wound healing materials [9] and drug-testing and delivery platforms [10] [11]. Further applications include the creation of surgical models to inform complex surgeries and surgical training purposes [12]. Bioprinting offers many benefits in comparison to traditional tissue engineering.

This includes the ability to simultaneously print with multiple customised nozzles and biomaterials using customised printing equipment to create bespoke tissues and organs with precise material placement using various biomaterials and homogeneously dispersed cells and the ability to tune hydrogel scaffolds for desired physicochemical properties. However, it is important to state that bioprinting is not without its limitations and challenges. It should be noted here that bio-extrusion is a simpler form of bioprinting, where only the extruder motor is used, as opposed to bioprinting which uses further motors to facilitate movement of extruded material.

An enduring challenge of bioprinting is the development of biomaterials and bioinks with a suitable mix of physicochemical and biological properties for each associated printing methodology [13]. The fabrication of complex tissues and organs at high-resolution dictates a limited range of material properties to utilise. Printed constructs must facilitate cellular migration, survival and proliferation in addition to supporting the differentiation of embedded cells [14]. To this day there are no standardised bioinks for bioprinting, thus highlighting the manifold research difficulties in bioink development.

Traditionally, in order to improve the printability of bioinks and hydrogels, polymer concentration and/or cross-link density (number of chemical bonds between polymer chains) would be increased, usually resulting in an increase in viscosity. Bioinks with a high degree of cross-linking present as stiff constructs with sufficient mechanical strength for cell and tissue support and shape retention, illustrated in the blue 'fabrication' area within Figure 2-1 [15]. Conversely, cells tend to proliferate better in an aqueous environment, unhindered by dense polymer structures [16], therefore creating a dichotomy between printed construct stiffness and cell proliferation, this is represented by the yellow 'cell culture' zone within Figure 2-1.

In the case of bioinks with a low degree of cross-linking, resulting printed constructs cannot retain shape fidelity and thus spread across the print surface due to their insufficient mechanical properties. Therefore, most printed structures tend to have a moderate degree of cross-linking, illustrated within the green zone of Figure 2-1, labelled as the 'traditional biofabrication window'. The main challenge of bioprinting is to develop and print bioinks within this green biofabrication window, to create biological constructs which possess high shape fidelity and optimal physicochemical properties for their desired purpose.

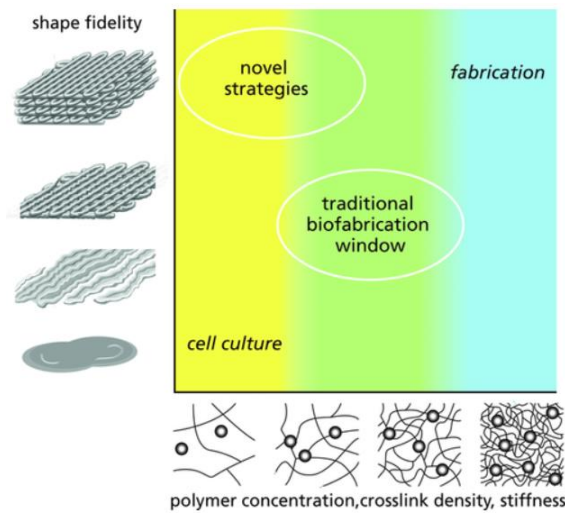


Figure 2-1. Biofabrication window graphic, illustrating the need to balance polymer concentration, cross-link density and stiffness with cell proliferation, migration and differentiation to obtain printed constructs with sufficient printing and biological characteristics [17].

A further major challenge to the successful bioprinting of large tissues and organs is that of achieving sufficient vascularisation. The maximum tissue diameter which can be cultured without the development of necrotic regions is generally quoted as approximately 200 μm [18], limited by the ability of cells to uptake oxygen and nutrients for proliferation (tissue-dependent). To date, only disorganised vasculature has been cultured, at greater than the diameter required for engineering of capillaries, which can measure 5 – 10 μm in vivo [19]. Therefore, recapitulating fully-branched vascular networks similar to those seen in vivo remains a major hurdle to overcome [20] [21].

Achieving sufficient resolution and small filament diameters is a further challenge to the successful integration of bioprinting into clinical settings [22]. It is assumed that printing cells at such small diameters would not affect their ability to secrete extracellular matrix (ECM) and create a suitable environment for growth and maturation. There are many organ types demanding a resolution which are currently unobtainable with current state-of-the-art bioprinting technologies, thus necessitating further technological advancements to meet these requirements. For example, cardiac muscle requires a resolution of 50 – 100 μm [23] whilst current bioprinting technologies have only achieved cell-laden constructs with a resolution of 100 – 200 μm [24]. Similarly, of the various structures found in the nephron (proximal/distal tubules etc.), the functional unit of the kidney, the finest areas can measure approximately 15 μm , however, the finest diameter achieved to date was achieved by Homan et al. [25], whereby acellular human renal proximal tubules measuring 100 μm in diameter were printed. The diameter requirements of these anatomical structures are summarised in Figure 2-2 below.

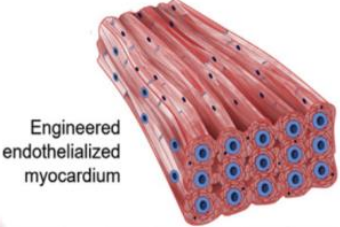
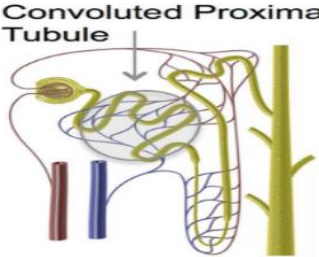
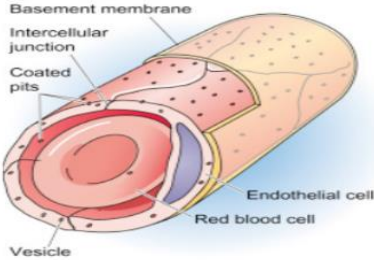
Structure	Diameter range	
Cardiac muscle	 <p data-bbox="627 327 746 394">Engineered endothelialized myocardium</p>	50 - 100 μm
Renal tubule	 <p data-bbox="635 456 967 501">Convoluted Proximal Tubule</p>	$\sim 15 \mu\text{m}$
Capillary	 <p data-bbox="624 745 999 1003">Basement membrane Intercellular junction Coated pits Vesicle Endothelial cell Red blood cell</p>	5 - 10 μm

Figure 2-2. Image showing the diameters required for the biofabrication of cardiac muscle [24], renal tubules within the nephron (the basic structural and functional unit of the kidney) [25]; and capillaries [26].

Given these limitations in the current state of the art of bioprinting, it is clear that there are many major hurdles to overcome to realise the potential of this ever-growing field, with the aim of the bioprinter being a common tool within clinical settings in the near future.

2.2.1. Bioprinting modalities

The possible modalities of 3D bioprinting can be categorised into three main categories, namely extrusion-based bioprinting (EBB), droplet-based bioprinting (DBB) and laser-assisted bioprinting (LAB) [27]. These modalities are summarised in Figure 2-3.

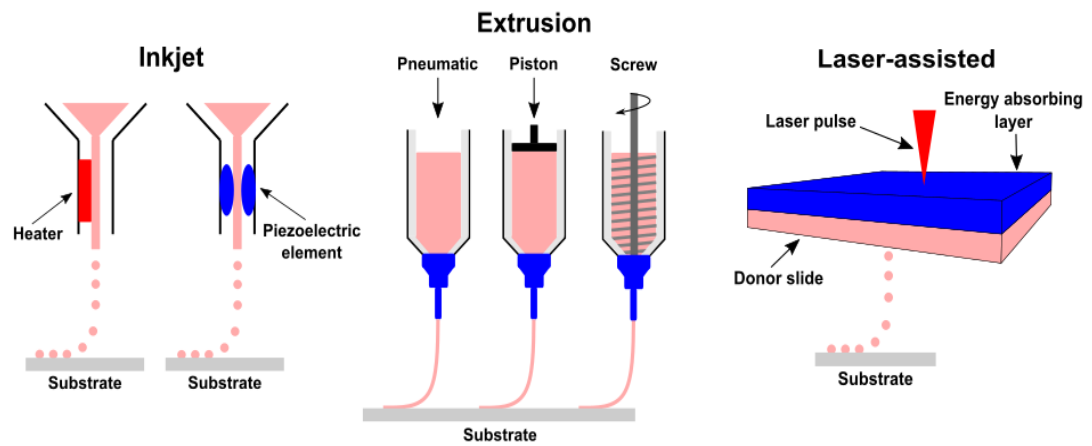


Figure 2-3. Schematic illustrating respective mechanisms for inkjet, extrusion and laser-based bioprinting.

The following sections aim to describe each methodology and summarise their relative advantages and disadvantages, concluding by justifying the selection of EBB for the work presented in the following chapters.

2.2.1.1. Extrusion based bioprinting

EBB involves the positive displacement of material through a nozzle by an applied force, which can be either pneumatic, mechanical (piston/screw) or solenoid-assisted. EBB combines a fluid dispensing platform, to dispense bioink, and an automated robotic system, to provide computer-controlled three-dimensional print head movement to allow the precise deposition of biomaterials in cylindrical filament form. The various options for EBB are summarised in Figure 2-4.

(a) Pneumatic-based extrusion bioprinting

Pneumatic-based EBB employs pressurised air in a simple valve-free configuration or, in a minority of cases where high precision is required, valve-based systems. Pneumatic-based EBB requires the use of sterile air to prevent bioink contamination, therefore air filters or more expensive pre-sterilised air tanks are needed.

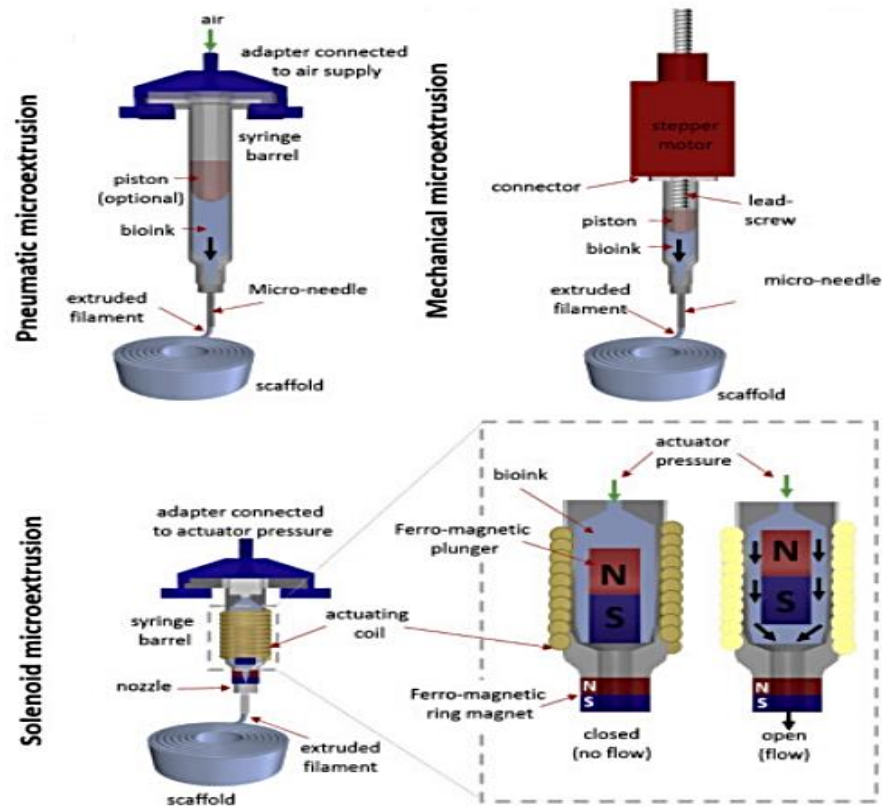


Figure 2-4. Extrusion based bioprinting modalities, highlighting the key features of pneumatic, mechanical and solenoid microextrusion, adapted from [28].

The applied air pressure must be sufficient to overcome the bioink surface tension in the nozzle and it must be within a stable range in order to produce stable, continuous and uniform filaments. The printing speed and bioink rheological properties must also be finely tuned. If the pressure is too high or too low, discontinuities will appear in printed filaments due to unstable material flow, leading to unstable printed structures. Pneumatic printing systems also have difficulties achieving smooth printing of semi-solid or solid bioinks and usually require another material medium to eject the bioink through the nozzle orifice [29].

(b) Solenoid extrusion bioprinting

Solenoid EBB employs a solenoid valve to control material flow through a printing nozzle orifice, in which the contact between a floating ferromagnetic plunger and a ring magnet is controlled by applying electrical pulses to the solenoid coil. Energising the solenoid coil results in loss of contact between the plunger and ring magnets whilst removing this current results in the valve closing, thus allowing fine control of material flow through the nozzle. Solenoid-based microextrusion can achieve sub-microlitre resolution on printing bioinks [30] and is useful for printing low viscosity materials which require UV or ionic cross-linking mechanisms [31].

Despite the high resolution and accuracy achievable using solenoid EBB, there are a number of limitations to account for. Firstly, there is a time delay between energising the coil and the valve physically opening, thus leading to inaccuracies between desired models and resulting prints. Secondly, the plunger can unintentionally compress the valve sealing between the plunger and the valve seat, due to the soft seal created here, leading to further time delays. There is also a requirement for high actuation pressure in order to eject high viscosity bioinks, potentially leading to further printing inaccuracies. Furthermore, solenoid EBB becomes unreliable when utilising a temperature-controlled nozzle system as fluctuations in bioink temperature lead to variations in bioink viscosity, resulting in the need for different valve opening times due to the ability of the bioink to flow changing with temperature [32].

(c) Mechanical microextrusion bioprinting

Mechanical microextrusion EBB utilises pistons or screw-driven options, whereby pistons generally provide more control of bioink flow whilst screw-driven systems allow for more spatial control and is preferred for higher viscosity materials but generate comparably larger pressure drops, potentially leading to a greater degree of damage to cells. Mechanical microextrusion systems benefit from low cost, portability, easy setup and programming and also don't require air tanks, compressors and sterilisation units associated with pneumatic EBB systems or the need for solenoids and costly valves. These systems also benefit from allowing printing of semi-solid or solid bioinks such as cell aggregates [33].

With regards to the disadvantages of using EBB, the resolution of EBB is often quoted to be on the order of 100 to 200 μm [34] [35], which is comparably lower than the 10 to 50 μm achieved using DBB [36] and the 5 μm possible using LAB [37]. This limitation in the resolution of EBB results in difficulties in the precise positioning and patterning of cells.

The minimisation of cellular shear stress upon nozzle ejection and printing resolution are major technical challenges of extrusion-based bioprinting both of which are not mutually exclusive [38]. Usually non-Newtonian fluids are utilised, whereby viscosity and shear response are important; thixotropic (shear-thinning) substances are the most desirable here. It is imperative that extrudable materials can easily overcome surface tension and are capable of rapid gelation for shape retention without unwanted flow on print beds. Additionally, the substrate should have surface roughness with low wettability to allow prints to adhere to surfaces with shape retention [39]. Given these rheological demands, this limits the choice of useable bioinks in EBB, however EBB retains the widest array of bioinks to select in comparison to the other printing methodologies.

Despite these disadvantages, EBB systems possess many advantages over the other options, including the ability of EBB modules to be portable, low-cost and can easily incorporate CAD software and images in order to automatically print structures from custom designs or medical images on demand, highlighting the convenience of EBB in creating 3D cell-laden constructs.

EBB is the most economical of the three bioprinting modalities as it does not require the use of costly and/or sophisticated equipment in comparison to DBB and LBB, such as valves, sensors and lasers and there is a wide range of printable viscosities (30 to 6×10^7 mPas), thus proving EBB as the most versatile of the three main modalities [40].

2.2.1.2. Droplet based bioprinting

DBB involves the ejection of individual, discrete drops of material by applying energy sources such as electricity, acoustics and heat to material reservoirs [41]. There are three possible methodologies when applying DBB: acoustic droplet ejection [42], micro-valve printing [43] and inkjet printing [44]. Inkjet printing borrows the same concept used in traditional paper inkjet printing and can be further classified into two categories: continuous inkjet printing (CIJ) and drop-on-demand printing. Drop-on-demand inkjet printing techniques include thermal [45], piezoelectric [46], electrostatic [47] and electrohydrodynamic jetting [48]. In the field of tissue engineering, drop-on-demand inkjet printing is preferred to continuous printing due to it being more economical, easier to use and its ability to create complex and multi-material patterns [49]. Additionally, CIJ is further limited as it requires low viscosity fluids and higher dropping velocity, which impairs the final resolution of the printed structure [50].

(a) Acoustic droplet ejection

Acoustic droplet ejection employs an acoustic field to cause the ejection of droplets from a liquid reservoir, which holds the liquid in place within very small channels, holding the liquid in place without any leakage due to surface tension. When the force of applied acoustic waves exceeds that of the surface tension, droplets are formed. The mechanism of the acoustic droplet ejection process is depicted in Figure 2-5.

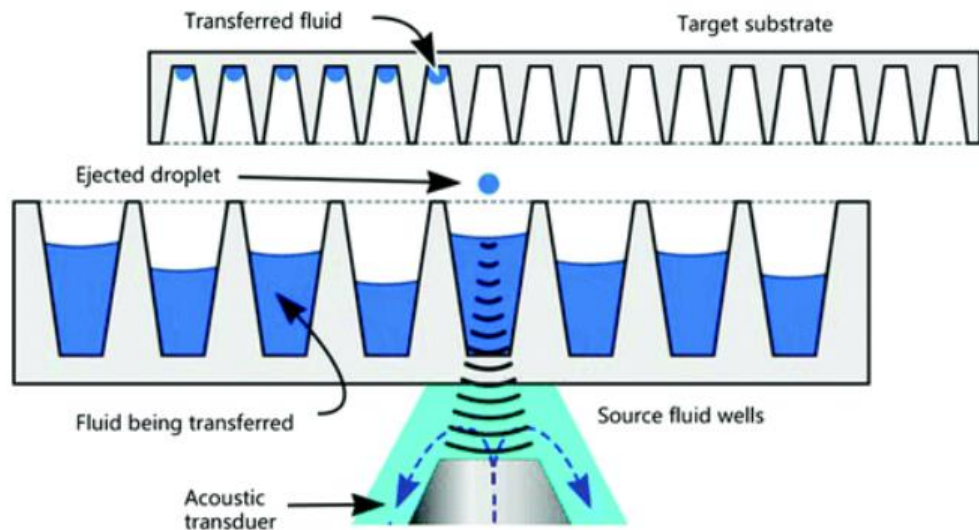


Figure 2-5. Schematic diagram depicting the acoustic droplet ejection process [51].

Acoustic bioprinting provides the advantage of not exposing encapsulated cells to adverse conditions, such as heat, high pressure, voltage or shear stresses [52]. However, apparatus using acoustics can be influenced by external disturbances, such as vibrations and noise, resulting in undesirable droplet ejection. Furthermore, the forces generated by acoustic fields may not be adequate to form droplets of viscous materials such as hydrogels or bioinks with high cell concentrations [51].

(b) Microvalve-based bioprinting

Microvalve-based bioprinting involves the use of a pressurised reservoir of liquid bioink and a nozzle with an electromechanical solenoid microvalve-controlled orifice. In typical configurations, the print head contains a solenoid coil and a plunger, which blocks the nozzle orifice when no voltage is applied. On application of voltage to the solenoid coil, a magnetic field is produced, pulling the plunger upwards and thus unblocking the nozzle orifice. When the nozzle is open, if the back pressure in the bioink reservoir is sufficient to overcome the orifice surface tension, the pressure gradient forces the bioink through the orifice. The applied pressure and valve opening (gating) time work in tandem to close the plunger, sealing the orifice and causing the formation of bioink droplets. The main elements of the micro-valve bioprinting process can be seen in Figure 2-6.

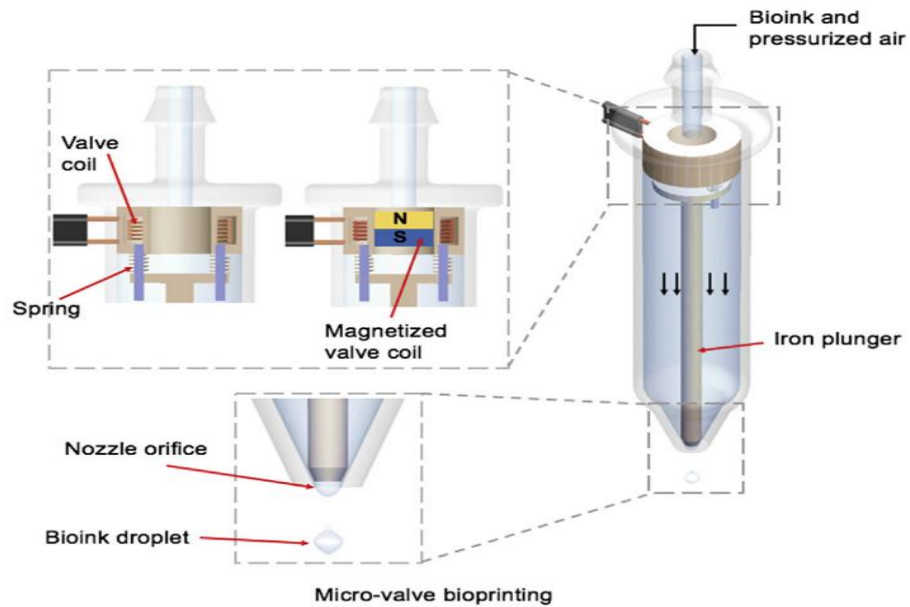


Figure 2-6. Schematic diagram showing the key elements of micro-valve bioprinting [53].

The advantage of valve printing is that it offers high throughput (approximately 1000 droplets per second) [54] and allows precise material and cellular positioning using multiple print heads at high viability [55]. Conversely, valve-based printing is limited as it can only use a limited range of material viscosities (~ 1 to 200 mPa.s) and cell densities due to the tendency for nozzles to clog [56].

(c) Inkjet bioprinting

In essence, inkjet bioprinting involves the physical manipulation of a bioink solution to produce droplets. Gravity, atmospheric pressure and the rheological properties of the bioink solution are utilised in order to eject droplets onto the receiving substrate. The bioink solution is held in place by the surface tension experienced at the nozzle orifice. Droplets are formed when pressure pulses are introduced to the bioink reservoir from an actuator, leading to the bioink overcoming the surface tension. Actuators may be thermal, piezoelectric or electrostatic in nature [57]. A schematic overview of inkjet printing is provided in Figure 2-7.

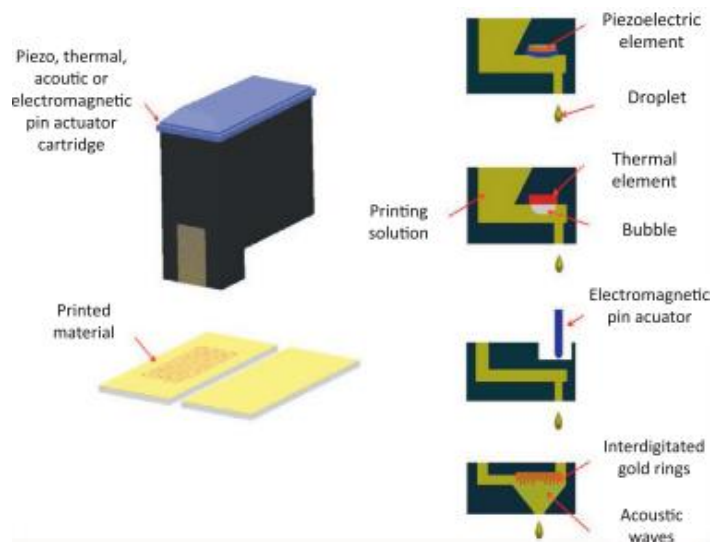


Figure 2-7. Schematic overview of inkjet printing, illustrating the various options for actuation [58].

There are many advantages to using DBB over EBB and LAB. Firstly, DBB allows for the easiest means of patterning as it is very difficult to produce heterogeneity in a gentle manner using EBB and the embedding of multiple biomaterials is challenging using LAB. Moreover, DBB can achieve higher resolution in comparison to EBB, owing to the small volume of material deposited with each droplet, and has comparable resolution with LAB [59].

DBB also benefits from high-speed and high-throughput in a reproducible manner, an attractive set of characteristics for manner industries, such as cancer screening and drug testing [60] [61].

In addition, the printing process of DBB is non-contact in nature, therefore print heads will not make contact with bioprinted constructs, thus preventing the morphology of structures from being distorted or destroyed, as can be the case with EBB, or any unexpected increases in clearance between the nozzle orifice and substrate [62].

In contrast, there are also many drawbacks to using DBB, bioinks in DBB should have low viscosity (3.5 to 12 mPas [63]) and have a non-fibrous structure, to allow easy flow through tubing and nozzles, to avoid the major problem of orifice clogging. The need for low viscosity is, however, problematic as it is challenging for low-viscosity materials to change form into a solid-state structure. Bioinks must also be rheopectic (shear thickening) in nature to allow droplets to form upon ejection from nozzles [64]. Due to these issues, many biomaterials which are widely used in the tissue engineering world, such as high viscosity hydrogels, cell aggregates and micro-carriers, cannot be utilised with DBB [65].

Despite the benefit of the non-contact nature of DBB, droplets can rapidly gel in the air and may not assemble the structure correctly, depending on the gelling nature of the printed material. A further issue with DBB is that of the inherent mechanical weakness of materials, due to the aforementioned restrictions imposed on physicochemical properties to avoid nozzle clogging [66]. Measures such as treatment by adding materials post-print or reinforcing structures with strong nanofibres or polymers can alleviate these issues to some extent however, at the further expense of time or cost [67].

Other limitations of DBB include the need to use low cell concentrations to prevent nozzle clogging and there is a risk of thermal and mechanical stress to cells through the various types of actuators used. Furthermore, non-uniformities in droplet size and issues with droplet directionality, in addition to inaccurate cell encapsulation, are additional hurdles to overcome when using DBB [68].

2.2.1.3. Laser based bioprinting

LAB makes use of laser energy to print liquids onto support substrates at high-precision. LAB can be achieved by two separate means – cell transfer-based and photo-polymerisation. Cell transfer-based operations can involve laser-guided direct writing [69] or laser-induced forward transfer (LIFT) [70], whereby bioink is ejected from a reservoir to the substrate by laser, thus allowing a jet to be produced. The bioink in cell-transfer laser systems should be capable of adhering to substrates whilst possessing low surface tension to allow uniform spreading on the surface without dripping. In addition, the bioink should be capable of transforming thermal energy into kinetic energy with ease whilst also displaying high viscoelasticity and swift gelation to allow jet formation. The LAB process is detailed in Figure 2-8.

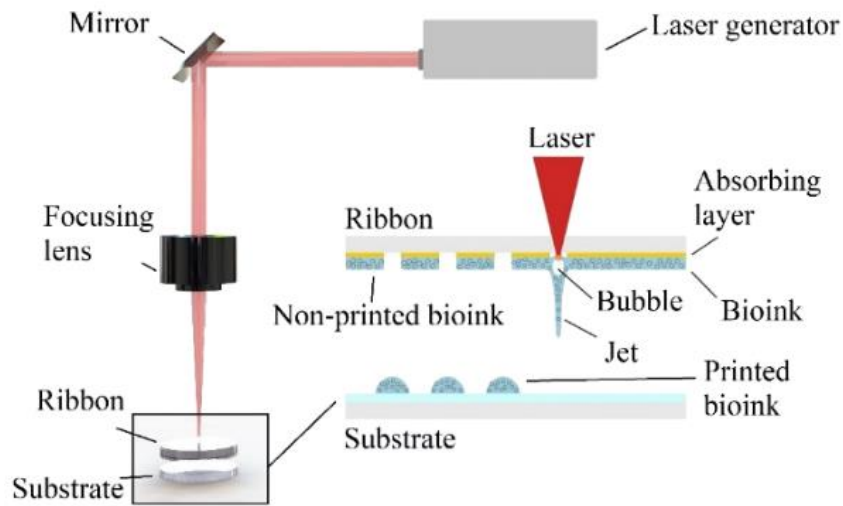


Figure 2-8. Structure and main components of a laser-assisted bioprinter [71]. Note: non-printed bioink may be re-used in a subsequent procedure if cells are not exposed to ambient conditions for a significant period, to avoid cell death (1-6 hours, cell type dependent).

Processes involving photo-polymerisation includes stereolithography (SLA) [72] and two-photon polymerisation (2PP) [73], in which the laser beam selectively causes the solidification of a photo-curable bioink via polymerisation. The use of non-toxic, water-soluble photo-initiators and light absorbers allow photo-polymerisation to occur, resulting in the manufacture of tissue constructs with uniform layer thickness.

LAB possesses many unique advantages over the other printing modalities. Firstly, LAB boasts the highest printing accuracy and resolution, down to micron level [74], which allows single cell or aggregate printing at high cell concentrations [75]. As LAB has no need for nozzles, this avoids the nozzle blockage issues associated with EBB and DBB, even with very high viscosity bioinks, and also eliminates shear stress-induced cell injury and death. The approximate printable viscosity range using LAB is 1 to 300 mPas [76]. LAB can achieve high throughput, up to approximately 5 kHz [77], and can also print cells at high cell viability [78].

With regards to the limitations of LAB, firstly, the high cost and cumbersome nature of LAB equipment is a significant limitation in the adoption of LAB in clinical settings [79]. Therefore, due to these high costs, LAB is considered to be a more immature printing methodology compared to DBB and EBB as research appears to be more focussed on understanding the relationship between laser parameters, such as intensity, pulse time and wavelength, on droplet size and the quality of printed patterns [80].

Furthermore, photo-polymerisation processes suffer from excessive fabrication times, unwanted interactions between the laser light and cells, potentially leading to cell malfunction and death, and also there is a need for a photo-crosslinkable bioink and crosslinking agent, which can bring toxicity issues for cells as well as limiting the range of compatible materials to choose from. Cell transfer printing techniques can suffer from thermal and mechanical-induced shock damage to cells from the laser source in addition to random and gravitational cell settling in printing solutions which can lead to inhomogeneous cell distribution in printed structures [81].

2.2.1.4. Comparison between bioprinting modalities

Given the previous descriptions of each of the three bioprinting modalities, a comparative summary is shown in Table 2-1 below.

Table 2-1. Comparative summary between EBB, DBB and LAB, comparing achievable resolution, bioink viscosity range and cost.

Bioprinting modality	Resolution achievable	Bioink viscosity range	Cost
EBB	100 to 200 μm	30 to 6×10^7 mPas	Low
DBB	10 to 50 μm	3.5 to 12 mPas	Medium
LAB	5 μm	1 to 300 mPas	High

Given the advantages possessed by EBB over DBB and LAB, primarily the printable viscosity range and low cost, the goal of this work was to utilise this technology to improve printing resolution. A piston-driven mechanical extrusion setup was chosen as it provides an easy-to-use, low-cost printing solution with the capability to print key materials identified for this work, such as collagen and alginate. Improving the printing resolution using EBB would contribute a technological advancement in the production of bespoke, transplantable tissue-based constructs due to an improvement in the ability to precisely place cells and biomaterials at desired locations within printed constructs to create functional higher-order tissues and organs.

2.2.2. The bioink

3D bioprinting makes use of the bioink, a term used to describe the combination of biomaterials printed by the bioprinter to fabricate complex 3D biological structures. An ideal bioink will possess a perfect combination of mechanical, rheological and biological properties to facilitate the printing, maturation and function of the target tissue or organ [82]. A bioink may include a combination of hydrogel, cells, ECM materials such as collagen and hyaluronic acid (HA) [83] in addition to proteins such as fibrin/fibrinogen [84], silk fibroin [85] and growth factors [86].

Moreover, speciality chemicals, such as graphene [87] [88], synthetic polymer or metallic nanoparticles [89] [90] and hydroxyapatite [91] may also be added to facilitate the maturation of specific tissues.

There are many challenges to the successful development of bioinks and it is important to note that to this date there are currently no standardised bioinks available for any tissue type found in the human body, thus highlighting the litany of difficulties in bioink research and development.

The selection of constituent materials to form a bioink must satisfy a range of requirements for successful tissue printing and subsequent tissue development. These requirements include printability, mechanical stiffness, structural stability, biodegradability and biocompatibility. A summary of bioink requirements is displayed in Figure 2-9.

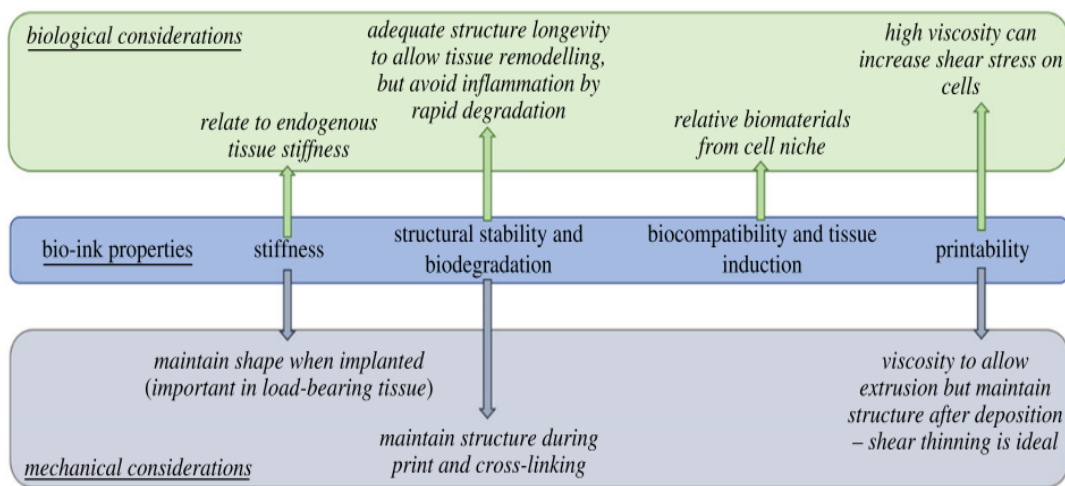


Figure 2-9. The primary properties of bio-ink material have biological and mechanical effects in the engineered tissue [92]. Note: structural stability may refer to both physical and chemical structure.

The printability of a bioink rests in its rheology, namely the ability of the material to be dispensed and to also retain shape fidelity on printing completion [93]. Viscosity and solution homogeneity play large roles in the overall printability of bioinks and are major determinants of the success of the printing process. If bioink viscosity is too high, high shear forces will be required to overcome these viscous forces to allow material flow, often resulting in cell damage and death in addition to nozzle clogging. In contrast, bioinks with low-viscosity usually print structures with low definition due to the flowing of material on the printing substrate after ejection from the nozzle. Low-viscosity bioinks can also result in a less homogenous mixture and nozzle clogging due to cell settling around the nozzle orifice [94].

An ideal characteristic for a bioink is to display shear thinning behaviour, whereby shear forces reduces the solution viscosity and thus allow for easier flow and lower overall shear forces being applied to encapsulated cells whilst maintaining print resolution [95].

The stiffness or Young's modulus of a material measures the ability of a solid material to resist deformation under tension or compression. Owing to their unique natures, different tissues therefore possess varying stiffness values and require varying types and magnitudes of mechanobiological cues to maintain functionality or to assist in the differentiation of stem cells [96] [97] [98]. For example, the stiffness of brain tissue can be as low as 0.1 kPa whereas cortical bone can possess a stiffness in excess of 25 GPa [99]. In vitro 2D cell culture suffers from culturing cells in tissue culture plastics which have undesirably high stiffness values (~1 GPa) which places cells in an environment which is deleterious for their survival [100] [101] [102]. The major advantage of culturing cells in a 3D-printed biomaterial environment is that a more native tissue-like environment can be mimicked. There is a further advantage of bioprinted bioinks over traditional 2D culture in that bioinks can be carefully modified to finely tune the physicochemical properties of said bioinks for printing and concurrent tissue culture in order to match the bioink to the desired tissue type.

The ability of the bioprinting platform to print constructs which maintain the desired shape is essential for the successful fabrication of native-like tissues. In addition to the aforementioned issue of low-viscosity bioinks spreading on printing substrates and hence affecting shape fidelity, cross-linking parameters must also be finely controlled. In the absence of cross-linking, bioinks generally present as low viscosity and will therefore spread on the substrate; excessive cross-linking meanwhile can lead to lamination, characterised by the failure of the structure to coalesce which may lead to mechanical problems [103].

Therefore, the chosen bioink cross-linking process must be tightly controlled in order to produce constructs with sufficient viscosity to retain shape integrity and to also prevent layer lamination in order to facilitate coalescence of successive layers as they are printed. Each printed layer must also possess sufficient mechanical strength to withstand the weight of following layers without deformation or collapsing.

Furthermore, printed bioink scaffolds intended for transplantation must allow sufficient time for cells to integrate, secrete ECM and form new tissue prior its degradation, thus solely leaving behind functional tissue.

It is therefore imperative that the rate of degradation is such that enough cells are retained in the scaffold to provide tissue functionality to scaffolds without eliciting excessive immunological (macrophage build-up) or toxicological issues and also to avoid a scenario where the scaffold fails to degrade in the body, leading to a failure of the construct to repair the target tissue [104]. The biodegradability of printed structures can be tuned by modifying the physicochemical properties of the selected bioink components in addition to the manipulation of cross-linking processes [105].

The bioactivity of a biomaterial is an important aspect to understand as it is important to comprehend cell-material interactions and the potential of materials to form tissues or to simply exist as a mechanical support material which may also elute useful biomaterials. For example, alginate, a commonly used porous biomaterial, is bioinert and non-bioactive, therefore the immune response will not be elicited and cells will not attach and their mobility will be restricted on encapsulation within alginate structures [106]. However, alginate is useful both as a mechanical support material but also to encapsulate biomolecules such as growth factors for time-dependent release [107]. Conversely, bioactive materials such as collagen and hyaluronic acid possess RGD (arginine-glycine-aspartate) amino acid groups which facilitate the interaction with cellular integrin receptors to provide cell attachment, which is necessary for cell survival and proliferation [108]. However, collagen is also involved in the immune response, where it is secreted by myofibroblasts, which may lead to tissue fibrosis, therefore care must be taken on material selection to prevent undesirable cell-material interactions on implantation [109].

2.2.2.1. Hydrogels as bioinks

The key structural component of bioinks is the hydrogel. Hydrogels are polymer-based structures of hydrophilic nature, with the ability to swell in high water content surroundings. Upon gelation, hydrogels provide the three-dimensional architecture required for cells to survive and proliferate [110]. With bioprinting, a major consideration is that the hydrogel degradation rate should be commensurate with the rate of formation of new tissue to ensure the structure can be maintained during host integration [111]. A summary of the requirements of hydrogels for 3D bioprinting using bioinks is displayed in Table 2-2.

Table 2-2. Hydrogel requirements for 3D bioprinting using bioinks.

3D Structure	High porosity, integrin-activated, stiffness
Viscosity	Shear stress: shear-thinning/shear-thickening
Surface tension	Retention inside nozzle until printing. Limited spreading, spraying, spilling upon printing
Gelation	Rapid gelation via crosslinking, shape-retention
Physical properties	Molecular mass, concentration, composition, temperature sensitivity, diffusion properties
Cell integration	Minimal viability loss during printing due to nozzle shear stress. Cell differentiation, proliferation, growth, tissue formation

Hydrogels can be broadly classified into two categories: natural and synthetic. Generally, natural hydrogel materials offer high biocompatibility and biodegradability whilst innately having the structure to support cell migration, adhesion, maintenance and growth, with the major drawback of lacking the mechanical strength to support their own weight and can also suffer from batch-to-batch variability [112]. Conversely, synthetic materials possess the mechanical strength to retain shape and structural integrity but generally suffer from poor biocompatibility and are largely non-biodegradable. In the case where synthetic hydrogels are biodegradable, there may be a risk of toxicity or immunogenicity issues caused by resulting degradation products [113]. A summary of the ideal requirements of engineered tissues is presented in Table 2-3, by adaptation of a table created by Catto et al. [114].

Table 2-3. Ideal requirements of engineered tissues [114].

Biocompatibility	<ul style="list-style-type: none"> • Non-toxic • Non-immunogenic • Not susceptible to infection • Growth potential for paediatric patients • Non-cytotoxic degradation products
Mechanical properties	<ul style="list-style-type: none"> • Mechanical properties similar to native vessel to allow structural stability • Adequate suture retention/ neighbouring vessel integration
Processability	<ul style="list-style-type: none"> • Low manufacturing costs • Readily available with many different sizes • Sterilisable • Easy storage

Some of the most commonly used natural hydrogels include alginate, collagen and chitosan [115], whilst synthetic polymers such as Pluronic F-127, PEG (polyethylene glycol) and PCL (polycaprolactone) are widely used for scaffold fabrication purposes [116].

2.2.2.2. Alginate as a hydrogel

Alginate, or alginic acid, as one of the most common bioprinting hydrogels, presents as a naturally-occurring, water-soluble, anionic polysaccharide derived from the cell walls of brown algae. Alginate exists as a linear copolymer composed of blocks of (1,4)-linked β -D-mannuronate (M) and α -L-guluronate (G). Alginates differ in G and M ratios (G/M ratio) and block length depending on source. These blocks may exist as consecutive G- or M- blocks or in alternating MG- (or GM-) blocks. Alginate benefits from biocompatibility, low toxicity and low-cost and is highly desirable in biomedical applications due to its ability to cross-link to create a highly-tuneable, three-dimensional, mechanically-stable scaffold network which can be used as an extracellular matrix mimic as a cell and tissue scaffold material [117]. By manipulating the type of alginate used (molecular weight, G/M ratio, pH, concentration and viscosity), the alginate shell mechanical and degradation properties may be finely tuned. In addition, the wide use and study of alginate is boosted by its regulatory approval status with the US Food and Drug Administration (FDA) [118], thus eliminating notoriously long lab-to-patient approval times. Figure 2-10 presents the chemical structure of alginate, highlighting the G- and M- and GM-blocks.

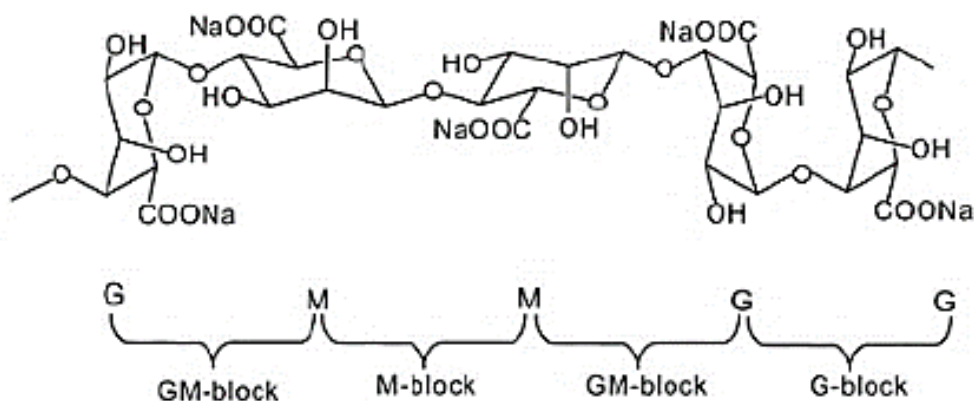


Figure 2-10. Sodium alginate chemical structure, illustrating the G-, M- and MG-blocks as part of the polymer chain [119].

Divalent cations such as calcium, strontium and barium bind preferentially to the carboxylic acid groups located on G-blocks. However, it has been found that M- and MG-blocks may also participate in the ionic bonding process [120]. The most commonly-used cation, Ca^{2+} , may bind to G- and MG-blocks, barium (Ba^{2+}) may bind to G- and M-blocks whereas strontium (Sr^{2+}) binds solely to G-blocks [121]. This facilitates ionic bonding between neighbouring alginate chains to form a three-dimensional, porous hydrogel structure capable of being used as a scaffold material in cell and tissue engineering. The affinity of alginate for divalent cations has been proven to decrease in the following order: $\text{Pb} > \text{Cu} > \text{Cd} > \text{Ba} > \text{Sr} > \text{Ca} > \text{Co, Ni, Zn} > \text{Mn}$ [122]. The gelling and ion-binding properties of alginate is affected by the specific properties and choice of divalent cation [123].

Upon cross-linking, alginate hydrogels allow the diffusion of water into the cross-linked three-dimensional network, resulting in volume swelling. Swelling is largely dependent on the cross-linking ratio, a measure of the number of moles of cross-linking agent to the number of moles of hydrogel polymer repeating units. It has been shown that as the cross-linking ratio increases, through an increase in the concentration of the cross-linking agent, swelling ability diminishes, showing an inverse proportionality link between cross-linking ratio and swelling. An increase in the degree of cross-linking leads to a more compact hydrogel structure and a subsequent reduction in the capacity for water uptake [124]. Alginate pH has also been shown to affect swelling, whereby low levels of swelling were observed in acidic environments [125]. Figure 2-11 illustrates the alginate cross-linking mechanism, where an 'egg box-like' structure is produced.

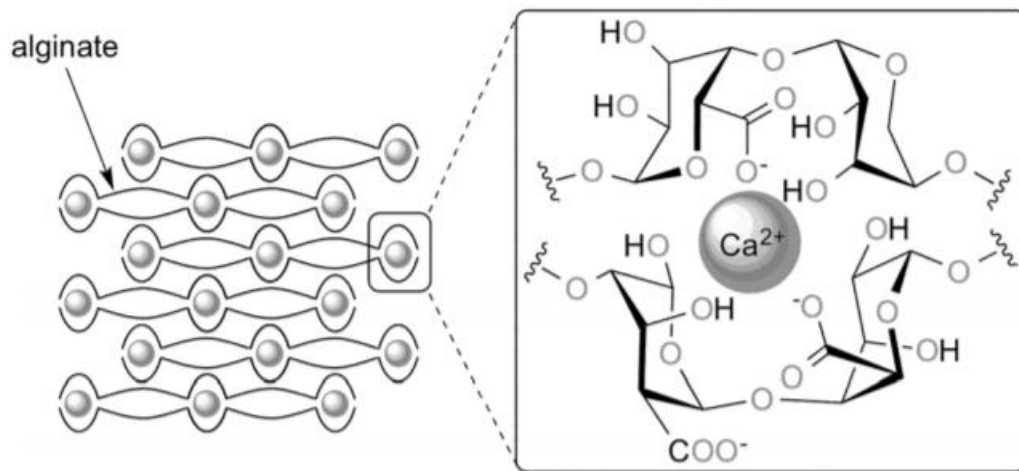


Figure 2-11. Alginate cross-linking mechanism using Ca^{2+} to produce an 'egg box-like' structure, adapted from [126].

Cross-linked alginate structures are susceptible to degradation caused by various ions contained in cell culture media, including phosphate, sodium, potassium and magnesium [127]. It is therefore imperative that cross-linked alginate structures retain integrity for sufficient time to facilitate ECM and tissue formation and maturation prior to any in vivo testing [128]. If required, alginate structures may be readily dissolved, primarily by means of chelation, using chemicals such as EDTA (ethylenediaminetetraacetic acid) and sodium citrate to remove divalent cations from the cross-linked alginate structure. A further, non-ionic, alginate degradation mechanism is by the enzymatic breakdown of the alginate backbone using the enzyme alginate lyase [129]. The degradation of alginate scaffolds should result in the production of high-viability, fine diameter transplantable tissue filaments.

2.2.2.3. Collagen

Collagens are the most abundant protein type in the human body and are a vital structural component in the ECM of many tissues. Collagen is categorized into 28 subtypes, with types I, II and III making up 80–90% of the collagen in the human body, whereby type I collagen is the most expressed of the three [130]. Figure 2-12 summarises the various types of collagen and their relative locations within the human body. Collagen I is also the most-studied collagen type, owing to its excellent biocompatibility and mechanical properties.

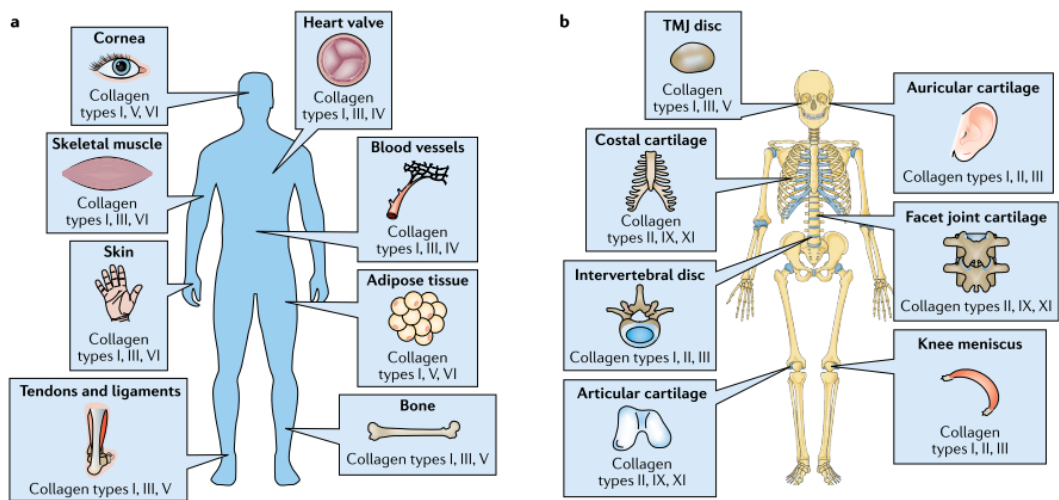


Figure 2-12. Image illustrating the locations of the different types of collagen in the human body. Three of the most abundant collagen types are displayed for non- cartilage tissues (panel a) and cartilage tissues (panel b). TMJ, temporomandibular joint [130].

Collagen type I exists as a heterotrimer molecule whereby in the majority of configurations the trimer structure consists of two $\alpha 1(1)$ chains and one $\alpha 2(1)$ chain; in the minority of cases the homotrimeric form of three $\alpha 1(1)$ chains is present. These three chains are strongly held together through a combination of covalent and hydrogen bonds to form a triple helix strand structure, known as tropocollagen. Triple helix strands may self-assemble in a hierarchical order, leading to the formation of strong collagen fibres found in the body [131], as is illustrated in Figure 2-13. Each chain consists of in excess of 1000 amino acids, measuring approximately 300 nm in length and 1-5 nm in width [132].

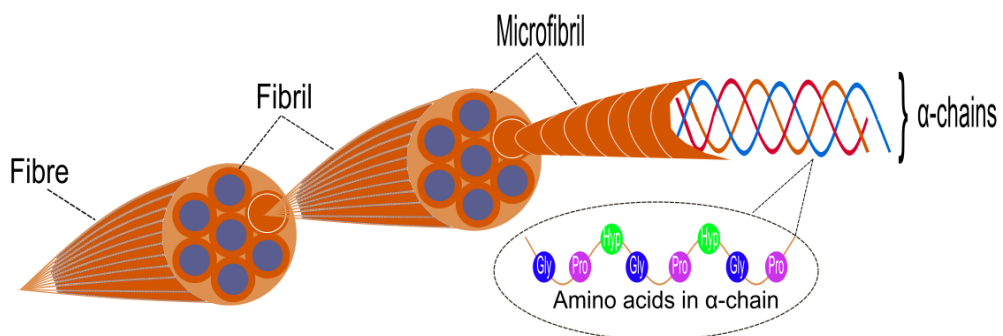


Figure 2-13. Illustration of collagen hierarchical organisation from tropocollagen to complete fibres.

Within the collagen triple helix structure, there is a glycine (Gly) residue located in every third position. The collagen structure may therefore be described by the repeating sequence of Gly-X-Y triads whereby proline (Pro) in the X-position and 4-hydroxyproline (Hyp) in the Y-position represent the most common triplet (10.5%). The Gly-Pro-Hyp triplet provides vital structural stabilisation to mammalian collagen triple helices [133]

Rat tail tendon, porcine and bovine skin-derived collagen type I are the most commonly-used sources of collagen. In addition, an abundant but currently under-studied source of collagen is marine collagen, which is mainly harvested from the skin, scales and bones of fish, molluscs and from various tissues of marine invertebrates. Marine collagen benefits from a reduced risk of disease transmission and in its inherent abundance, however, there is a lack of clinical studies to assess the therapeutic effects of marine collagen-based scaffolds for tissue engineering in humans [134].

Despite the benefits of using the current gold standard animal-derived form of collagen, there are risks which must be addressed to limit adverse reactions on clinical use of these therapies. There is a risk of infectious disease transmission arising from the various purification processes [135] [136] in addition to immunogenicity issues on integration with host tissues and batch-to-batch variability [137] [138].

Human-derived collagen has also been developed as an alternative but suffers from high cost and batch-to-batch variation resulting from factors such as age, ethnicity and environment, leading to undesirable mechanical and chemical issues such as increased resistance to collagenase, decreased elasticity and loss of osmotic swelling capacity [139] [140]. Furthermore, recombinant collagen sources benefit from the ability to produce chemically-identical batches at scale whilst avoiding pathogenic infection [141]. However, the combination of low yield, high cost and the failure of recombinant collagens to achieve the desired post-translational modifications observed with native collagen have prevented successful adoption of this technology in most research labs across the world [142]. Furthermore, there are many methods which can be employed to extract collagen from tissues, including alkali, acid, enzymatic and acid-driven salting-out extraction [143] [144].

Rat tail tendon-derived collagen was selected as the collagen source for the work presented in this thesis, primarily due to the combination of low-cost [145], plentiful supply, predictable concentration and relative ease of processing and purification using an acetic acid extraction process [146].

The acetic acid extraction process leads to the decomposition of collagen fibres and fibrils into collagen aggregates consisting of collagen monomers suspended within the acetic acid solution. These small aggregates self-assemble in vitro at neutral pH, with sufficient ionic strength and at room temperature and appear identical to those seen in vivo, therefore allowing in vitro studies to provide accurate model studies [147]. Self-assembled collagen gels exhibit excellent biocompatibility and can be formed into any shape capable of confinement for studies.

Unfortunately, these collagen gels are mechanically weak, due to inherent low biomechanical stiffness and elasticity in addition to their rapid biodegradation which leads to their unsuitability for in vivo studies [148], however, cellular remodelling of collagen may overcome this limitation [149]. Collagen is naturally degraded by matrix metalloproteases (MMPs) specifically collagenases [150] and serine proteases such as trypsin [151]. This consequently bestows control of ECM degradation and remodelling to embedded cells within the engineered collagen construct, thus allowing cells to remodel the collagen to their specific needs and requirements. Figure 2-14 illustrates the various forms of collagen which can be used in practice in addition to providing a representative example of haematoxylin and eosin staining of a collagen hydrogel scaffold.

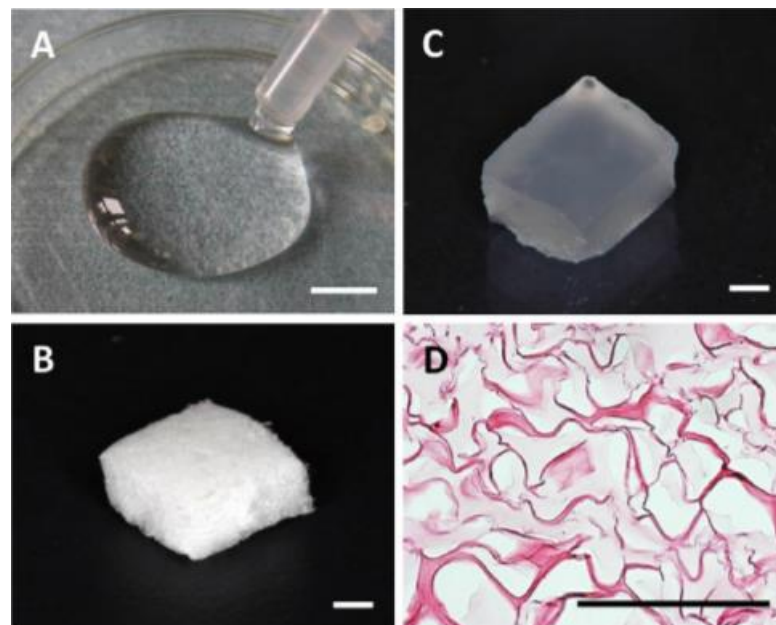


Figure 2-14. A: Bovine-derived collagen hydrogel, B: Collagen sponge, C: Collagen hydrogel scaffold, D: Haematoxylin and eosin staining of collagen hydrogel scaffold. Scale bars: A = 5 mm, B and C = 1 mm, D = 100 μm [152].

In many cases, however, the use of cross-linking or tissue-engineered scaffolds to mechanically support collagen gels in vitro is essential [153]. The mechanical properties of collagen may be improved by use of chemical cross-linkers including glutaraldehyde [154] and carbodiimide [155] or by physical means, such as UV irradiation [156], freeze drying [157] and heating through dehydrothermal treatment (DHT) [158].

In addition, collagen may also be enhanced by blending with natural and synthetic polymers such as hyaluronic acid and PLA [159].

Interestingly, an analogue of collagen, collagen methacrylamide (CMA), has been developed, which retains the natural properties of collagen but becomes rapidly photo-cross-linkable using UV light and also thermo-reversible due to the addition of methacrylate groups to lysine residues on the collagen protein backbone. This process allows control of the mechanical and bioactive properties of CMA by manipulating the cross-linking conditions, such as UV exposure time, photo-initiator type and its relative concentration, thus rendering CMA a very attractive material for tissue engineering [160]. Figure 2-15 exemplifies the difference between the gelation mechanisms of type I and methacrylated collagens.

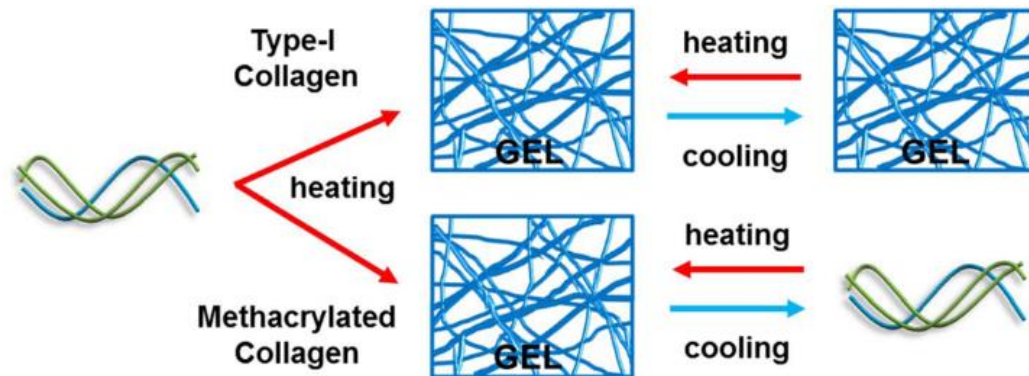


Figure 2-15. Comparison between the gelation mechanisms of type I collagen and methacrylated collagen, illustrating the ability of thermo-reversible methacrylated collagen to retain fibre ultrastructure with changing temperature [160].

A further consideration to make upon utilisation of collagen for tissue engineering purposes is that to achieve a high level of tissue functionality it is imperative that self-assembled collagen fibrils are aligned appropriately to achieve the intended tissue geometry, in the case of fibrous tissue engineering fibrils would ideally be aligned parallel to the walls of a cylindrical scaffold in order to facilitate the alignment and subsequent aggregation of seeded cells [161].

2.2.2.4. Cells

With regards to the integration of cells into hydrogels to form printable bioinks, cells can be added to hydrogels by simple mixing of cell pellets in media with hydrogel, allowing cell encapsulation. Additionally, cells may be printed when in a more tissue-like state, in the case of tissue spheroids or organoids [162], allowing more robust organ-like in vitro cell studies. Interestingly, tissue strands have also been used, whereby Yu et al. [163] harvested cells and microinjected them into tube-shaped semi-permeable capsules to obtain tissue strands upon cell aggregation. This allowed scaffold-free fabrication of tissue strands without the need for hydrogel or delivery medium.

With regards to the choice of cell form, there are a few limitations and challenges to understand to lead to successful tissue development. On progressing from single cells, particularly from stem cells followed by primary or differentiated cells, to cell aggregates or spheroids and finally to organoids and tissue strands, cells gain more tissue-like, specialised function, which naturally facilitates the growth and production of further tissue due to the desired architecture and cell signalling being readily available for newly-produced or migrated cells to utilise, as opposed to the need for growth media supplementation [164]. In addition, as the size of the cell precursor becomes larger, issues with nutrient availability and lack of vascularisation arise, leading to necrosis, thus limiting the use of higher-level options, such as spheroids and organoids. In addition, larger constructs will also be subject to larger shear forces on printing with nozzle-based printing platforms to achieve fine filament diameters, potentially leading to considerable cell damage and death [165] [166].

For the experiments detailed in Chapter 5, adipose-derived stem cells (ADSCs) were utilised for cell seeding applications. ADSCs offer many advantages over other cell types for a variety of reasons. Firstly, ADSCs are relatively easier to harvest due to the minimally-invasive nature of accessing adipose tissue in comparison to other popular stem cell types, such as mesenchymal stem cells (MSCs) which are usually derived from bone marrow or umbilical cord blood [167]. ADSCs bypass the ethical difficulties faced when using embryonic stem cells (ESCs), meanwhile, there is no need for reprogramming of adult cells, necessitating the use of expensive transcription factors and extra processing steps, when using induced pluripotent stem cells (iPSCs). ADSCs also possess minimal immunogenicity [168] and have the ability to secrete useful growth factors and cytokines [169]. Finally, owing to the multipotency of ADSCs, various tissue types may be engineered through this single cell source, a major advantage to co-culture scenarios.

2.3. Engineering of tissue fibres

Given that many tissues of the human body are aligned in structure and orientation, such as vasculature [170], nerves [171] and articular cartilage [172], correct alignment of cells and biomaterials during tissue engineering is vital to achieve and maintain tissue-specific function. In the body, the surrounding ECM environment helps to regulate cell alignment, surface topography and cell signalling thus tissue engineered constructs must also achieve this by mimicking the structure of the native ECM [173]. Therefore, successful fabrication of fine diameter biomaterial filaments, or fibres, can provide the foundations for the production of higher-order tissue or organ constructs with correct biomaterial alignment by using these filaments as the building blocks.

In this respect, the current limitation of tissue engineering is that biological constructs with degrees of cell and ECM alignment comparable to native tissue are yet to be fabricated [174] [175] due to material and resolution limitations; however, this is a challenge in which the field is endeavouring to overcome. Efforts are being directed towards researching a combination of new biomaterials to achieve better cell alignment and physicochemical properties, such as smectic liquid crystal elastomer coatings with nano-grooves, which have demonstrated excellent ability to align human dermal fibroblasts over large areas [176]. An overview of smectic liquid crystal use for cell alignment is shown in Figure 2-16.

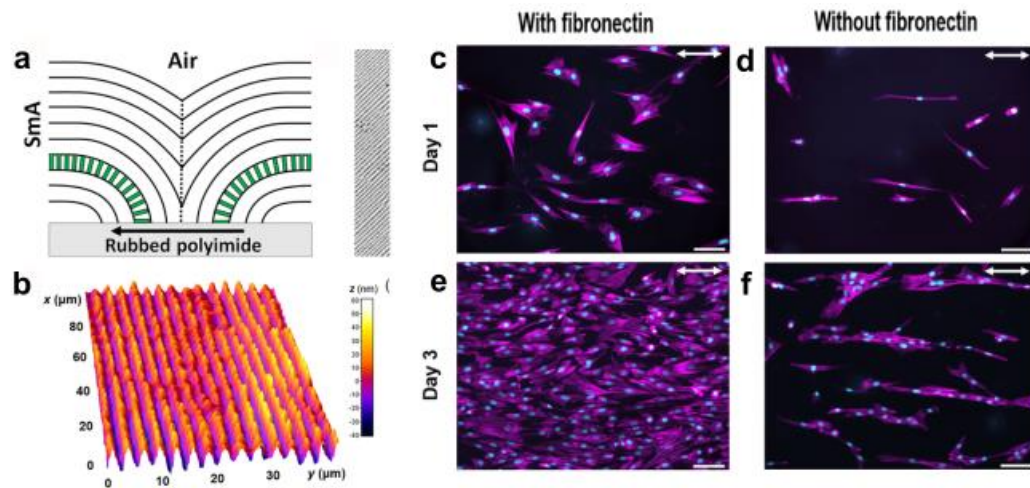


Figure 2-16. (a) Schematic representation of the oily streak structures at the air/smectic A (SmA) liquid crystal (LC) interface. The green ellipsoids represent liquid crystal molecular orientation within SmA layer. (b) R-DHM texture of the surface profile of SmA LCE grooved substrate. (c – f) Fluorescent microscopy images, Day 1 of human dermal fibroblasts (hDF) grown on (c) fibronectin coated and (d) fibronectin-free nanogrooved SmA LCE substrates, showing that aspect ratio (AR) of hDFs plated on fibronectin-free substrate is ~2 times higher. Day 3 of hDFs grown on (e) fibronectin coated and (f) fibronectin-free nanogrooved substrates. The arrows represent the direction of the nanogrooves. Actin filaments stained with Alexa Fluor 488 phalloidin are presented in purple, while the cyan regions indicate the nuclei stained with DAPI. Scale bars 100 μm [176].

Additionally, the use of highly-conductive, electrospun MXene nanofibres (two-dimensional metal carbides) have shown excellent biocompatibility and have displayed enhanced differentiation of mesenchymal stem cells into osteoblasts for bone tissue engineering, aided by the possession of outstanding mechanical properties and large surface area (see Figure 2-17) [177].

Furthermore, efforts are also being directed towards reducing filament diameters, to achieve more precise cell and biomaterial placement, using techniques such as direct laser writing with two-photon polymerisation and digital light processing in combination with bioprinting [178] [179].

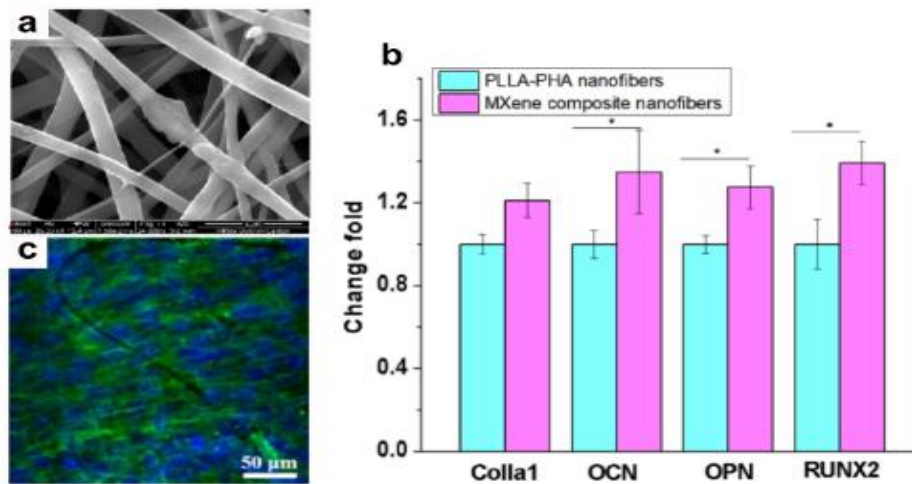


Figure 2-17. (a) SEM image of MXene composite nanofibers (24x magnification). (b) Osteogenic differentiation of BMSCs after 14 days of culture on samples, n=4. (c) Fluorescent images of BMSCs after 5 days of culture on samples, showing F-actin filaments stained in green and cell nuclei stained blue [177].

Tissue engineered filaments can be used in multiple configurations, ranging from aligned electrospun fibres, micropatterns, aligned or channelled structures or in combinations of these different aligned structural configurations. These options have been used in the engineering of many different tissue types, ranging from nerves [180] to muscle fibres [181], tendon [182] and dentine (dentin) [183] [184]. An overview of the application of aligned tissue engineered structures is displayed in Figure 2-18.

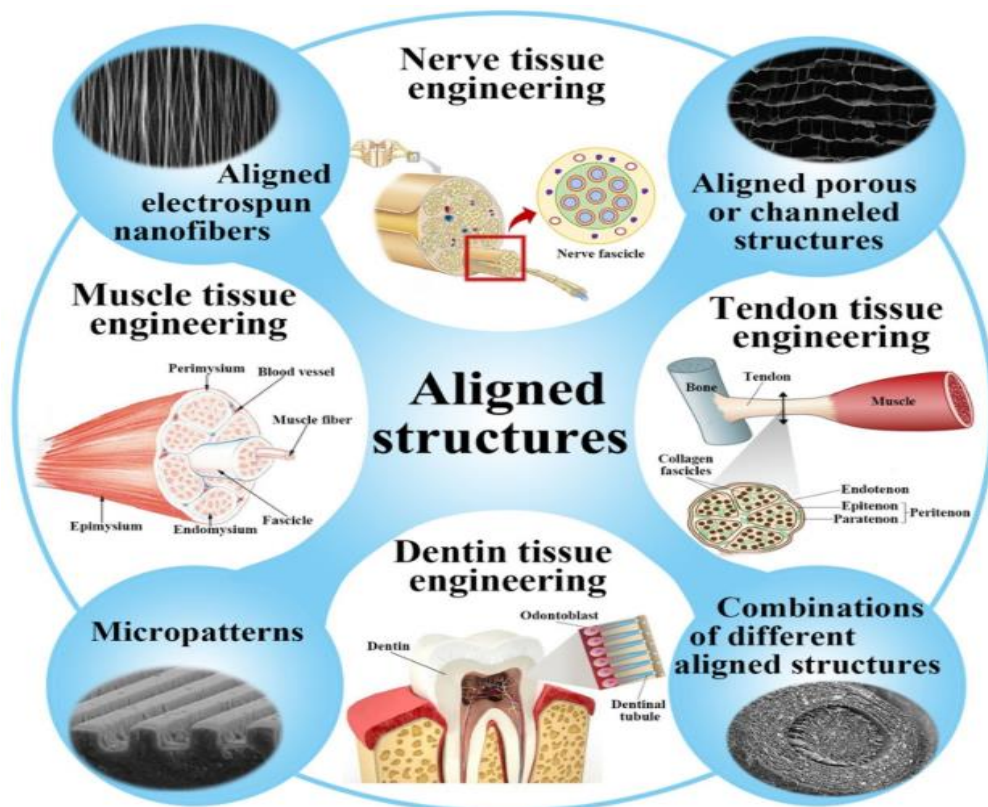


Figure 2-18. Schematic of the biofabrication of aligned structures, including aligned electrospun nanofibers, aligned porous or channelled structures, micro-patterns and combinations thereof, and their applications in nerve, skeletal muscle, tendon and dentin tissue engineering [184].

Whilst electrospinning involves applying a high-voltage to a polymer fluid in order to eject jets of fine filaments through a spinneret, which are then collected and cured to obtain nanoscale fibres, the process for fabricating aligned nanofibres is slightly different. Magnetic electrospinning involves the use of two magnets attached to a conventional electrospinning apparatus and a low concentration of magnetic material is added to the polymer solution. Employing magnets allows the generation of a magnetic field which aligns spun fibres in parallel and fibres attached to magnets are stretched, leading to an efficient, facile and controllable process to generate aligned nanofibres [185] [186]. A schematic of the magnetic electrospinning process is shown in Figure 2-19.

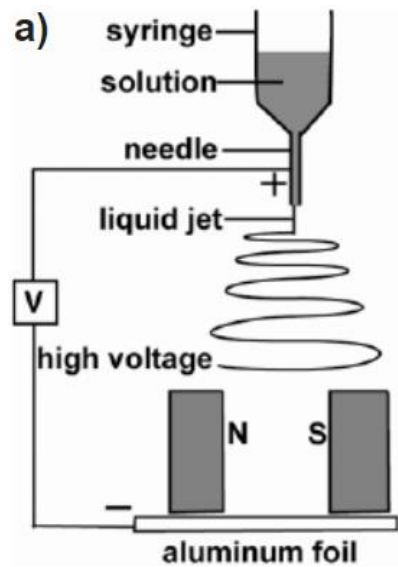


Figure 2-19. Illustration of the apparatus used for magnetic electrospinning to generate aligned fibres [185].

Material micropatterning can be employed in order to study various aspects of cell behaviour in vitro and can provide a platform to mimic native tissue architecture. For example, by manipulating the divergence angle of micropatterns, cell migration direction can be controlled and by additionally changing the micropattern width, the migration speed may also be controlled (see Figure 2-20) [187].

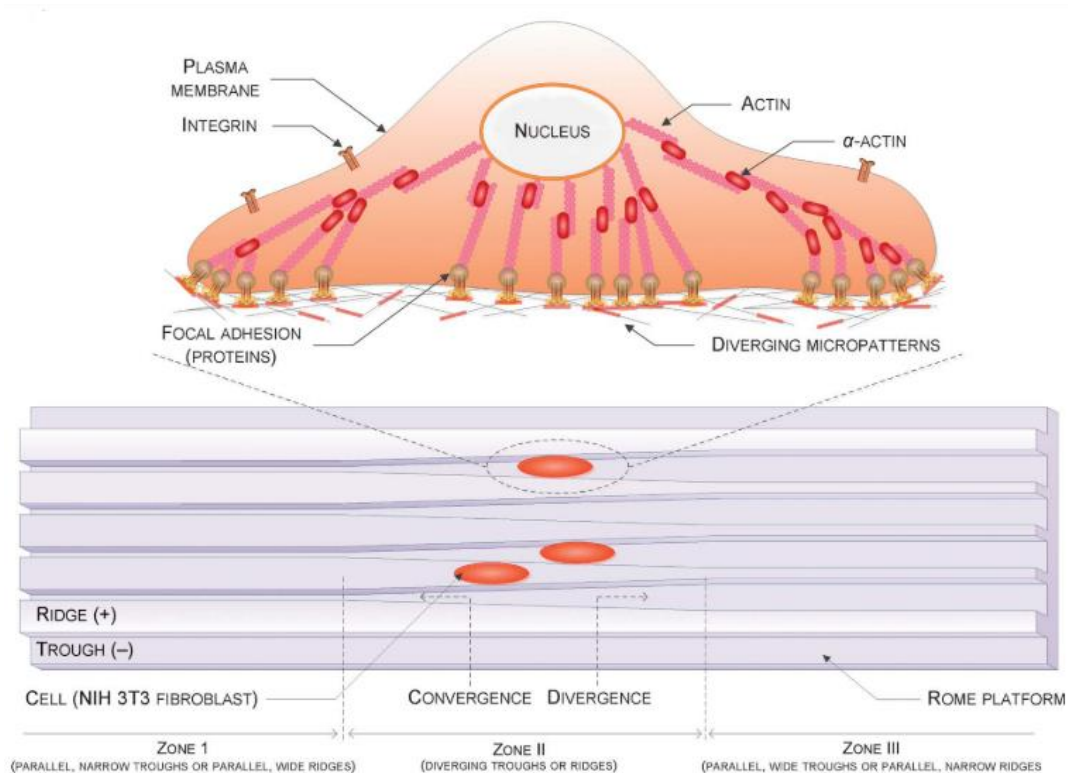


Figure 2-20. A schematic of the Rome (biocompatible, UV-curable polymer) platform composed of parallel and narrow troughs (zone I), diverging troughs (zone II), and parallel and wide troughs (zone III). This assay creates the gradient of physical spatial cues using the micropatterns, thus imposing one-directional morphological polarity on adherent cells [187].

In addition, micropatterns may also induce mechanotransduction [188] and affect stem cell fate by alterations to cell morphology [189]. Biological micropatterning generally involves chemical structure patterning and physical patterning by manipulating surface topology [190]. Micropatterning techniques include photolithography and soft lithography [191], laser-guided techniques [192] and piezoelectric inkjet bioprinting [193].

Aligned porous or channelled structures can be created using directional freezing, otherwise referred to as ice-templating or freeze-casting (see Figure 2-21). Directional freezing involves freezing the material solution to be casted with subsequent freeze-drying under vacuum to sublimate the solvent, thus leaving the porous material behind. As the solute is repelled by the solvent crystals during the freezing process, it is squeezed among them, leaving behind aligned porous channels on completion of the freeze-drying process. The solvent nucleates and crystallises along the direction of the temperature gradient generated by the freezing process, thus the orientation of the crystals and resulting pores can be controlled by manipulation of parameters such as solution physicochemical properties, freezing temperature and structure geometry [194] [195].

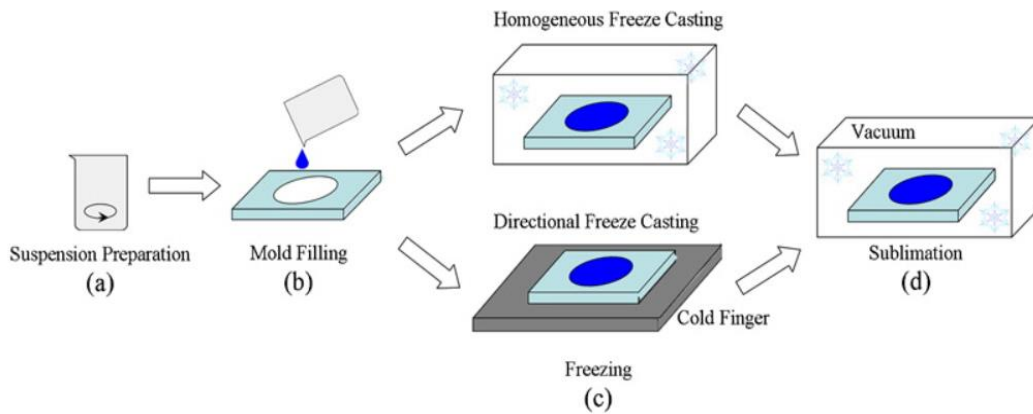


Figure 2-21. Illustration of the freeze-casting process, with options of homogenous freeze casting or directional freeze casting after mould filling [196].

The freeze-casting process can produce structures which can physically guide cell orientation [197], increase scaffold mechanical properties [198] and provide additional control of pore uniformity and overall structure [199].

2.3.1. Tissue engineering approaches for the fabrication of tissue fibres

There has been many different tissue engineering approaches to the fabrication of tissue micro-fibres, ranging from extrusion [200] and electrospinning (ES) [201] to interfacial polyelectrolyte (polyion) complexation (IPC), where fibres are formed through ionic interactions at the interface of polymers of opposing charge [202]. In addition, further alternative methods such as syringe dipping, suture-based composite fibre generation and centrifugal spinning (CS) have also been demonstrated and will now be discussed in further detail.

In 2016, Kalisky et al. [203] used successive syringe dipping, firstly using calcium chloride and sodium alginate to create a calcium alginate hydrogel whereby a cylindrical capillary was formed on removal of the syringe needle (see Figure 2-22). Mouse bone marrow stromal precursor cells were embedded within a type I rat tail collagen solution (5.0 mg/ml) at a seeding density of 50×10^6 cells/ml and injected into the newly-created capillary and cultured over 15 days to form high-viability cell filaments of approximately 200 μm diameter along the collagen backbone. This method benefits from its simplicity and versatility, however, it suffers from having very large (multiple millimetres) shell thicknesses for the first 24 hours of culture, therefore limiting nutrient diffusion. On shell dissolution after 24 hours, cell-seeded collagen fibres were left to culture without any scaffold, leading to major difficulties in fibre manipulation for movement or transplantation purposes due to the inherent mechanical weakness of collagen.

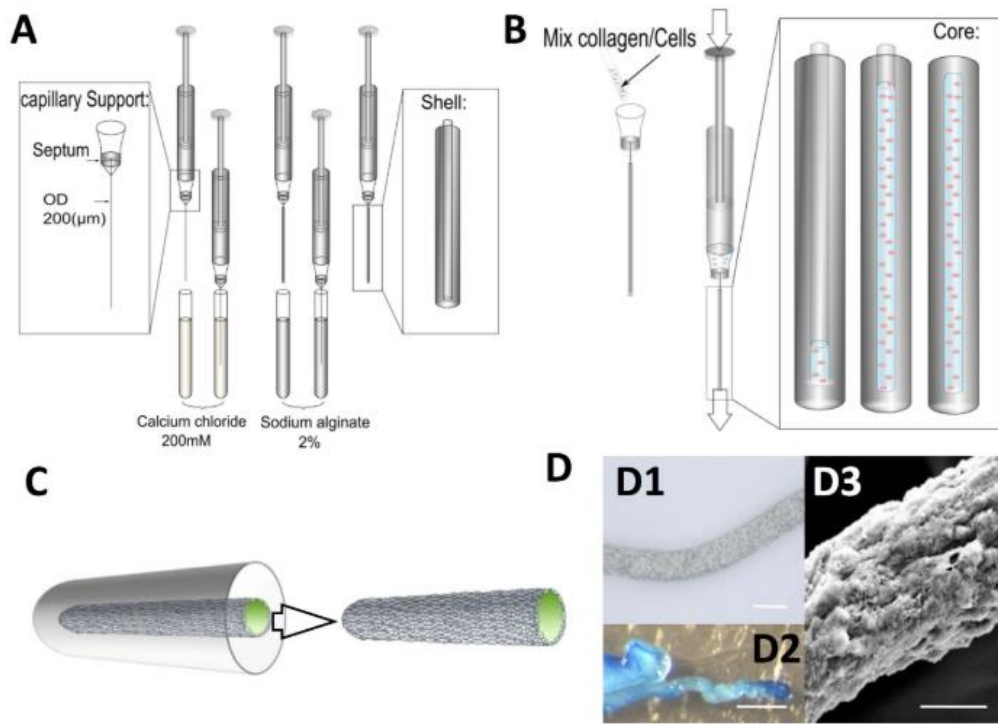


Figure 2-22. Fabrication procedure of the core-shell fibres. (A) Production of the shell using successive alginate coatings. (B) Production of the core by the substitution of the capillary with collagen/cell suspension. (C) Ability to separate the core from the shell after 24 h of culture. (D1) Representative contrast phase microscopy of a fibre at day 4 (scale = 150 μm). (D2) Representative coloration with methyl blue of a fibre at day 4 (scale = 500 μm). (D3) Representative scanning Electron Microscopy of a fibre at day 4 (scale = 50 μm) [203].

In 2017, Costa-Almeida et al. [204] used a previously-developed textile technique whereby non-absorbable silk surgical suture threads were drawn through a sequence of baths coating with a hydrogel mixture of 1.5% alginate and 10% GelMA (both w/v) to create composite fibres, with alginate cross-linking using calcium chloride and UV cross-linking of GelMA. Human tendon-derived cells (hTDCs) were embedded within the hydrogel mixture and composite fibres were subsequently braided, allowing the combination of multiple cell types. Embedded hTDCs remained viable for 21 days. This method benefits from being highly customisable, with various material concentrations and cross-linking times to manipulate in order to control hydrogel thickness. However, this method did not appear to facilitate cell aggregation into fibres with the utilised cell-seeding density (2.5×10^6 cells/ml) [205] and the use of non-absorbable suture material may require an undesirable removal surgery (See Figure 2-23) [206].

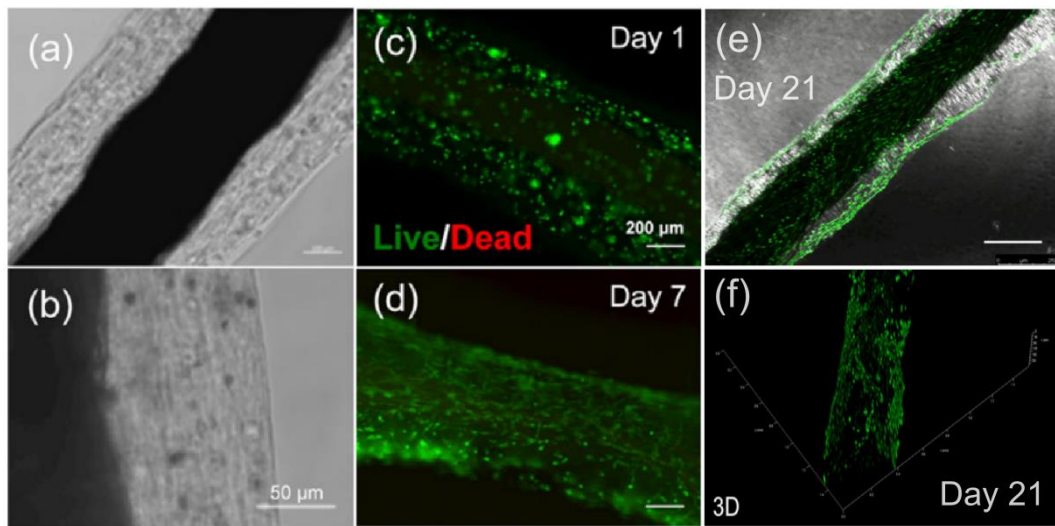


Figure 2-23. Viability of human tendon-derived cells encapsulated in composite fibres (silk suture threads coated in 1.5% alginate/ 10% GelMA). (a and b) Optical microscope images of cell-laden composite fibres after 7 days in culture. Scale bars, (a) 100 and (b) 50 μm . (c and d) Live/dead images of human tendon-derived cells encapsulated within composite fibres after (c) 1 and (d) 7 days in culture. Live cells are green (calcein acetoxymethyl), and dead cells are red (propidium iodide). (e–f) Confocal microscope images of live/dead staining of human tendon-derived cells encapsulated within composite fibres after 21 days in culture. (e) Live/dead image merged with brightfield channel. Scale bars, 250 μm . (f) Three-dimensional reconstruction [205].

Centrifugal spinning is a further method for the fabrication of nano-scale fibres at high speed and low cost. With centrifugal spinning the fluid is situated within a spinning head and is accelerated to increase rotational speed up to thousands of rpm (revolutions per minute). Upon the rotational velocity reaching a critical value, the centrifugal force exceeds the fluid surface tension, resulting in the ejection of a liquid jet from one or more nozzle tips on the spinning head. This liquid jet experiences stretching, caused by inertial forces, to produce fibres as the fluid evaporates, a process based on that of the production of cotton candy [207] [208]. The CS method benefits from a higher production rate and finer fibre diameters in comparison to the electrospinning methodology. Figure 2-24 provides a schematic summary of the CS method.

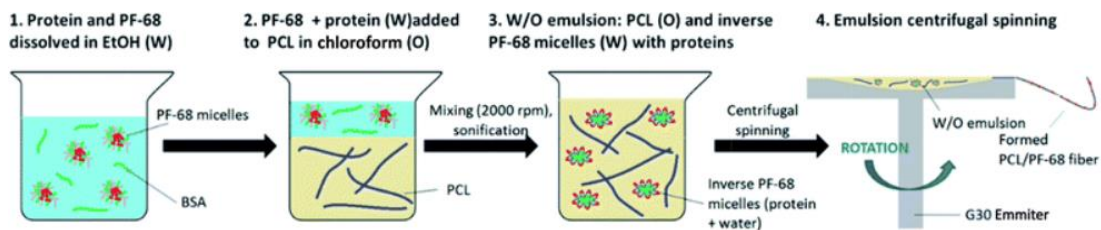


Figure 2-24. Schematic of the emulsion centrifugal spinning process, exemplified by the use of protein and PF-68 dissolved in ethanol (EtOH) which is then added to PCL in chloroform, mixed and subjected to the centrifugal spinning process [209].

In 2017, Buzgo et al. [209] used CS with a voltage of 48 V and the rotational speed set to 11,000 rpm, by using a water-in-oil emulsion, with PCL dissolved in chloroform as the continuous phase and pluronic F-68 (a non-ionic surfactant) dissolved in ethanol as the droplet phase to produce nanofibres seeded with 3T3 fibroblasts and MG63 osteoblasts with demonstrated proliferative ability. The conclusion of this study suggested that the platform was suitable for protein release studies due to showing improved fibroblast and osteoblast metabolic activity and proliferation, however, this platform seems unable to facilitate tissue fibre formation as cellular aggregation into filament-like structures was not demonstrated (see Figure 2-25).

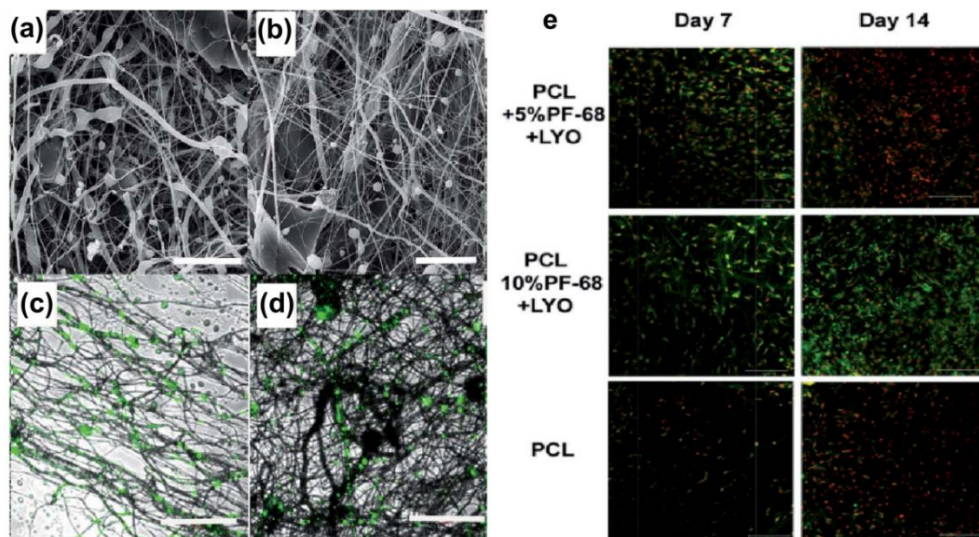


Figure 2-25. Morphology and viability of nanofibers fabricated using centrifugal spinning. (a) SEM image of 40% PCL + 10% PF-68 + LYO. (b) SEM image of 40% PCL + 5% PF-68 + LYO. (c) Confocal image of 40% PCL + 10% PF-68 + FITC-BSA. (d) Confocal image of 40% PCL + 5% PF-68 + FITC-BSA. (e) Confocal microscopy images of coaxial nanofibers seeded with MG-63 cells and platelet lyophilisates (LYO), on days 7 and 14 of culture. Cells were stained with DiOC (3,3'-dihexyloxacarbocyanine iodide, green colour) and propidium iodide (red colour). Scale bars in (a) and (b) = 50 μm ; scale bars in (c) and (d) = 200 μm (unavailable for (e)) [209].

In 2021, Norzain and Lin [210] used combined CS with ES, known as centrifugal electrospinning (CES), with voltages up to 15 kV and rotational speeds up to 3000 rpm, to produce aligned PCL nanofibres capable of supporting the viability and elongation of human fibroblast cells along the direction of the aligned fibres for 14 days, with fibre diameters in the 200 - 400 nm range (see Figure 2-26). Despite this success, there was no observed aggregation of cells into a tissue filament. Furthermore, the CES method requires cell seeding to occur post-fabrication, adding an undesirable further step to the manufacturing process, due to the use of toxic solvents having deleterious effects on cellular survival [211] and long cell infiltration times into electrospun scaffolds [212].

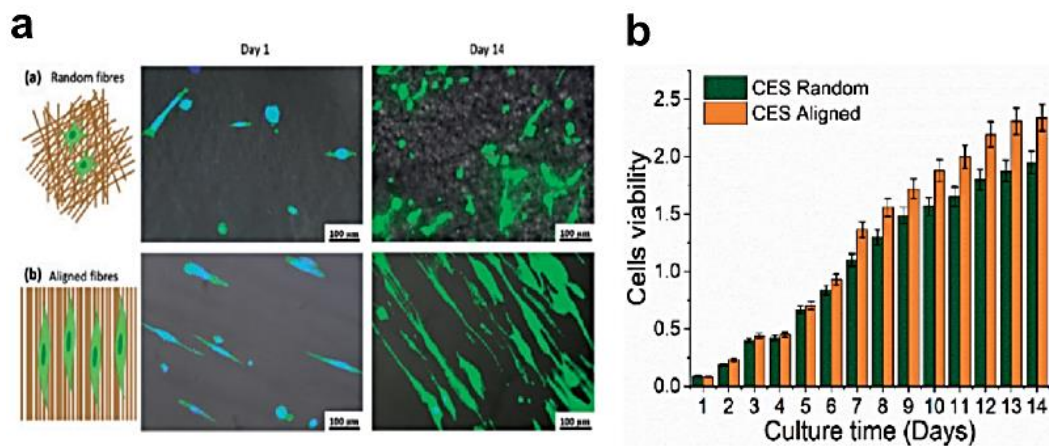


Figure 2-26. (a) morphology of human fibroblasts seeded on PCL nanofibres fabricated using the centrifugal electrospinning method, with either random or aligned orientation. Cell nuclei are stained blue using DAPI (4',6-diamidino-2-phenylindole dihydrochloride). (b) cell viability of human fibroblast cells seeded within randomly-oriented and aligned scaffolds over a 14-day culture period [210].

In summary, tissue engineering approaches have contributed significantly to the progression of tissue filament and fibre engineering. Despite this progress, there are still many limitations and bottlenecks of these approaches. Fortunately, the introduction of bioprinting as a viable tissue engineering platform can contribute to overcome these limitations. Bioprinting facilitates accurate and homogenous placement and distribution of cells on scaffold materials [213] in addition to having the capacity for precise formulations of bioinks containing multiple biomaterials and cell types which can be extruded in a simultaneous manner [214] whilst allowing the tuning of biomaterial physicochemical properties for desired cell-biomaterial interactions [215]. Moreover, the ability to tune biomaterial properties confers greater control of stem cell differentiation (if stem cells are utilised), at any stage of the culture process, therefore increasing the likelihood of producing target terminally-differentiated cell types and tissues [216].

2.4. Coaxial bio-extrusion

On the challenge of printing and extruding cell-laden tissue filaments, it is imperative to contain all biomaterials necessary for the formation and maturation of tissue fibres within a porous hydrogel scaffold, which also acts to provide mechanical support to cultured tissues. It is also essential to fabricate hydrogel scaffolds as rapidly as possible to provide instantaneous stability and containment to extruded cells and biomaterials within the extruded construct.

In response to these requirements, an attractive methodology for the extrusion of tissue fibres and filaments is coaxial bio-extrusion (or simply coaxial extrusion). This approach employs a coaxial nozzle in order to extrude organised structures whereby two nozzles are concentrically aligned to allow extrusion of core-shell structures, whereby ECM with embedded cells are located within the inner core nozzle; meanwhile, the hydrogel solution is extruded through the outer shell nozzle, creating an annular shape whilst flowing through the nozzle. A schematic summary of the coaxial extrusion process is shown in Figure 2-27.

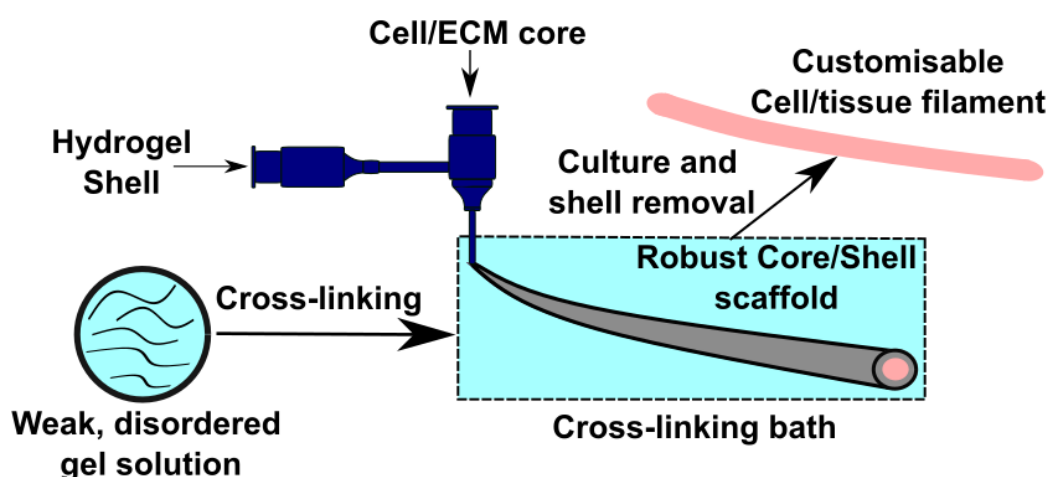


Figure 2-27. Basic overview of coaxial bio-extrusion, showing cross-linking of hydrogel solution to fabricate robust, cylindrical core/shell tissue filament scaffolds.

Alginate is ubiquitously used as the hydrogel solution due to its ability to rapidly crosslink to create a hollow, robust, porous, three-dimensional cross-linked scaffold on contact with a cross-linking bath containing divalent ions, which is usually 100 mM CaCl_2 [217].

Originally developed by Shin et al. [218] in 2007 by combining glass pipettes with a PDMS (Polydimethylsiloxane) chip, coaxial bio-extrusion involves the use of a coaxial nozzle which contains two input ports, the outer shell and the inner core, which, when combined, allow concentric flow. The Shin et al. process is presented in Figure 2-28.

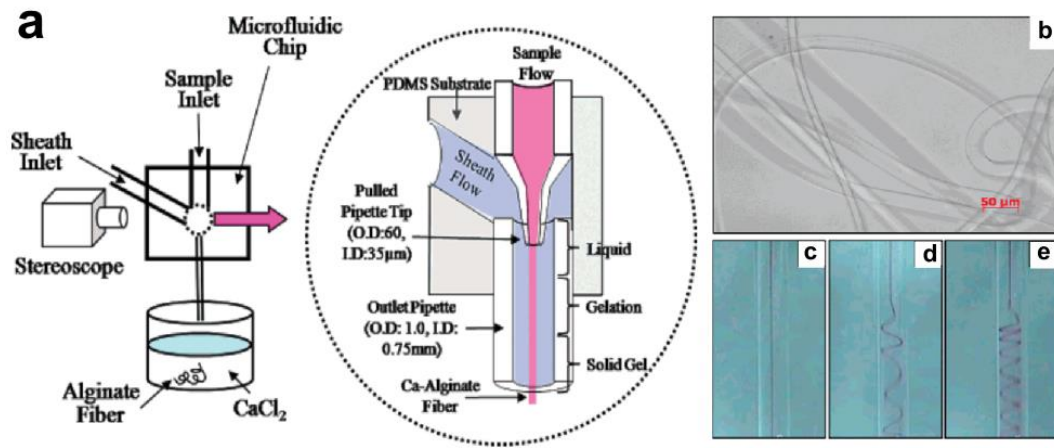


Figure 2-28. Overview of calcium alginate microfibre generation system. (a) Schematic of microfibre generation apparatus and principle of gelation (dotted circle). (b) Calcium alginate fibres generated by using microfluidic system. (c-e) Formation of spiral curl of alginate solution in the outlet pipet according to the flow changes: (c) sheath flow rate: 20 mL/h, sample flow rate: 1 μL/min; (d) sheath flow rate: 20 mL/h, sample flow rate: 3 μL/min; (e) sheath flow rate: 20 mL/h, sample flow rate: 5 μL/min [218].

Whilst Shin et al. used co-flow of an alginate core stream and a CaCl₂ solution shell stream to produce calcium alginate fibres, in 2008, Sugiura et al. [219] produced hollow calcium alginate micro-tubes by adding sodium alginate in the shell stream, coupled with calcium chloride (CaCl₂) simultaneously flowing in the core nozzle and extruding into a CaCl₂ cross-linking bath (see Figure 2-29).

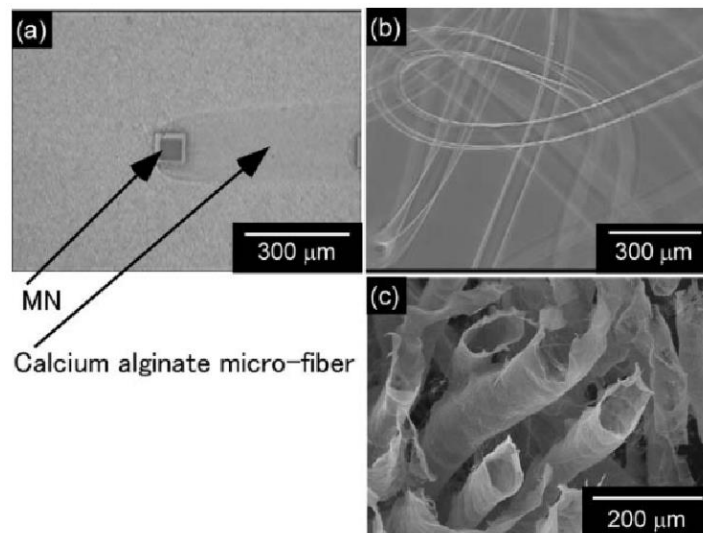


Figure 2-29. Formation of alginate micro-fibres and micro-tubes. (a) Formation process of calcium alginate micro-fibres. Note: MN = micro-nozzle. (b) The recovered calcium alginate micro-fibres. (c) SEM photograph of cross section of lyophilized alginate-PLL-alginate micro-tubes [219].

Monovalent Na^+ ions within alginate are displaced by divalent Ca^{2+} ions through ion exchange to initiate alginate cross-linking between neighbouring carboxylic acid groups to produce a porous, mechanically-stable, tubular hydrogel network of calcium alginate. These partially cross-linked structures may be further cross-linked in the cross-linking bath over time; other divalent cations such as Sr^{2+} or Ba^{2+} [220] may be used in place of or synergistically with Ca^{2+} to tune the alginate shell mechanical properties.

In 2013, Onoe et. al. [221] used this platform to fabricate high-viability metres-long cell-laden filaments of various cell types, including rat cardiomyocyte and cortical cells in addition to HUVECs (human umbilical vein endothelial cells). This was achieved using a microfluidic apparatus by employing cells embedded within a neutralised, type I collagen solution (acid and pepsin-solubilised rat tail-derived) in the core nozzle. Collagen thermal self-assembly occurred within the lumen of the tubular alginate scaffolds to produce mechanically-stabilised cell-laden filaments. Further, differentiation of neural stem cells (NSCs) within pepsin-solubilised collagen was demonstrated, with maintenance of differentiated state on day 77 also shown, therefore providing proof-of-concept of in situ stem cell differentiation and maintained expression of the differentiated phenotype within coaxially extruded cell-hydrogel scaffolds (see Figure 2-30).

Due to the extrusion process lasting less than one minute and due to filaments immediately being removed from the cross-linking bath post-extrusion and washed (usually with saline solution) the effect of exposure of any cells to 100 mM CaCl_2 solution is negligible [222].

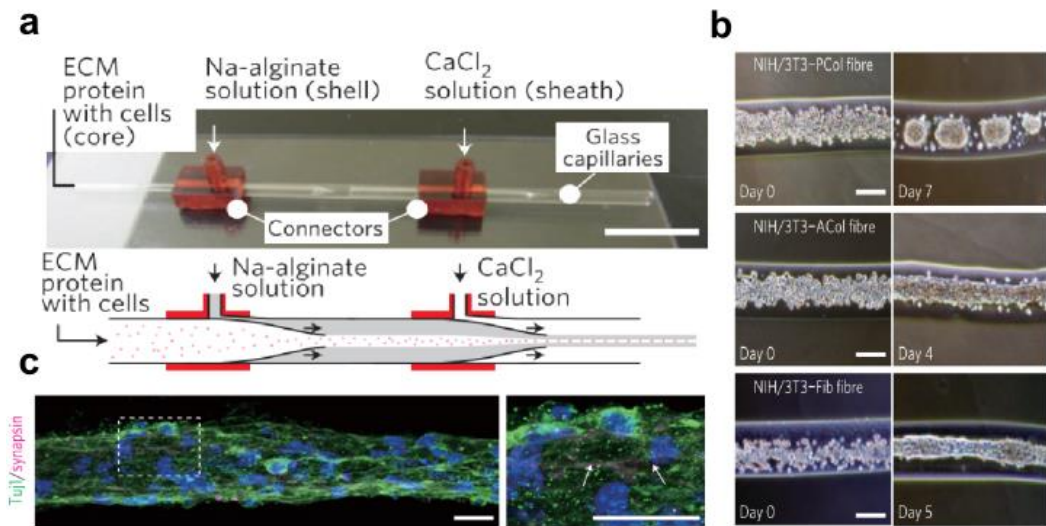


Figure 2-30. Formation of a metre-long cell-laden microfibre. (a) An image (top) and an explanatory illustration (bottom) of the double-coaxial laminar flow microfluidic device. The device was composed of pulled glass capillaries and connectors. A double-coaxial laminar flow consisting of a pre-gel solution of ECM proteins with cells (core), a pre-gel solution of Na-alginate (shell) and a CaCl_2 solution (sheath) was generated in the device, and a cell-containing ECM-protein/Ca-alginate core-shell hydrogel microfibre was continuously formed. (b) Sequential images of the behaviours of NIH/3T3 cells in the different types of ECM protein. NIH/3T3 cells in ACol and Fib formed cell fibres. In contrast, NIH/3T3 cells in PCol did not form cell fibres. (c) Immunofluorescence staining of NSC-PCol fibres with differentiation induction for 77 days. The arrows indicate synaptic clusters (right). TuJ1, green; synapsin, magenta; nuclei, blue. Scale bars in (b) = 100 μm , (c) = 20 μm [221].

The coaxial extrusion approach benefits from a high level of customisation, from hydrogel and bath components and their respective concentrations to the number of input nozzles and their respective internal diameters and geometries [223]. In addition, filament or hollow tube diameter may also be tuned by manipulating nozzle configuration, diameter and flow rates. Moreover, multiple materials may be mixed to create multiple input reservoirs for the extruder to select from in addition to multi-layer structures with lengths in excess of one metre, which may be formed upon the use of multi-axial nozzles [224]. In addition, cells may be added to the shell nozzle in order to create cell-laden tubular structures, this would provide the benefit of cells being closer to their source of nutrition as opposed to cells in the centre of a filament with a tubular scaffold structure, thus aiding cellular long-term viability [225].

Coaxial extrusion, as a versatile tissue engineering platform, has the potential to produce transplantable tissue filaments and tissues, which may be used for tissue or organ-on-a-chip studies, is a viable platform for drug and oncological studies as well as providing a valid model to compare 2D and 3D cellular studies, with the added advantage of being able to implement cell co-cultures. This change in targeted use may simply be achieved by a change of extrusion materials or by modification to extrusion hardware and/or software.

2.5. Challenges and limitations of coaxial bio-extrusion

Due to coaxial bio-extrusion being a nascent field, there are many obstacles to overcome in order to realise this technology in a clinical setting. Firstly, due to the need for rapid cross-linking of the hydrogel scaffold shell material to produce robust scaffolds which will provide sufficient mechanical support for core filaments, there is an inherent limitation in materials which can be used in the shell nozzle, of which alginate is the predominant choice. Therefore, bioink compatibility and formulation remains a major barrier to the progress of this technology as a wider array of rapidly cross-linkable materials are required [226].

Due to the need for nozzles, in the case of reducing filament diameters, lower nozzle sizes and the addition of cells will lead to higher shear stress and damage to cells. This issue becomes manifold with the use of multiple nozzles, as careful selection of bioink formulations, extrusion flow rates and nozzle sizes will be required for each nozzle [227]. Moreover, as there is a requirement for multi-nozzle configurations to fabricate hierarchical structures such as nerve, muscle and vasculature, there is a corresponding increase in nozzle fabrication cost, which may become prohibitive for clinical use, there is therefore a need to produce low-cost, robust, biocompatible nozzles with comparable performance to current commercial options [228]. This cost saving will also aid in situations where nozzle blockages and/or corrosion necessitate disposal of nozzles in use.

Furthermore, as coaxial bio-extrusion facilitates facile extrusion of multiple cell types, work must be done to optimise media formulations to provide each cell type with sufficient nutrition and stimuli [229]. Configurations using minimum essential media and more complex, cell-specific media combinations have been utilised, however, understanding of co-culture media systems is not as developed in comparison to single-cell systems, therefore more work must be done to address this issue [230].

2.6. Recent advances in coaxial bio-extrusion for tissue fibre production

From 2013 onwards, various advances within the coaxial bio-extrusion field have occurred, largely due to advances in understanding of materials coupled with developments in printing and extrusion technologies and methodologies. First synthesised in 2000 [231], the use of gelatin methacryloyl (GelMA) [232], a semi-synthetic methacrylated version of gelatin (hydrolysed collagen), has become common within the coaxial bio-extrusion community due to its low cost and immunogenicity, room-temperature stability and greater mechanical properties in comparison to collagen [233].

GelMA is also highly tuneable, whereby its physicochemical properties and hence degradability may be controlled by modifications to the synthesis reaction scheme [234] and cross-linking process [235]. However, GelMA suffers from inferior biological performance in comparison to collagen [236] [237] and low viscosity, leading to the requirement to extrude with high concentrations to allow rapid gelation through UV cross-linking, leading to limitations in printability (or extrudability) [238] [239]. Furthermore, the cross-linking process can be harmful to cell viability if the UV exposure time or cross-linker concentration are not suitably controlled [240].

Despite these shortcomings, GelMA has been used to extrude high viability, small diameter fibres. Shao et al. [241] used modified nozzles to extrude GelMA microfibrils of various shapes, from straight and wavy to double aligned and double helix configurations, with reported acellular fibre diameters under 100 μm . This platform was tested by embedding HUVEC cells within GelMA cores, showing cellular proliferation for both straight and helical fibre morphologies with an additional demonstration of extruding tubular GelMA structures with viable HUVECs present in the lumen; cellular filament diameters were measured at upwards of 200 μm (see Figure 2-31).

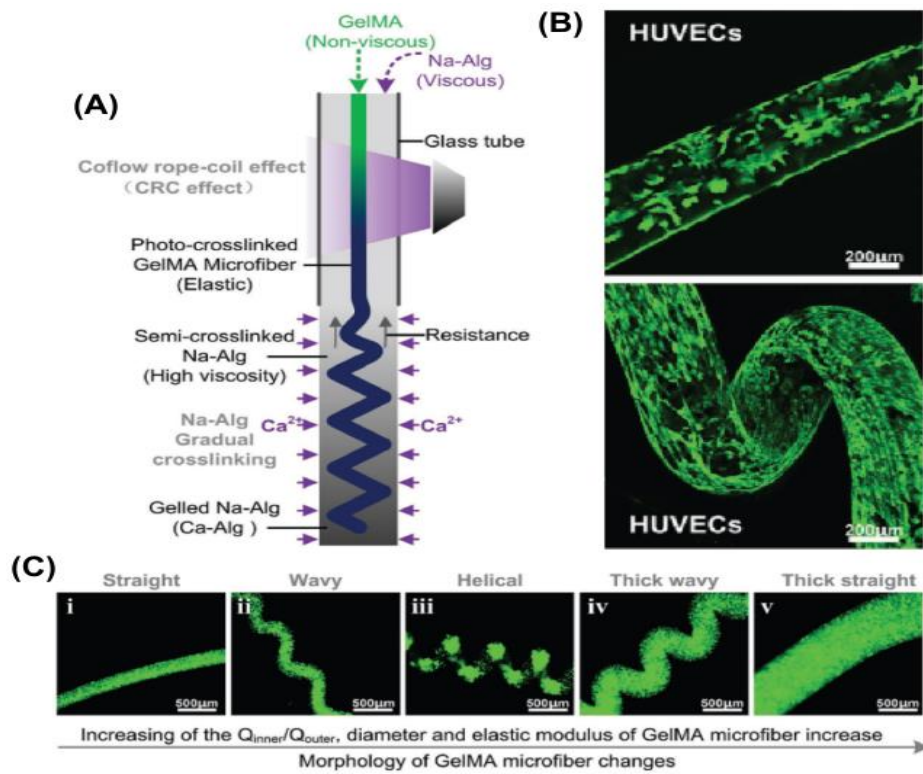


Figure 2-31. Fabrication of GelMA microfibres and its potential applications in tissue engineering. A) The schematic of fabrication of the heterotypic GelMA microfibers based on the CRC effect. B) Confocal laser-scanning microscopy images of the cell-laden GelMA microfibers revealed the cellular morphology after 10 days of culture. C) The morphology of GelMA microfibers changed with increasing of the flow rate ratio ($Q_{GelMA}/Q_{Na,Alg}$), and the morphological change process of the GelMA microfibers was straight–wavy–helical–thick wavy–thick straight. The experimental flow rate conditions were $Q_{GelMA}/Q_{Na,Alg} = 5:400, 10:400, 30:400, 50:150, 60:100 \mu\text{L min}^{-1}$, respectively in (i–v). [242].

In 2018, bio-extrusion nozzles were 3D printed by Morimoto et al. [243] using a photopolymer resin and a commercial stereolithography printer. Termed ‘microfluidic modules’, the printed nozzle configuration consisted of two or three nozzle housings which, when combined, created a multiple-input modular printing nozzle capable of extruding sub 200- μm , triple-layered cell-laden collagen fibres within an alginate shell using fluorescently-labelled NIH/3T3 cells. A summary of this work is displayed in Figure 2-32.

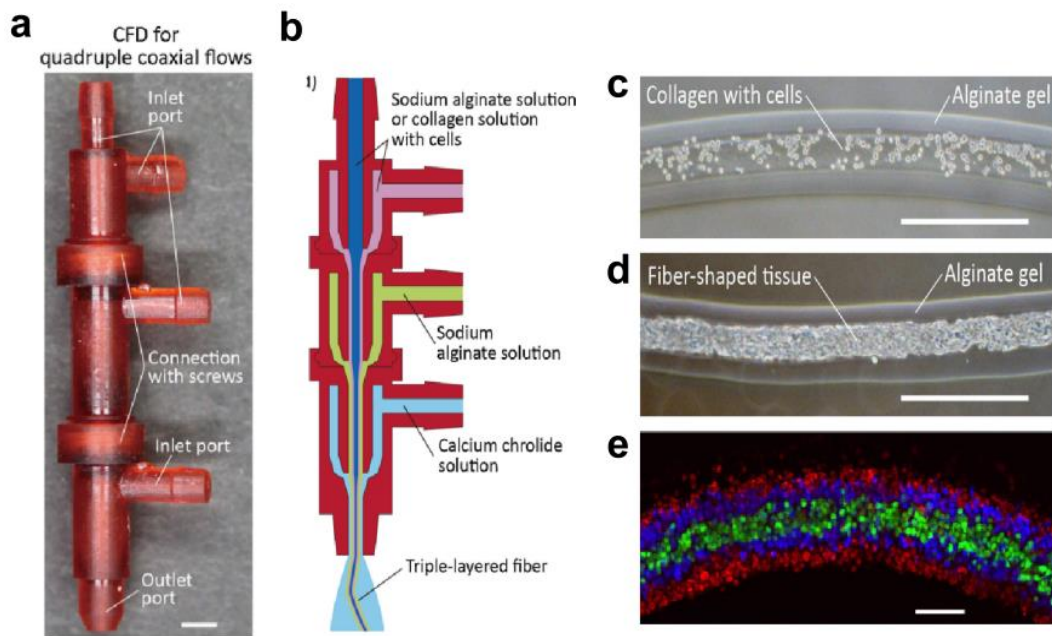


Figure 2-32. (a) Image of quadruple coaxial co-flow device (CFD) microfluidic device composed of the individual microfluidic modules. (b) Formation of triple-layered alginate gel fibers (use of sodium alginate solution) multi-layered cell-laden fibres (use of collagen solution with cells) using the CFD for quadruple coaxial flow. (c) Image of (c) a cell-laden fibre (day 0) and (d) a cell fibre (day 4) formed with the CFD. (e) Confocal image of a triple-layered cell-laden collagen in multi-layered cell-laden fibre. Scale bars: (a) 2 mm, (c, d) 500 μm , (e) 100 μm [243].

This low-cost and versatile method benefits from allowing full control on printed nozzle dimensions and geometries by making simple changes to CAD models in addition to saving on nozzle costs in comparison to the use of traditional machined metallic nozzles and associated housings.

2.7. Progress in coaxial bio-extrusion of small diameter tissue fibre coaxial bio-extrusion

With the addition of cells to collagen within core/shell scaffold structures to produce tissue filaments, there are many added challenges and considerations to make. Firstly, the porosity of the hydrogel scaffold material must be sufficient such that oxygen and all required nutrients, cells and growth factors can freely diffuse through the scaffold shell walls in addition to migrating through to the core of the extruded ECM filament to make contact with cells at the farthest distance from the outer surface of the scaffold, located along the centre line of the lumen. A pictorial summary of these requirements is shown in Figure 2-33.

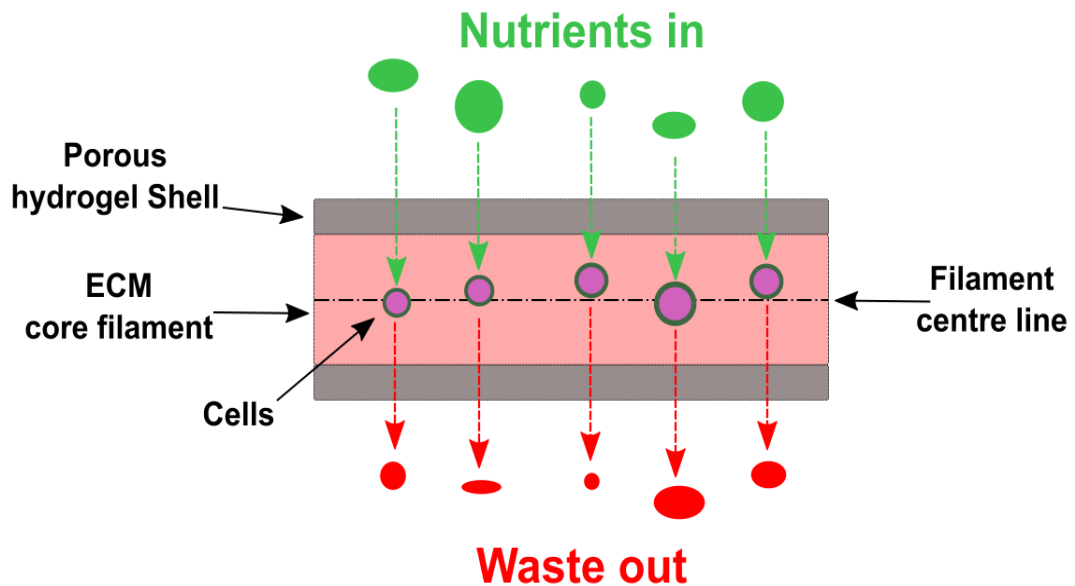


Figure 2-33. Schematic showing diffusion of nutrients and waste through porous hydrogel scaffold into the core of an ECM tissue filament.

Similarly, waste material from cellular metabolism and scaffold degradation in addition to dead cells and cellular debris must be swiftly ejected from the hydrogel scaffold material, a process which would normally be performed by macrophages within the body. It is imperative that no necrotic regions are formed within the bulk of the tissue filament as this can lead to major structural and functional failures within the engineered tissue [244]. In bioengineered tissues, the diffusion limit of oxygen is in the 100 to 200 μm range; thicker tissues, in the absence of vasculature, will be subject to necrosis. It is therefore essential to limit the extruded ECM filament diameter to a maximum of 200 μm in cases possessing a lack of vasculature in order to avoid tissue necrosis [245].

Further to tackling the issue of diffusion limitations, coaxial bio-extrusion of fine filament diameters may lead to successful fabrication of many fine fibrous tissues within the human body which are currently difficult to engineer or are unviable alternatives to gold standard surgical autografting. For example, the smallest diameter nerve fibres in the body, unmyelinated group C fibres, can range from 0.2 – 1.5 μm in diameter [246] whilst the largest fibres, heavily myelinated group A fibres, measure between 1 and 20 μm in diameter, an arguably more achievable diameter range for coaxial bio-extrusion in the short-term future. Meanwhile, muscle fibres are comparatively larger than nerve fibres, typically measuring 20 - 100 μm in diameter and represent an easier target filament diameter to achieve [247].

The minimal filament diameter achieved using coaxial bio-extrusion is largely determined by a combination of extrusion parameters, material rheological properties, nozzle orifice diameter and the presence of cells and the corresponding cell seeding density. Therefore, optimisation and balance between these aspects must be achieved to improve on current minimal filament diameter standards [248] [249].

In 2016, Yeo et al. [250] employed a novel aerosol cross-linking process using 10 wt. % CaCl_2 ejected from a humidifier and a pneumatic coaxial bio-extrusion methodology in order to fabricate 4.0 wt.% alginate-shelled mesh structures with a minimum diameter of approximately $134.0 \pm 45.0 \mu\text{m}$. The core nozzle internal diameter was $500 \mu\text{m}$ while the shell nozzle possessed an internal diameter of $750 \mu\text{m}$. Adipose-derived stem cells (hASCs here) were embedded within 2.0 wt. % porcine tendon-derived collagen at a density of 6.7×10^6 cells/ml and printed within the core of the coaxial nozzle to generate cell-collagen core filaments of approximately $300 \mu\text{m}$ in diameter with high post-print viability ($> 90.0\%$). The advantages of using a collagen core over a pure alginate core were also demonstrated by firstly differentiating the ADSCs to provide a hepatocyte-like phenotype and subsequently showing that the metabolic function of cells within pure alginate was lower than that of a collagen core by testing levels of hepatocyte-specific secreted albumin and expression of TDO-2. This paper succeeded in showing that ADSCs could be coaxially extruded and retain high viability however, the extrusion conditions were apparently not optimal for the aggregation of cells into tissue filaments and the minimal filament diameter was above that of the recommended level for avascular tissues (see Figure 2-34).

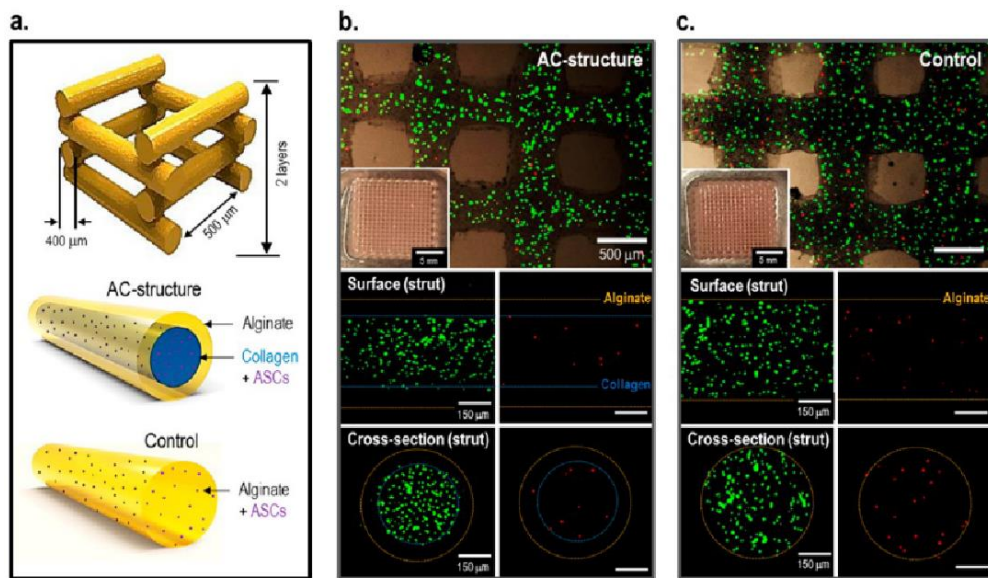


Figure 2-34. Optical and fluorescence images of the hASCs-laden mesh structure and control structure. (a) Schematic images for designing AC structure and control. Optical and fluorescence (live = green, dead = red) images of (b) hASCs-laden structure (AC structure) having core (cell-laden collagen)-sheath (alginate) structure and (c) a control with hASCs-laden alginate [250].

Furthermore, in 2017, Liang et al. [251] implemented a nozzle-assisted electrohydrodynamic coaxial printing platform to fabricate uniform acellular hydrogel filaments of approximately 80 μm in diameter, using 3% alginate solution within the core of a coaxial nozzle and 3% CaCl₂ dissolved within a 2% agarose solution (all w/v) as the shell input. By applying a 4.5 kV voltage to the printing nozzle, the diameter of filaments appeared smaller for all three tested nozzles with differing internal diameters (160 – 410 μm) against the non-voltage control cases, although no statistical analysis was performed here. By adding rat myocardial cells (H9C2) cells, embedded within the alginate solution at 1.0×10^6 cells/ml, 30-layer cell-seeded alginate lattices were fabricated, with cell channels measuring between 100 and 200 μm (see Figure 2-35).

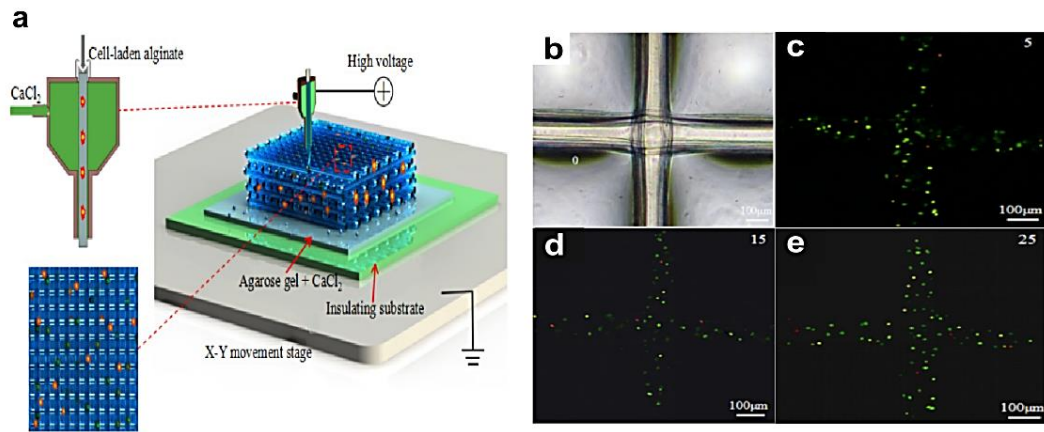


Figure 2-35. (a) Schematic of coaxial nozzle-assisted electrohydrodynamic printing for microscale cell-laden constructs. (b) Microscopic images of the electrohydrodynamic 3D printed cell-laden constructs with a layer number of 30 in total. (c– e) Cell distribution at specific layer of 5, 15 and 25 respectively [251].

Viability was claimed to have remained quantitatively above 90% (however no timestamps were provided on the accompanying figures). No cellular aggregation was observed and individual layer (layers 5, 15 and 25) cellular presence appeared sparse and insufficient for aggregation despite achieving suitable filament diameter, which may be a drawback of embedding cells within alginate, a non-bioactive material known to limit cell migration, thus hindering the ability of cells to aggregate into higher-order tissues [252].

A further step forward was taken by Wang et al. in 2019 [253] whereby fine diameter, high-viability cell-collagen filaments within a 1.0% alginate-5% GelMA (both w/v) cylindrical shell were fabricated using a microfluidic chip consisting of glass capillaries of 300 μm internal diameter. Dual CaCl₂ and UV cross-linking was used to cross-link the alginate-GelMA shell, firstly by immersion printing into a CaCl₂ bath (1.5%, w/v), followed by irradiation using 405 nm light for 30 seconds to cure the GelMA component.

Filaments containing MC3T3-E1 cells were cultured for 9 days and possessed a diameter of approximately 70 μm, optimised by manipulating core flowrates on printing GelMA core filaments and applying this to collagen (see Figure 2-36).

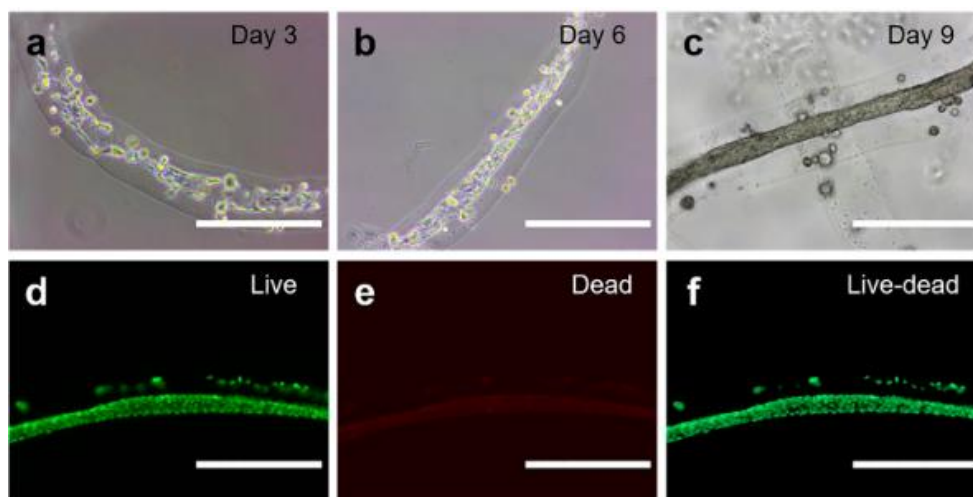


Figure 2-36. (a–c) Images of cell-laden double-layer microfibers after culturing for 3, 6 and 9 days, respectively. (d–f) Fluorescence microscope images of live/dead stained MC3T3-E1 cells after 9 days of culture. Scale bars, 400 μm [253].

A further strategy to produce fine diameter cell filaments may be through the use of complex coacervation, whereby placing a hydrogel consisting of charged polyions into a liquid bath containing ions of opposing charge leads to charge compensation and expulsion of water from the hydrogel and subsequent shrinking and reduction in hydrogel size. In 2020, Gong et al. [254] placed negatively-charged coaxially-extruded 0.5 – 2.5% (w/v) methacrylated hyaluronic acid (HAMA) hollow cylindrical scaffolds within a bath of positively-charged 2.0% (w/v) chitosan, a polymer derived from the exoskeletons of arthropods [255], (dissolved in 1.0% (w/v) acetic acid), leading to the shrinking of the hollow HAMA tubes to 3 - 8 times their original control volumes (see Figure 2-37). For example, the inner diameter of coaxially extruded HAMA/ 0.5% (w/v) alginate tubes was reduced from $301 \pm 3 \mu\text{m}$ to $37 \pm 3 \mu\text{m}$.

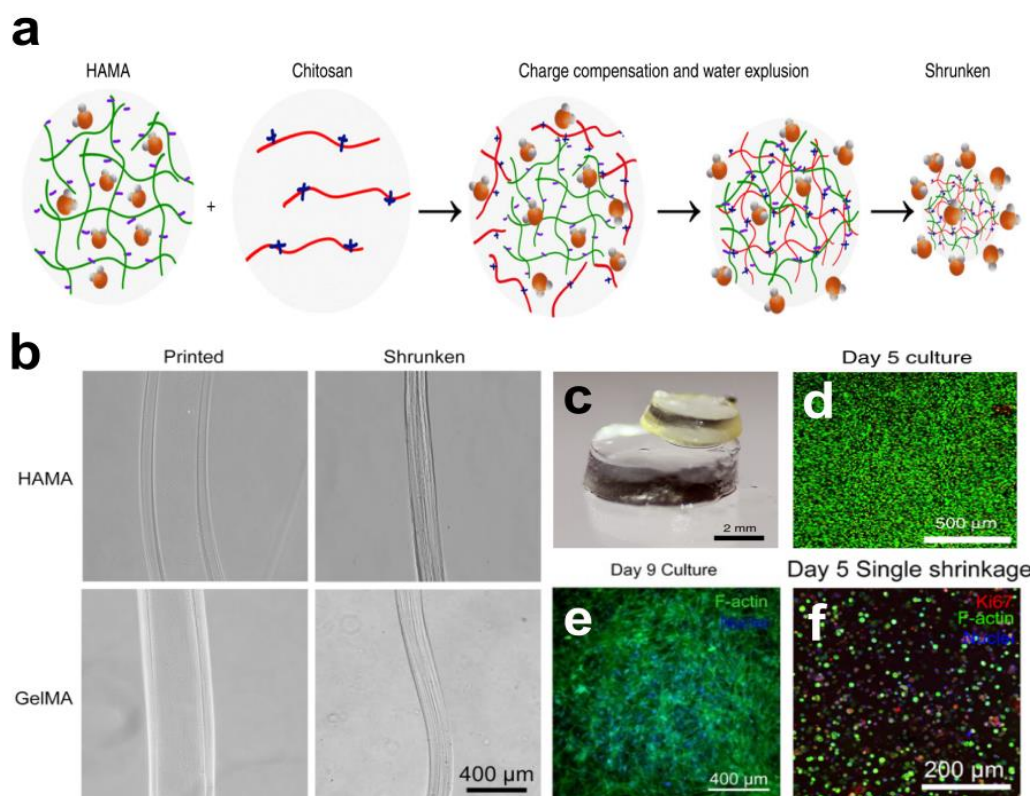


Figure 2-37. (a) Schematics showing the shrinking effect based on charge compensation. (b) Micrographs showing the coaxial printing of cannular (tubular) HAMA-based constructs before (top-left) and after (top-right) and GelMA-based constructs before (bottom-left) and after (bottom-right) 24 h of shrinkage in 2.0 w/v% HM_w (high molecular weight) chitosan dissolved in 1.0 v/v% acetic acid aqueous solution. (c) Photograph showing size change of fabricated HAMA hydrogel (1.0 w/v%) before (lower) and after (upper) shrinking in 2.0 w/v% MM_w chitosan dissolved in 1.0 v/v% acetic acid aqueous solution. (d) Micrograph showing live (green)/dead (red) staining of MCF-7 cells embedded in GelMA/HAMA constructs following a successive shrinking process. (e) The spreading of C2C12 embedded in the GelMA/HAMA constructs before and after shrinking with morphological observation of cells for 9 days, stained for F-actin (green) and nuclei (blue). (f) Fluorescence micrograph of MCF-7 cells in GelMA/HAMA constructs after single shrinkage, stained for Ki67 (red), F-actin (green), and nuclei (blue) [254].

It was predicted that the complex coacervation methodology could be applied to many tissue engineering scenarios, including tissue filament fabrication. This approach was also tested using GelMA to understand the broadness of applicability of complex coacervation. GelMA constructs at a concentration of 5.0% (w/v) shrank to 55% of their original diameters upon immersion in the same chitosan solution as the HAMA constructs, thanks to the net negative charge of GelMA under neutral pH and acidic conditions [256]. Similarly, shrinking of alginate, a negatively-charged polymer, was also demonstrated, whereby 2.0% (w/v) alginate cross-linked with 300 mM $CaCl_2$ shrank to between $27.7 \pm 1.0\%$ and $37.6 \pm 1.2\%$ of original volume, depending on the molecular weight of chitosan bath used for complex coacervation.

This method was also confirmed to apply in cell seeding applications, using multiple cells types, including MCF-7 (human breast cancer cells), C2C12 (mouse skeletal muscle cells) and HUVEC cells, with preservation of cell viability in a cell type-dependent manner, using both single and successive step (2X) shrinking.

2.8. Traditional drug testing methodologies

For accurate study of diseases and pathologies, it is currently essential to use cellular models to study tissue response to various drugs employed for the treatment of these ailments, primarily in terms of toxicity and efficacy. Figure 2-38 demonstrates the options for cell source, culture components and technological advancements towards developing more relevant organotypic tissue models for drug development.

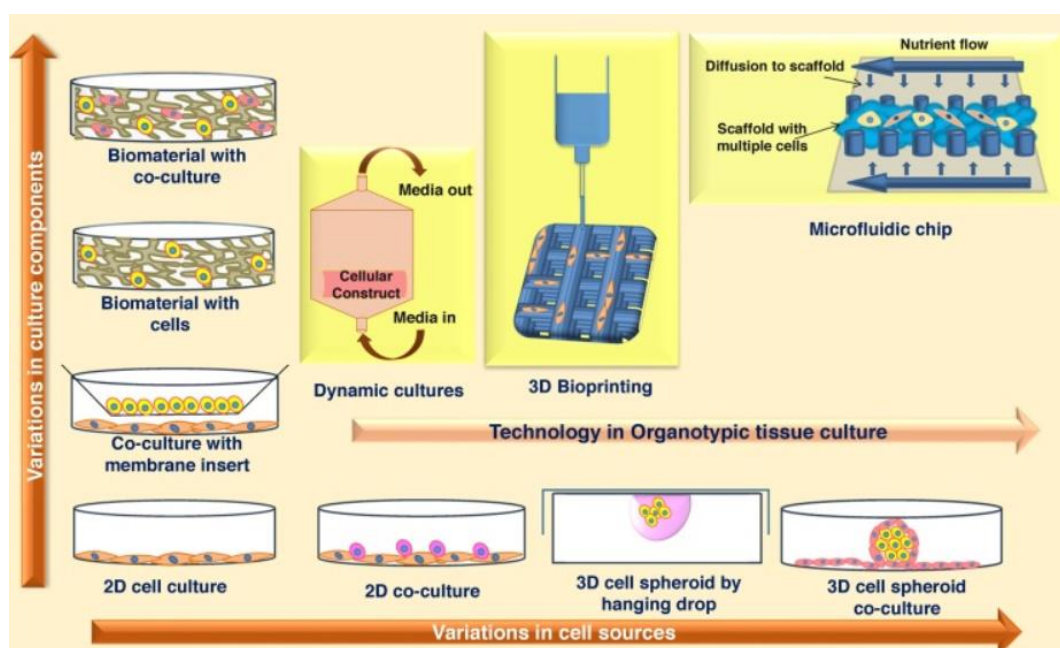


Figure 2-38. Schematic representation of the variations in cell sources, culture components and advancements in technology toward the development of more appropriate *in vitro* organotypic tissue models [257].

With reference to Figure 2-38, there are a variety of configurations in which cellular models may be applied, including two-dimensional monolayers, three-dimensional spheroid (or organoid) culture and 3D tissue engineered or bioprinted tissue/organ-on-a-chip devices.

2.8.1. Cell monolayer testing

For over a century, conventional *in vitro* drug testing has relied on the use of cells (either primary or immortalised) in monolayer culture to model cellular response to developed compounds.

Although, these two-dimensional assays are well-established and have contributed significant advances in the number of available drugs on the market for a multitude of ailments, there are major limitations to their use [258].

Monoculture studies are devoid of structural complexity and the tissue microenvironment required for a truly biomimetic study. Moreover, there is an absence of cell-cell and cell-ECM signalling and interaction which hinders the ability of the 2D assay to truly recapitulate the 3D in vivo environment [259]. For example, cellular response to anticancer drugs differs between 2D and 3D environments in that gene expression and cellular migration, proliferation and viability, amongst other factors, are all disparate. Furthermore, monoculture studies in 2D are known to be labour-intensive, costly and time-consuming [260]. Given these limitations, research and development of drug testing is focussed on moving away from traditional 2D cell monoculture studies towards more accurate biomimetic environments based on 3D cell culture, where more physiologically-relevant results can be obtained.

2.8.2. Spheroid culture

Multicellular spheroids, or organoids, hold a substantial advantage over cell monolayer models for use in drug toxicity testing, in that they possess innate physiological structure and function, providing a more predictable and comparable environment to the body. Moreover, spheroids can provide organotypic cell densities, thus the combination of cell-cell and cell-ECM interactions are comparable with what would be expected in the body, therefore facilitating differentiation and maintenance of phenotype [261]. These high cell densities are essential to provide accurate models of diseases such as fibrosis or cancer, wherein disease progression is characterised by deteriorations in cell-cell and cell-ECM interactions. Spheroid culture models have facilitated the engineering of in vitro fibrosis models of various organs, including heart [262], liver [263] and kidney [264]. Additionally, the use of high cell seeding densities in cancer models results in engineered oxygen gradients which are comparable with the native tumour micro-environment [265]. Examples of spheroids cultured from different cell types can be found in Figure 2-39.

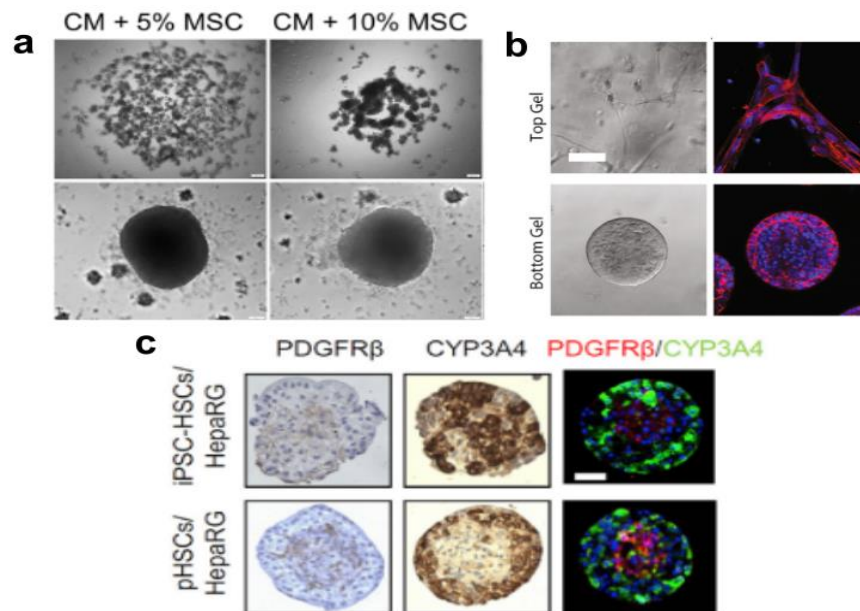


Figure 2-39. Examples of spheroids generated from different cell types. (a) Representative image of CMs (cardiomyocytes) and MSCs (mesenchymal stem cells) differentiated from the same hESC (human embryonic stem cell) line when co-cultured as 3D spheroids for day 1 (top) and 7 (bottom). Cardiac spheroid formation was dependent on the ratio of MSCs to CMs. Scale bars, 100 μ m [262]. (b) bright field images (left panel) and F-actin immunostaining (right panel; red, F-actin; blue, DAPI) of the two different cell types seeded in hydrogel. Bottom layer: HKC-8 (human kidney proximal tubular cells) spheroids; upper layer: spreading renal fibroblast [264]. (c) Representative haematoxylin staining of spheroid paraffin sections of iPSC-HSCs (induced pluripotent stem cell-hepatic stellate-like cell) with HepaRG (iPSC-HSCs/HepaRG) and pHSCs (primary HSCs) with HepaRG (pHSCs/HepaRG) spheroids. Shown are immunostaining and immunofluorescence of PDGFR β (platelet-derived growth factor receptor beta, in red) and CYP3A4 (in green) in iPSC-HSCs/ HepaRG and pHSCs/HepaRG spheroids. Scale bars, 50 μ m. [263]

Despite the manifold benefits on use of spheroid cultures it is difficult to control their patterning at scale, therefore providing a barrier in introducing heterogeneity and consequent tissue function within in vitro cell models. This issue subsequently results in difficulties in tracking disease progression and transient tissue response to drugs [266]. However, as coaxial bio-extrusion of spheroids has been demonstrated [267] [268], it may also be possible to adapt the coaxial bio-extrusion process to implement spheroids in place of single cells. This modification will allow a study of engineered tissue with more native-like characteristics. Greater control of cellular response to shear stress will be required due to the large sized spheroids being susceptible to damage through shear stress [269]. This may be achieved by controlling parameters such as bioink viscosity and extrusion velocities.

2.8.3. Tissue-engineered drug testing platforms

Tissue engineering attempts at creating drug testing platforms have focussed on the development of tissue or organ chips. These transparent devices are designed to encapsulate multiple cell types within miniature three-dimensional biomimetic structures which can simulate the function of various tissues or organs of the body. This facilitates tissue-tissue interfaces and cellular communication *in vitro* and the study of physiologically-predictable reactions to various stimuli, such as drugs and biomolecules. Chips may be designed to possess pre-defined shapes which can recapitulate the structure of organs, such as the liver sinusoid [270] or the proximal tubule of the kidneys [271]. Moreover, chips employ microfluidic technology to provide fluid flow through constructs for the delivery of nutrients and the removal of waste products [272] [273]. Figure 2-40 demonstrates the array of tissue chip platforms which have been developed from different cell types.

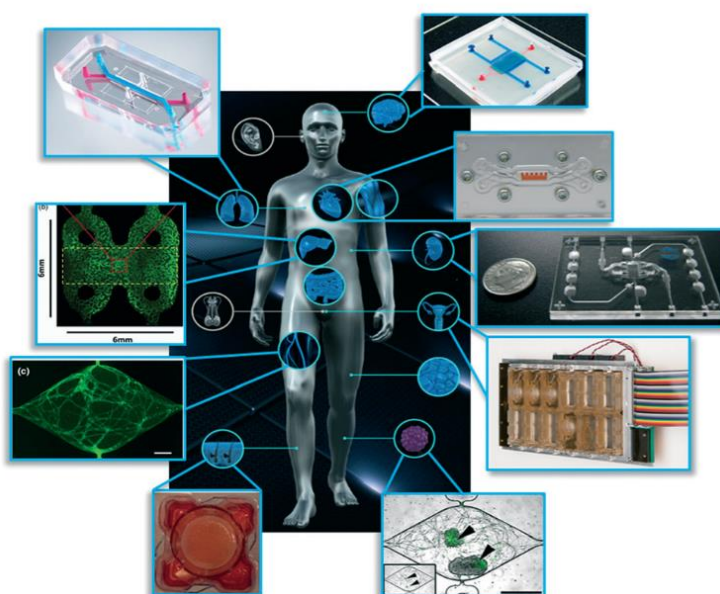


Figure 2-40. Array of tissue chip platforms which have been developed. These include (clockwise from top right) a blood–brain barrier, cardiac muscle, kidney proximal tubule, female reproductive tract, vascularized tumour, skin epidermis, vasculature, liver, and lung [274].

These three-dimensional chip devices benefit from having the potential to provide more detailed toxicity data during standard drug screening processes by identifying any unseen issues during screening of ‘borderline’ drugs. Borderline drugs may be described as those which have demonstrated toxicity of which appears minor or limited and these effects may be reduced through further development.

Furthermore, tissue engineered chips have the potential to provide more physiologically-relevant data on cell-drug interactions, due to the enhanced level of structural and cellular complexity in comparison with standard 2D cellular models [274].

Although there is large promise in tissue chip platforms, there are still many limitations to overcome. Firstly, organ scaling between systems remains a major challenge. As organ systems are required to produce physiologically-relevant outputs which are commensurate with other organs in the body, it is imperative that linked miniature organs are of compatible size. For example, a linked liver and kidney system will give physiologically irrelevant results if the liver module is doubly larger than the kidney system, due to inaccurate scaling. Scaling inaccuracies result from the complex nature of translating complex in vivo organs down to the micro scale [275] [276].

In addition, it is difficult for these microfluidic systems to account for and accurately reproduce physiological responses which are dependent on circumstances such as age, genetics, environment and demographic, amongst many other factors. Moreover, on connecting multiple organ systems, there is a requirement for a universal culture medium or blood mimic which can provide optimal nutrition and waste removal for many different cell types. Recent approaches have included mixing the waste stream from one system with fresh tissue-specific media for the next system [277] and adding in barriers between systems which mimic endothelial barriers between cells and flowing media [278] [279]. Further technical challenges to overcome in order to realise organ-on-a-chip technology include the avoidance of flow-impeding bubbles into chips, maintaining sterility and predictability, using physiologically-relevant cell types and maintaining their viability, introducing different oxygen levels and media flow rates between organ systems [280] [281].

2.8.4. Bioprinting and extrusion for drug testing

Furthermore, bioprinting and extrusion, as a tissue engineering technique, holds the advantage of automation, stability, predictability and the ability to produce biomimetic 3D models, thereby streamlining the path to regulatory approval during drug development and testing [282]. Bioprinting also provides a platform to accurately fabricate functional mini-organs or organ-on-a-chip tissue arrays [283] by combining bioprinting and suitable bioinks containing cell spheroids with microfluidic chips. In doing so, high-throughput, long-term study of the pharmacological and toxicological effects of test drugs on mini-organs can be achieved whilst applying physiologically-relevant mechanical forces with real-time monitoring [284]. Figure 2-41 demonstrates the process of bioprinting cell-laden hydrogels onto microfluidic chips to create tissue chips.

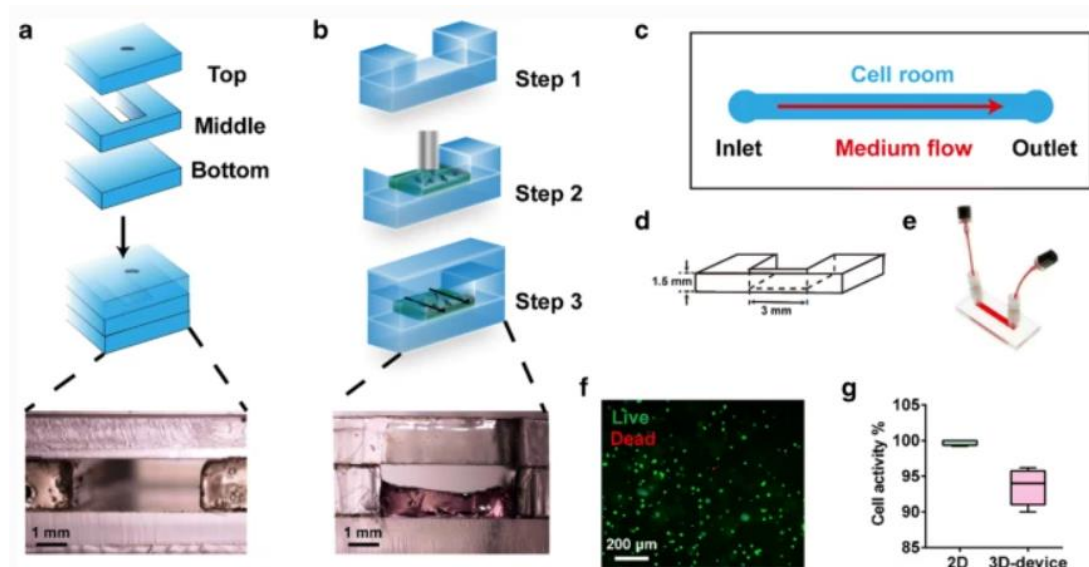


Figure 2-41. Fabrication of cell-laden hydrogels using bioprinting onto a microfluidic chip. (a) The fabrication of a microfluidic chip. Scale bar = 1 mm. (b) Procedure of cell-laden hydrogel bioprinting on a microfluidic chip. Scale bar = 1 mm. (c) Abridged general view of the microfluidic chip. (d) Dimensions of the microfluidic channel. (e) A completed microfluidic chip integrated with bioprinting is shown. (f), (g) Cell viability was identified by a live/dead assay immediately after bioprinting (live cells in green, dead cells in red). Scale bar = 200 μm [285].

Coaxial bio-extrusion of tissue filaments particularly provides a novel method for high throughput, low-cost drug testing due to the potential for study of fibrous tissues which can contain cells that are aligned along customisable extruded ECM filament fibres, mechanically-supported and protected by porous hydrogel scaffolds. In doing so, this provides a more native-like biomimetic environment as opposed to typical tissue engineered, non-anatomically-relevant patches or chips [286]. In addition, as it is possible to modify the minimal filament diameter of coaxial extruded tissue filaments by manipulation of flow parameters, this provides a further benefit of the coaxial bio-extrusion platform for drug testing, as different fibrous tissue thicknesses may be studied, therefore adding precision to the platform. Finally, simultaneous, multi-material, temperature-controlled extrusion and printing adds versatility to the platform, facilitating multi-parameter studies.

2.9. Conclusions

To summarise, a literature overview has been performed, which firstly provided background information on the field of bioprinting, with an overview of the various bioprinting and extrusion modalities and of bioinks and their constituent components, with a detailed overview of alginate, collagen and cell configurations which can be utilised. The review progressed into a focus on the field of tissue engineering and the associated advantages and disadvantages of traditional tissue engineering techniques for filament and fibre production, with a concluding remark on how bio-extrusion could overcome these disadvantages, mainly due to the ability to precisely and simultaneously deposit multiple combinations of bioinks, which have been fine-tuned for optimal biological and physicochemical properties, with spatiotemporal control.

Furthermore, coaxial bio-extrusion and its benefits were introduced, with benefits such as the ability to easily customise filament diameter, number of layers and biological and physicochemical properties, amongst others. Additionally, the versatility of this methodology in the targeted use of extruded filaments was explained, ranging from tissue engineering, in vitro cell studies (2D vs 3D, co-culture), drug development and cancer studies.

A final section expanded on the variety of cellular drug testing methodologies which may be employed to provide analyses of cell and tissue response to various drugs. The benefits and limitations of simple 2D models, spheroids, tissue engineering and bio-extruded organ-on-a-chip models were presented, concluding by demonstrating that bio-extruded models are superior systems, in that more biomimetic, anatomically-accurate and easily customisable tissue filaments may be fabricated and studied using bioprinting and bio-extrusion technologies.

The coaxial bio-extrusion platform is currently limited in that the smallest diameter which has been achieved to date for extruded cell filaments in an ECM-like material is in excess of 50 μm whilst finer filaments are required to use coaxial extruded filaments as the building blocks for the fabrication of higher-order tissues and organs in addition to the need for the production of fine fibrous tissues, such as muscle and nerve. The necessity for fine filaments largely rests in the need for correct cell and biomaterial positioning to achieve sufficient cell and biomaterial alignment, cell signalling, nutrition and vascularisation, leading to the development of transplantable tissues, organs and fibres.

On the basis of the information presented in this review, the overall aim of this work was to develop a coaxial bio-extrusion platform to demonstrate extrusion of fine diameter stem cell-laden tissue filaments with the capability to retain long-term viability in culture.

Further objectives were to develop a hydrogel scaffold material capable of resisting degradation by culture media to maintain tissue filament integrity. In addition, it was also desirable to demonstrate extrusion with multiple cell types and to present an initial assessment of the viability of the coaxial extrusion platform for use in drug testing applications, providing the benefit of a more natural in vivo-like environment to study drug-cell interactions in comparison to traditional two-dimensional methods.

2.10. References

- [1] X. Liu, B. Chi, Z. Jiao, J. Tan, F. Liu, and W. Yang, "A large-scale double-stage-screw 3D printer for fused deposition of plastic pellets," *J. Appl. Polym. Sci.*, vol. 134, no. 31, p. 45147, Aug. 2017.
- [2] X. Fu, X. Zhang, and Z. Huang, "Axial crushing of Nylon and Al/Nylon hybrid tubes by FDM 3D printing," *Compos. Struct.*, vol. 256, p. 113055, Jan. 2021.
- [3] E. O. Olakanmi, "Selective laser sintering/melting (SLS/SLM) of pure Al, Al-Mg, and Al-Si powders: Effect of processing conditions and powder properties," *J. Mater. Process. Technol.*, vol. 213, no. 8, pp. 1387–1405, Aug. 2013.
- [4] A. Vyatskikh, S. Delalande, A. Kudo, X. Zhang, C. M. Portela, and J. R. Greer, "Additive manufacturing of 3D nano-architected metals," *Nat. Commun.*, vol. 9, no. 1, pp. 1–8, 2018.
- [5] P. Parandoush, C. Zhou, and D. Lin, "3D Printing of Ultrahigh Strength Continuous Carbon Fiber Composites," *Adv. Eng. Mater.*, vol. 21, no. 2, p. 1800622, Feb. 2019.
- [6] P. Rando and M. Ramaioli, "Food 3D printing: Effect of heat transfer on print stability of chocolate," *J. Food Eng.*, vol. 294, p. 110415, Apr. 2021.
- [7] S. V. Murphy and A. Atala, "3D bioprinting of tissues and organs," *Nat. Biotechnol.*, vol. 32, no. 8, pp. 773–785, 2014.
- [8] N. Vermeulen, G. Haddow, T. Seymour, A. Faulkner-Jones, and W. Shu, "3D bioprint me: A socioethical view of bioprinting human organs and tissues," *J. Med. Ethics*, vol. 43, pp. 618–624, Sep. 2017.
- [9] M. Albanna *et al.*, "In Situ Bioprinting of Autologous Skin Cells Accelerates Wound Healing of Extensive Excisional Full-Thickness Wounds," *Sci. Rep.*, vol. 9, p. 1856, Dec. 2019.
- [10] E. Ning *et al.*, "3D bioprinting of mature bacterial biofilms for antimicrobial resistance drug testing," *Biofabrication*, vol. 11, p. 045018, Sep. 2019.
- [11] S. J. Trenfield *et al.*, "Shaping the future: recent advances of 3D printing in drug delivery and healthcare," *Expert Opin. Drug Deliv.*, vol. 16, no. 10, pp. 1081–1094, Oct. 2019.

- [12] Z. M. Jessop, A. Al-Sabah, M. D. Gardiner, E. Combella, K. Hawkins, and I. S. Whitaker, "3D bioprinting for reconstructive surgery: Principles, applications and challenges," *J. Plast. Reconstr. Aesthetic Surg.*, vol. 70, no. 9, pp. 1155–1170, Sep. 2017.
- [13] M. Mobaraki, M. Ghaffari, A. Yazdanpanah, Y. Luo, and D. K. Mills, "Bioinks and bioprinting: A focused review," *Bioprinting*, vol. 18, p. e00080, Jun. 2020.
- [14] B. Derby, "Printing and prototyping of tissues and scaffolds," *Science*, vol. 338, no. 6109. American Association for the Advancement of Science, pp. 921–926, 16-Nov-2012.
- [15] J. Malda *et al.*, "25th anniversary article: Engineering hydrogels for biofabrication," *Advanced Materials*, vol. 25, no. 36. John Wiley & Sons, Ltd, pp. 5011–5028, 01-Sep-2013.
- [16] C. A. Deforest and K. S. Anseth, "Advances in bioactive hydrogels to probe and direct cell fate," *Annual Review of Chemical and Biomolecular Engineering*, vol. 3. Annual Reviews, pp. 421–444, 12-Jun-2012.
- [17] S. Khalil and W. Sun, "Bioprinting endothelial cells with alginate for 3D tissue constructs," *J. Biomech. Eng.*, vol. 131, no. 11, Nov. 2009.
- [18] R. Suntornnond, E. Yong, S. Tan, J. An, and C. K. Chua, "A highly printable and biocompatible hydrogel composite for direct printing of soft and perfusable vasculature-like structure," *Sci. Rep.*, no. November, pp. 1–11, 2017.
- [19] A. N. Al-Shura, "Vascular function and circulation," in *Mechanisms of Action in Disease and Recovery in Integrative Cardiovascular Chinese Medicine*, Academic Press, 2021, pp. 49–58.
- [20] F. Maiullari *et al.*, "A multi-cellular 3D bioprinting approach for vascularized heart tissue engineering based on HUVECs and iPSC-derived cardiomyocytes," *Sci. Rep.*, vol. 8, no. 1, pp. 1–15, Sep. 2018.
- [21] L. Gao *et al.*, "Large cardiac muscle patches engineered from human induced-pluripotent stem cell-derived cardiac cells improve recovery from myocardial infarction in swine," *Circulation*, vol. 137, no. 16, pp. 1712–1730, 2018.

- [22] J. M. Lee, W. L. Ng, and W. Y. Yeong, “Resolution and shape in bioprinting: Strategizing towards complex tissue and organ printing,” *Appl. Phys. Rev.*, vol. 6, no. 1, p. 011307, 2019.
- [23] A. K. Miri *et al.*, “Effective bioprinting resolution in tissue model fabrication,” *Lab Chip*, vol. 19, no. 11, pp. 2019–2037, Jun. 2019.
- [24] Y. S. Zhang *et al.*, “Bioprinting 3D microfibrinous scaffolds for engineering endothelialized myocardium and heart-on-a-chip,” *Biomaterials*, vol. 110, pp. 45–59, 2016.
- [25] K. A. Homan *et al.*, “Bioprinting of 3D Convulated Renal Proximal Tubules on Perfusable Chips,” *Sci. Rep.*, vol. 6, pp. 1–13, 2016.
- [26] B. M. Carlson, “The Circulatory System,” in *The Human Body*, Academic Press, 2019, pp. 271–301.
- [27] I. Holland, J. Logan, J. Shi, C. McCormick, D. Liu, and W. Shu, “3D biofabrication for tubular tissue engineering,” *Bio-Design Manuf.*, vol. 1, no. 2, pp. 89–100, 2018.
- [28] I. T. Ozbolat, “Extrusion-Based Bioprinting,” in *3D Bioprinting: Fundamentals, Principles and Applications*, 2017, pp. 93–124.
- [29] S. Ramesh *et al.*, “Extrusion bioprinting: Recent progress, challenges, and future opportunities,” *Bioprinting*, vol. 21, p. e00116, Mar. 2021.
- [30] S. Bammesberger, A. Ernst, N. Losleben, L. Tanguy, R. Zengerle, and P. Koltay, “Quantitative characterization of non-contact microdispensing technologies for the sub-microliter range,” *Drug Discov. Today*, vol. 18, no. 9–10, pp. 435–446, May 2013.
- [31] M. Hospodiuk, K. K. Moncal, M. Dey, and I. T. Ozbolat, “Extrusion-Based Biofabrication in Tissue Engineering and Regenerative Medicine,” in *3D Printing and Biofabrication*, Springer, Cham, 2018, pp. 255–281.
- [32] A. N. Leberfinger, K. K. Moncal, D. J. Ravnicek, and I. T. Ozbolat, “3D Printing for Cell Therapy Applications,” in *Cell Therapy*, Humana Press, Cham, 2017, pp. 227–248.
- [33] S. Boularaoui, G. Al Hussein, K. A. Khan, N. Christoforou, and C. Stefanini, “An overview of extrusion-based bioprinting with a focus on induced shear stress and its effect on cell viability,” *Bioprinting*, vol. 20, p. e00093, Dec. 2020.

- [34] B. Duan, L. A. Hockaday, K. H. Kang, and J. T. Butcher, “3D Bioprinting of heterogeneous aortic valve conduits with alginate/gelatin hydrogels,” *J. Biomed. Mater. Res. - Part A*, vol. 101 A, no. 5, pp. 1255–1264, May 2013.
- [35] K. Hölzl, S. Lin, L. Tytgat, S. Van Vlierberghe, L. Gu, and A. Ovsianikov, “Bioink properties before, during and after 3D bioprinting,” *Biofabrication*, vol. 8, no. 3, p. 032002, Sep. 2016.
- [36] S. Tasoglu and U. Demirci, “Bioprinting for stem cell research,” *Trends Biotechnol.*, vol. 31, no. 1, pp. 10–19, Jan. 2013.
- [37] I. T. Ozbolat and Y. Yu, “Bioprinting toward organ fabrication: Challenges and future trends,” *IEEE Trans. Biomed. Eng.*, vol. 60, no. 3, pp. 691–699, 2013.
- [38] R. Suntornnond, E. Tan, J. An, and C. Chua, “A Mathematical Model on the Resolution of Extrusion Bioprinting for the Development of New Bioinks,” *Materials (Basel)*, vol. 9, no. 9, p. 756, Sep. 2016.
- [39] A. Schwab, R. Levato, M. D’Este, S. Piluso, D. Eglin, and J. Malda, “Printability and Shape Fidelity of Bioinks in 3D Bioprinting,” *Chem. Rev.*, vol. 120, no. 19, pp. 11028–11055, Oct. 2020.
- [40] N. Jones, “Science in three dimensions: The print revolution,” *Nature*, vol. 487, no. 7405, pp. 22–23, Jul. 2012.
- [41] N. G. Durmus, S. Tasoglu, and U. Demirci, “Bioprinting: Functional droplet networks,” *Nat. Mater.*, vol. 12, no. 6, pp. 478–479, May 2013.
- [42] S. Jentsch, R. Nasehi, C. Kuckelkorn, B. Gundert, S. Aveic, and H. Fischer, “Multiscale 3D Bioprinting by Nozzle-Free Acoustic Droplet Ejection,” *Small Methods*, vol. 5, no. 6, p. 2000971, Jun. 2021.
- [43] W. L. Ng, J. M. Lee, W. Y. Yeong, and M. Win Naing, “Microvalve-based bioprinting-process, bio-inks and applications,” *Biomaterials Science*, vol. 5, no. 4. The Royal Society of Chemistry, pp. 632–647, 28-Mar-2017.
- [44] J. Zhang, E. Wehrle, M. Rubert, and R. Müller, “3d bioprinting of human tissues: Biofabrication, bioinks and bioreactors,” *International Journal of Molecular Sciences*, vol. 22, no. 8. Multidisciplinary Digital Publishing Institute (MDPI), 02-Apr-2021.
- [45] X. Cui and T. Boland, “Human microvasculature fabrication using thermal inkjet printing technology,” *Biomaterials*, vol. 30, no. 31, pp. 6221–6227, Oct. 2009.

- [46] H. Wijshoff, “The dynamics of the piezo inkjet printhead operation,” *Physics Reports*, vol. 491, no. 4–5. North-Holland, pp. 77–177, 01-Jun-2010.
- [47] E. Lepowsky, M. Muradoglu, and S. Tasoglu, “Towards preserving post-printing cell viability and improving the resolution: Past, present, and future of 3D bioprinting theory,” *Bioprinting*, vol. 11. Elsevier B.V., 01-Sep-2018.
- [48] M. S. Onses, E. Sutanto, P. M. Ferreira, A. G. Alleyne, and J. A. Rogers, “Mechanisms, Capabilities, and Applications of High-Resolution Electrohydrodynamic Jet Printing,” *Small*, vol. 11, no. 34. John Wiley & Sons, Ltd, pp. 4237–4266, 01-Sep-2015.
- [49] L. Liu, Z. Xiong, R. Zhang, L. Jin, and Y. Yan, “A novel osteochondral scaffold fabricated via multi-nozzle low-temperature deposition manufacturing,” *J. Bioact. Compat. Polym.*, vol. 24, no. SUPPL.1, pp. 18–30, May 2009.
- [50] I. Angelopoulos, M. C. Allenby, M. Lim, and M. Zamorano, “Engineering inkjet bioprinting processes toward translational therapies,” *Biotechnology and Bioengineering*, vol. 117, no. 1. John Wiley & Sons, Ltd, pp. 272–284, 01-Jan-2020.
- [51] Q. Guo, X. Su, X. Zhang, M. Shao, H. Yu, and D. Li, “A review on acoustic droplet ejection technology and system,” *Soft Matter*, vol. 17, no. 11. The Royal Society of Chemistry, pp. 3010–3021, 25-Mar-2021.
- [52] U. Demirci and G. Montesano, “Single cell epitaxy by acoustic picolitre droplets,” *Lab Chip*, vol. 7, no. 9, pp. 1139–1145, Aug. 2007.
- [53] H. Gudapati, M. Dey, and I. Ozbolat, “A comprehensive review on droplet-based bioprinting: Past, present and future,” *Biomaterials*, vol. 102, pp. 20–42, Sep. 2016.
- [54] W. Lee *et al.*, “Multi-layered culture of human skin fibroblasts and keratinocytes through three-dimensional freeform fabrication,” *Biomaterials*, vol. 30, no. 8, pp. 1587–1595, Mar. 2009.
- [55] L. Horvath, Y. Umehara, C. Jud, F. Blank, A. Petri-Fink, and B. Rothen-Rutishauser, “Engineering an in vitro air-blood barrier by 3D bioprinting,” *Sci. Rep.*, vol. 5, no. 1, pp. 1–8, Jan. 2015.
- [56] V. Lee *et al.*, “Design and fabrication of human skin by three-dimensional bioprinting,” *Tissue Eng. - Part C Methods*, vol. 20, no. 6, pp. 473–484, Jun. 2014.

- [57] B. Derby, “Inkjet printing of functional and structural materials: Fluid property requirements, feature stability, and resolution,” *Annu. Rev. Mater. Res.*, vol. 40, pp. 395–414, Jul. 2010.
- [58] L. Moroni *et al.*, “Biofabrication: A Guide to Technology and Terminology,” *Trends Biotechnol.*, pp. 1–19, 2017.
- [59] M. Nooranidoost, D. Izbassarov, S. Tasoglu, and M. Muradoglu, “A computational study of droplet-based bioprinting: Effects of viscoelasticity,” *Phys. Fluids*, vol. 31, no. 8, p. 081901, Aug. 2019.
- [60] J. I. Rodríguez-Dévora, B. Zhang, D. Reyna, Z. D. Shi, and T. Xu, “High throughput miniature drug-screening platform using bioprinting technology,” *Biofabrication*, vol. 4, no. 3, p. 035001, Jun. 2012.
- [61] F. Xu, J. Celli, I. Rizvi, S. Moon, T. Hasan, and U. Demirci, “A three-dimensional in vitro ovarian cancer coculture model using a high-throughput cell patterning platform,” *Biotechnol. J.*, vol. 6, no. 2, pp. 204–212, Feb. 2011.
- [62] G. M. Cooper *et al.*, “Inkjet-based biopatterning of bone morphogenetic protein-2 to spatially control calvarial bone formation,” *Tissue Eng. - Part A*, vol. 16, no. 5, pp. 1749–1759, 2010.
- [63] C. C. Chang, E. D. Boland, S. K. Williams, and J. B. Hoying, “Direct-write bioprinting three-dimensional biohybrid systems for future regenerative therapies,” *J. Biomed. Mater. Res. - Part B Appl. Biomater.*, vol. 98 B, no. 1, pp. 160–170, Jul. 2011.
- [64] M. Hospodiuk, M. Dey, D. Sosnoski, and I. T. Ozbolat, “The bioink: A comprehensive review on bioprintable materials,” *Biotechnol. Adv.*, vol. 35, no. 2, pp. 217–239, 2017.
- [65] U. A. Gurkan *et al.*, “Engineering anisotropic biomimetic fibrocartilage microenvironment by bioprinting mesenchymal stem cells in nanoliter gel droplets,” *Mol. Pharm.*, vol. 11, no. 7, pp. 2151–2159, Jul. 2014.
- [66] A. B. Dababneh and I. T. Ozbolat, “Bioprinting Technology: A Current State-of-the-Art Review,” *J. Manuf. Sci. Eng. Trans. ASME*, vol. 136, no. 6, Dec. 2014.
- [67] T. Xu *et al.*, “Hybrid printing of mechanically and biologically improved constructs for cartilage tissue engineering applications,” *Biofabrication*, vol. 5, no. 1, p. 015001, Nov. 2013.

- [68] Z. Zhang, B. Wang, D. Hui, J. Qiu, and S. Wang, "3D bioprinting of soft materials-based regenerative vascular structures and tissues," *Compos. Part B Eng.*, vol. 123, pp. 279–291, 2017.
- [69] D. J. Odde and M. J. Renn, "Laser-guided direct writing for applications in biotechnology," *Trends Biotechnol.*, vol. 17, no. 10, pp. 385–389, Oct. 1999.
- [70] S. Michael *et al.*, "Tissue Engineered Skin Substitutes Created by Laser-Assisted Bioprinting Form Skin-Like Structures in the Dorsal Skin Fold Chamber in Mice," *PLoS One*, vol. 8, no. 3, p. e57741, Mar. 2013.
- [71] L. Koch *et al.*, "Laser bioprinting of human induced pluripotent stem cells - The effect of printing and biomaterials on cell survival, pluripotency, and differentiation," *Biofabrication*, vol. 10, no. 3, p. 035005, Apr. 2018.
- [72] K. Arcaute, B. Mann, and R. Wicker, "Stereolithography of spatially controlled multi-material bioactive poly(ethylene glycol) scaffolds," *Acta Biomater.*, vol. 6, no. 3, pp. 1047–1054, Mar. 2010.
- [73] A. Ovsianikov *et al.*, "Laser Photofabrication of Cell-Containing Hydrogel Constructs," *Langmuir*, vol. 30, no. 13, pp. 3787–3794, Apr. 2014.
- [74] V. S. Cheptsov, S. I. Tsykina, N. V. Minaev, V. I. Yusupov, and B. N. Chichkov, "New microorganism isolation techniques with emphasis on laser printing," *Int. J. Bioprinting*, vol. 5, no. 1, p. 165, 2019.
- [75] V. Keriquel *et al.*, "In situ printing of mesenchymal stromal cells, by laser-assisted bioprinting, for in vivo bone regeneration applications," *Sci. Rep.*, vol. 7, no. 1, pp. 1–10, May 2017.
- [76] S. Derakhshanfar, R. Mbeleck, K. Xu, X. Zhang, W. Zhong, and M. Xing, "3D bioprinting for biomedical devices and tissue engineering: A review of recent trends and advances," *Bioact. Mater.*, vol. 3, no. 2, pp. 144–156, Jun. 2018.
- [77] B. Guillotin *et al.*, "Laser assisted bioprinting of engineered tissue with high cell density and microscale organization," *Biomaterials*, vol. 31, no. 28, pp. 7250–7256, Oct. 2010.
- [78] C. Dou, V. Perez, J. Qu, A. Tsin, B. Xu, and J. Li, "A State-of-the-Art Review of Laser-Assisted Bioprinting and its Future Research Trends," *ChemBioEng Rev.*, vol. 8, no. 5, p. Early View, 2021.

- [79] J. M. Unagolla and A. C. Jayasuriya, “Hydrogel-based 3D bioprinting: A comprehensive review on cell-laden hydrogels, bioink formulations, and future perspectives,” *Applied Materials Today*, vol. 18. NIH Public Access, p. 100479, 01-Mar-2020.
- [80] C. Mandrycky, Z. Wang, K. Kim, and D. H. Kim, “3D bioprinting for engineering complex tissues,” *Biotechnol. Adv.*, vol. 34, no. 4, pp. 422–434, Jul. 2016.
- [81] I. T. Ozbolat, “Laser-Based Bioprinting,” in *3D Bioprinting: Fundamentals, Principles and Applications*, 2017, pp. 165–197.
- [82] P. S. Gungor-Ozkerim, I. Inci, Y. S. Zhang, A. Khademhosseini, and M. R. Dokmeci, “Bioinks for 3D bioprinting: An overview,” *Biomaterials Science*, vol. 6, no. 5. Royal Society of Chemistry, pp. 915–946, 01-May-2018.
- [83] A. Mazzocchi, M. Devarasetty, R. Huntwork, S. Soker, and A. Skardal, “Optimization of collagen type I-hyaluronan hybrid bioink for 3D bioprinted liver microenvironments,” *Biofabrication*, vol. 11, p. 015003, Jan. 2019.
- [84] R. Sharma, I. P. M. Smits, L. De La Vega, C. Lee, and S. M. Willerth, “3D Bioprinting Pluripotent Stem Cell Derived Neural Tissues Using a Novel Fibrin Bioink Containing Drug Releasing Microspheres,” *Front. Bioeng. Biotechnol.*, vol. 8, p. 57, Feb. 2020.
- [85] Z. Zheng *et al.*, “3D Bioprinting of Self-Standing Silk-Based Bioink,” *Adv. Healthc. Mater.*, vol. 7, no. 6, p. 1701026, Mar. 2018.
- [86] F. E. Freeman and D. J. Kelly, “Tuning alginate bioink stiffness and composition for controlled growth factor delivery and to spatially direct MSC Fate within bioprinted tissues,” *Sci. Rep.*, vol. 7, no. 1, pp. 1–12, 2017.
- [87] X. Zhou *et al.*, “3D bioprinted graphene oxide-incorporated matrix for promoting chondrogenic differentiation of human bone marrow mesenchymal stem cells,” *Carbon N. Y.*, vol. 116, pp. 615–624, May 2017.
- [88] J. Li, X. Liu, J. M. Crook, and G. G. Wallace, “3D Printing of Cytocompatible Graphene/Alginate Scaffolds for Mimetic Tissue Constructs,” *Front. Bioeng. Biotechnol.*, vol. 8, p. 824, Jul. 2020.
- [89] K. Zhu *et al.*, “Gold Nanocomposite Bioink for Printing 3D Cardiac Constructs,” *Adv. Funct. Mater.*, vol. 27, no. 12, p. 1605352, Mar. 2017.

- [90] E. Trampe *et al.*, “Functionalized Bioink with Optical Sensor Nanoparticles for O2 Imaging in 3D-Bioprinted Constructs,” *Adv. Funct. Mater.*, vol. 28, no. 45, p. 1804411, Nov. 2018.
- [91] Q. Wang *et al.*, “3D-Printed Atsttrin-Incorporated Alginate/Hydroxyapatite Scaffold Promotes Bone Defect Regeneration with TNF/TNFR Signaling Involvement,” *Adv. Healthc. Mater.*, vol. 4, no. 11, pp. 1701–1708, Aug. 2015.
- [92] G. Skeldon, B. Lucendo-Villarin, and W. Shu, “Three-dimensional bioprinting of stem-cell derived tissues for human regenerative medicine,” *Philos. Trans. R. Soc. B Biol. Sci.*, vol. 373, no. 1750, p. 20170224, Jul. 2018.
- [93] N. Paxton, W. Smolan, T. Böck, F. Melchels, J. Groll, and T. Jungst, “Proposal to assess printability of bioinks for extrusion-based bioprinting and evaluation of rheological properties governing bioprintability,” *Biofabrication*, vol. 9, no. 4, p. 044107, Nov. 2017.
- [94] Y. He, F. Yang, H. Zhao, Q. Gao, B. Xia, and J. Fu, “Research on the printability of hydrogels in 3D bioprinting,” *Sci. Rep.*, vol. 6, no. 1, pp. 1–13, Jul. 2016.
- [95] T. K. Merceron and S. V. Murphy, “Hydrogels for 3D bioprinting applications,” in *Essentials of 3D Biofabrication and Translation*, Elsevier Inc., 2015, pp. 249–270.
- [96] Y. Liu *et al.*, “The stiffness of hydrogel-based bioink impacts mesenchymal stem cells differentiation toward sweat glands in 3D-bioprinted matrix,” *Mater. Sci. Eng. C*, vol. 118, p. 111387, Jan. 2021.
- [97] N. Huebsch *et al.*, “Harnessing traction-mediated manipulation of the cell/matrix interface to control stem-cell fate,” *Nat. Mater.*, vol. 9, no. 6, pp. 518–526, 2010.
- [98] A. C. Daly, S. E. Critchley, E. M. Rencsok, and D. J. Kelly, “A comparison of different bioinks for 3D bioprinting of fibrocartilage and hyaline cartilage,” *Biofabrication*, vol. 8, no. 4, p. 045002, Oct. 2016.
- [99] M. B. Schaffler and D. B. Burr, “Stiffness of compact bone: Effects of porosity and density,” *J. Biomech.*, vol. 21, no. 1, pp. 13–16, 1988.
- [100] M. E. Ogle, G. Doron, M. J. Levy, and J. S. Temenoff, “Hydrogel culture surface stiffness modulates mesenchymal stromal cell secretome and alters senescence,” *Tissue Eng. - Part A*, vol. 26, no. 23–24, pp. 1259–1271, Dec. 2020.

- [101] R. G. Wells, “The role of matrix stiffness in regulating cell behavior,” *Hepatology*, vol. 47, no. 4, pp. 1394–1400, Apr. 2008.
- [102] J. D. Mih, A. S. Sharif, F. Liu, A. Marinkovic, M. M. Symer, and D. J. Tschumperlin, “A multiwell platform for studying stiffness-dependent cell biology,” *PLoS One*, vol. 6, no. 5, p. e19929, 2011.
- [103] A. G. Tabriz, C. G. Mills, J. J. Mullins, J. A. Davies, and W. Shu, “Rapid fabrication of cell-laden alginate hydrogel 3D structures by micro dip-coating,” *Front. Bioeng. Biotechnol.*, vol. 5, no. FEB, p. 13, Feb. 2017.
- [104] C. Vepari and D. L. Kaplan, “Silk as a biomaterial,” *Prog. Polym. Sci.*, vol. 32, no. 8–9, pp. 991–1007, Aug. 2007.
- [105] Z. Wu, X. Su, Y. Xu, B. Kong, W. Sun, and S. Mi, “Bioprinting three-dimensional cell-laden tissue constructs with controllable degradation,” *Sci. Rep.*, vol. 6, no. 1, p. 24474, 2016.
- [106] M. Shachar, O. Tsur-Gang, T. Dvir, J. Leor, and S. Cohen, “The effect of immobilized RGD peptide in alginate scaffolds on cardiac tissue engineering,” *Acta Biomater.*, vol. 7, no. 1, pp. 152–162, Jan. 2011.
- [107] H. J. Kong, D. Kaigler, K. Kim, and D. J. Mooney, “Controlling rigidity and degradation of alginate hydrogels via molecular weight distribution,” *Biomacromolecules*, vol. 5, no. 5, pp. 1720–1727, Sep. 2004.
- [108] Y. Huang, Q. Luo, X. Li, F. Zhang, and S. Zhao, “Fabrication and in vitro evaluation of the collagen/hyaluronic acid PEM coating crosslinked with functionalized RGD peptide on titanium,” *Acta Biomater.*, vol. 8, no. 2, pp. 866–877, Feb. 2012.
- [109] T. A. Wynn, “Cellular and molecular mechanisms of fibrosis,” *J. Pathol.*, vol. 214, no. 2, pp. 199–210, Jan. 2008.
- [110] A. C. Jen, M. C. Wake, and A. G. Mikos, “Review: Hydrogels for cell immobilization,” *Biotechnol. Bioeng.*, vol. 50, no. 4, pp. 357–364, Mar. 1996.
- [111] O. Jeon, D. S. Alt, S. M. Ahmed, and E. Alsberg, “The effect of oxidation on the degradation of photocrosslinkable alginate hydrogels,” *Biomaterials*, vol. 33, no. 13, pp. 3503–3514, May 2012.

- [112] M. C. Catoira, L. Fusaro, D. Di Francesco, M. Ramella, and F. Boccafoschi, “Overview of natural hydrogels for regenerative medicine applications,” *J. Mater. Sci. Mater. Med.*, vol. 30, p. 115, Oct. 2019.
- [113] K. Y. Lee and D. J. Mooney, “Hydrogels for tissue engineering,” *Chem. Rev.*, vol. 101, no. 7, pp. 1869–1879, Jul. 2001.
- [114] V. Catto, S. Farè, G. Freddi, and M. C. Tanzi, “Vascular Tissue Engineering: Recent Advances in Small Diameter Blood Vessel Regeneration,” *ISRN Vasc. Med.*, vol. 2014, pp. 1–27, 2014.
- [115] L. Li *et al.*, “Natural hydrogels for cartilage regeneration: Modification, preparation and application,” *J. Orthop. Transl.*, vol. 17, pp. 26–41, Apr. 2019.
- [116] U. S. K. Madduma-Bandarage and S. V. Madihally, “Synthetic hydrogels: Synthesis, novel trends, and applications,” *J. Appl. Polym. Sci.*, vol. 138, no. 19, p. 50376, May 2020.
- [117] K. Y. Lee and D. J. Mooney, “Alginate: Properties and biomedical applications,” *Prog. Polym. Sci.*, vol. 37, no. 1, pp. 106–126, Jan. 2012.
- [118] J. Sun and H. Tan, “Alginate-based biomaterials for regenerative medicine applications,” *Materials (Basel)*, vol. 6, no. 4, pp. 1285–1309, 2013.
- [119] B. Wang *et al.*, “Alginate-based composites for environmental applications: a critical review,” *Crit. Rev. Environ. Sci. Technol.*, vol. 49, no. 4, pp. 318–356, Feb. 2019.
- [120] I. Donati, S. Holtan, Y. A. Mørch, M. Borgogna, M. Dentini, and G. Skjåk-Bræk, “New hypothesis on the role of alternating sequences in calcium-alginate gels,” *Biomacromolecules*, vol. 6, no. 2, pp. 1031–1040, Mar. 2005.
- [121] Y. A. Mørch *et al.*, “Binding and leakage of barium in alginate microbeads,” *J. Biomed. Mater. Res. - Part A*, vol. 100, no. 11, pp. 2939–2947, 2012.
- [122] H. Thiele and K. Hallich, “Kapillarstrukturen in ionotropen Gelen,” *Kolloid-Zeitschrift*, vol. 151, no. 1, pp. 1–12, 1957.
- [123] Y. A. Mørch, I. Donati, B. L. Strand, and G. Skjåk-Bræk, “Effect of Ca²⁺, Ba²⁺, and Sr²⁺ on alginate microbeads,” *Biomacromolecules*, vol. 7, no. 5, pp. 1471–1480, May 2006.

- [124] N. A. Peppas, P. Bures, W. Leobandung, and H. Ichikawa, "Hydrogels in pharmaceutical formulations," *European Journal of Pharmaceutics and Biopharmaceutics*, vol. 50, no. 1. Elsevier, pp. 27–46, 03-Jul-2000.
- [125] V. Pillay and R. Fassihi, "In vitro release modulation from crosslinked pellets for site-specific drug delivery to the gastrointestinal tract. I. Comparison of pH-responsive drug release and associated kinetics," *J. Control. Release*, vol. 59, no. 2, pp. 229–242, May 1999.
- [126] M. J. Costa, A. M. Marques, L. M. Pastrana, J. A. Teixeira, S. M. Sillankorva, and M. A. Cerqueira, "Physicochemical properties of alginate-based films: Effect of ionic crosslinking and mannuronic and guluronic acid ratio," *Food Hydrocoll.*, vol. 81, pp. 442–448, 2018.
- [127] O. Smidsrød and G. Skjåk-Bræk, "Alginate as immobilization matrix for cells," *Trends Biotechnol.*, vol. 8, no. C, pp. 71–78, Jan. 1990.
- [128] N. C. Hunt, A. M. Smith, U. Gbureck, R. M. Shelton, and L. M. Grover, "Encapsulation of fibroblasts causes accelerated alginate hydrogel degradation," *Acta Biomater.*, vol. 6, no. 9, pp. 3649–3656, Sep. 2010.
- [129] B. Zhu and H. Yin, "Alginate lyase: Review of major sources and classification, properties, structure-function analysis and applications," *Bioengineered*, vol. 6, no. 3. Taylor and Francis Inc., pp. 125–131, 2015.
- [130] B. J. Bielajew, J. C. Hu, and K. A. Athanasiou, "Collagen: quantification, biomechanics and role of minor subtypes in cartilage," *Nat. Rev. Mater.*, vol. 5, no. 10, pp. 730–747, 2020.
- [131] C. H. Lee, A. Singla, and Y. Lee, "Biomedical applications of collagen," *Int. J. Pharm.*, vol. 221, no. 1–2, pp. 1–22, Jun. 2001.
- [132] K. Henriksen and M. A. Karsdal, "Type I Collagen," in *Biochemistry of Collagens, Laminins and Elastin: Structure, Function and Biomarkers*, Elsevier Inc., 2016, pp. 1–11.
- [133] M. D. Shoulders and R. T. Raines, "Collagen Structure and Stability," *Annu. Rev. Biochem.*, vol. 78, no. 1, pp. 929–958, Jun. 2009.

- [134] Y. S. Lim, Y. J. Ok, S. Y. Hwang, J. Y. Kwak, and S. Yoon, “Marine collagen as a promising biomaterial for biomedical applications,” *Mar. Drugs*, vol. 17, no. 8, p. 467, Aug. 2019.
- [135] A. K. Lynn, I. V. Yannas, and W. Bonfield, “Antigenicity and immunogenicity of collagen,” *J. Biomed. Mater. Res. - Part B Appl. Biomater.*, vol. 71, no. 2, pp. 343–354, Nov. 2004.
- [136] M. Gauza-Włodarczyk, L. Kubisz, S. Mielcarek, and D. Włodarczyk, “Comparison of thermal properties of fish collagen and bovine collagen in the temperature range 298–670 K,” *Mater. Sci. Eng. C*, vol. 80, pp. 468–471, Nov. 2017.
- [137] L. Cooperman and D. Michaeli, “The immunogenicity of injectable collagen. II. A retrospective review of seventy-two tested and treated patients,” *J. Am. Acad. Dermatol.*, vol. 10, no. 4, pp. 647–651, 1984.
- [138] E. O. Osidak, V. I. Kozhukhov, M. S. Osidak, and S. P. Domogatsky, “Collagen as bioink for bioprinting: A comprehensive review,” *Int. J. Bioprinting*, vol. 6, no. 3, pp. 1–10, Apr. 2020.
- [139] O. Shoseyov, Y. Posen, and F. Grynspan, “Human collagen produced in plants more than just another molecule,” *Bioengineered*, vol. 5, no. 1, p. 49, Aug. 2013.
- [140] E. Davison-Kotler, W. S. Marshall, and E. García-Gareta, “Sources of collagen for biomaterials in skin wound healing,” *Bioengineering*, vol. 6, no. 3, p. 56, Jun. 2019.
- [141] J. A. Werkmeister and J. A. M. Ramshaw, “Recombinant protein scaffolds for tissue engineering,” *Biomed. Mater.*, vol. 7, no. 1, p. 012002, Jan. 2012.
- [142] T. Wang, J. Lew, J. Premkumar, C. L. Poh, and M. Win Naing, “Production of recombinant collagen: state of the art and challenges,” *Eng. Biol.*, vol. 1, no. 1, pp. 18–23, Jun. 2017.
- [143] H. Yang and Z. Shu, “The extraction of collagen protein from pigskin,” *J. Chem. Pharm. Res.*, vol. 6, no. 2, pp. 683–687, 2014.
- [144] R. Naomi, P. M. Ridzuan, and H. Bahari, “Current insights into collagen type i,” *Polymers (Basel)*, vol. 13, no. 16, p. 2642, Aug. 2021.
- [145] M. Ahmed, A. K. Verma, and R. Patel, “Collagen extraction and recent biological activities of collagen peptides derived from sea-food waste: A review,” *Sustain. Chem. Pharm.*, vol. 18, p. 100315, Dec. 2020.

- [146] N. Rajan, J. Habermehl, M.-F. Coté, C. J. Doillon, and D. Mantovani, "Preparation of ready-to-use, storable and reconstituted type I collagen from rat tail tendon for tissue engineering applications," *Nat. Protoc.*, vol. 1, no. 6, pp. 2753–2758, Jan. 2007.
- [147] F. H. Silver, J. W. Freeman, and G. P. Seehra, "Collagen self-assembly and the development of tendon mechanical properties," *J. Biomech.*, vol. 36, no. 10, pp. 1529–1553, Oct. 2003.
- [148] M. Achilli and D. Mantovani, "Tailoring mechanical properties of collagen-based scaffolds for vascular tissue engineering: The effects of pH, temperature and ionic strength on gelation," *Polymers (Basel)*, vol. 2, no. 4, pp. 664–680, Dec. 2010.
- [149] C. Bonnans, J. Chou, and Z. Werb, "Remodelling the extracellular matrix in development and disease," *Nat. Rev. Mol. Cell Biol.*, vol. 15, no. 12, pp. 786–801, Dec. 2014.
- [150] G. S. Lazarus, R. S. Brown, J. R. Daniels, and H. M. Fullmer, "Human granulocyte collagenase," *Science (80-.)*, vol. 159, no. 3822, pp. 1483–1485, Mar. 1968.
- [151] T. L. Willett, R. S. Labow, N. C. Avery, and J. M. Lee, "Increased proteolysis of collagen in an in vitro tensile overload tendon model," *Ann. Biomed. Eng.*, vol. 35, no. 11, pp. 1961–1972, Nov. 2007.
- [152] A. Kato *et al.*, "Combination of Root Surface Modification with BMP-2 and Collagen Hydrogel Scaffold Implantation for Periodontal Healing in Beagle Dogs," *Open Dent. J.*, vol. 9, no. 1, pp. 52–59, 2015.
- [153] C. Dong and Y. Lv, "Application of collagen scaffold in tissue engineering: Recent advances and new perspectives," *Polymers (Basel)*, vol. 8, no. 2, p. 42, Feb. 2016.
- [154] C. R. Lee, A. J. Grodzinsky, and M. Spector, "The effects of cross-linking of collagen-glycosaminoglycan scaffolds on compressive stiffness, chondrocyte-mediated contraction, proliferation and biosynthesis," *Biomaterials*, vol. 22, no. 23, pp. 3145–3154, Dec. 2001.
- [155] S. N. Park, J. C. Park, H. O. Kim, M. J. Song, and H. Suh, "Characterization of porous collagen/hyaluronic acid scaffold modified by 1-ethyl-3-(3-dimethylaminopropyl)carbodiimide cross-linking," *Biomaterials*, vol. 23, no. 4, pp. 1205–1212, Feb. 2002.

- [156] D. V. Bax, N. Davidenko, S. W. Hamaia, R. W. Farndale, S. M. Best, and R. E. Cameron, “Impact of UV- and carbodiimide-based crosslinking on the integrin-binding properties of collagen-based materials,” *Acta Biomater.*, vol. 100, pp. 280–291, Dec. 2019.
- [157] H. Schoof, J. Apel, I. Heschel, and G. Rau, “Control of pore structure and size in freeze-dried collagen sponges,” *J. Biomed. Mater. Res.*, vol. 58, no. 4, pp. 352–357, Jan. 2001.
- [158] B. Bavaresco, R. Comín, N. A. Salvatierra, and M. P. Cid, “Three-dimensional printing of collagen and hyaluronic acid scaffolds with dehydrothermal treatment crosslinking,” *Compos. Commun.*, vol. 19, pp. 1–5, Jun. 2020.
- [159] S. S. Liao, F. Z. Cui, W. Zhang, and Q. L. Feng, “Hierarchically Biomimetic Bone Scaffold Materials: Nano-HA/Collagen/PLA Composite,” *J. Biomed. Mater. Res. - Part B Appl. Biomater.*, vol. 69, no. 2, pp. 158–165, May 2004.
- [160] K. E. Drzewiecki *et al.*, “Methacrylation induces rapid, temperature-dependent, reversible self-assembly of type-i collagen,” *Langmuir*, vol. 30, no. 37, pp. 11204–11211, Sep. 2014.
- [161] M. Betsch *et al.*, “Incorporating 4D into Bioprinting: Real-Time Magnetically Directed Collagen Fiber Alignment for Generating Complex Multilayered Tissues,” *Adv. Healthc. Mater.*, vol. 7, no. 21, p. 1800894, Nov. 2018.
- [162] K. T. Lawlor *et al.*, “Cellular extrusion bioprinting improves kidney organoid reproducibility and conformation,” *Nat. Mater.*, vol. 20, pp. 260–271, Feb. 2021.
- [163] Y. Yu *et al.*, “Three-dimensional bioprinting using self-assembling scalable scaffold-free ‘tissue strands’ as a new bioink,” *Sci. Rep.*, vol. 6, no. 1, p. 28714, 2016.
- [164] J. Zhang, E. Wehrle, M. Rubert, and R. Müller, “3d bioprinting of human tissues: Biofabrication, bioinks and bioreactors,” *Int. J. Mol. Sci.*, vol. 22, no. 8, Apr. 2021.
- [165] Y. Ren *et al.*, “Developments and Opportunities for 3D Bioprinted Organoids,” *Int. J. Bioprinting*, vol. 7, no. 3, p. 364, 2021.
- [166] B. D. Humphreys, “Bioprinting better kidney organoids,” *Nat. Mater.*, vol. 20, no. 2, pp. 128–130, Jan. 2021.
- [167] C. Cavallo *et al.*, “Comparison of alternative mesenchymal stem cell sources for cell banking and musculoskeletal advanced therapies,” *J. Cell. Biochem.*, vol. 112, no. 5, pp. 1418–1430, 2011.

- [168] K. McIntosh *et al.*, “The Immunogenicity of Human Adipose-Derived Cells: Temporal Changes In Vitro,” *Stem Cells*, vol. 24, no. 5, pp. 1246–1253, 2006.
- [169] J. M. Gimble, A. J. Katz, and B. A. Bunnell, “Adipose-derived stem cells for regenerative medicine,” *Circulation Research*, vol. 100, no. 9. NIH Public Access, pp. 1249–1260, May-2007.
- [170] B. Liu *et al.*, “Role of cyclic strain frequency in regulating the alignment of vascular smooth muscle cells in vitro,” *Biophys. J.*, vol. 94, no. 4, pp. 1497–1507, Feb. 2008.
- [171] A. Bozkurt *et al.*, “In vitro cell alignment obtained with a Schwann cell enriched microstructured nerve guide with longitudinal guidance channels,” *Biomaterials*, vol. 30, no. 2, pp. 169–179, Jan. 2009.
- [172] A. J. Sophia Fox, A. Bedi, and S. A. Rodeo, “The basic science of articular cartilage: Structure, composition, and function,” *Sports Health*, vol. 1, no. 6, pp. 461–468, Nov. 2009.
- [173] A. G. Alvarado and G. Chauhan, “Nanofiber alignment for biomedical applications,” *Mater. Today Proc.*, p. In Press, Nov. 2020.
- [174] E. Cady, J. A. Orkwis, R. Weaver, L. Conlin, N. N. Madigan, and G. M. Harris, “Micropatterning decellularized ecm as a bioactive surface to guide cell alignment, proliferation, and migration,” *Bioengineering*, vol. 7, no. 3, pp. 1–14, 2020.
- [175] J. Kim, A. J. Boys, L. A. Estroff, and L. J. Bonassar, “Combining TGF- β 1 and Mechanical Anchoring to Enhance Collagen Fiber Formation and Alignment in Tissue-Engineered Menisci,” *ACS Biomater. Sci. Eng.*, vol. 7, no. 4, pp. 1608–1620, Apr. 2021.
- [176] G. Babakhanova, J. Krieger, B. X. Li, T. Turiv, M. H. Kim, and O. D. Lavrentovich, “Cell alignment by smectic liquid crystal elastomer coatings with nanogrooves,” *J. Biomed. Mater. Res. - Part A*, vol. 108, no. 5, pp. 1223–1230, May 2020.
- [177] R. Huang *et al.*, “MXene Composite Nanofibers for Cell Culture and Tissue Engineering,” *ACS Appl. Bio Mater.*, vol. 3, no. 4, pp. 2125–2131, Apr. 2020.
- [178] J. Song, C. Michas, C. S. Chen, A. E. White, and M. W. Grinstaff, “From Simple to Architecturally Complex Hydrogel Scaffolds for Cell and Tissue Engineering Applications: Opportunities Presented by Two-Photon Polymerization,” *Adv. Healthc. Mater.*, vol. 9, no. 1, p. 1901217, Jan. 2020.

- [179] Y. Shen *et al.*, “DLP printing photocurable chitosan to build bio-constructs for tissue engineering,” *Carbohydr. Polym.*, vol. 235, p. 115970, May 2020.
- [180] J. Liu, B. Zhang, L. Li, J. Yin, and J. Fu, “Additive-lathe 3D bioprinting of bilayered nerve conduits incorporated with supportive cells,” *Bioact. Mater.*, vol. 6, no. 1, pp. 219–229, Jan. 2021.
- [181] M. Ebrahimi, S. Ostrovidov, S. Salehi, S. B. Kim, H. Bae, and A. Khademhosseini, “Enhanced skeletal muscle formation on microfluidic spun gelatin methacryloyl (GelMA) fibres using surface patterning and agrin treatment,” *J. Tissue Eng. Regen. Med.*, vol. 12, no. 11, pp. 2151–2163, Nov. 2018.
- [182] S. Wu, Y. Wang, P. N. Streubel, and B. Duan, “Living nanofiber yarn-based woven biotextiles for tendon tissue engineering using cell tri-culture and mechanical stimulation,” *Acta Biomater.*, vol. 62, pp. 102–115, Oct. 2017.
- [183] G. M. Ahmed, E. A. Abouauf, N. Abubakr, C. E. Dörfer, and K. F. El-Sayed, “Tissue Engineering Approaches for Enamel, Dentin, and Pulp Regeneration: An Update,” *Stem Cells Int.*, vol. 2020, 2020.
- [184] K. Lu *et al.*, “Biofabrication of aligned structures that guide cell orientation and applications in tissue engineering,” *Bio-Design Manuf.*, vol. 4, no. 2, pp. 258–277, Jan. 2021.
- [185] D. Yang, B. Lu, Y. Zhao, and X. Jiang, “Fabrication of aligned fibrous arrays by magnetic electrospinning,” *Adv. Mater.*, vol. 19, no. 21, pp. 3702–3706, Nov. 2007.
- [186] B. Sun *et al.*, “Electrospun anisotropic architectures and porous structures for tissue engineering,” *J. Mater. Chem. B*, vol. 3, no. 27, pp. 5389–5410, Jul. 2015.
- [187] S. H. Yoon, Y. K. Kim, E. D. Han, Y. H. Seo, B. H. Kim, and M. R. K. Mofrad, “Passive control of cell locomotion using micropatterns: The effect of micropattern geometry on the migratory behavior of adherent cells,” *Lab Chip*, vol. 12, no. 13, pp. 2391–2402, Jun. 2012.
- [188] K. N. Dahl, A. J. S. Ribeiro, and J. Lammerding, “Nuclear shape, mechanics, and mechanotransduction,” *Circ. Res.*, vol. 102, no. 11, pp. 1307–1318, Jun. 2008.
- [189] R. Peng, X. Yao, and J. Ding, “Effect of cell anisotropy on differentiation of stem cells on micropatterned surfaces through the controlled single cell adhesion,” *Biomaterials*, vol. 32, no. 32, pp. 8048–8057, Nov. 2011.

- [190] F. L. Yap and Y. Zhang, "Protein and cell micropatterning and its integration with micro/nanoparticles assembly," *Biosens. Bioelectron.*, vol. 22, no. 6, pp. 775–788, Jan. 2007.
- [191] J. Friguglietti *et al.*, "Novel Silicon Titanium Diboride Micropatterned Substrates for Cellular Patterning," *Biomaterials*, vol. 244, p. 119927, Jun. 2020.
- [192] C. Ma, T. Qu, B. Chang, Y. Jing, J. Q. Feng, and X. Liu, "3D Maskless Micropatterning for Regeneration of Highly Organized Tubular Tissues," *Adv. Healthc. Mater.*, vol. 7, no. 3, p. 1700738, Feb. 2018.
- [193] E. Gantumur, M. Kimura, M. Taya, M. Horie, M. Nakamura, and S. Sakai, "Inkjet micropatterning through horseradish peroxidase-mediated hydrogelation for controlled cell immobilization and microtissue fabrication," *Biofabrication*, vol. 12, no. 1, p. 011001, Oct. 2020.
- [194] S. Deville, E. Saiz, and A. P. Tomsia, "Freeze casting of hydroxyapatite scaffolds for bone tissue engineering," *Biomaterials*, vol. 27, no. 32, pp. 5480–5489, Nov. 2006.
- [195] S. E. Naleway, K. C. Fickas, Y. N. Maker, M. A. Meyers, and J. McKittrick, "Reproducibility of ZrO₂-based freeze casting for biomaterials," *Mater. Sci. Eng. C*, vol. 61, pp. 105–112, Apr. 2016.
- [196] W. L. Li, K. Lu, and J. Y. Walz, "Freeze casting of porous materials: Review of critical factors in microstructure evolution," *Int. Mater. Rev.*, vol. 57, no. 1, pp. 37–60, Jan. 2012.
- [197] N. L. Francis *et al.*, "An ice-templated, linearly aligned chitosan-alginate scaffold for neural tissue engineering," *J. Biomed. Mater. Res. - Part A*, vol. 101, no. 12, pp. 3493–3503, Dec. 2013.
- [198] I. Nelson, L. Gardner, K. Carlson, and S. E. Naleway, "Freeze casting of iron oxide subject to a tri-axial nested Helmholtz-coils driven uniform magnetic field for tailored porous scaffolds," *Acta Mater.*, vol. 173, pp. 106–116, Jul. 2019.
- [199] L. Fan, J. L. Li, Z. Cai, and X. Wang, "Creating Biomimetic Anisotropic Architectures with Co-Aligned Nanofibers and Macrochannels by Manipulating Ice Crystallization," *ACS Nano*, vol. 12, no. 6, pp. 5780–5790, Jun. 2018.

- [200] M. Khanmohammadi, S. Sakai, and M. Taya, "Fabrication of single and bundled filament-like tissues using biodegradable hyaluronic acid-based hollow hydrogel fibers," *Int. J. Biol. Macromol.*, vol. 104, pp. 204–212, Nov. 2017.
- [201] Y. F. Goh, I. Shakir, and R. Hussain, "Electrospun fibers for tissue engineering, drug delivery, and wound dressing," *J. Mater. Sci.*, vol. 48, no. 8, pp. 3027–3054, Apr. 2013.
- [202] A. C. A. Wan, M. F. A. Cutiongco, B. C. U. Tai, M. F. Leong, H. F. Lu, and E. K. F. Yim, "Fibers by interfacial polyelectrolyte complexation – processes, materials and applications," *Mater. Today*, vol. 19, no. 8, pp. 437–450, Oct. 2016.
- [203] J. Kalisky *et al.*, "An easy-to-use and versatile method for building cell-laden microfibres," *Sci. Rep.*, vol. 6, no. 1, p. 33328, 2016.
- [204] M. Akbari *et al.*, "Composite living fibers for creating tissue constructs using textile techniques," *Adv. Funct. Mater.*, vol. 24, no. 26, pp. 4060–4067, 2014.
- [205] R. Costa-Almeida *et al.*, "Cell-laden composite suture threads for repairing damaged tendons," *J. Tissue Eng. Regen. Med.*, vol. 12, no. 4, pp. 1039–1048, 2018.
- [206] J. B. Suzuki and R. R. Resnik, "Wound Dehiscence: Incision Line Opening," in *Misch's Avoiding Complications in Oral Implantology*, Elsevier, 2017, pp. 417–419.
- [207] X. Zhang and Y. Lu, "Centrifugal spinning: An alternative approach to fabricate nanofibers at high speed and low cost," *Polym. Rev.*, vol. 54, no. 4, pp. 677–701, 2014.
- [208] N. O. Muniz, F. A. Vechietti, G. R. Anesi, G. V. Guinea, and L. A. L. Dos Santos, "Blend-based fibers produced via centrifugal spinning and electrospinning processes: Physical and rheological properties," *J. Mater. Res.*, vol. 35, no. 21, pp. 2905–2916, Nov. 2020.
- [209] M. Buzgo *et al.*, "Emulsion centrifugal spinning for production of 3D drug releasing nanofibres with core/shell structure," *RSC Adv.*, vol. 7, no. 3, pp. 1215–1228, 2017.
- [210] N. A. Norzain and W. C. Lin, "Orientated and diameter-controlled fibrous scaffolds fabricated using the centrifugal electrospinning technique for stimulating the behaviours of fibroblast cells," *J. Ind. Text.*, p. 152808372098812, Jan. 2021.
- [211] J. Hong, M. Yeo, G. H. Yang, and G. Kim, "Cell-electrospinning and its application for tissue engineering," *International Journal of Molecular Sciences*, vol. 20, no. 24. MDPI AG, 02-Dec-2019.

- [212] S. N. Jayasinghe, “Cell electrospinning: A novel tool for functionalising fibres, scaffolds and membranes with living cells and other advanced materials for regenerative biology and medicine,” *Analyst*, vol. 138, no. 8, pp. 2215–2223, Mar. 2013.
- [213] P. Rider, Ž. P. Kačarević, S. Alkildani, S. Retnasingh, and M. Barbeck, “Bioprinting of tissue engineering scaffolds,” *J. Tissue Eng.*, vol. 9, pp. 1–16, Sep. 2018.
- [214] B. Grigoryan *et al.*, “Development, characterization, and applications of multi-material stereolithography bioprinting,” *Sci. Rep.*, vol. 11, no. 1, pp. 1–13, 2021.
- [215] J. Lewicki, J. Bergman, C. Kerins, and O. Hermanson, “Optimization of 3D bioprinting of human neuroblastoma cells using sodium alginate hydrogel,” *Bioprinting*, vol. 16, p. e00053, Dec. 2019.
- [216] E. S. Bishop *et al.*, “3-D bioprinting technologies in tissue engineering and regenerative medicine: Current and future trends,” *Genes and Diseases*, vol. 4, no. 4. Chongqing yi ke da xue, di 2 lin chuang xue yuan Bing du xing gan yan yan jiu suo, pp. 185–195, 01-Dec-2017.
- [217] G. Gao *et al.*, “Tissue Engineered Bio-Blood-Vessels Constructed Using a Tissue-Specific Bioink and 3D Coaxial Cell Printing Technique: A Novel Therapy for Ischemic Disease,” *Adv. Funct. Mater.*, vol. 27, no. 33, pp. 1–12, 2017.
- [218] S. J. Shin *et al.*, “‘On the fly’ continuous generation of alginate fibers using a microfluidic device,” *Langmuir*, vol. 23, no. 17, pp. 9104–9108, Aug. 2007.
- [219] S. Sugiura, T. Oda, Y. Aoyagi, M. Satake, N. Ohkohchi, and M. Nakajima, “Tubular gel fabrication and cell encapsulation in laminar flow stream formed by microfabricated nozzle array,” *Lab Chip*, vol. 8, no. 8, pp. 1255–1257, Jul. 2008.
- [220] A. G. Tabriz, M. A. Hermida, N. R. Leslie, and W. Shu, “Three-dimensional bioprinting of complex cell laden alginate hydrogel structures,” *Biofabrication*, vol. 7, no. 4, Dec. 2015.
- [221] H. Onoe *et al.*, “Metre-long cell-laden microfibres exhibit tissue morphologies and functions,” *Nat. Mater.*, vol. 12, no. 6, pp. 584–590, 2013.
- [222] I. Dmour and M. O. Taha, “Natural and semisynthetic polymers in pharmaceutical nanotechnology,” in *Organic Materials as Smart Nanocarriers for Drug Delivery*, William Andrew Publishing, 2018, pp. 35–100.

- [223] S. C. Millik *et al.*, “3D printed coaxial nozzles for the extrusion of hydrogel tubes toward modeling vascular endothelium,” *Biofabrication*, vol. 11, no. 4, Jul. 2019.
- [224] X. Dai *et al.*, “Coaxial 3D bioprinting of self-assembled multicellular heterogeneous tumor fibers,” *Sci. Rep.*, vol. 7, no. 1, pp. 1–12, 2017.
- [225] Q. Gao *et al.*, “3D Bioprinting of Vessel-like Structures with Multilevel Fluidic Channels,” *ACS Biomater. Sci. Eng.*, vol. 3, no. 3, pp. 399–408, 2017.
- [226] L. Shao, Q. Gao, C. Xie, J. Fu, M. Xiang, and Y. He, “Directly coaxial 3D bioprinting of large-scale vascularized tissue constructs,” *Biofabrication*, vol. 12, no. 3, p. 035014, May 2020.
- [227] G. Cidonio, M. Glinka, J. I. Dawson, and R. O. C. Oreffo, “The cell in the ink: Improving biofabrication by printing stem cells for skeletal regenerative medicine,” *Biomaterials*, vol. 209, pp. 10–24, Jul. 2019.
- [228] R. Attalla, E. Puersten, N. Jain, and P. R. Selvaganapathy, “3D bioprinting of heterogeneous bi- and tri-layered hollow channels within gel scaffolds using scalable multi-axial microfluidic extrusion nozzle,” *Biofabrication*, vol. 11, p. 015012, 2019.
- [229] K. G. Battiston, J. W. C. Cheung, D. Jain, and J. P. Santerre, “Biomaterials in co-culture systems: Towards optimizing tissue integration and cell signaling within scaffolds,” *Biomaterials*, vol. 35, no. 15, pp. 4465–4476, May 2014.
- [230] A. Kjar, B. McFarland, K. Mecham, N. Harward, and Y. Huang, “Engineering of tissue constructs using coaxial bioprinting,” *Bioact. Mater.*, vol. 6, no. 2, pp. 460–471, Feb. 2021.
- [231] A. I. Van Den Bulcke, B. Bogdanov, N. De Rooze, E. H. Schacht, M. Cornelissen, and H. Berghmans, “Structural and rheological properties of methacrylamide modified gelatin hydrogels,” *Biomacromolecules*, vol. 1, no. 1, pp. 31–38, 2000.
- [232] K. Yue, G. Trujillo-de Santiago, M. M. Alvarez, A. Tamayol, N. Annabi, and A. Khademhosseini, “Synthesis, properties, and biomedical applications of gelatin methacryloyl (GelMA) hydrogels,” *Biomaterials*, vol. 73, pp. 254–271, 2015.
- [233] B. Kong *et al.*, “Fiber reinforced GelMA hydrogel to induce the regeneration of corneal stroma,” *Nat. Commun.*, vol. 11, no. 1, pp. 1–12, Dec. 2020.

- [234] B. H. Lee, H. Shirahama, N. J. Cho, and L. P. Tan, “Efficient and controllable synthesis of highly substituted gelatin methacrylamide for mechanically stiff hydrogels,” *RSC Adv.*, vol. 5, no. 128, pp. 106094–106097, 2015.
- [235] P. Comeau and T. Willett, “A Carbodiimide Coupling Approach for PEGylating GelMA and Further Tuning GelMA Composite Properties,” *Macromol. Mater. Eng.*, p. 2000604, Dec. 2020.
- [236] F. Tabatabaei, K. Moharamzadeh, and L. Tayebi, “Fibroblast encapsulation in gelatin methacryloyl (GelMA) versus collagen hydrogel as substrates for oral mucosa tissue engineering,” *J. Oral Biol. Craniofacial Res.*, vol. 10, no. 4, pp. 573–577, Oct. 2020.
- [237] T. Liu, W. Weng, Y. Zhang, X. Sun, and H. Yang, “Applications of Gelatin Methacryloyl (GelMA) Hydrogels in Microfluidic Technique-Assisted Tissue Engineering,” *Molecules*, vol. 25, no. 22. NLM (Medline), p. 5305, 13-Nov-2020.
- [238] W. Liu *et al.*, “Coaxial extrusion bioprinting of 3D microfibrous constructs with cell-favorable gelatin methacryloyl microenvironments,” *Biofabrication*, vol. 10, p. 024102, 2018.
- [239] I. Pepelanova, K. Kruppa, T. Scheper, and A. Lavrentieva, “Gelatin-methacryloyl (GelMA) hydrogels with defined degree of functionalization as a versatile toolkit for 3D cell culture and extrusion bioprinting,” *Bioengineering*, vol. 5, no. 3, p. 55, Sep. 2018.
- [240] N. E. Fedorovich, M. H. Oudshoorn, D. van Geemen, W. E. Hennink, J. Alblas, and W. J. A. Dhert, “The effect of photopolymerization on stem cells embedded in hydrogels,” *Biomaterials*, vol. 30, no. 3, pp. 344–353, Jan. 2009.
- [241] L. Shao *et al.*, “Fiber-Based Mini Tissue with Morphology-Controllable GelMA Microfibers,” *Small*, vol. 14, no. 44, p. 1802187, Nov. 2018.
- [242] L. Shao *et al.*, “Fiber-Based Mini Tissue with Morphology-Controllable GelMA Microfibers,” *Small*, vol. 14, no. 44, 2018.
- [243] Y. Morimoto, M. Kiyosawa, and S. Takeuchi, “Three-dimensional printed microfluidic modules for design changeable coaxial microfluidic devices,” *Sensors Actuators, B Chem.*, vol. 274, pp. 491–500, Nov. 2018.
- [244] F. J. O’Brien, “Biomaterials & scaffolds for tissue engineering,” *Materials Today*, vol. 14, no. 3. Elsevier B.V., pp. 88–95, 01-Mar-2011.

- [245] E. C. Novosel, C. Kleinhaus, and P. J. Kluger, “Vascularization is the key challenge in tissue engineering,” *Adv. Drug Deliv. Rev.*, vol. 63, no. 4, pp. 300–311, Apr. 2011.
- [246] A. R. Ward, “Electro-Muscle Stimulation Therapy,” in *Comprehensive Biomedical Physics*, vol. 10, Elsevier, 2014, pp. 231–253.
- [247] J. Feher, “Contractile Mechanisms in Skeletal Muscle,” in *Quantitative Human Physiology*, 2nd ed., Elsevier, 2017, pp. 305–317.
- [248] A. K. Miri *et al.*, “Effective bioprinting resolution in tissue model fabrication,” *Lab Chip*, vol. 19, no. 11, pp. 2019–2037, May 2019.
- [249] W. Sun *et al.*, “The bioprinting roadmap,” *Biofabrication*, vol. 12, no. 2, p. 022002, Feb. 2020.
- [250] M. G. Yeo, J. S. Lee, W. Chun, and G. H. Kim, “An Innovative Collagen-Based Cell-Printing Method for Obtaining Human Adipose Stem Cell-Laden Structures Consisting of Core-Sheath Structures for Tissue Engineering,” *Biomacromolecules*, vol. 17, no. 4, pp. 1365–1375, 2016.
- [251] H. Liang, J. He, J. Chang, B. Zhang, and D. Li, “Coaxial nozzle-assisted electrohydrodynamic printing for microscale 3D cell-laden constructs,” *Int. J. Bioprinting*, vol. 4, no. 1, p. 127, 2017.
- [252] A. D. Augst, H. J. Kong, and D. J. Mooney, “Alginate hydrogels as biomaterials,” *Macromol. Biosci.*, vol. 6, no. 8, pp. 623–633, Aug. 2006.
- [253] G. Wang *et al.*, “Microfluidics-based fabrication of cell-laden hydrogel microfibers for potential applications in tissue engineering,” *Molecules*, vol. 24, no. 8, 2019.
- [254] J. Gong *et al.*, “Complexation-induced resolution enhancement of 3D-printed hydrogel constructs,” *Nat. Commun.*, vol. 11, no. 1, pp. 1–14, Mar. 2020.
- [255] J. K. Francis Suh and H. W. T. Matthew, “Application of chitosan-based polysaccharide biomaterials in cartilage tissue engineering: A review,” *Biomaterials*, vol. 21, no. 24, pp. 2589–2598, Dec. 2000.
- [256] H. Shirahama, B. H. Lee, L. P. Tan, and N. J. Cho, “Precise tuning of facile one-pot gelatin methacryloyl (GelMA) synthesis,” *Sci. Rep.*, vol. 6, no. 1, pp. 1–11, Aug. 2016.

- [257] J. Radhakrishnan, S. Varadaraj, S. K. Dash, A. Sharma, and R. S. Verma, "Organotypic cancer tissue models for drug screening: 3D constructs, bioprinting and microfluidic chips," *Drug Discov. Today*, vol. 25, no. 5, pp. 879–890, May 2020.
- [258] S. Knowlton, S. Onal, C. H. Yu, J. J. Zhao, and S. Tasoglu, "Bioprinting for cancer research," *Trends Biotechnol.*, vol. 33, no. 9, pp. 504–513, Sep. 2015.
- [259] D. P. Ivanov *et al.*, "In vitro co-culture model of medulloblastoma and human neural stem cells for drug delivery assessment," *J. Biotechnol.*, vol. 205, pp. 3–13, Jul. 2015.
- [260] W. Zhu, B. Holmes, R. I. Glazer, and L. G. Zhang, "3D printed nanocomposite matrix for the study of breast cancer bone metastasis," *Nanomedicine Nanotechnology, Biol. Med.*, vol. 12, no. 1, pp. 69–79, Jan. 2016.
- [261] Y. Yan, J. Bejoy, J. Xia, K. Griffin, J. Guan, and Y. Li, "Cell population balance of cardiovascular spheroids derived from human induced pluripotent stem cells," *Sci. Rep.*, vol. 9, no. 1, Dec. 2019.
- [262] M. O. Lee *et al.*, "Modelling cardiac fibrosis using three-dimensional cardiac microtissues derived from human embryonic stem cells," *J. Biol. Eng.*, vol. 13, no. 1, Feb. 2019.
- [263] M. Coll *et al.*, "Generation of Hepatic Stellate Cells from Human Pluripotent Stem Cells Enables In Vitro Modeling of Liver Fibrosis," *Cell Stem Cell*, vol. 23, no. 1, pp. 101-113.e7, Jul. 2018.
- [264] B. Nugraha *et al.*, "Monitoring and manipulating cellular crosstalk during kidney fibrosis inside a 3D in vitro co-culture," *Sci. Rep.*, vol. 7, no. 1, pp. 1–11, Nov. 2017.
- [265] E. C. Costa, A. F. Moreira, D. de Melo-Diogo, V. M. Gaspar, M. P. Carvalho, and I. J. Correia, "3D tumor spheroids: an overview on the tools and techniques used for their analysis," *Biotechnol. Adv.*, vol. 34, no. 8, pp. 1427–1441, Dec. 2016.
- [266] A. C. Daly, M. D. Davidson, and J. A. Burdick, "3D bioprinting of high cell-density heterogeneous tissue models through spheroid fusion within self-healing hydrogels," *Nat. Commun.*, vol. 12, no. 1, 2021.
- [267] D. F. Duarte Campos *et al.*, "Bioprinting Cell- and Spheroid-Laden Protein-Engineered Hydrogels as Tissue-on-Chip Platforms," *Front. Bioeng. Biotechnol.*, vol. 8, Apr. 2020.

- [268] S. Swaminathan, Q. Hamid, W. Sun, and A. M. Clyne, "Bioprinting of 3D breast epithelial spheroids for human cancer models," *Biofabrication*, vol. 11, no. 2, pp. 025003–025003, Jan. 2019.
- [269] A. Blaeser, D. F. Duarte Campos, U. Puster, W. Richtering, M. M. Stevens, and H. Fischer, "Controlling Shear Stress in 3D Bioprinting is a Key Factor to Balance Printing Resolution and Stem Cell Integrity," *Adv. Healthc. Mater.*, vol. 5, no. 3, pp. 326–333, Feb. 2016.
- [270] P. J. Lee, P. J. Hung, and L. P. Lee, "An artificial liver sinusoid with a microfluidic endothelial-like barrier for primary hepatocyte culture," *Biotechnol. Bioeng.*, vol. 97, no. 5, pp. 1340–1346, Aug. 2007.
- [271] S. Naik *et al.*, "A 3d renal proximal tubule on chip model phenocopies lowe syndrome and dent ii disease tubulopathy," *Int. J. Mol. Sci.*, vol. 22, no. 10, May 2021.
- [272] C. Oleaga *et al.*, "Multi-Organ toxicity demonstration in a functional human in vitro system composed of four organs," *Sci. Rep.*, vol. 6, no. 1, pp. 1–17, Feb. 2016.
- [273] H. Azizgolshani *et al.*, "High-throughput organ-on-chip platform with integrated programmable fluid flow and real-time sensing for complex tissue models in drug development workflows," *Lab Chip*, vol. 21, no. 8, pp. 1454–1474, 2021.
- [274] L. A. Low and D. A. Tagle, "Tissue chips-innovative tools for drug development and disease modeling," *Lab Chip*, vol. 17, no. 18, pp. 3026–3036, Sep. 2017.
- [275] J. P. Wikswo *et al.*, "Scaling and systems biology for integrating multiple organs-on-a-chip," *Lab Chip*, vol. 13, no. 18, pp. 3496–3511, Aug. 2013.
- [276] C. L. Stokes, M. Cirit, and D. A. Lauffenburger, "Physiome-on-a-Chip: The Challenge of 'scaling' in Design, Operation, and Translation of Microphysiological Systems," *CPT Pharmacometrics Syst. Pharmacol.*, vol. 4, no. 10, pp. 559–562, Oct. 2015.
- [277] L. Verneti *et al.*, "Functional Coupling of Human Microphysiology Systems: Intestine, Liver, Kidney Proximal Tubule, Blood-Brain Barrier and Skeletal Muscle," *Sci. Rep.*, vol. 7, Feb. 2017.
- [278] I. Maschmeyer *et al.*, "A four-organ-chip for interconnected long-term co-culture of human intestine, liver, skin and kidney equivalents," *Lab Chip*, vol. 15, no. 12, pp. 2688–2699, Jun. 2015.

- [279] Q. Wu *et al.*, “Organ-on-a-chip: Recent breakthroughs and future prospects,” *Biomed. Eng. Online*, vol. 19, no. 1, pp. 1–19, Feb. 2020.
- [280] E. Moradi, S. Jalili-Firoozinezhad, and M. Solati-Hashjin, “Microfluidic organ-on-a-chip models of human liver tissue,” *Acta Biomater.*, vol. 116, pp. 67–83, Oct. 2020.
- [281] Q. Ramadan and M. Zourob, “Organ-on-a-chip engineering: Toward bridging the gap between lab and industry,” *Biomicrofluidics*, vol. 14, no. 4, p. 041501, Jul. 2020.
- [282] W. Peng, P. Datta, B. Ayan, V. Ozbolat, D. Sosnoski, and I. T. Ozbolat, “3D bioprinting for drug discovery and development in pharmaceuticals,” *Acta Biomater.*, vol. 57, pp. 26–46, Jul. 2017.
- [283] S. Knowlton and S. Tasoglu, “A Bioprinted Liver-on-a-Chip for Drug Screening Applications,” *Trends Biotechnol.*, vol. 34, no. 9, pp. 681–682, Sep. 2016.
- [284] D. Huh, G. A. Hamilton, and D. E. Ingber, “From 3D cell culture to organs-on-chips,” *Trends Cell Biol.*, vol. 21, no. 12, pp. 745–754, Dec. 2011.
- [285] M. Abudupataer *et al.*, “Bioprinting a 3D vascular construct for engineering a vessel-on-a-chip,” *Biomed. Microdevices*, vol. 22, no. 1, pp. 1–10, Dec. 2020.
- [286] C. Colosi *et al.*, “Microfluidic Bioprinting of Heterogeneous 3D Tissue Constructs Using Low-Viscosity Bioink,” *Adv. Mater.*, vol. 28, no. 4, pp. 677-684a, Jan. 2016.

3. Materials and Methods

3.1. Coaxial extrusion

3.1.1. Hydrogel preparation

Sodium alginate powder (Protanal LF 10/60 FT, FMC Corporation, Philadelphia, PA, US) was dissolved in dH₂O, sterile filtered (0.2 μm) and then loaded into a 5ml luer-lock syringe (BD Plastipak, UK).

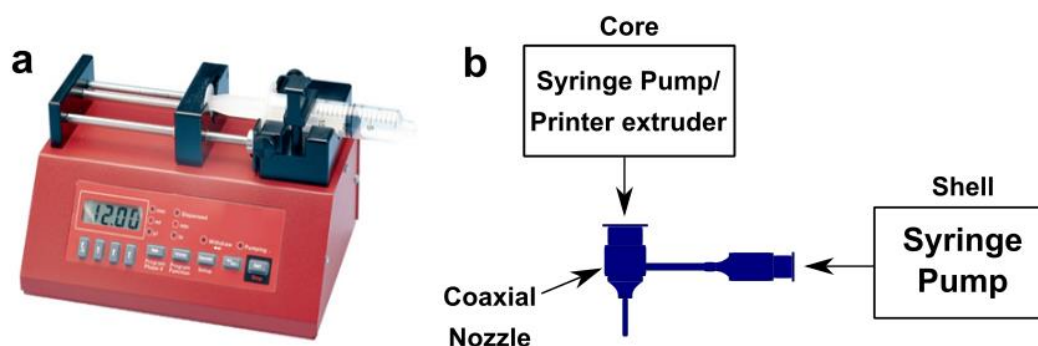


Figure 3-1. (a) Aladdin 300 syringe pump fitted with a 20ml disposable syringe. (b) schematic showing pump and extruder connections to the coaxial nozzle housing for the extrusion process.

The 5ml syringe was installed into a commercial syringe pump (Aladdin 300, World Precision Instruments, Stevenage, UK, see Figure 3-1) and connected to the 19G (686 μm) shell inlet of the coaxial nozzle housing using polypropylene nozzle fittings and silicone tubing (Cole Parmer, Eaton Socon, UK).

3.1.2. Cell culture

Rat-derived adipose-derived stem cells (ADSCs) were isolated and donated by the University of Glasgow Institute of Molecular Cell & Systems Biology. Cells were cultured in Minimum Essential Media (MEM) alpha cell culture media with L-glutamine and phenol red pH indicator (Life Technologies, Paisley, UK) and supplemented with 10% (v/v) fetal bovine serum (FBS) (Biosera, Nuaille, France) and 1% (v/v) penicillin/ streptomycin (Corning Life Sciences, UK) at 37°C and 5% CO₂. After 3 or 4 days in culture, media was removed, non-adherent cells were removed using Dulbecco's Phosphate-Buffered Saline (DPBS, modified to not contain CaCl₂ and MgCl₂) (Sigma Aldrich, UK) and fresh media was added. Cells were passaged every seven days, at a ratio of 1:2. Once confluence reached 80%, cells were washed with DPBS, detached by incubating with tryple express (Life Technologies, Paisley, UK) for 3 min at 37°C and 5% CO₂.

The cells were then centrifuged at 200g and 4°C and supernatant was removed by pipetting. Cells could then be re-suspended in the chosen biomaterial for extrusion. To achieve high cell densities (up to 15×10^6 cells/ml), up to four 150 cm³ (surface area) flasks were utilised at one time.

ADSC cells were subjected to the differentiation protocol as described by Dezawa et. al. [1] to display a Schwann cell-like phenotype (dADSCs). At passage 2 dADSCs were cultured in MEM supplemented with 1 mM β -mercaptoethanol (Sigma-Aldrich, UK) for 24 hours followed by treatment using 35 ng/ml all-trans-retinoic acid.

ADSC cells were cultured in the differentiated state by the addition of four growth factors to ADSC growth media at the following final concentrations: forskolin (14 μ M, Sigma Aldrich, UK), Recombinant human neuregulin-1 (NRG1-beta 1/HRG1-beta 1 EGF Domain Protein, 250 ng/ml, R&D Systems, UK), referred to as glial growth factor (GGF), human basic fibroblastic growth factor (hBFGF, 10 ng/ml, Sigma-Aldrich, UK) and platelet-derived growth factor-AA (PDGF, 5 ng/ml, Merck Millipore, UK). Once confluence reached 80%, cells were washed with DPBS, detached by incubating with trypsin in 0.25% EDTA (ethylenediaminetetraacetic acid) (Life Technologies, Paisley, UK) for 5 min at 37°C and 5% CO₂. The cells were then centrifuged at 200g and 4°C and supernatant was removed by pipetting. Cells could then be re-suspended in the chosen biomaterial for extrusion.

3.1.3. Production of collagen hydrogel

A collagen stock solution was prepared according to an adapted version of a well-established protocol [2] [3], using rat tails provided by the Biological Procedures Unit at the University of Strathclyde.

Dialysis tubing was cut to lengths of approximately 50 cm and simmered in a 50% ethanol solution on a hot plate in a fume cupboard. The dialysis tubing was then simmered in a solution of distilled water containing 10 mM NaHCO₃ and 1mM EDTA (both Sigma Aldrich, UK) followed by simmering in distilled water and subsequent storing of the tubing in distilled water at 4 °C for later use [4].

The outer skin of the rat tail tendons was stripped and cut using sterilised forceps and scalpels. The tendons were then pulled from the tail and placed in a petri dish containing sterile distilled water. The tendons were then weighed and extracted into a 0.5M acetic acid solution (in distilled water; Sigma Aldrich, UK) to give a 1% w/v extract (1g tendon in 100 ml 0.5M acetic acid). This solution was left for 48 hours at 4 °C.

The extract was then filtered using a sterile bottle top filter (0.2 μm). The membrane filter was replaced using 4 layers of sterile gauze (to prevent pieces of tendon passing into the filtrate). The dialysis tubing was then rinsed in 0.1x DMEM (Dulbecco's Modified Eagle Medium; Life Technologies, Paisley, UK) in distilled water. One end of the dialysis tubing was then tied and the collagen solution was poured into the tubing using a sterile filter funnel.

The open end of the tubing was then tied to seal the collagen solution within the dialysis tubing. The closed dialysis tubing containing the collagen solution was then dialysed against the 0.1x DMEM solution for 24 hours at 4 $^{\circ}\text{C}$.

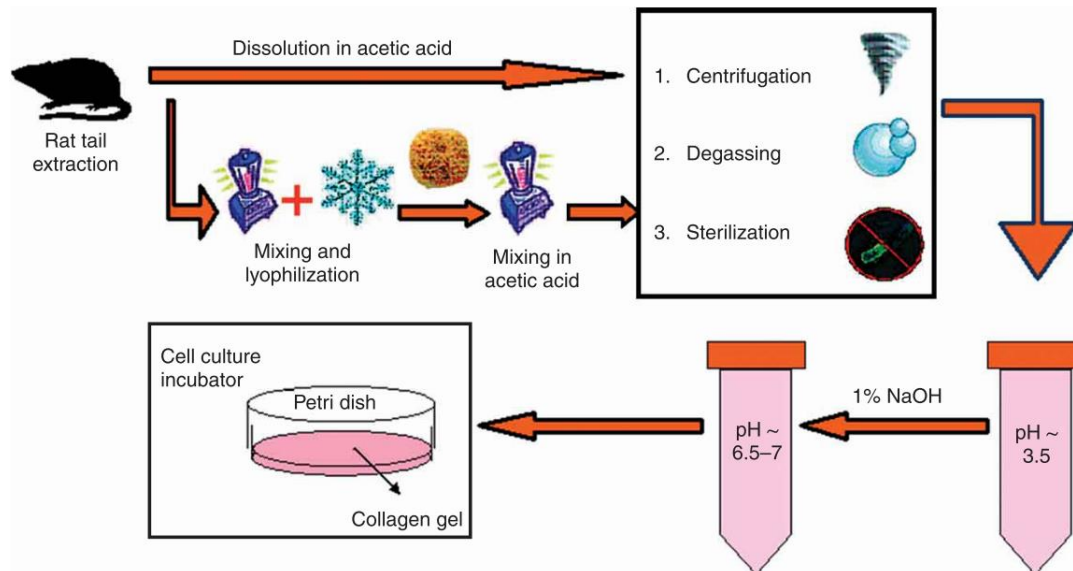


Figure 3-2. Schematic representation of the process, from collagen extraction to cell culture and through sterilization [2]

The collagen solution was then removed from the dialysis tubing and placed into centrifuge bottles and sterilised by centrifugation, at 15,350g for 2 hours at 6 $^{\circ}\text{C}$. The supernatant was transferred, by pipetting, into sterilised bottles and 3 ml of this solution was then pipetted into 3 pre-weighed petri dishes and allowed to dry at 37 $^{\circ}\text{C}$ (see Figure 3-2 for full process). This allowed calculation of the collagen solids content within the sterilised stock solution. The sterilised stock solution can now be used for biological experimentation purposes [5] [6].

3.1.4. Collagen bioink production

The collagen stock solution was neutralised by adding 200 mM HEPES buffer solution, DMEM (x10) in 0.4M NaOH solution (2:1 by volume), 0.1M NaOH solution and 0.1% (v/v) acetic acid (all Sigma Aldrich, UK). The solvent for all solutions was dH_2O and all solutions were sterilised using a 0.2 μm filter (Sartorius Stedim Biotech, Göttingen, Germany).

The neutralised collagen solution was then diluted using 0.1% acetic acid to the desired concentration [7] [8] [9]. It should be noted that no particular endotoxin (lipopolysaccharide) control measures were employed; it was assumed that the use of sterile equipment ensured the absence of endotoxins.

3.1.5. Extrusion process

Single cell pellets were suspended in the neutralised collagen solution (100% v/v), in an ice bath to prevent collagen self-assembly, by gentle pipetting, to form a bioink. The bioink was then loaded into a 1ml luer-slip syringe (BD Plastipak, UK) and fitted to the 27G (210 μ m) core inlet of a customised stainless-steel coaxial nozzle (Ramé-hart Instrument Company, Succasunna, NJ, USA, see Figure 3-3). It should be noted that various core nozzle diameters may be used, given the core nozzles are removable and can be screwed into the coaxial nozzle housing.

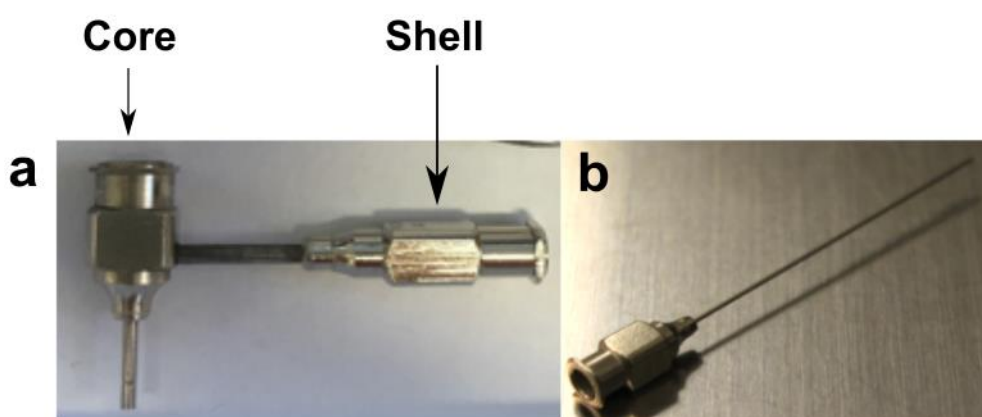


Figure 3-3. Coaxial nozzle components. (a) Stainless steel coaxial nozzle housing, showing horizontal shell inlet and vertical core inlet, in which (b) a stainless steel removable core nozzle can be screwed into

A crosslinking bath of sterile-filtered (0.2 μ m) 100 mM calcium chloride solution (in dH₂O) (Sigma Aldrich, UK) was placed under the coaxial nozzle. Upon the establishment of continuous co-flow exiting the coaxial nozzle tip, the coaxial nozzle was submerged in the crosslinking bath of calcium chloride. Due to immediate crosslinking upon contact between sodium alginate exiting the nozzle tip and the calcium chloride bath, forceps were used to draw the flow from the coaxial nozzle through the crosslinking bath.

Upon the termination of extrusion, fibres were left to crosslink within the CaCl₂ bath for a specified time (usually 10 min, unless otherwise stated). This allowed the formation of mechanically-stable, porous, core-shell cell-hydrogel scaffolds with calcium alginate hydrogel shells and cell-collagen cores.

In cases where secondary cross-linking was employed, barium chloride (Sigma Aldrich, UK) or strontium chloride (Fisher Scientific, UK) were dissolved in dH₂O to provide secondary cross-linking baths.

Upon the completion of primary CaCl₂ cross-linking, extruded structures were removed and washed with phosphate buffered saline, 1x (PBS) (Fisher Scientific, UK) prior to submersion in either the BaCl₂ or SrCl₂ solutions, with further PBS washing on completion prior to incubation in culture media.

Extruded fibres were then cut into smaller sections using forceps and placed into separate wells of cell culture plates (Corning Incorporated, NY, USA). Fresh culture media was then added to each scaffold and constructs were left to incubate at 37°C and 5% CO₂.

3.1.6. Staining and microscopy

To analyse collagen fibre morphology and continuity over time, the aforementioned coaxial extrusion process was used without the presence of cells in the collagen solution. Extruded fibres were removed from the crosslinking bath, washed with DPBS three times and imaged (with either 4x or 10x magnification) get parameters using a compound microscope (Brunel SP50, Brunel Microscopes, UK) and ScopeImage software (version 9.0, Bioimager Inc., Concord, ON, Canada).

To analyse cell viability, fluorescein diacetate (FDA) and propidium iodide (PI) (both Sigma Aldrich, UK) were used as live/dead stains. Culture media was removed from the wells of the culture well plate and each well was washed three times with modified DPBS. Small sections (~ 10mm) were removed from each cultured fibre and placed into individual wells of a 24-well plate (Corning Incorporated, NY, USA). DPBS was firstly added to each well followed by PI in DPBS, which was added to each well at a concentration of 2 µl/L (stock concentration = 1 mg/ml). After 30 minutes of incubation, FDA in dimethyl sulfoxide (DMSO) (stock concentration = 2 mg/ml) was added at a concentration of 1 µl/L.

An inverted epifluorescence microscope (Nikon Eclipse TE300) was used for image generation, using Metamorph software (Version 7.1.0.0, Molecular Devices Inc. Sunnyvale, CA, USA). FITC and TRITC filters were used to image live and dead cells respectively, at magnifications of 40x, 100x and 200x. The following wavelengths were used for these filters: FITC excitation = 470 nm, emission = 515-555 nm. TRITC excitation = 540nm, emission 565-605 nm. ImageJ software was used for image processing and quantitative analysis of viability. An example of typical live and dead images can be seen in Figure 3-4 below.

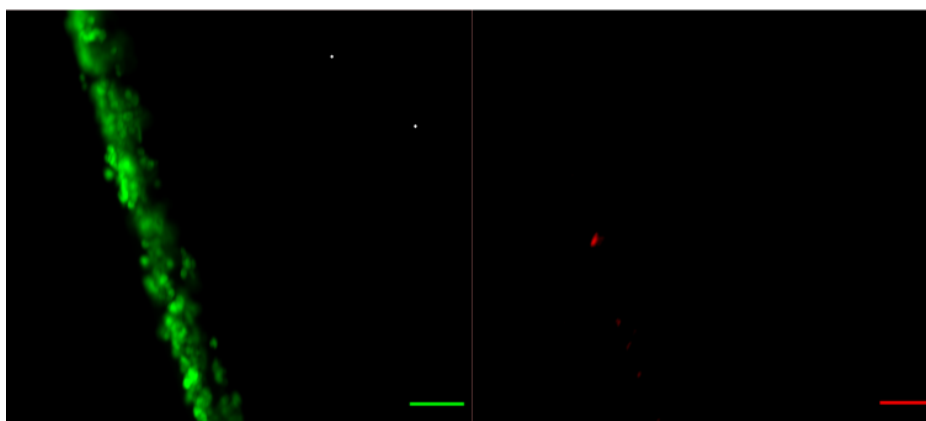


Figure 3-4. Typical live/dead images, showing live cells in green (left) and dead cells in red (right), generated using ImageJ software.

Quantitative analysis of viability involved the use of the ‘threshold’, ‘watershed’ and ‘analyze particles’ functions within the ImageJ GUI (graphical user interface), whereby separate ‘live’ and ‘dead’ images were converted to greyscale images, background pixels were removed, pixels were separated into distinct sections and counted using a lower size limit, to separate viable (or dead) cells from cell debris. An example of this process is displayed in Figure 3-5, using the live image from Figure 3-4.

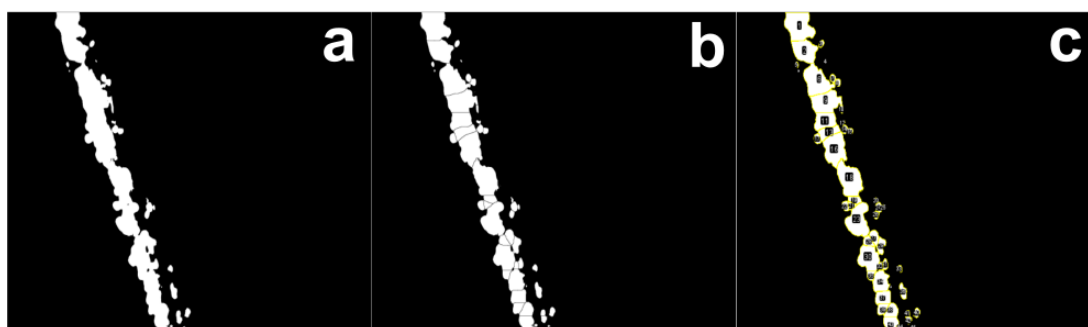


Figure 3-5. Example of the ‘Threshold’ (a), ‘Watershed’ (b) and ‘Analyze particles’ (c) functions within ImageJ software, allowing the conversion of an image into distinct regions, thus allowing quantification of cell viability.

Cell viability can then be calculated using Equation 3.1:

$$\text{Cell viability} = \frac{n(\text{live})}{n(\text{live} + \text{dead})} \times 100\% \quad (3.1)$$

Where:

n = number of cells

OriginPro software (version 2019b, OriginLab Corporation, MA, USA) was used for graphing and statistical analysis.

3.2. Drug testing

Hepatoma derived HepaRG cells (HPRGC10; Thermofisher UK) were maintained in William's E Medium with phenol red pH indicator (Fisher Scientific, UK) supplemented with 10% FBS, 1% penicillin/streptomycin, 1% 100x Glutamax (Fisher Scientific, UK), 5 µg/ml insulin, human recombinant, zinc solution (Fisher Scientific, UK), and 50.0 µM hydrocortisone 21-hemisuccinate sodium salt (Sigma Aldrich, UK).

For drug studies, Acetaminophen (APAP), Rifampicin, Prednisolone and Azathioprine powders were utilised (Sigma-Aldrich UK). Amiodarone hydrochloride was also utilised (Selleck Chemicals UK). APAP solid powder was weighed out using an analytical balance (Sartorius 1412 MP8-1, Sartorius AG, Göttingen, Germany) and dissolved in cell culture media, to form a stock solution, which was diluted in ten-fold steps to the required concentration and added to the wells of a 24-well plate for testing. All other drug powders were weighed out and dissolved in DMSO to form stock solutions at 10x the required concentration prior to addition to culture media where a ten-fold dilution occurred, to permit the required final drug concentration in culture media within the wells of a 24-well plate for testing. Culture media containing each drug were then added to coaxial extruded collagen/alginate scaffolds containing HepaRG cells, which were within the wells of a culture well plate, cut to measure approximately 10 mm in length, therefore controlling the number of cells per sample.

Scaffolds were then placed in an incubator at 37 °C, 5% CO₂ for the desired period of time prior to live/dead imaging using an inverted fluorescent microscope and performing CYP 3A4 assays using a conventional plate reader.

3.2.1. LC₅₀ data fitting

The dose response sigmoidal curves for acetaminophen and azathioprine were plotted by adding the concentration (x-axis) and viability data (y-axis) into the program using the 'Logistic' function within OriginPro software, of which is shown in Equation 3.2.

$$y = \frac{A_1 + A_2}{1 + (x/x_0)^p} + A_2 \quad (3.2)$$

Where:

A₁ = Initial y-value

A₂ = Final y-value

x₀ = Centre x-value

p = Power

Due to a poor fit with the Logistic function, the dose-response curve for amiodarone was fitted using the ‘DoseResp’ sigmoidal curve fitting equation by adding in concentration and viability data to the program, this equation is shown in Equation 3.3.

$$y = \frac{A_2 - A_1}{1 + 10^{(\log x_0)p}} \quad (3.3)$$

Where:

A1 = Bottom asymptote

A2 = Top asymptote

Log_{x₀} = Central x-value

p = Variable Hill slope parameter

3.2.2. CYP 3A4 assay

The CYP 3A4 assay was performed using the P450-Glo CYP3A4 Luciferin-PFBE cell-based biochemical assay (V8902, Promega, UK, see Figure 3-6). In essence, this assay tests the levels of CYP3A4 enzyme released by hepatocytes, through luminescence measurements, in response to the presence of CYP-inducing drugs, whereby enzyme activity is directly proportional to luminescent activity.

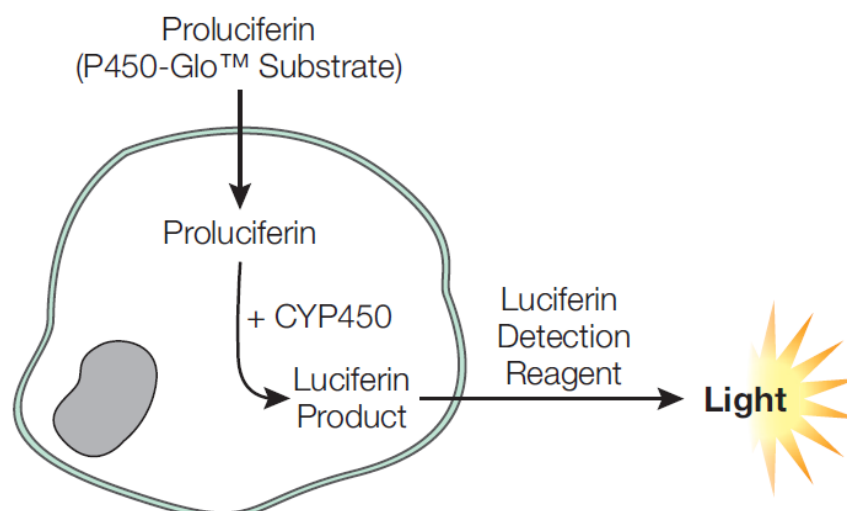


Figure 3-6. Cell-based P450-Glo™ Assay principle. A P450-Glo™ substrate (proluciferin) enters cells from the culture medium. Inside the cell, a P450 enzyme converts the proluciferin to a luciferin product, and luciferin is formed and detected with Luciferin Detection Reagent (LDR) [10].

The CYP solution was firstly thawed and covered in foil to prevent photolysis.

The culture media of each well of the culture plate containing the HepaRG-collagen-alginate scaffolds was removed and washed with PBS. Media (320 μ l) and CYP solution (0.8 μ l) was added to each well, in addition to 4 empty wells for control purposes. The plate was then incubated at 37 °C, 5% CO₂ for 24 hours.

The luciferin detection agent was prepared by transferring the entire contents of the bottle of the reconstitution buffer to the amber bottle containing the Luciferin Detection Reagent. A small volume of media (25 μ l) was taken from each culture well and was added to wells of an opaque white 96-well plate at room temperature. An equal volume of the luciferin detection reagent (25 μ l) was then added to each well of the 96-well plate to initiate the reaction. A typical plate layout is shown in Figure 3-7.

	1	2	3	4	5	6	7	8	9	10	11	12
A	0	0	0	0	0	0	0	0	0			
	μ M	μ M	μ M	μ M	μ M	μ M	μ M	μ M	μ M			
B	5	5	5	5	5	5	5	5	5			
C	10	10	10	10	10	10	10	10	10			
D	20	20	20	20	20	20	20	20	20			
E												
F												
G												
H	BACKGROUND											

Figure 3-7. Example 96-well plate layout, using drug concentrations of 0 – 20 μ M, to read for CYP 3A4 activity reading using a luminometer.

The plate was then left for 20 minutes to allow the reaction to process prior to reading luminescence using a luminometer (Flexstation 3, Molecular Devices, San Jose, CA, USA) with an integration time of 0.5 seconds/well (no filters or fluorescence used).

3.3. Measuring and statistical analysis

Filament diameter was calculated by firstly assuming a circular filament cross section. Small sections (measuring approximately 10 mm in length) were cut from each sample for measuring purposes.

Diameter measurements were performed using ImageJ software (National Institutes of Health, USA) and measurements for each level of magnification were calibrated using an eyepiece graticule. Light microscopy images were used for measuring filament diameter in Chapter 4.

For the cell-seeded filament images shown in Chapters 5 and 6, brightfield images were used to generate filament diameter data.

With each sample image, where the filament appeared uniform in diameter, the diameter measurement of the filament was taken once across the middle of the filament length. In cases where the filament did not appear fully uniform in diameter, this measurement was taken once across a section of filament which was perceived to be the most representative section. This was repeated for all samples to give the mean, sample standard deviation and standard error (usually $n = 3$). The standard deviation for samples taken across many time points was calculated as the population standard deviation.

In a manner similar to measurements for filament diameter, shell diameter and wall thickness data displayed in Chapter 4 were found by measuring the outer and/or internal diameter once across the mid-section of light microscopy images of samples, where the alginate shell wall appeared black in colour. Sample and population means were calculated in the same manner as the filament measuring process.

To statistically compare between multiple groups of data, a one-way ANOVA (analysis of variance) was used, with the significance level set to 0.05. Where significance was observed, Tukey's post hoc test was used to compare means.

To calculate uncertainties in material concentrations, the absolute uncertainty was found by finding the square root of the sum of the squared relative errors and multiplying by the final concentration, of which is demonstrated in Equation 3.4 below [11].

$$u(c) = \sqrt{\left(\frac{u(m)}{m}\right)^2 + \left(\frac{u(M)}{M}\right)^2 + \left(\frac{u(V)}{V}\right)^2} \cdot c \quad (3.4)$$

Where:

$u(x)$ = Measurement uncertainty in parameter 'x'.

m = Mass, g

M = Molecular mass, g/mol

V = Volume, ml

c = Final concentration, mM

The measurement uncertainty in mass measured ± 0.5 mg; the uncertainty in molecular mass measured ± 0.5 mg/mol and the uncertainty in volume ranged from ± 0.5 μ l to 0.25 ml, due to the use of pipettes and measuring cylinders.

3.4. Hardware and modifications for coaxial extrusion

3.4.1. Introduction

This section is dedicated to the development process of the extrusion platform used to engineer core/shell cell-seeded and collagen filaments. The aspects covered here range from the basic printer frame and extruder design to the electronics operating firmware. In addition, the development of an extruder temperature control system, to control nozzle tip and print bed temperature, is also detailed in later sections. It should be noted that the initial aim here was to allow three-dimensional printing; however, only one-dimensional extrusion was achieved.

A pre-assembled Prusa Mk2s three-dimensional (3D) printer (Prusa Research, Prague, Czechia) was chosen to serve as the foundation for the extrusion system (see Figure 3-8). The frame, stepper motors and power supply unit (PSU) remained as is, whilst the LCD screen and electronics board housings were used to house alternative electronics. The Prusa Mk2s printing system proves a very versatile platform for modification due to its modular and portable nature, in addition to being easily modifiable, with a plethora of open-source hardware and software modifications currently available online.

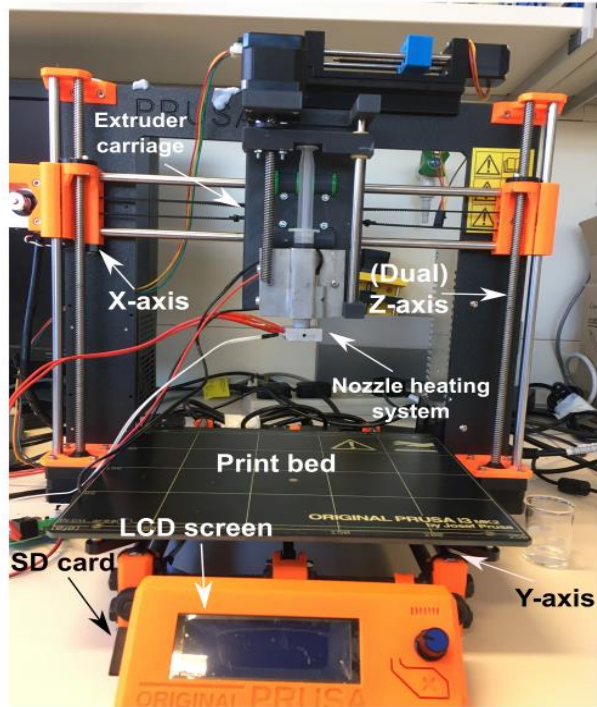


Figure 3-8. Modified Prusa Mk2s Printer overview, showing single-syringe configuration in extruder carriage, complete with syringe and nozzle heater systems.

In addition, the moveable extruder housing was redesigned to facilitate the mechanical extrusion of syringes containing hydrogels and bioinks, as opposed to the supplied fused deposition modelling (FDM) housing, which typically prints using thermoplastic filaments.

3.4.2. Electronics

The supplied electronics board with the Prusa Mk2s was the Mini-RAMBo (RepRap Arduino-compatible Mother Board), designed to be a convenient, all-in-one motherboard capable of reliable, high-performance 3D printing (see Figure 3-9). The board was one of many produced as a result of the open-source RepRap (rapidly replicating) project [12], aimed at producing self-replicating 3D printers. However, the board was not conducive to coaxial printing due to the lack of capacity to easily drive further stepper motors.

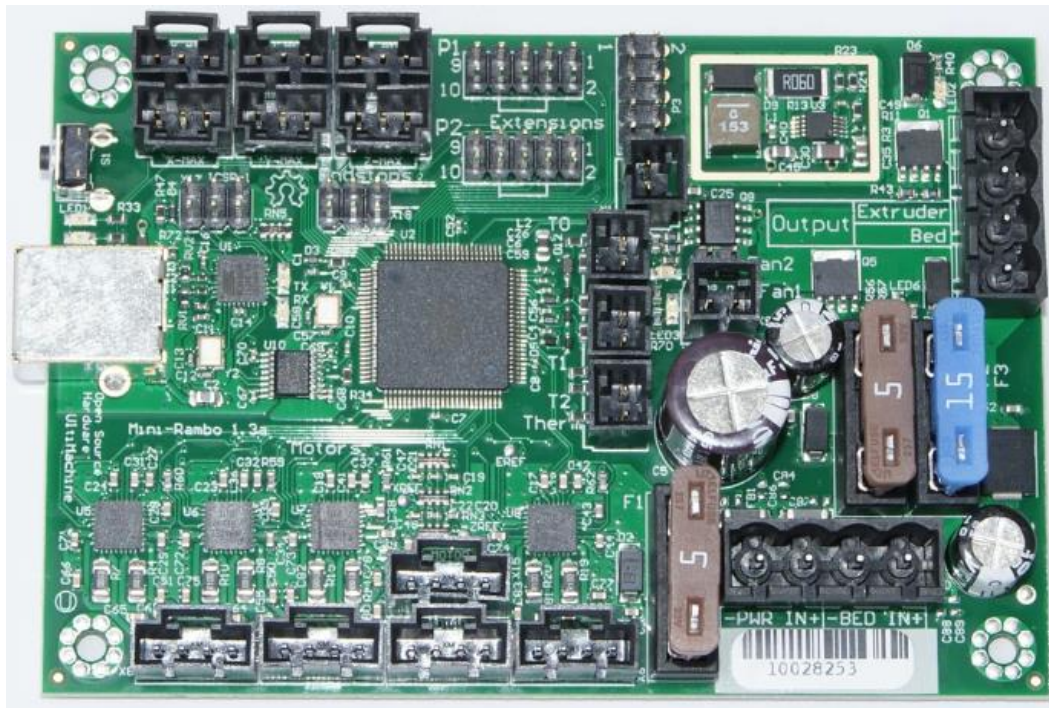


Figure 3-9. Mini RAMBo board supplied with Prusa Mk2s 3D printers.

A minimum of six NEMA17 stepper motors were required for coaxial printing using the dual-z axis printer, with the two z-axis motors being driven by the same driver. Upon multiple attempts at using the extruder driver to drive two extruders, it appeared simpler to use an alternative board, one with the capacity for further extruder motors, if further multi-material extrusion was required.

The RAMPS 1.4 board (RepRap Arduino Mega Pololu Shield; Robotdigg.com, Shanghai, China) was designed to fit all of the required electronics required for a RepRap at low cost on a single, open-source board (see Figure 3-10) [13]. The RAMPS board interfaces with an Arduino Mega 2560 microcontroller (Arduino.cc, UK) and, importantly, was designed to have ample capacity for expansion, facilitating the use of further motors and cooling fans, amongst other uses.

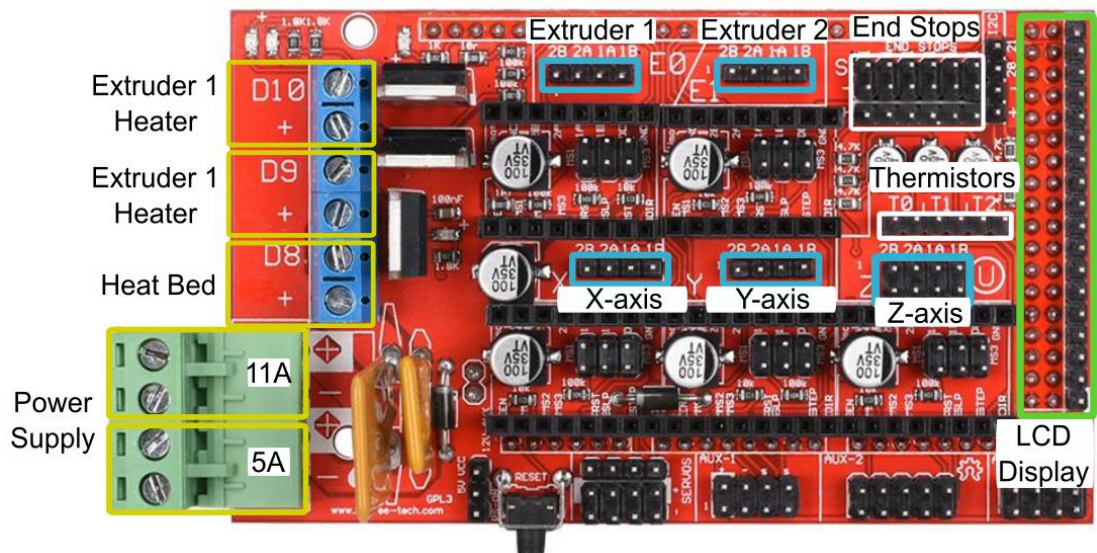


Figure 3-10. RAMPS 1.4 board, showing key connectors, with extension pins situated along the bottom row (not highlighted).

The RAMPS board and affixed Pololu A4988 stepper drivers (Pololu Robotics and Electronics, Las Vegas, NV, USA; operating with micro-stepping activated at 16 micro-steps per step) demand 12V from the PSU whilst the heated bed (Prusa Research, Prague, Czechia) runs at 24V. In addition, the RepRap smart 2004 LCD controller (Robotdigg.com, Shanghai, China) acted as the user interface, complete with an SD card slot for direct printing using g-code files.

3.4.3. Firmware

The operating firmware of choice was Marlin (Marlinfw.org). This open-source firmware is very common in the RepRap world due to its reliability, easy-to-use interface and its ability to be customised to meet specific user requirements at an affordable price. To enable bio-extrusion, the default firmware settings (version 1.1.9) were modified through the open-source Arduino Integrated Development Environment (IDE) software (version 1.8.8). The reasons for these changes are listed in Table 3-1.

Table 3-1. Settings changes to 'Configuration.h' file within Marlin firmware version 1.1.9 to enable bio-extrusion. Note K_p = proportional gain of PID controller, K_i = integral gain of PID controller, K_d = derivative gain of PID controller.

Line	Default	Modified	Notes
134	#define MOTHERBOARD BOARD_RAMPS_14_EFB	#define MOTHERBOARD BOARD_RAMPS_14_EEB	Activates second extruder
149	#define EXTRUDERS 1	#define EXTRUDERS 2	Allowing use of second extruder

313	#define TEMP_SENSOR_0 1	#define TEMP_SENSOR_0 5	Activates thermistor for extruder 1
318	#define TEMP_SENSOR_BED 0	#define TEMP_SENSOR_BED 5	Activates thermistor for print bed
367	#define BANG_MAX 255	#define BANG_MAX 64	Limits current when using P control to approx. 25%
371	//#define PID_AUTOTUNE_MENU	#define PID_AUTOTUNE_MENU	Activates PID auto-tuning to user interface
383	#define DEFAULT_Kp 22.2	#define DEFAULT_Kp 33.59	K _p tuning
384	#define DEFAULT_Ki 1.08	#define DEFAULT_Ki 4.61	K _i tuning
385	#define DEFAULT_Kd 114	#define DEFAULT_Kd 61.22	K _D tuning
416	//#define PIDTEMPBED	#define PIDTEMPBED	Activates PID control for bed
434	#define DEFAULT_bedKp 10.00	#define DEFAULT_bedKp 28.30	Bed K _p tuning
435	#define DEFAULT_bedKi 1.04	#define DEFAULT_bedKi 1.04	Bed K _i tuning
	#define DEFAULT_bedKd 305.4	#define DEFAULT_bedKd 511.63	Bed K _D tuning
456	#define PREVENT_COLD_EXTRUSION	//#define PREVENT_COLD_EXTRUSION	Allows room temperature extrusion
457	#define EXTRUDE_MINTEMP 170	#define EXTRUDE_MINTEMP 5	Reduces minimum software-permitted temperature of extruders
611	#define DEFAULT_AXIS_STEPS_PER_UNIT { 80, 80, 4000, 500 }	#define DEFAULT_AXIS_STEPS_PER_UNIT { 100, 100, 400, 397.38 [, 397.38] }	Steps/mm values for each stepper motor
882	#define X_BED_SIZE 200	#define X_BED_SIZE 250	Changing print bed X axis size
883	#define Y_BED_SIZE 200	#define Y_BED_SIZE 205	Changing print bed Y axis size
1226	//#define EEPROM_SETTINGS	#define EEPROM_SETTINGS	Allows saving of new settings to memory
1429	//#define SDSUPPORT	#define SDSUPPORT	Allows use of SD card
1532	//#define REPRAP_DISCOUNT_SMART_CONTROLLER	#define REPRAP_DISCOUNT_SMART_CONTROLLER	Enables LCD controller

Furthermore, to aid system development and control, many software packages were used. To create cost-effective 3D-printed parts for the printer, a computer-aided design (CAD) software, Autodesk Inventor Professional 2020 (64-bit version, Build 168; Autodesk Inc., San Diego, California, USA) was firstly used to design these parts.

This resulted in the generation of stl (stereolithography) files. These stl files were then transformed into a printable g-code file, used ubiquitously with CNC machines, using an open-source layer-slicing programme (slic3r v1.2.9; slic3r.org). G-code files are read by printers, using removable SD cards, allowing 3D printing. The material of choice was PLA, owing to its structural stability at low-cost. When precise control and custom g-code commands were required, an open-source software with a graphical user interface (GUI), Pronterface (Pronterface.com), was used.

3.5. Coaxial extrusion schematics

The coaxial extrusion system was developed through multiple iterations, starting from a microfluidic system, to a hybrid extruder-external pump setup to finally having a modular extrusion system. This progression in technology was facilitated by developments in knowledge of Arduino microcontrollers and g-code programming.

3.5.1. V1 - Syringe pump and Arduino Micro

The first iteration of the coaxial extrusion system consisted of the creation of an in-house, Arduino Micro-powered (Aduino.cc, UK) syringe pump as the primary (core) extruder, atop a steel-framed acrylic box (to allow placement of Arduino pump at height), and the aforementioned Aladdin 300 commercial syringe pump acted as the secondary (shell) extruder, with these two streams merging within the previously described coaxial nozzle (see Figure 3-11). The images displayed in Figure 3-11 and Figure 3-12 were created using Fritzing open-source software (v0.8.7b; Fritzing.org).

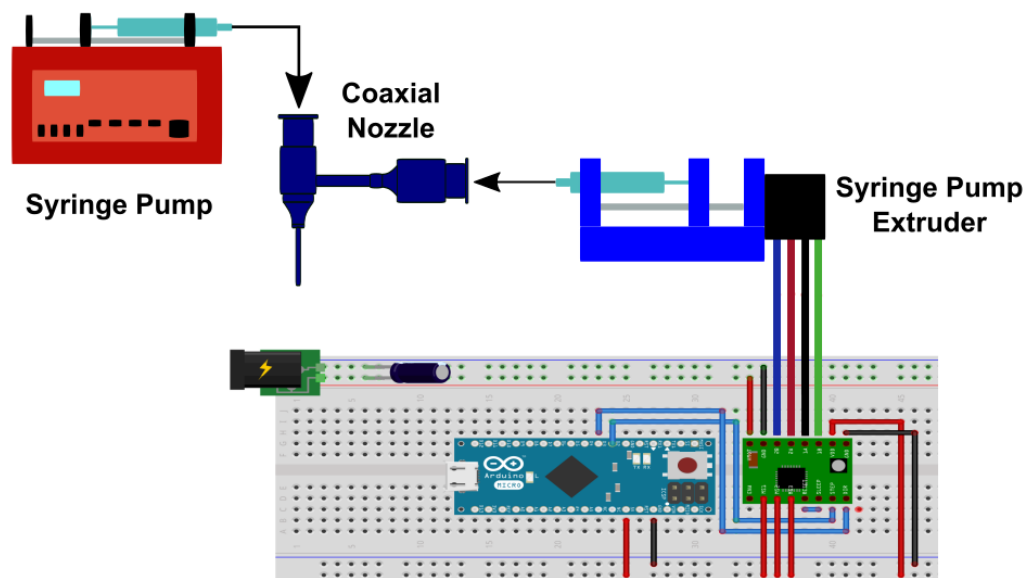


Figure 3-11. First iteration of the coaxial extrusion system, using a commercial syringe pump and a syringe pump extruder for the input streams (image designed using Fritzing v0.8.7b open-source software).

This system did not utilise print head movement and the only active stepper motors were the two extruder motors, therefore only extrusion was possible here (as opposed to printing with a movable print head) therefore this system did not allow three-dimensional printing but was capable of producing coaxial cell-collagen filaments and provided the foundation for the development of the technology, towards a portable modular system with integrated electronics to control multiple motors running simultaneously for multi-material coaxial printing.

On the note of stream synchronisation and line priming, due to there being different tubing lengths for each stream and different core/shell flow rates being implemented, the system required priming to ensure that the stream exiting the coaxial nozzle possessed both alginate and collagen. The nozzle was deemed primed and ready to print when the slightly yellow-coloured alginate stream exiting the coaxial nozzle tip possessed a red/pink colour. The changing colour of the alginate stream was a consequence of mixing with the collagen stream prior to immersion in the cross-linking bath. This colour change was assumed to be due to the presence of phenol red pH indicator contained in the culture media within the collagen solution.

With this configuration, there was a need to replace the large commercial syringe pump in order to use a smaller version, one which could be mounted on the printer frame to facilitate portability of the system.

Creating a modular and portable system would permit easier transport and configuration of the system for operation, such as between a laboratory benchtop and into a sterile environment, which is necessary for cell extrusion and printing to avoid cell death due to pathogens in open air.

3.5.2. V2 - Extruder and Arduino Micro

In the second iteration of this system, a lower footprint in-house fabricated extruder replaced the commercial syringe pump, thus improving the portability of the system. The in-house fabricated printer extruder consisted of a 3D-printed PLA block affixed with a NEMA17 stepper motor (bipolar, 200 steps/revolution, rated current = 1.2A, phase inductance = 3,5 mH, with lead screw; Robotdigg.com, Shanghai, China) aligned with an 8.0 mm diameter stainless steel rod (grade 304) articulating with a linear bearing (Ebay.co.uk, UK), thus allowing movement of a 3D-printed PLA piston (see Figure 3-8) to extrude material from a syringe. The printer extruder also possessed the syringe temperature control module, which is discussed in more detail in section 3.6. Figure 3-12 provides a schematic, which demonstrates the main components of this system and associated electrical connections.

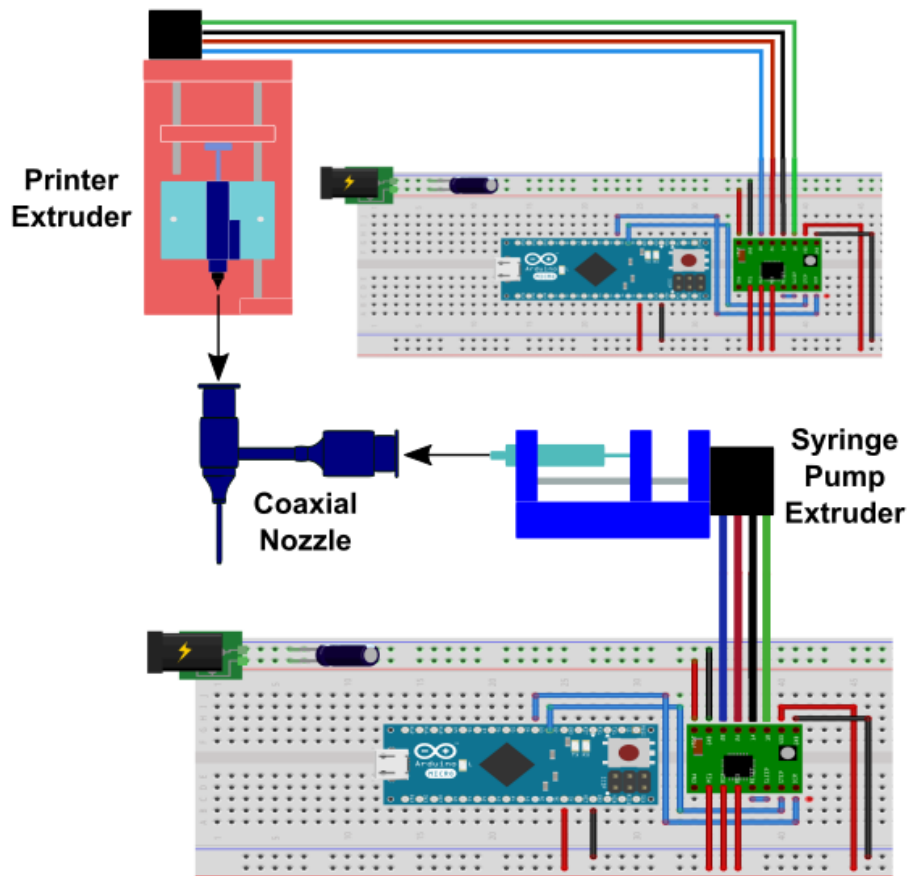


Figure 3-12. Second iteration of the coaxial extrusion system, separately using the printer extruder and a syringe pump extruder for the input streams (image designed using Fritzing v0.8.7b open-source software).

A limitation of this system was the need to separately activate each extruder due to each extruder operating using separate Arduino Micro microcontrollers, thus leading to issues with losing some material at the beginning and end of the experiment during activation and deactivation of the two extruders. Due to the low volumes and high value of collagen and cells, this was a very undesirable system. This issue was particularly an issue at the commencement of the experiment where excess alginate at the nozzle tip would lead to a nozzle blockage when submerging the nozzle in the cross-linking bath to create tubular alginate shells. It was clear that the next stage of development would involve facilitating simultaneous extrusion of both streams, allowing commencement and termination of the experiment with the push of a single button, to eliminate undesirable material losses.

3.5.3. V3 - Arduino UNO dual-stepper control

The third iteration of the extrusion system built on the second by facilitating controlled simultaneous dual-motor extrusion, by employing an Elegoo UNO microcontroller (Elegoo.com) and two Pololu A4988 stepper drivers (see Figure 3-13).

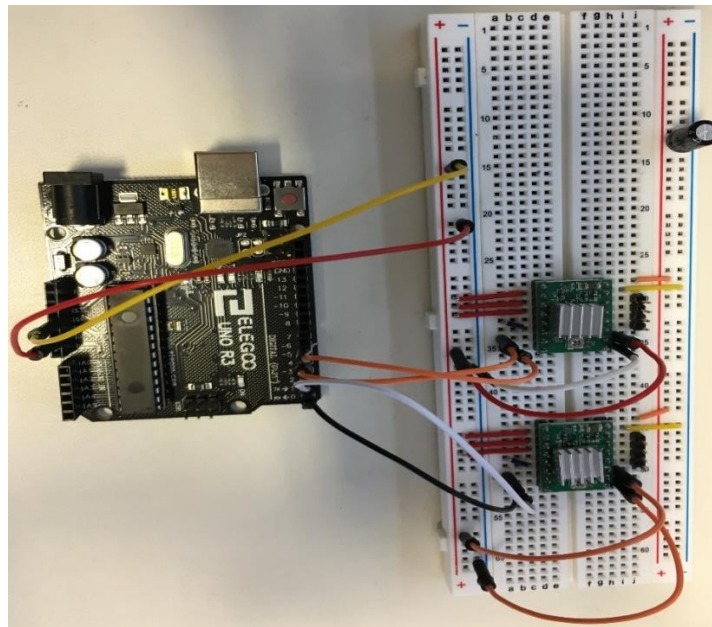


Figure 3-13. Elegoo Uno dual-stepper circuit, illustrating the external Arduino Uno microcontroller and two A4988 stepper drivers

This Elegoo Uno circuit permitted simultaneous coaxial extrusion by interfacing each stepper motor with each stepper motor driver in the electrical circuit displayed in Figure 3-13 and activating the extrusion system with a single Arduino code, thus eliminating material waste and nozzle blockage issues caused by excess alginate at the nozzle tip. At this stage, there was a desire to take this working circuit and place all components on a convenient single physical block with robust connections to avoid accidentally displacing a wire and prematurely ending the experiment. In addition, it was also desirable to employ buttons to simply activate the system without relying on a wall outlet switch, adding convenience and enhanced usability into the system.

3.5.4. V4 - StepperUNO

An external supplier (Lechacal.com) independently took the Arduino UNO system and assembled it into a standalone system, named ‘StepperUNO’ (see Figure 3-14 below), whereby the Arduino UNO and stepper motor drivers (A4988) were combined into a single circuit board, with a detachable LCD screen installed into the centre of the board. This allowed the integration of the StepperUNO system into the extrusion module to provide portability. It should be noted that this system did not allow simultaneous use of the printer XYZ motors, therefore if 3D coaxial printing was required, it would be necessary to separately start the object g-code file (modified with no extruder movement instructions) along with the StepperUNO.

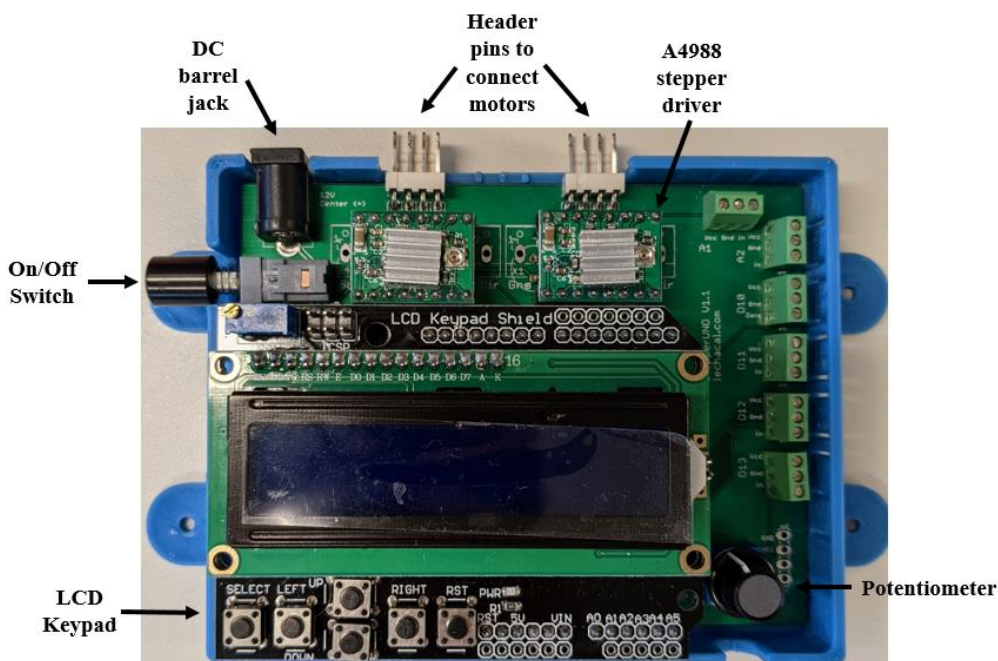


Figure 3-14. StepperUNO hardware, showing key hardware features. Note: on-board potentiometer (bottom right) was disabled for all extruding operations within this work.

The Arduino code was adjusted to implement use of the LCD screen, whereby the screen would display which motor(s) was selected in addition to the selected rotational direction.

A limitation of this configuration is that the unit requires connection to a computer to change flow rates; however, it is possible to implement analogue changes using the on-board potentiometer.

3.5.5. Stepper motor calibration

In order to calibrate stepper motor rotational speeds and find their corresponding syringe flow rates, a calibration experiment was undertaken, tailored to the previously described StepperUNO system. Firstly, the stepper step delay was set to a fixed value within the code and a 1 ml BD Plastipak syringe was inserted within a stepper motor-controlled extrusion block. The syringe was filled with water (used for convenience) and subsequently dispensed into an empty dish and placed on top of a zeroed gravimetric scale. By recording the dispensing time, the volumetric flow rate could be calculated by assuming the density of water = 1.0 g/ml. A 30 gauge (152 μm) internal diameter tapered nozzle was fitted to the syringe, in order to minimise the measuring error by reducing droplet size. By graphing the step delay between micro-steps (D) against the volumetric flow rate (Q), an empirical formula to relate these two parameters was found and is displayed in Figure 3-15.

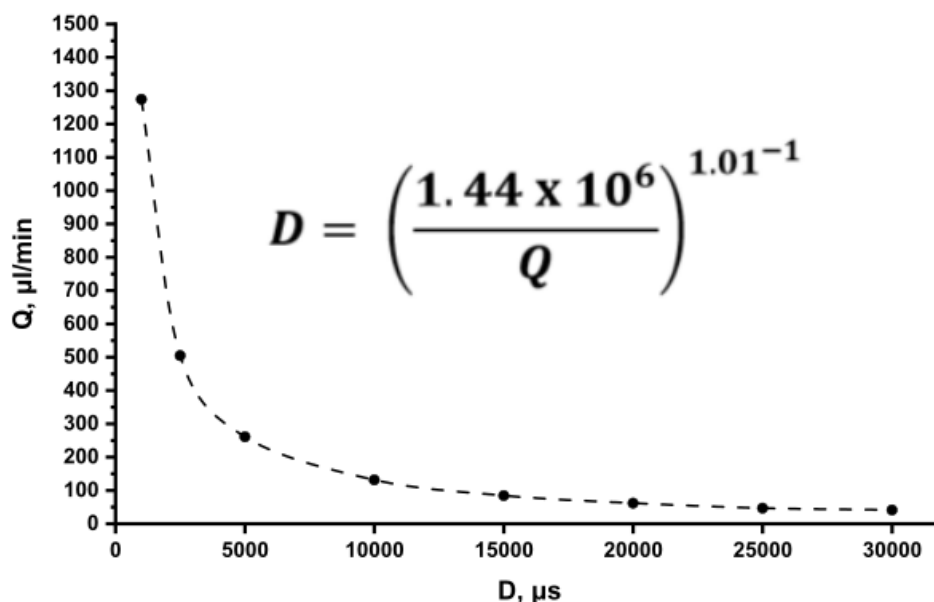


Figure 3-15. Calibration graph for 1 ml syringe extrusion, including trend line equation, using StepperUNO hardware and Arduino software.

By creating the calibration graph presented in Figure 3-15, an empirical equation for the included trend line was found. This allowed the interpolation of the flow rate value and simple manipulation of the Arduino code to set desired flow rates, within the given range, from approximately 0.04 to 1.27 ml/min. The measurement uncertainty of the aforementioned Sartorius weighing scales was ± 0.5 mg and the measurement uncertainty of the timer (Apple iPhone 6S, Apple Inc., Cupertino, CA, USA) was ± 5 ms. The resulting measurement uncertainty in volumetric flow rates ranged from ± 0.50 $\mu\text{l}/\text{min}$ (1.25%) at $Q = 0.04$ ml/min to ± 0.81 $\mu\text{l}/\text{min}$ (0.06%) when $Q = 1.27$ ml/min.

To find the formula for a 5 ml BD Plastipak syringe, the formula linking the 1ml case was manipulated by multiplying by the ratio of the 5ml syringe to the 1ml syringe, in terms of ml/mm.

Table 3-2. Extrusion syringe dimensions for 1ml and 5ml BD Plastipak syringes.

Syringe size	Diameter, mm	Length, mm	Volume, ml ($\pi r^2 h$)	ml/mm (V/L)
1ml	4.78	58.0	1.04	0.018
5ml	12.10	45.0	5.17	0.115

$$\text{Syringe } \frac{\text{ml}}{\text{mm}} \text{ ratio } \left(\frac{5 \text{ ml}}{1 \text{ ml}} \right) = \frac{0.115 \text{ ml/mm}}{0.018 \text{ ml/mm}} = 6.389 \quad (3.5)$$

$$Q (5 \text{ ml}) = 6.389Q (1\text{ml}) \quad (3.6)$$

Therefore, by substitution:

$$D (5 \text{ ml}) = \left(\frac{1.44 \times 10^6 \times 6.389}{Q (5\text{ml})} \right)^{1.01^{-1}} \quad (3.7)$$

This formula was successfully tested over a variety of flow rates to confirm experimental accuracy prior to implementation.

The step delay value can be converted into rpm using Equation 3.8 below.

$$\text{rpm} = \frac{60 \frac{\text{S}}{\text{min}} \times 10^6 \frac{\mu\text{S}}{\text{S}}}{\text{S} \times \text{N} \times \text{D}} \quad (3.8)$$

Where:

S = steps per revolution (200 here)

N = number of micro-steps per step (16 here)

The formula to convert between volumetric flow rate and step delay shown in Figure 3-15 was utilised with Equation 3.8 to calculate the minimal and maximal stepper motor operating rpm used with each extruder during the coaxial extrusion experiments detailed in subsequent chapters. The relationship between flow rate, step delay and rpm is shown in Table 3-3 below, applicable to the use of the 1ml syringes described earlier in this chapter.

Table 3-3. Conversion between volumetric flowrate, step delay and stepper motor rpm using a 1.0 ml disposable BD plastipak syringe.

Q, ml/min	D, μs	Motor speed, rpm
0.1	13,097.6	1.4
6.0	227.3	82.5

On analysis of the stepper motor rpm values listed in Table 3-3, the highest stepper motor operating rpm was 82.5 rpm when using a flow rate of 6.0 ml/min. Given that commercial stepper motors do not lose torque until around 300 to 400 rpm, it seemed a safe assumption that extruded filaments were not subject to pulsatile flow. Pulsatile flow occurs when the stepper motor is operating beyond its operational limits, at higher rpm values, where lead screw torque is lost. Pulsatile flow would lead to changing filament or shell diameter, which would affect the integrity of diameter measurements made in the subsequent experimental chapters of this thesis.

3.6. Development of nozzle and bed temperature control systems

This section describes the development of a temperature control system to be implemented with the modular coaxial extrusion system. The aim was to facilitate deposition of fine diameter heated droplets of agarose solution, a linear polysaccharide with many biological applications, complete with droplet solidification on contact with a chilled print bed in a repeatable manner.

3.6.1. Background information and theory

3.6.1.1. Agarose

Agarose is a non-ionic linear polysaccharide extracted from red algae, consisting of alternating repeating units of agarobiose. Agarobiose is a disaccharide consisting of β -D-galactose and 3,6-anhydro-L-galactose units (see Figure 3-16).

Agarose is similar to alginate in that it is non-bioactive and is non-biodegradable in humans. However, the simple thermal gelation properties of its hydrogels makes agarose attractive in bioprinting and extrusion applications to create structures with complex geometries.

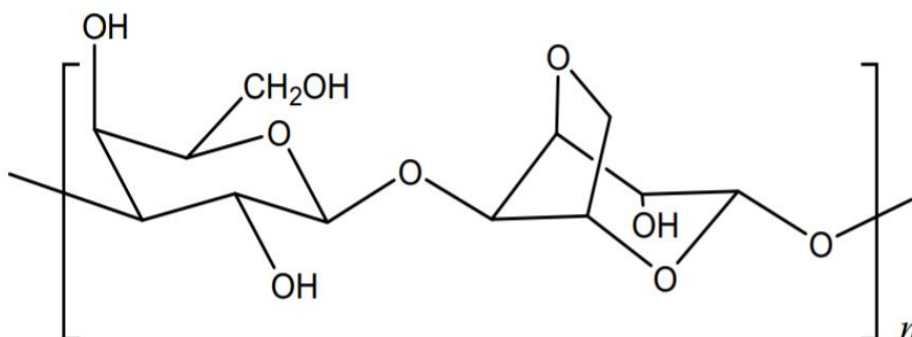


Figure 3-16. Agarose disaccharide molecular structure, showing β -D-galactose and 3,6-anhydro-L-galactose units.

Moreover, agarose hydrogels are thermo-sensitive, exhibiting thermal hysteresis with its liquid-to-gel phase transition. The gelation and melting temperature vary depending on agarose source and concentration. The melting temperature may range from approximately 70 to 95 °C and the gelation temperature can range from approximately 25 to 42 °C [14]. Given this thermal hysteresis, agarose is notoriously difficult to print and deposit. However, low melting temperature agaroses are available, with melting temperatures of around 65 °C. Agarose hydrogels are attractive for studies due to the simple thermal gelation mechanism, thus there are no requirements for additional cross-linking [15]. The agarose used within this work had a gelation temperature of 38.0 ± 2.0 °C.

The targeted use of agarose in this work was for the repeatable deposition of agarose droplets (sub-50 μm) to be embedded within bacterial samples for analytical purposes using biosensors. An important aspect of this work was to create a system facilitating the rapid cooling and gelation of deposited liquid droplets, therefore a portable Peltier device-enabled (Ebay.co.uk) chilled bed was created in addition to the aforementioned extruder heating system.

3.6.1.2. The Peltier effect

On application of current through two different conductive materials connected in series, heat may be generated or lost at the electrified junction between these two materials. This is known as the Peltier effect. Importantly, the direction of current flow between materials dictates whether heat is generated or lost. An image of a typical Peltier device is shown in Figure 3-17.

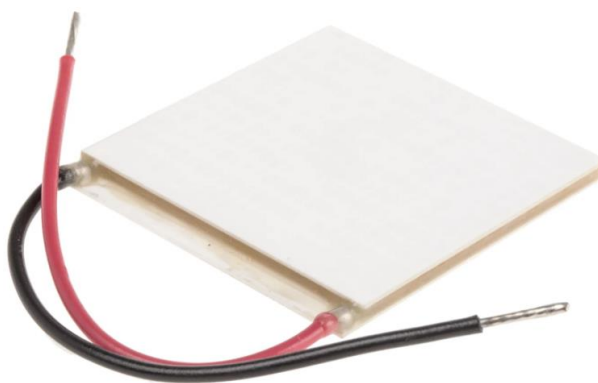


Figure 3-17. Peltier device, showing inlet wires, which can be reversed to choose which side of the device is cooled or heated.

Modern Peltier devices employ the Peltier effect and are built in a matrix arrangement of alternating blocks of p- and n-type semiconductors, sandwiched between thermally-conductive plates, usually using ceramics such as Alumina (Al_2O_3). A typical Peltier effect circuit is presented in Figure 3-18.

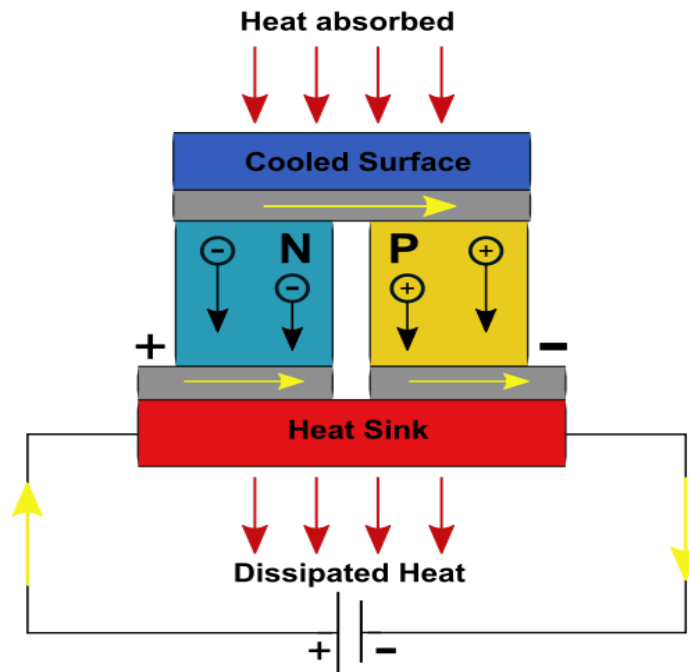


Figure 3-18. Peltier effect circuit composed of n- and p-type semiconductors, illustrating the generation of cold and hot sides on the same block.

Consequently, the device operates such that separate hot and cold sides develop and are maintained thanks to the high electrical conductivity and low thermal conductivity of the semiconductor materials. These thermally polarised sides may then be placed in contact with objects in order to apply or remove heat for temperature control purposes.

3.6.1.3. W1209 thermostat controller

For basic temperature control, the widely available, low-cost thermostat controller (W1209; Amazon UK) was used in conjunction with a Peltier device. The supplied thermistor was inserted and fixed in place within the aluminium syringe housing of the extruder configuration, feeding temperature information back to the thermostat unit. The thermistor was fitted using a grub screw fit and thermal paste was added in the interstitial space between the thermistor and housing. The fitting of the thermistor within the aluminium housing is shown in Figure 3-19.

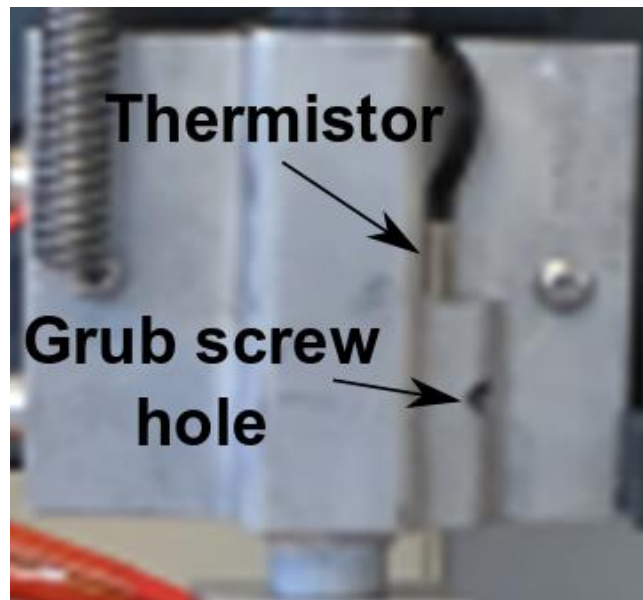


Figure 3-19. Location of W1209 thermistor within aluminium syringe housing, where it is locked in place using a grub screw.

A major disadvantage to the W1209 thermostat system was that it only had capacity for simple ‘bang-bang’ temperature control. ‘Bang-bang’ control simply turns power off once the set point has been reached during heating or turns on when the temperature drops below the set point during cooling.

The major operational disadvantage of this setup was that the temperature would swing ± 2.0 °C around the set point of 85.0 °C, when visually inspecting the seven-segment display on the W1209 module, across a timespan of approximately fifteen minutes. This error was deemed unacceptable in the early stages, as heat loss from the nozzle tip had to be minimised to avoid the build-up of excessive temperature gradients between the aluminium housing and the nozzle tip. Due to the need for control within 0.5 °C, it was clear that a more precise temperature control system was required.

3.6.1.4. PID control

A Proportional Integral Derivative (PID) control system was later chosen for the control of temperature of the syringe extruder system. PID controllers use feedback control loops to constantly calculate the error, $e(t)$, between the set point (desired value) and the current variable under study and subsequently applies corrections to manipulate process variables, known as control variables, to produce the control function, $u(t)$. This control function is sent to an actuator in order to reduce the error to bring the process output, $y(t)$, closer to the set point. These corrections are based on three mathematical calculations involving the transient error term, namely Proportional (P), Integral (I) and Derivative (D) [16].

A simple example of PID control would be increasing the flow of cold water flowing through an electronically controlled valve and into a liquid tank to reduce the tank temperature to the desired set point.

PID control was implemented in the extruder heating system by manipulating the 12V pulsed-width modulation (PWM) current provided to the heating element. PWM simply manipulates the period of time that heat is being applied, in a duty cycle, and rapidly switches on and off in pulses to control the application of current to the heating element to maintain process temperature. PID control was enabled on the Marlin firmware and the PID parameters were tuned using the PID auto tune g-code (M301 for extruder, M303 for bed). PID tuning allowed control of extruder temperature within ± 0.4 °C (with a target of ± 0.5 °C) with an initial set point of 50 °C. This was not tested for other set points, which would affect the stability of the PID control system.

3.6.2. Development of a temperature-controlled extruder

To facilitate temperature-controlled extrusion it was necessary to integrate a heating system within the moveable extruder carriage on the printer frame. An extruder heating system requires a heat source, a means of measuring real-time temperature and apparatus for controlling the temperature.

3.6.2.1. Initial heating extruder configuration

The first iteration of the heating system employed a PLA extruder housing fitted with a widely-available 50W Peltier device (TEC1-12706) situated between a heat sink (Banggood.com) and an in-house fabricated aluminium syringe housing, using zinc oxide-based thermal paste (RS Components) to eliminate any air gaps to aid conduction (see Figure 3-20).

Luer lock tapered-tip stainless steel nozzles, with internal diameter ranging from 0.2 to 0.4 mm, (Adhesive Dispensing Ltd, UK) were used in conjunction with luer lock syringes to dispense 1% (w/v) agarose solution (Carl Roth GmbH, Karlsruhe, Germany) within the temperature-controlled extruder system.

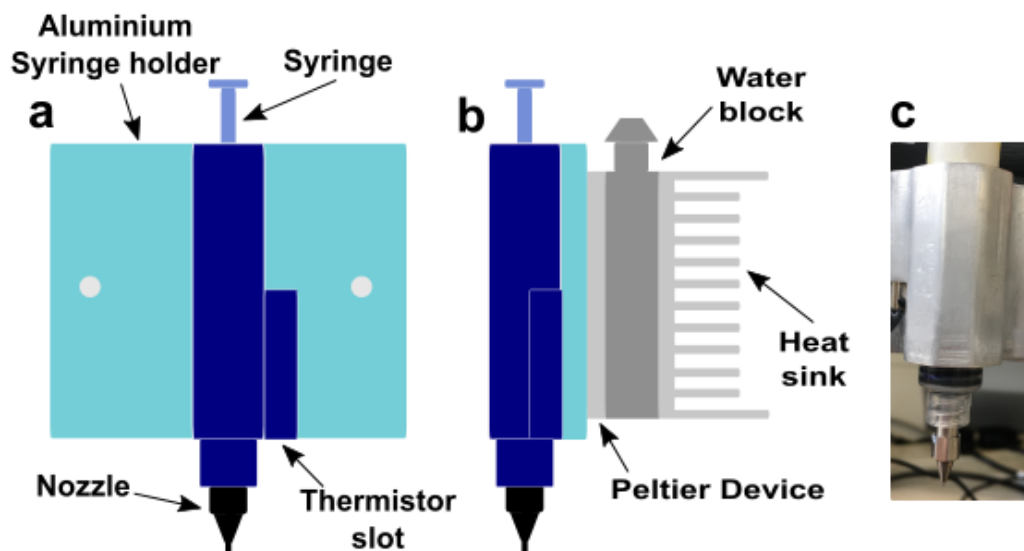


Figure 3-20. Peltier syringe temperature control module. (a) Front elevation; (b) right side elevation, (c) front elevation photo showing steel nozzle locked into syringe contained within aluminium heater housing.

A water block (Banggood.com) was fitted between the Peltier device and the heat sink, facilitating the circulation of water through the water block to dump excess heat in cases where cooling the syringe housing below room temperature may have been required, owing to the unique nature of a Peltier device being able to heat or cool, depending on input wire polarity. The circulation of water would have an effect on temperature stability, therefore if this was to be employed, further work would be needed to suitably control the final extrusion temperature. Due to the configuration used here, the heat sink effectively acted as a convenient point to connect to the aluminium syringe housing, holding the Peltier device and water block in place. A tapered stainless steel nozzle was utilised for the extrusion of heated agarose, in order to improve the nozzle heat transfer performance in comparison to a blunt nozzle [17] (see Figure 3-21).



Figure 3-21. Tapered stainless steel luer lock nozzle used for heated extrusion of agarose.

It should be noted that the use of an aluminium nozzle would provide significantly greater heat transfer however, small diameter aluminium nozzles (target = approximately 200 μm) could not be procured for this work, as the aim was to minimise droplet volume. In addition, fluid flow is comparably easier with a tapered nozzle than using a blunt needle due to the higher shear stresses and velocities in addition to a lower fluid residence time. This situation is desirable for acellular extrusion however it is important to reiterate that the inverse is desired for cell extrusion due to the propensity for high shear stress to cause cell damage [18]

3.6.2.2. New extruder carriage and syringe holder design

With the first iteration employing a Peltier device to control the syringe barrel temperature, the syringe barrel Peltier heater temperature was set to 95.0 $^{\circ}\text{C}$, to melt the agarose. However, solidification occurred within the unheated stainless steel nozzle as the nozzle tip averaged at 36.5 $^{\circ}\text{C}$, below the average gelation temperature. This tip temperature was measured using a digital thermometer (Keplin digital food thermometer, Amazon, UK), in contact with the nozzle tip for approximately one minute to allow thermal equilibrium to be reached.

It was necessary for more heat to be transferred to or retained by the extrusion nozzle in order to raise the temperature above the gelation temperature of agarose. Initial attempts involved the use of cotton insulation to retain heat within the syringe barrel and the placement of thermal paste between the aluminium syringe holder and the syringe barrel, to improve conduction.

Upon the failure of both methods to avoid agarose gelation within the nozzle, an aluminium heating block was fabricated, to be placed over the stainless steel nozzle and fitted using thermal paste to eliminate air gaps in order to enhance conduction (see Figure 3-22). This configuration succeeded in raising the nozzle tip temperature to an average of 40.0 $^{\circ}\text{C}$ with the syringe holder Peltier heater set point temperature at 95.0 $^{\circ}\text{C}$, this was unfortunately not enough to completely avoid agarose gelation within the nozzle. The relatively poor thermal conductivity of stainless steel may have been a factor here.

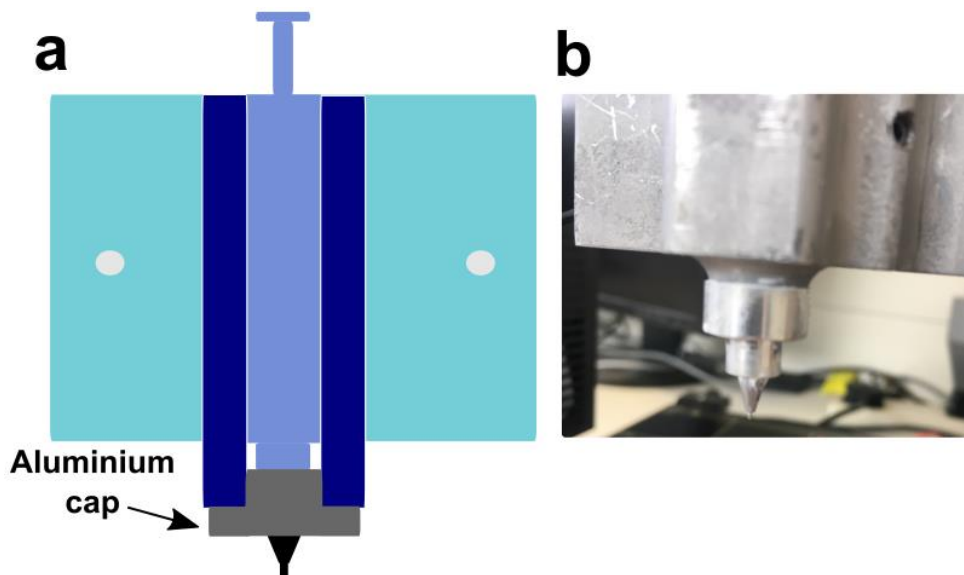


Figure 3-22. Extruder heating system with aluminium nozzle cap to mitigate air gap between nozzle and aluminium housing. (a) Schematic illustration showing cap placement at bottom of housing, (b) photo showing stainless steel nozzle aluminium cap over aluminium housing, with nozzle tip protruding from cap bottom.

At this stage, it was evident that the nozzle required closer contact heating; however, space under the current aluminium syringe-heating block was limited, therefore applying an extension block proved very difficult. Therefore, a secondary heating source was required. Many options were considered to rectify this issue, ranging from silicone heater mats, coil heaters and aluminium nozzles, however, due to the small nozzle base diameter, the wrapping of heating elements was not an option. Further, the smallest internal diameter aluminium nozzle available on the market was deemed unable to achieve the desired sub-50 μm diameter.

3.6.2.3. Nozzle heating block

At this stage, it was decided that a reasonable and convenient option was to employ a nozzle-heating block. The nozzle heating block system consisted of a 26 x 26 x 10mm block of aluminium with holes machined in-house to fit a stainless steel nozzle, cylindrical cartridge heater (Amazon.com, UK) and thermistor (cartridge type Semitec 104Gt 100k, E3D-online, UK). The cartridge heater and thermistor were linked to PID-controlled programming using the RAMPS electronics board of the printer whilst the extruder syringe heater was heated and controlled using the previously described Peltier heating module. A schematic representation of this configuration is shown in Figure 3-23.

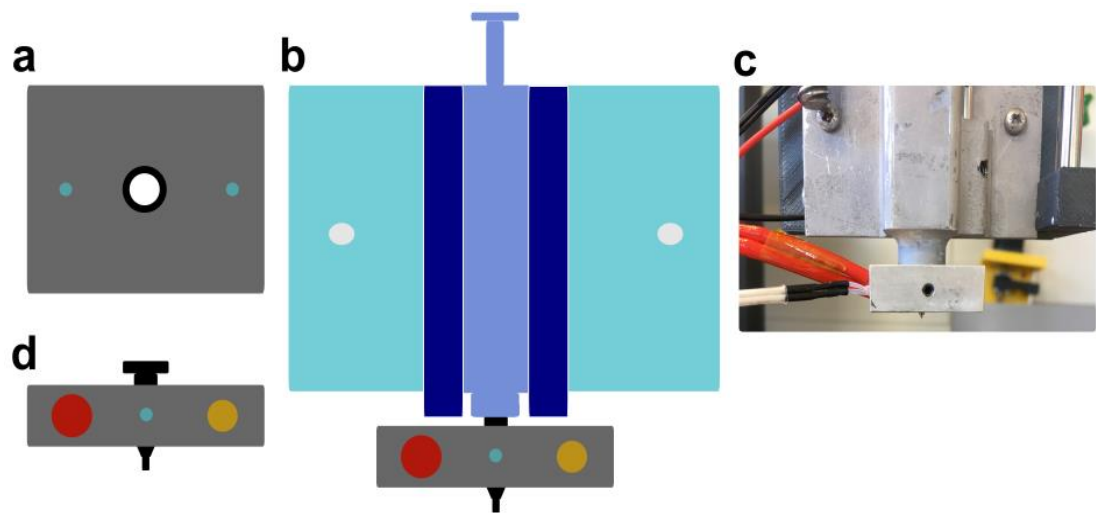


Figure 3-23. Extruder heating system with aluminium nozzle heater block, fitted with heat cartridge (red) and thermistor (orange) and showing grub screw holes (blue). (a) Schematic plan view of heater block. (b) front elevation schematic illustration of complete extruder heating system, (c) photo of nozzle heating system showing Peltier device wires in black and red (top left) and heat cartridge (red) and thermistor (white) wires (bottom left) (d) schematic nozzle heating block front elevation.

A final modification to further limit heat loss from the nozzle surface was the embedding of an aluminium epoxy putty (RS Components, UK) into the space between the nozzle and the nozzle-heating block, to limit heat loss to the environment. With this configuration, the nozzle tip temperature increased to an average of 53.5 °C with a nozzle heater set point temperature of 90.0 °C. In addition, the nozzle heater set point was lowered to 65.0 °C and the tip temperature was recorded to have an average of 42.0 °C, thus remaining above the gelation temperature and allowing deposition at a lower nozzle heater set point temperature when compared to earlier configurations.

3.6.3. Cooling bed configuration

In addition to the nozzle heating system, a chilled printing bed was developed in order to provide rapid cooling and gelation of agarose superior to room temperature cooling, with an initial target of 5.0 °C. A Peltier device was utilised in order to provide cooling to an aluminium plate whilst an aluminium heat sink and 12V DC fan (Banggood.com) were used to remove the heat produced by the hot side of the Peltier device. In addition, a water block was also used in this configuration to provide capacity for water-based cooling of the hot side, if required. The chilled bed was open to the environment; the utilised configuration is displayed in Figure 3-24.

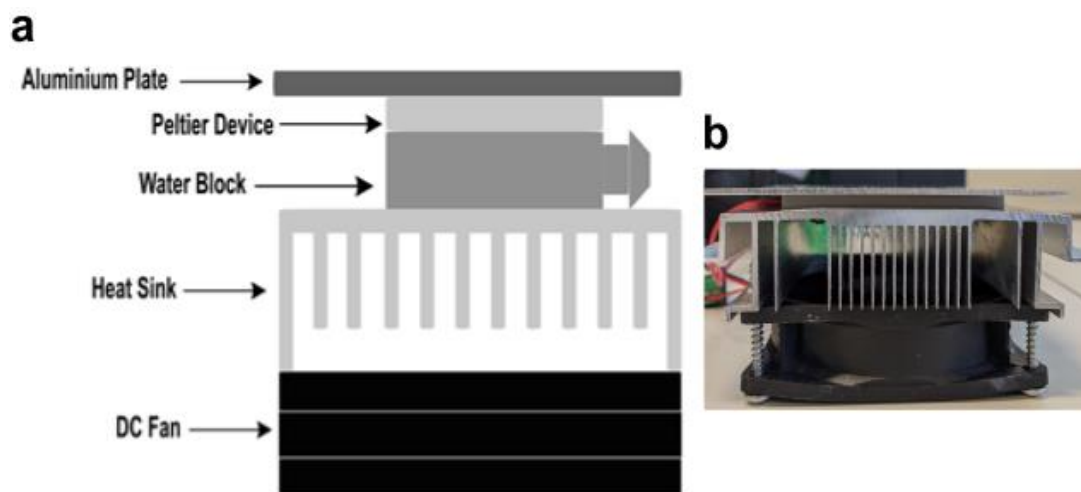


Figure 3-24. Peltier-cooled chilled bed (a) schematic illustration and (b) photo of hardware.

Different configurations and orientations of the cooling system were considered in the event of not achieving sufficiently low temperatures, whereby multiple parallel or stacked Peltier devices in addition to multiple fans and heat sinks could be utilised. When the thermostat temperature was set to 4.0 °C the bed temperature ranged ± 1.1 °C around the set point using simple bang-bang control, measured using the aforementioned digital thermometer for approximately one minute of contact time, where the temperature reading has stabilised.

3.7. Initial testing results

To deposit agarose droplets, a g-code file was developed, in which a fixed volume of alginate would be ejected onto 12 pre-set points onto a glass slide, in a 4x3 array. The aim was to deposit equally sized droplets onto the substrate, to analyse droplet size, and to analyse the accuracy of the process prior to aiming for fine droplet deposition by modifying the ejected volume of agarose in future tests.

An important parameter which was controlled in these tests was the dwell parameter (S); this denotes the period of time between completing extrusion at one point prior to moving to the next point. It was imperative to provide enough time for viscous agarose drops to fall or coalesce at the nozzle tip prior to moving to the next point, to avoid drops falling outside the designated points or to avoid the formation of oversized droplets or agarose-free points, all of which are evidenced in Figure 3-25.



Figure 3-25. Glass slide showing deposited agarose droplets, with non-uniform sizes and points with an absence of agarose, caused by temperature-related nozzle blockage issues.

Using the latest iteration of the nozzle heating system, limited repeatability of agarose deposition was achieved. With the syringe and nozzle heater set temperatures set to 95°C, deposition would initially facilitate the formation of 1 – 3 uniform droplets, as seen in Figure 3-25, however, the nozzle would subsequently block, this was assumed to be due to heat leaking from the parts of the nozzle not in contact with the aluminium heating block. Moreover, due to agarose being retained in the nozzle between the completion of the ejection of agarose at one point and moving to the next point and extruding again, it may be this element of fluid had sufficient time to be cooled by the surrounding air and solidify within the nozzle, hence leading to nozzle blockage.

Given that the set temperatures could not be increased further, due to boiling of the agarose solution, the conclusion was that the hardware required further modification. An attempt was made at wrapping a PID-controlled copper wire around the nozzle and affixing a thermistor to the nozzle body and subsequently wrapping the nozzle in a heat-insulating tape (see Figure 3-26). However, this increase in nozzle volume resulted in difficulties in fixing and removing the nozzle from syringes in addition to wire unwinding leading to electrical conduction issues, with undesired electrification of alginate drops.



Figure 3-26. Aluminium syringe heater affixed with coil-wrapped nozzle heater wrapped in insulating tape, showing copper and thermistor wires (green).

Besides further improvements to the nozzle heating approach, it is recommended to use a syringe material with high thermal conductivity, such as aluminium in addition to an aluminium nozzle. The drawback of this approach is that the syringes are considerably more expensive than the standard disposable plastic syringes, however this appears to be the most suitable next step in terms of temperature control, as this approach allows considerably more heat transfer from the heating systems to the fluid within the syringe and nozzle in comparison to the use of plastic syringes.

Furthermore, also implementing PID temperature control to the syringe heater would provide finer syringe temperature control, as opposed to the current simple bang-bang control, which would reduce the likelihood of agarose leaking through the nozzle tip due to unwanted vaporisation of agarose in the syringe. As the high temperature set points utilised for the syringe during this work were up to 95.0 °C, undesirable temperature overshoots were experienced once the process temperature reached the set point during bang-bang control (± 1.5 °C), therefore the actual syringe temperature reached approximately 96.5 °C before natural cooling was initiated on the switching off of the heating input.

3.8. Conclusion

To summarise, this section has documented the progression of the development of both the coaxial extrusion system to facilitate the extrusion of fine diameter cell-laden collagen filaments in addition to the progress in the nozzle heating and bed cooling systems.

Further work is required in transitioning the extrusion system into a fully 3D coaxial system, by adding capacity for the XYZ axis motors to be activated simultaneously with the extruder motors. Furthermore, additional work is required to facilitate repeatable agarose droplet extrusion in absence of nozzle blockage issues. To that end, it is recommended for future work to transition from using plastic (polypropylene), disposable syringes to stainless steel syringes or using materials with significantly higher thermal conductivities than polypropylene, to avoid the issue of heat leakage between syringe and the environment.

Given this technological progress, the following chapter utilises the coaxial extrusion system described within this chapter to demonstrate the successful production of fine diameter collagen fibres contained within hollow, cylindrical alginate hydrogel scaffolds. This highlights the versatility of this extrusion platform, in that extrusion of hydrogel droplets and collagen filaments which can be seeded with various cell types, with the option of utilising a temperature-controlled nozzle, is possible through the implementation of an additional syringe pump and a customisable coaxial nozzle system.

3.9. References

- [1] M. Dezawa, I. Takahashi, M. Esaki, M. Takano, and H. Sawada, "Sciatic nerve regeneration in rats induced by transplantation of *in vitro* differentiated bone-marrow stromal cells," *Eur. J. Neurosci.*, vol. 14, no. 11, pp. 1771–1776, Dec. 2001.
- [2] N. Rajan, J. Habermehl, M.-F. Coté, C. J. Doillon, and D. Mantovani, "Preparation of ready-to-use, storable and reconstituted type I collagen from rat tail tendon for tissue engineering applications," *Nat. Protoc.*, vol. 1, no. 6, pp. 2753–2758, Jan. 2007.
- [3] F. H. Silver and R. L. Trelstad, "Type I collagen in solution. Structure and properties of fibril fragments," *J. Biol. Chem.*, vol. 255, no. 19, pp. 9427–9433, Oct. 1980.
- [4] J. Habermehl *et al.*, "Preparation of ready-to-use, stockable and reconstituted collagen," *Macromol. Biosci.*, vol. 5, no. 9, pp. 821–828, Sep. 2005.
- [5] F. Boccafoschi, J. Habermehl, S. Vesentini, and D. Mantovani, "Biological performances of collagen-based scaffolds for vascular tissue engineering," *Biomaterials*, vol. 26, no. 35, pp. 7410–7417, Dec. 2005.
- [6] C. H. Lee, A. Singla, and Y. Lee, "Biomedical applications of collagen," *Int. J. Pharm.*, vol. 221, no. 1–2, pp. 1–22, Jun. 2001.
- [7] T. Elsdale and J. Bard, "Collagen substrata for studies on cell behavior," *J. Cell Biol.*, vol. 54, no. 3, pp. 626–637, 1972.
- [8] E. Bell, B. Ivarsson, and C. Merrill, "Production of a tissue-like structure by contraction of collagen lattices by human fibroblasts of different proliferative potential *in vitro*," *Proc. Natl. Acad. Sci. U. S. A.*, vol. 76, no. 3, pp. 1274–1278, 1979.
- [9] S. Itai *et al.*, "Cell-encapsulated chitosan-collagen hydrogel hybrid nerve guidance conduit for peripheral nerve regeneration," *Biomed. Microdevices*, vol. 22, no. 4, pp. 1–9, Nov. 2020.
- [10] Promega Corporation, "P450-Glo Assays," Madison, WI, 2016.
- [11] A. S. Morris and R. Langari, "Statistical analysis of measurements subject to random errors," in *Measurement and Instrumentation*, Academic Press, 2021, pp. 75–132.
- [12] A. Su and S. J. Al'Aref, "History of 3D printing," in *3D Printing Applications in Cardiovascular Medicine*, Elsevier, 2018, pp. 1–10.

- [13] N. G. Skrzypczak, N. G. Tanikella, and J. M. Pearce, “Open source high-temperature RepRap for 3-D printing heat-sterilizable PPE and other applications,” *HardwareX*, vol. 8, no. e00130, Oct. 2020.
- [14] M. R. Letherby and D. A. Young, “The gelation of agarose,” *J. Chem. Soc. Faraday Trans. 1 Phys. Chem. Condens. Phases*, vol. 77, no. 8, pp. 1953–1966, Jan. 1981.
- [15] T. K. Merceron and S. V. Murphy, “Hydrogels for 3D bioprinting applications,” in *Essentials of 3D Biofabrication and Translation*, Elsevier Inc., 2015, pp. 249–270.
- [16] C. Zhao and L. Guo, “Towards a theoretical foundation of PID control for uncertain nonlinear systems,” *Automatica*, vol. 142, no. 110360, Aug. 2022.
- [17] Y. He, D. Jiao, G. Pei, X. Hu, and L. He, “Experimental study on a three-dimensional pulsating heat pipe with tandem tapered nozzles,” *Exp. Therm. Fluid Sci.*, vol. 119, p. 110201, Nov. 2020.
- [18] T. Billiet, E. Gevaert, T. De Schryver, M. Cornelissen, and P. Dubruel, “The 3D printing of gelatin methacrylamide cell-laden tissue-engineered constructs with high cell viability,” *Biomaterials*, vol. 35, no. 1, pp. 49–62, Jan. 2014.

4. Collagen Filament Extrusion

4.1. Introduction

This chapter focuses on the engineering aspects concerned with the extrusion of concentric core/shell collagen/alginate scaffolds capable of future cell seeding, thus facilitating the fabrication of various cell and tissue filaments. Many aspects of these extruded collagen filaments within the core of cross-linked alginate shells were analysed, including diameter, morphology and continuity. The key parameters which were analysed include the ratio of flow rates between the core and shell nozzles and their magnitudes, crosslinking bath components, concentrations and exposure times in addition to collagen concentration.

The overarching aim of this work was to extrude repeatable, fine diameter, continuous collagen filaments of uniform diameter and to produce a parameter control guide in order to customise extruded tissue filaments to match patient anatomy but also to provide a foundation for future work involving different materials to address the limitations of the current configuration.

There are many parameters which were not studied in this chapter, mainly related to the mechanics of alginate hydrogel scaffolds. Porosity and stiffness were identified as key aspects to be aware of from the onset of this work and would be addressed on an ad hoc basis.

4.2. Background information and theory

4.2.1. Alginate

As has previously been discussed in Chapter 2, alginate is a natural, biocompatible, water-soluble polymer capable of cross-linking via G- and M- block ionic bonding using divalent cations such as Ca^{2+} and Ba^{2+} , to produce highly-tuneable, three-dimensional, mechanically-stable hydrogels which can be used as an extracellular matrix (ECM) mimic as a cell and tissue scaffold material [1].

It is important to be aware that cross-linked alginate structures may be degraded by various ions contained in cell culture media, including phosphate, sodium, potassium and magnesium [2]. It is therefore essential that cross-linked alginate structures retain integrity in culture for sufficient time to facilitate ECM/cell filament formation and maturation prior to any in vivo testing [3].

Alginate scaffolds may also be dissolved and removed from culture dishes on an ad hoc basis, primarily by means of chelation, using EDTA (ethylenediaminetetraacetic acid) [4] and/or sodium citrate [5] or enzymatically using alginate lyase [6].

4.2.2. Collagen type I

Type I collagen is the most abundant collagen type in the human body and is expressed in almost all connective tissues and the ECM as a result of its excellent biocompatibility and mechanical properties.

Collagen I is commonly extracted from the collagen fibres within rat tail tendons by solubilisation in acetic acid [7] to facilitate in vitro experimentation. Collagen aggregates may self-assemble in vitro given neutral pH, suitable ionic strength and room temperature. These self-assembled aggregates appear identical to those seen in vivo, therefore allowing accurate experimental comparison [8]. Self-assembled collagen gels exhibit excellent biocompatibility and can be modelled into many shapes, to mimic various parts of the anatomy.

However, collagen gels are mechanically weak as they are of low stiffness and elasticity. Further, collagen gels biodegrade rapidly, leading to their unsuitability for in vivo studies [9]. In many cases, however, the use of tissue-engineered hydrogel scaffolds, such as alginate, or collagen cross-linking to mechanically support collagen gels in vitro is essential [10]. In addition, collagen is naturally degraded and remodelled by cell-secreted matrix metalloproteases (MMPs) specifically collagenases [11] and proteases such as trypsin [12]. This gives control of remodelling of the ECM environment to any embedded cells within the engineered collagen construct, thus allowing cells to remodel the collagen to their specific needs and requirements [13].

4.2.3. Shear Stress

As a fluid flows through a cylindrical pipe, the section of fluid located at the surface boundary (walls) of the vessel experiences a frictional force acting in the opposite direction of the flow due to the roughness of the surface. Consequently, the element of fluid adjacent to this surface layer experiences an equal but opposite force. These equal but opposing forces are known as shear forces and the resulting stress is known as the shear stress. As a result of this layer-by-layer flow retardation, the flow velocity profile ranges from zero at the boundary surface, due to the no-slip condition dictating that at a fluid-solid boundary the fluid velocity is zero, until a sufficient distance from the surface is reached, such that flow velocity is, arbitrarily, 90.0 to 99.9% of the undisturbed free stream velocity. The region of fluid affected by this reduction of flow is known as the boundary layer.

For a Newtonian fluid, the shear stress is defined as:

$$\tau(y) = \mu \frac{du}{dy} \quad (4.1)$$

Where:

τ = shear stress

μ = fluid viscosity

u = flow velocity

y = flow height above boundary surface

Cellular shear stress becomes a major issue with low nozzle diameter. There is a trade-off between shear stress and minimal filament diameter whereby decreasing filament diameter by using finer nozzle diameters results in an increase in shear stress, resulting in a potential reduction in post-extrusion cellular viability when a shear stress threshold is achieved. Short-term exposure to high levels of shear stress can affect post-extrusion cell viability but also can contribute to long-term changes in the proliferation potential of viable cells. It is therefore critical that the minimal filament diameter and resulting shear stress are finely balanced to achieve optimal filament diameter for a given nozzle diameter without compromising cellular viability and phenotype [14].

4.2.4. Reynolds number

The Reynolds number is a dimensionless number which is defined as the ratio between inertial and viscous forces experienced by a moving fluid. The calculation of the Reynolds number allows prediction of fluid flow patterns

$$Re = \frac{\rho U d}{\mu} \quad (4.2)$$

Where:

Re = Reynolds number

ρ = fluid density

U = average fluid velocity

d = vessel diameter

μ = fluid dynamic viscosity

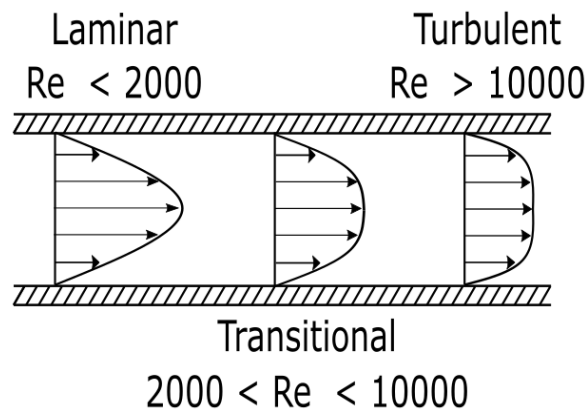


Figure 4-1. Flow profiles of a viscous fluid flowing in a cylindrical pipe, showing flow regimes for varying Reynolds numbers.

When $Re < 2000$ the fluid flow is described as laminar, whereby the viscous forces are dominant and the fluid velocity profile for laminar flow is parabolic in nature, as is illustrated in Figure 4-1.

When $2000 < Re < 10,000$, the flow is in a transitional state in which turbulent circulating currents (eddies) are developing.

With $Re > 10,000$, the flow is described as fully-developed turbulent flow where inertial forces are dominant and chaotic eddy currents are present, causing some elements of the fluid to recirculate and flow in different directions and at different velocities across the cross-section of the vessel with the fluid flow in the boundary layer to be unsteady. The flow profile for turbulent flow is in the shape of a flattened parabola. Due to the low diameters and flow rates used here, the flow regime of collagen and alginate is always laminar.

4.3. Deriving parameters affecting filament diameter

4.3.1. Derivation of Navier-Stokes equation

Assuming a Newtonian, incompressible, viscous liquid flowing in a cylindrical pipe with radius, R , of uniform cross-sectional area, A , in the axial 'z' direction, as is illustrated in Figure 4-2

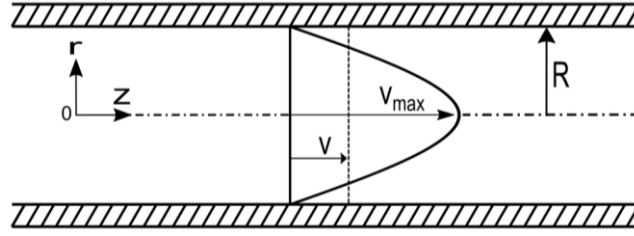


Figure 4-2. Laminar flow profile in a cylindrical pipe.

By applying the principal of conservation of mass, a time-dependent continuity equation may be developed.

To describe the three-dimensional unsteady movement of a viscous fluid, the Navier-Stokes equations may be used. These equations are used to describe the relationship between fluid pressure, velocity, temperature and density of a moving fluid. These equations arise from the application of Newton's second law of motion in combination with the concepts of conservation of mass, momentum and energy. Of particular interest here are the three equations describing viscous fluid conservation of momentum. These describe fluid motion in the radial (r), angular (θ) and axial (z) directions respectively, and are presented below, in cylindrical coordinates.

$$\begin{aligned} \rho \left(\frac{\partial v_r}{\partial t} + v_r \frac{\partial v_r}{\partial r} + \frac{v_\theta}{r} \frac{\partial v_r}{\partial \theta} - \frac{v_\theta^2}{r} + v_z \frac{\partial v_r}{\partial z} \right) \\ = -\frac{\partial P}{\partial r} + \rho g_r \\ + \mu \left[\frac{1}{r} \frac{\partial}{\partial r} \left(r \frac{\partial v_r}{\partial r} \right) - \frac{v_r}{r^2} + \frac{1}{r^2} \frac{\partial^2 v_r}{\partial \theta^2} - \frac{2}{r^2} \frac{\partial v_\theta}{\partial \theta} + \frac{\partial^2 v_r}{\partial z^2} \right] \end{aligned} \quad (4.3)$$

$$\begin{aligned} \rho \left(\frac{\partial v_\theta}{\partial t} + v_r \frac{\partial v_\theta}{\partial r} + \frac{v_\theta}{r} \frac{\partial v_\theta}{\partial \theta} - \frac{v_r v_\theta}{r} + v_z \frac{\partial v_\theta}{\partial z} \right) \\ = -\frac{1}{r} \frac{\partial P}{\partial \theta} + \rho g_\theta + \mu \left[\frac{1}{r} \frac{\partial}{\partial r} \left(r \frac{\partial v_\theta}{\partial r} \right) - \frac{v_\theta}{r^2} + \frac{1}{r^2} \frac{\partial^2 v_\theta}{\partial \theta^2} + \frac{2}{r^2} \frac{\partial v_r}{\partial \theta} + \frac{\partial^2 v_\theta}{\partial z^2} \right] \end{aligned} \quad (4.4)$$

$$\begin{aligned} \rho \left(\frac{\partial v_z}{\partial t} + v_r \frac{\partial v_z}{\partial r} + \frac{v_\theta}{r} \frac{\partial v_z}{\partial \theta} + v_z \frac{\partial v_z}{\partial z} \right) \\ = -\frac{\partial P}{\partial z} + \rho g_z + \mu \left[\frac{1}{r} \frac{\partial}{\partial r} \left(r \frac{\partial v_z}{\partial r} \right) + \frac{1}{r^2} \frac{\partial^2 v_z}{\partial \theta^2} + \frac{\partial^2 v_z}{\partial z^2} \right] \end{aligned} \quad (4.5)$$

Where:

ρ = fluid density

v_r, v_θ, v_z = fluid velocity in the radial, angular and axial directions respectively

t = time

r = distance from pipe centre line in radial direction ($0 < r < R$)

P = fluid pressure

g_r, g_θ, g_z = acceleration through application of body forces on fluid in the radial, angular and axial directions respectively

μ = fluid viscosity

These equations are insolvable in their current form but may be reduced by making a number of assumptions:

- Fluid flow is at steady state, therefore all differentials with respect to time may be ignored.
- The effects of gravity may be ignored by assuming no change in fluid elevation throughout the pipe ($g_r, g_\theta, g_z = 0$).
- There are no radial or angular forces acting on the fluid ($v_r, v_\theta = 0$).
- The flow is considered uniform, therefore $\frac{\partial v_z}{\partial z} = 0, \frac{\partial^2 v_z}{\partial z^2} = 0$
- There is no dependence of v_z on the angle θ , therefore $\frac{\partial^2 v_z}{\partial \theta^2} = 0$

Upon application of these assumptions, the first of the three equations now simply states $\frac{\partial P}{\partial r} = 0$. In a similar manner, the second equation states $\frac{\partial P}{\partial \theta} = 0$

The third equation, describing the axial flow conservation of momentum, is reduced to:

$$\frac{\partial P}{\partial z} = \mu \left[\frac{1}{r} \frac{\partial}{\partial r} \left(r \frac{\partial v_z}{\partial r} \right) \right] \quad (4.6)$$

4.3.2. Finding flow velocity distribution

By taking the simplified Navier-Stokes equation expressed in equation 4.6, it is possible to derive the expression for fluid velocity distribution. Firstly, by multiplying both sides by 'r' and rearranging:

$$\frac{r}{\mu} \frac{\partial P}{\partial z} = \frac{\partial}{\partial r} \left(r \frac{\partial v_z}{\partial r} \right) \quad (4.7)$$

By integrating both sides with respect to 'r', integrals may be constructed and partial differentials may be replaced with Leibniz's notation:

$$\int \frac{r}{\mu} \frac{dP}{dz} dr = \int \frac{d}{dr} \left(r \frac{dv_z}{dr} \right) dr \quad (4.8)$$

Upon integration and rearranging:

$$r \frac{dv_z}{dr} = \frac{r^2}{2\mu} \frac{dP}{dz} + C_1 \quad (4.9)$$

By dividing both sides by 'r' and constructing further integrals:

$$\int \frac{dv_z}{dr} dr = \int \frac{r}{2\mu} \frac{dP}{dz} + \frac{C_1}{r} dr \quad (4.10)$$

Integration yields:

$$v_z(r) = \frac{r^2}{4\mu} \frac{dP}{dz} + C_1 \ln(r) + C_2 \quad (4.11)$$

When applying the boundary conditions, the fluid velocity at $r = 0$ must be finite, therefore $C_1 = 0$; C_2 is determined when $v_z = 0$ and r is equal to the pipe radius, R , as is dictated by the no-slip condition:

$$C_2 = -\frac{1}{4\mu} \frac{dP}{dz} R^2 \quad (4.12)$$

Therefore by substitution of C_1 and C_2 into equation 4.11, the velocity distribution may be presented as:

$$v_z(r) = -\frac{1}{4\mu} \frac{dP}{dz} (R^2 - r^2) \quad (4.13)$$

This may also be displayed as:

$$v_z(r) = -\frac{1}{4\mu} \frac{dP}{dz} R^2 \left(1 - \frac{r^2}{R^2}\right) \quad (4.14)$$

From this equation, it is clear that the velocity distribution forms a paraboloid, whereby the maximum fluid velocity is observed at the pipe centreline, where $r = 0$:

$$v_{z,max} = -\frac{1}{4\mu} \frac{dP}{dz} R^2 \quad (4.15)$$

4.3.3. Derivation of Poiseuille's law

For simplification, let $v_z = v$

The volumetric flow rate of the fluid may be displayed as [15]:

$$Q = \int v \, dA = \int v \, 2\pi r \, dr \quad (4.16)$$

By substituting the velocity distribution equation (4.13) into equation 4.16, this equation becomes:

$$Q = \int_0^R -\frac{1}{4\mu} \frac{dP}{dz} (R^2 - r^2) 2\pi r \, dr \quad (4.17)$$

On integration and application of limits, a rearranged form of the Hagen-Poiseuille equation is achieved.

$$Q = -\frac{\pi}{8\mu} \frac{dP}{dz} R^4 \quad (4.18)$$

From this equation, the average fluid velocity can be found:

$$v_{avg} = \frac{Q}{\pi R^2} = -\frac{dP}{dz} \frac{R^2}{8\mu} = \frac{1}{2} v_{z,max} \quad (4.19)$$

It should be noted that Equation 4.19 states that there is an inverse proportionality relationship between fluid velocity/volumetric flow rate and viscosity. By substituting Equation 4.19 into equation 4.14, the fluid velocity may be expressed as a function of volumetric flow rate:

$$v(r) = 2v_{avg} \left(1 - \frac{r^2}{R^2}\right) = \frac{2Q}{\pi R^2} \left(1 - \frac{r^2}{R^2}\right) \quad (4.20)$$

4.3.4. Equation for coaxial diameters

When extruding using two fluids within a coaxial nozzle, whereby there is an inner core fluid and an outer shell fluid, by employing the fluid velocity distribution equation as a function of fluid flow rate, the theoretical coaxial core filament diameter, D_c , may be expressed as a function of volumetric flow rate. A schematic of a coaxial nozzle is illustrated in Figure 4-3 below.

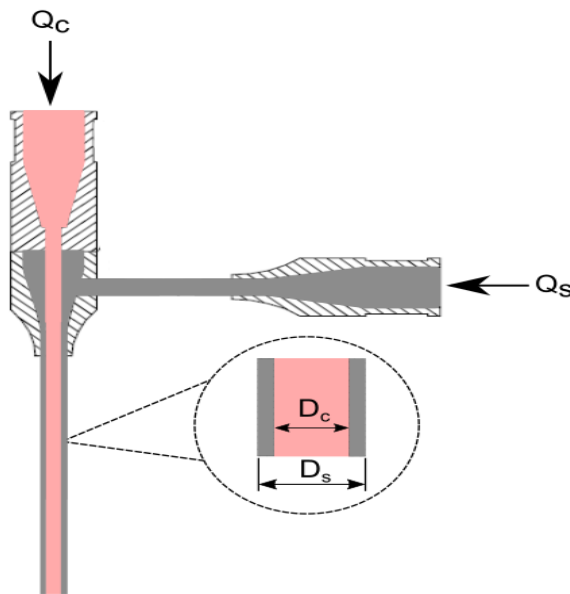


Figure 4-3. Coaxial nozzle cross section showing internal core/shell flowrates and resulting extruded diameters.

By combining equations 4.16 and equation 4.20, an equation for the core fluid flow rate, Q_c , can be formulated:

$$Q_c = \int_0^{\frac{D_c}{2}} \frac{2Q}{\pi R^2} \left(1 - \frac{r^2}{R^2}\right) 2\pi r dr \quad (4.21)$$

On integration and rearrangement:

$$\frac{Q_c R^2}{4Q} = \left[\frac{r^2}{2} - \frac{r^4}{4R^2} \right]_0^{\frac{D_c}{2}} \quad (4.22)$$

By applying the limits of integration and rearranging, a quadratic equation is obtained:

$$D_c^4 - 8R^2 D_c^2 + 16R^4 \frac{Q_c}{Q} = 0 \quad (4.23)$$

Solving this quadratic equation gives:

$$D_c^2 = 4R^2 \left(1 \pm \sqrt{\left(1 - \frac{Q_c}{Q}\right)} \right) \quad (4.24)$$

Solving for D_c by taking the square root of both sides and eliminating the positive term of the quadratic, as $D_c < 2R$:

$$D_c = \sqrt{1 - \sqrt{\left(1 - \frac{Q_c}{Q}\right)}} \cdot 2R \quad (4.25)$$

This may be re-written to express the core/shell diameter ratio as a function of the respective flow rate ratio:

$$\frac{D_c}{D_s} = \sqrt{1 - \sqrt{\left(\frac{Q_s}{Q_c + Q_s}\right)}} \quad (4.26)$$

Where:

D_s = shell outer diameter

Q_s = volumetric flow rate of shell fluid

Equation 4.26 states that the core and/or shell outer diameter may be controlled by simple manipulation of the respective flow rates. By increasing the flow rate ratio, there is a corresponding decrease in the diameter ratio.

This theoretical relationship was validated in practice by Xu et al. [16] by coaxial extruding using alginate as the core fluid and CaCl_2 solution as the shell fluid to produce calcium alginate filaments. However, it should be noted that experimental inaccuracies were present, due to effects from the viscosity of the alginate shell fluid, cross-linking effects and transverse diffusion occurring within the phase interface [17], resulting in slight deviations from the ideal model plot.

This relationship was additionally demonstrated in practice by Shao et. al [18] using gelatin methacryloyl (GelMA), a chemically-modified form of gelatin which is resistant to the thermal degradation effects suffered by pure gelatin, as the core fluid [19]. Sodium alginate was used as the shell fluid. By manipulating the flow rate of core GelMA solution, sub-100 μm diameter acellular filaments were successfully extruded.

Through the use of modelling software, Williams et. al. [20] demonstrated, using an alginate core and a calcium chloride shell solution, that when the shell flow velocity exceeds that of the core flow, the core flow begins to accelerate as a result of the transfer of momentum from the faster shell fluid. This acceleration results in the contraction of the core fluid, leading to a smaller filament diameter (see Figure 4-4). However, it should be noted that this observation is affected by the chosen cross-linking conditions. Furthermore, due to the inverse proportionality relationship between fluid flow rate and viscosity, as shown in Equation 4.19, a lower viscosity core fluid should theoretically lead to a faster fluid flow rate (and velocity) for a constant cross-sectional surface area. Therefore, by maintaining the velocity of the shell stream above that of the core stream and further increasing Q_s , a higher flow rate and greater transfer of momentum should be achieved with a comparably lower fluid viscosity, which may lead to a smaller filament diameter on momentum-induced acceleration.

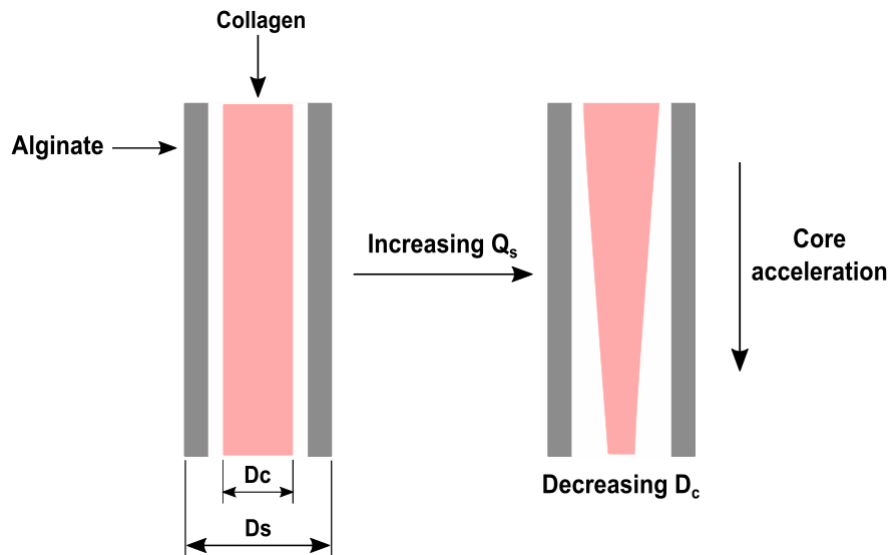


Figure 4-4. Extruded filament cross sections showing increasing Q_s leads to a reduction in core filament diameter.

With these findings, it therefore seemed viable that this relationship could be applied to produce fine diameter collagen filaments. The results of such experiments are detailed in the subsequent sections of this chapter.

4.4. Process description

Originally developed by Shin et.al [21] by combining glass pipettes with a PDMS (Polydimethylsiloxane) chip, coaxial extrusion involves the use of a coaxial nozzle which contains two input ports, the outer shell and the inner core, which, when combined, allow concentric flow. Whilst Shin et al. used co-flow of an alginate core stream and a CaCl_2 solution shell stream to produce calcium alginate fibres, Sugiura et. al [22] produced hollow calcium alginate tubes by adding sodium alginate in the shell stream, coupled with calcium chloride (CaCl_2) simultaneously flowing in the core nozzle and extruding into a CaCl_2 cross-linking bath.

Monovalent Na^+ ions within alginate are displaced by divalent Ca^{2+} ions to initiate alginate cross-linking to produce a porous, mechanically-stable, tubular hydrogel network of calcium alginate. These partially cross-linked structures may be further cross-linked in the cross-linking bath over time; other divalent cations such as Sr^{2+} or Ba^{2+} [23][24] may be used in place of Ca^{2+} to tune the alginate shell mechanical properties.

Onoe et. al. [25] used this platform to fabricate cell-laden filaments using microfluidic apparatus by employing a neutralised, type I collagen solution (acid and pepsin-solubilised rat tail-derived) in the core nozzle. Collagen thermal self-assembly occurred within the lumen of the tubular alginate scaffolds to produce mechanically-stabilised cell-laden filaments.

When cells are suspended within the collagen solution, cell-laden filaments may be produced. It should be noted that upon pH neutralisation and prior to extruding, the collagen solution must remain at low temperature, by use of an ice bath, for example, and extruded immediately to prevent self-assembly as this may lead to collagen gelation and consequential blockage within the extrusion nozzle. A detailed schematic of the coaxial extrusion process is found in Figure 2-27 whilst an image of extruded filaments may be found in Figure 4-5.

This versatile methodology allows the addition of further input nozzles, provides a choice of cell placement in the core or shell to produce cell filaments or tubular structures, the addition of further ECM materials or growth factors and also facilitates the implementation of other crosslinking cations, such as Sr^{2+} and Ba^{2+}

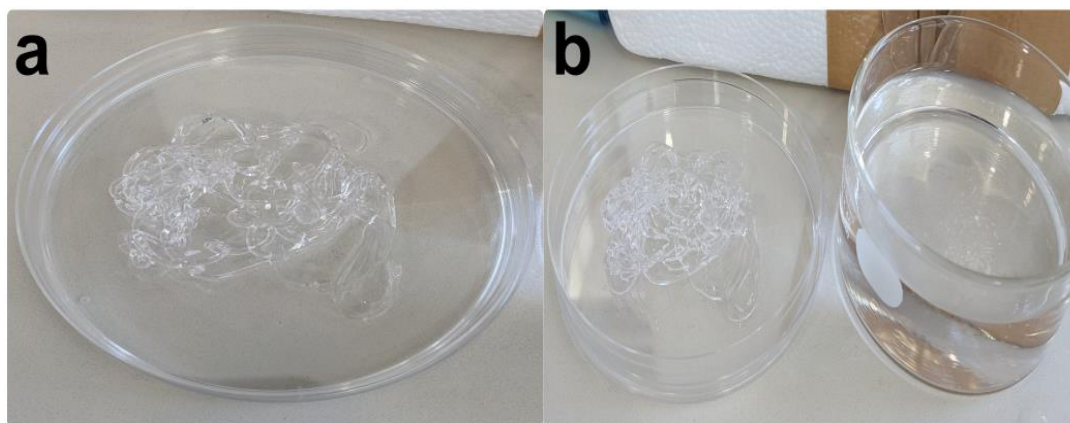


Figure 4-5. Photos showing piles of coaxial extruded alginate scaffolds (a) 90 mm petri dish containing freshly cross-linked tubular alginate scaffolds (b) petri dish aligned with glass cross-linking bath.

In the following experiments, the core nozzle internal diameter (ID) was 27G (203 μm) and the corresponding outer diameter (OD) was 22G (406 μm). The nozzle shell ID was 19G (690 μm) and the corresponding OD was 1070 μm . Alginate concentration in the shell was fixed at $2.0 \pm 0.03\%$ (w/v), due to this concentration providing a good balance between printing viscosity, mechanical strength and porosity for cell nutrient and waste diffusion [26] [27]. The collagen concentration in the core inlet was initially set to 3.0 mg/ml $\pm 0.11\%$, a commonly used concentration, as there are difficulties in trying to extrude higher concentrations due to higher viscosities, which can lead to printing failure and blocking of small diameter nozzles [28] [29]. Calcium chloride cross-linking bath concentration was initially fixed at 100 mM $\pm 9.0 \mu\text{M}$, a commonly used concentration to cross-link alginate, giving balance between rapid cross-linking, mechanical strength and limiting cellular exposure to deleterious concentrations of CaCl_2 [30] [31]. No post-extrusion crosslinking was initially employed.

Printed filaments were submerged and maintained in cell culture media, used to maintain cellular viability but used in this chapter to allow comparison between acellular and cellular filaments, which are discussed in the next chapter. Cell culture media was changed every 3 to 4 days (twice per working week).

4.5. Collagen filament diameter tuning

This section is dedicated to the experimental investigation of parameter effects on the extruded collagen filament diameter in order to inform later cell-seeding experiments to produce fine diameter, bespoke tissue filaments. Tested parameters include the effects of flow rate, cross-linking and collagen concentration, amongst others.

4.5.1. Shell flow rate and incubation time

Firstly, to establish the effect of changing the shell nozzle flow rate (Q_s) on collagen filament diameter, a study was devised in which the core flow rate (Q_c) was maintained at 0.1 ml/min whilst the shell flow rate was manipulated in order to change the core/shell flow rate ratio (Q_c/Q_s), which was set at three different flow ratios: 1:1, 1:2 and 1:4. This study also allowed the analysis of the effect of post-extrusion incubation time in cell culture media on the resulting extruded collagen filament diameter. Upon completion of the extrusion process, filaments were removed from the cross-linking bath, washed in PBS and subsequently incubated in cell culture media over a 14-day period.

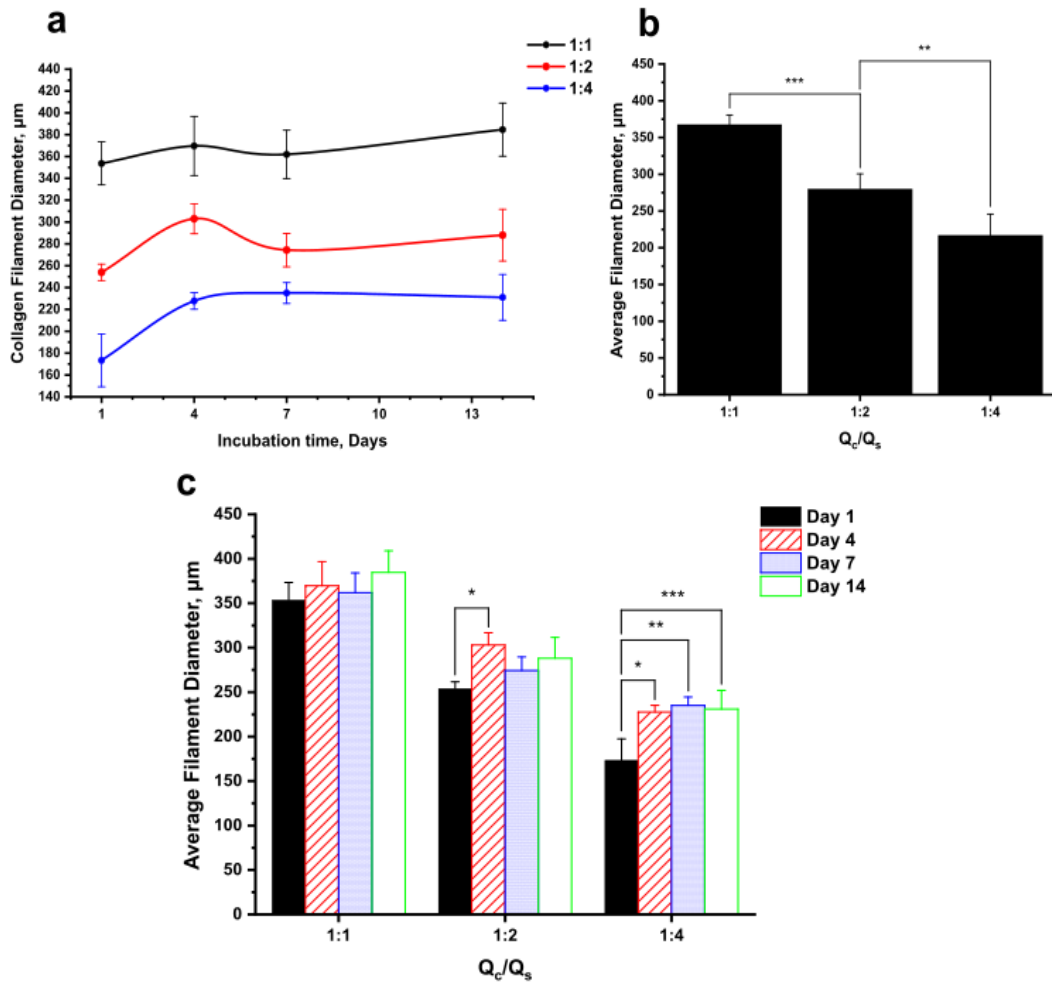


Figure 4-6. Effect of changing core/shell flow rate ratio on (a) collagen filament diameter over the 14-day incubation period. (b) 14-day average filament diameter for each Q_c/Q_s , (c) Effect of incubation time on filament diameter for each tested Q_c/Q_s . Data points represent mean \pm standard deviation (SD) ($n=3$). (* indicates $p < 0.05$; ** indicates $p < 0.01$ *** indicates $p < 0.001$). Statistical analysis performed using a one-way ANOVA test with Tukey's post hoc test. Legend in (a) denotes Q_c/Q_s for each series.

It was found that there is a significant effect of flow rate ratio manipulation on the 14-day average collagen filament diameter for all three cases shown in Figure 4-6 (b) ($p < 0.01$, one-way ANOVA with Tukey's post hoc test). Reducing Q_c/Q_s from 1:1 to 1:2 significantly reduced the average filament diameter from 367.5 ± 13.2 to 279.8 ± 20.8 μm ($p < 0.001$). A further reduction of Q_c/Q_s by 0.25, from 1:2 to 1:4, has also been shown to significantly reduce the filament diameter, to 216.8 ± 29.1 μm ($p < 0.01$). The conclusion taken into further experiments was that decreasing Q_c/Q_s leads to a finer collagen filament in the core of the alginate shell structure.

With regards to incubation time effects, displayed in Figure 4-6 (c), there was no significant effect on the diameter of the filaments extruded at a 1:1 flow rate ratio ($p > 0.05$, one-way ANOVA with Tukey's post hoc test). Using the same statistical testing, a significant difference was found between days 1 and 4 for both the 1:2 and 1:4 flow rate ratios ($p < 0.05$). No further significant differences were found between days 4, 7 and 14, indicating filament diameter stabilises after a maximum of 4 days when increasing shell flow rates higher than 1:1 up to 1:4. However, further testing is required to provide a definitive conclusion in this regard.

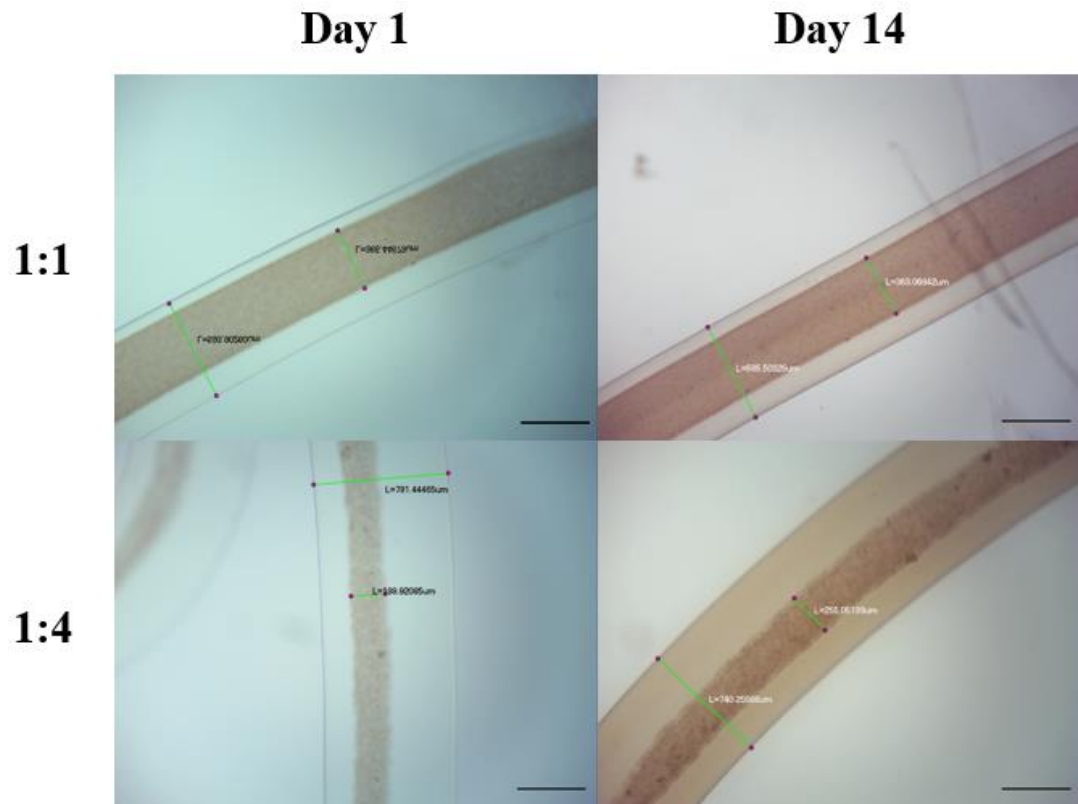


Figure 4-7. Representative light microscopy images of coaxial extruded collagen/alginate scaffolds using 1:1 and 1:4 core/shell flow rates at day 1 and day 14 of incubation in cell culture media, showing negligible effect of incubation time on filament morphology. Scale bars = 400 μm .

Incubation effects on filament morphology are illustrated in Figure 4-7, whereby representative images show negligible differences between filaments at day 1 and day 14 for both 1:1 and 1:4 core/shell flow rate ratios under light microscopy analysis. It is predicted that the addition of cells to these filaments would lead to an increase in collagen mass and cell number over time, leading to notable effects of incubation time on filament morphology.

In addition, further tests are required to analyse individual collagen fibril structure and alignment, whereby using multi-photon imaging, for example, would provide a more robust conclusion.

This microscopy technique permits nano-scale visualisation of individual collagen fibril morphology, as opposed to the macro scale filaments presented here, which contain many fibrils, which may not actually be aligned.

4.5.2. Incubation and cross-linking time effects

As hydrogel cross-linking is an integral factor in coaxial extrusion, maintaining scaffold integrity and porosity is essential to contain collagen filaments for culture. If the cross-linking time is insufficient, scaffolds will degrade too rapidly and be too weak to manipulate, causing collagen filaments to fragment *in vitro*; conversely, if the cross-linking time is too high, scaffolds may require a harsher, potentially toxic degradation treatment or may not degrade at all *in vivo*. It was therefore necessary to analyse the effect of post-extrusion cross-linking time in a cross-linking bath on collagen filament morphology and, secondly, on filament diameter, as there appears to not be any research available on this topic and there may be undocumented interactions between cross-linking time and collagen filament diameter.

Two groups of filaments were extruded into a 100 mM CaCl₂ bath and left to cross-link after extrusion for either 5 or 10 minutes; a third group was immediately washed following extrusion and hence not further exposed to CaCl₂ post-extrusion. All filaments were then washed in PBS and incubated in well plates containing cell culture media. The core/shell flow rate ratio used here was 1:4, for convenience. Filaments were imaged over a ten-day period, from day 4 to day 14.

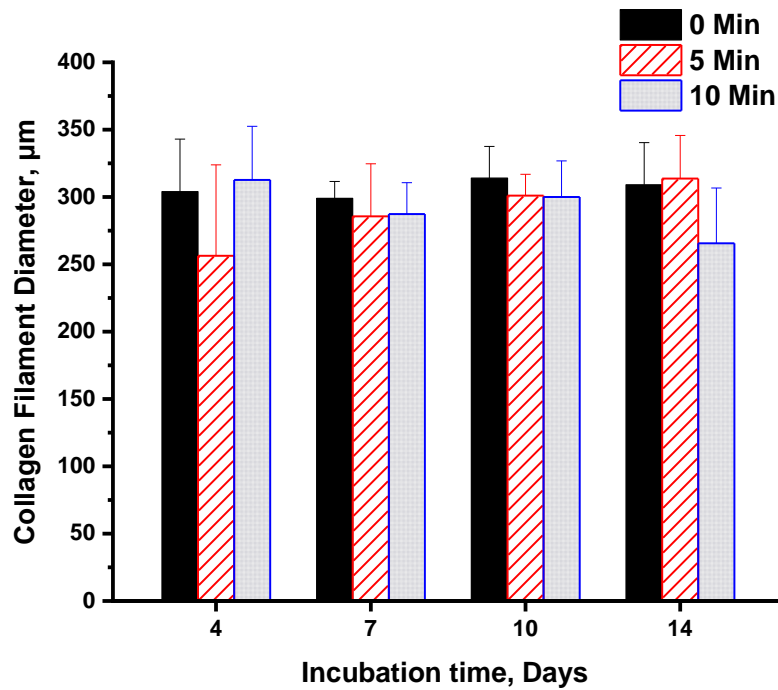


Figure 4-8. Effect of incubation and cross-linking time on collagen filament diameter within alginate shell, $Q_c = 0.05$ ml/min, $Q_s = 0.20$ ml/min. Data points represent mean \pm SD ($n = 3$).

Figure 4-8 illustrates no observed significant difference in filament diameter between all three cross-linking times used in this experiment ($p > 0.05$, one-way ANOVA). This was under the assumption that the filament cross-section was circular. Filament diameter ranged from 256.3 ± 67.6 μm for the 5-minute case on day 4 to 314.0 ± 23.5 μm on day 10 for the 0-minute condition. This indicates that, with a core/shell flow rate ratio of 1:4, alginate shell cross-linking time has no effect on collagen filament diameter in the core when using the coaxial nozzle configuration described in section 4.4. However, it should be noted that some of the error bars here measure approximately 25% of the value of the mean, suggesting large uncertainty and large confidence interval. Repeating this work with a larger sample size is necessary to give a firm conclusion on these observations.

This assumption was used to inform future experiment planning, in that a day-four measurement could be accurately quoted as the true collagen filament diameter for a given flow rate manipulation experiment. To confirm this conclusion however, this experiment should be performed with other flow rate ratios.

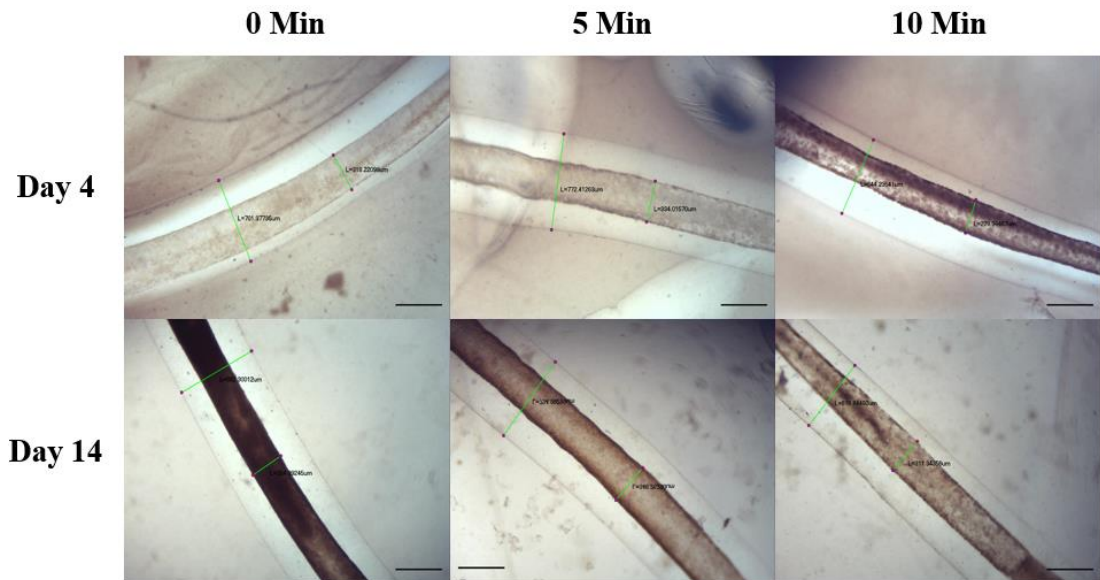


Figure 4-9. Day 4 and day 14 representative light microscopy images for three cross-linking conditions showing continuous, uniform collagen filaments contained within alginate shells in culture media. Scale bar = 400 µm.

Under light microscopy, the collagen filaments for all three experimental conditions appeared to retain their continuous, uniform morphology across the ten-day period in culture media, as shown by Figure 4-9. Additionally, the filaments observed at day 14 are assumed darker as a result of staining caused by continuous long-term exposure to phenol red, the pH indicator present in the culture media in which the cells were submerged in during the experimental period.

The preliminary conclusions drawn from this experiment were that post-extrusion cross-linking time of an alginate shell (up to 10 minutes) with 100 mM CaCl₂ does not have a significant effect on the diameter or uniformity of coaxial extruded collagen filaments. However, higher sample numbers are required to provide greater confidence and a robust conclusion on these observations.

4.5.3. Core flow rate tuning

The effect of changing the core nozzle flow rate (Q_c) on collagen filament diameter was also investigated. The shell flow rate (Q_s) was maintained at 0.5 ml/min whilst the core flow rate was increased in increments of 0.1 ml/min, from 0.1 to 0.5 ml/min. This corresponded to increasing Q_c/Q_s in increments of 0.2, from 1:5 up to 1:1 (0.5/0.5).

This experiment was conducted in order to reinforce the conclusion from the previous experiment, detailed in section 4.5.1, that decreasing Q_c/Q_s would again result in a smaller collagen filament diameter but with the manipulation of Q_c in this case. The experiment was conducted over a five-day period.

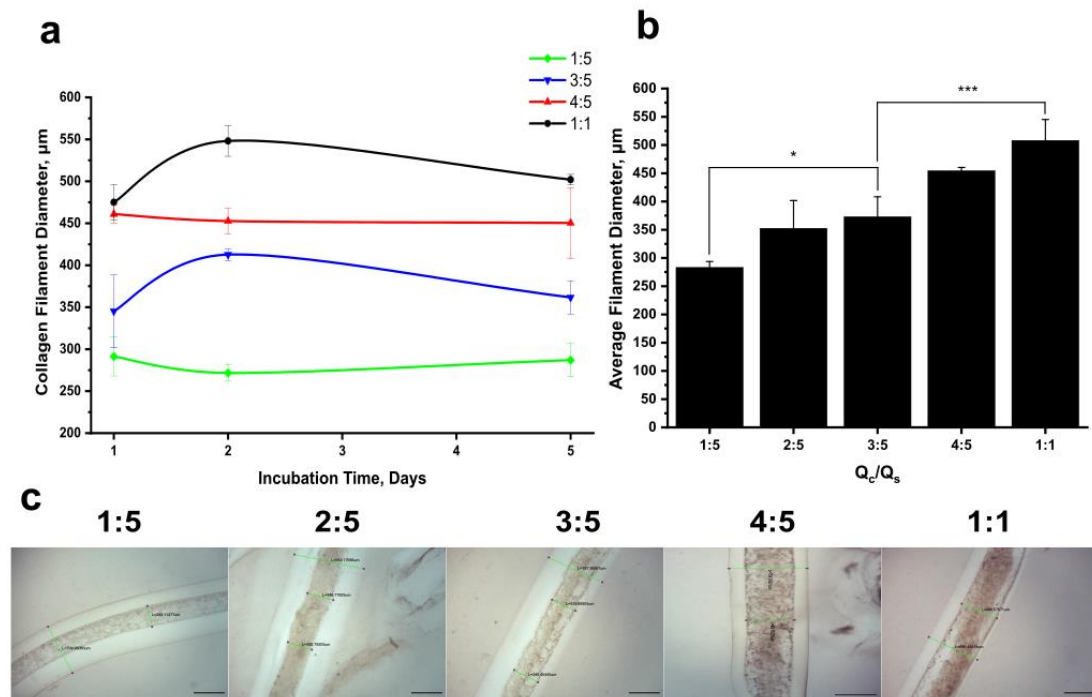


Figure 4-10. (a) Effect of changing Q_c on collagen filament diameter over the five-day experiment, $Q_s = 0.5$ ml/min. (b) 5-day average filament diameter for each corresponding Q_c/Q_s . (c) representative light microscopy images of collagen filaments in culture media. Data points represent mean \pm SD ($n = 3$). Scale bars = 400 μm . (2:5 ratio case omitted from (a) for clarity).

On analysis of Figure 4-10 (a), it is again observed that decreasing Q_c/Q_s from 1:1 up to 1:5 leads to a reduction in collagen filament diameter. It can be seen in Figure 4-10 (b) that the five-day average filament diameter significantly increases ($p < 0.05$) with an increase of Q_c/Q_s by 0.4, from 1:5 to 3:5. The collagen filament diameter at a flow rate ratio of 1:5 measured an average of $283.3 \pm 10.3 \mu\text{m}$, whilst the filament diameter for the 1:1 case was significantly larger ($p < 0.001$), at $508.3 \pm 36.9 \mu\text{m}$. Coupling these findings with previous findings, shown in section 4.5.1, it can be concluded that reducing Q_c/Q_s leads to a statistically significant change in the extruded collagen filament diameter.

4.5.4. Flow rate magnitude effects

It has been demonstrated that changing Q_c/Q_s leads to changes in the diameter of extruded collagen filaments. Another factor that must be taken into account is the magnitude of the flow rates used during coaxial extrusion when fixing Q_c/Q_s . An experiment was therefore undertaken in order to analyse the effect of flow rate magnitude on day 1 (24h post-extrusion) collagen filament and alginate shell diameter at an equal flow rate ratio for all cases (1:1 in this case). The baseline flow rate used was 0.1 ml/min and this was compared against 0.5 and 1.0 ml/min to investigate the effect of multiplying the utilised flow rates by five- and ten-fold.

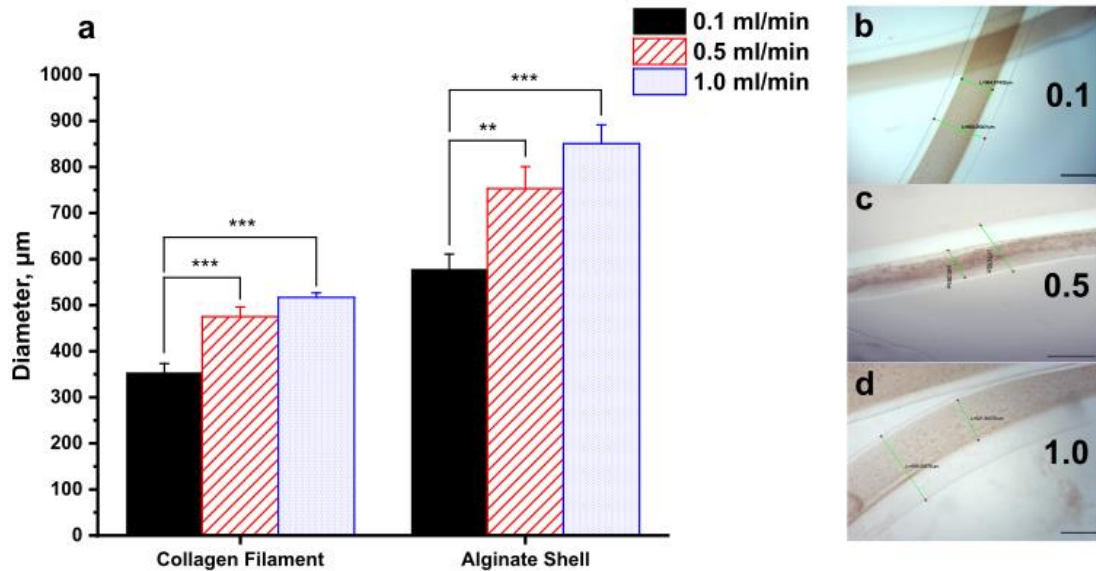


Figure 4-11. Effect of flow rate magnitude at equal flow rate ratio of 1:1 on day 1 collagen filament and alginate shell diameter. (a) effect of flow rate magnitude on collagen and shell outer diameter respectively. (b) – (d) representative light microscopy images of scaffolds in culture media showing collagen and shell diameters. Numbers within figures represent flow rates in ml/min. Data points represent mean \pm SD (n =3). Scale bars = 400 μ m.

It is evident in Figure 4-11 (a) that an increase in flow rate magnitude at a constant flow rate ratio leads to an increase in both the collagen filament and alginate shell diameter. The baseline collagen filament diameter at 0.1 ml/min was $353.7 \pm 19.6 \mu\text{m}$, this significantly increased ($p < 0.001$) to $475.0 \pm 21.0 \mu\text{m}$ with a five-fold increase at 0.5 ml/min. There was also a significant increase ($p < 0.001$) of the collagen diameter when increasing the baseline flowrate up to 1.0 ml/min, the collagen filament diameter further increased to $517.0 \pm 9.5 \mu\text{m}$ at 0.5 ml/min.

The same statistical trends are observed for the alginate shell diameter. At 0.1 ml/min the shell diameter is $578.0 \pm 33.0 \mu\text{m}$, this significantly increases when comparing to both the 0.5 ($p < 0.01$) and 1.0 ml/min ($p < 0.001$) cases, with a maximum of $851.0 \pm 40.7 \mu\text{m}$ recorded for the 1.0 ml/min case. The alginate shell diameter is also suspected to start to plateau at flow rates greater than 0.5 ml/min as there are no statistically significant differences observed between these two measurements. Given this data, it can be concluded that the flow rate magnitude has a significant effect on the resulting coaxial extruded collagen filament and alginate shell diameters. This observation may be due to the need to maintain continuity, where larger flow rates here are transiently distributing larger volumes of material across a fixed cross-sectional area (the nozzle outlet). This leads to the deposition of a greater volume of material within a fixed space, the consequence of which leads to a greater filament and shell diameter.

4.5.5. Effect of changing collagen concentration

On analysis of the work of by Chieh et al. [32], whereby MSC and bone marrow-derived stromal cells were embedded in collagen constructs and their transient degradation times were studied over time, it was demonstrated that lower collagen construct concentrations resulted in a more rapid cell-mediated collagen contraction. It therefore became a focus of study to assess if a reduction in collagen concentration would lead to significantly lower filament diameters without the presence of cells. Filaments were extruded using 1.0 mg/ml collagen ($\pm 0.15\%$) and compared to previous results using 3.0 mg/ml collagen, over a 21-day period of incubation. The flow rates used in this experiment were 0.1/0.4 ml/min ($Q_c/Q_s = 1:4$).

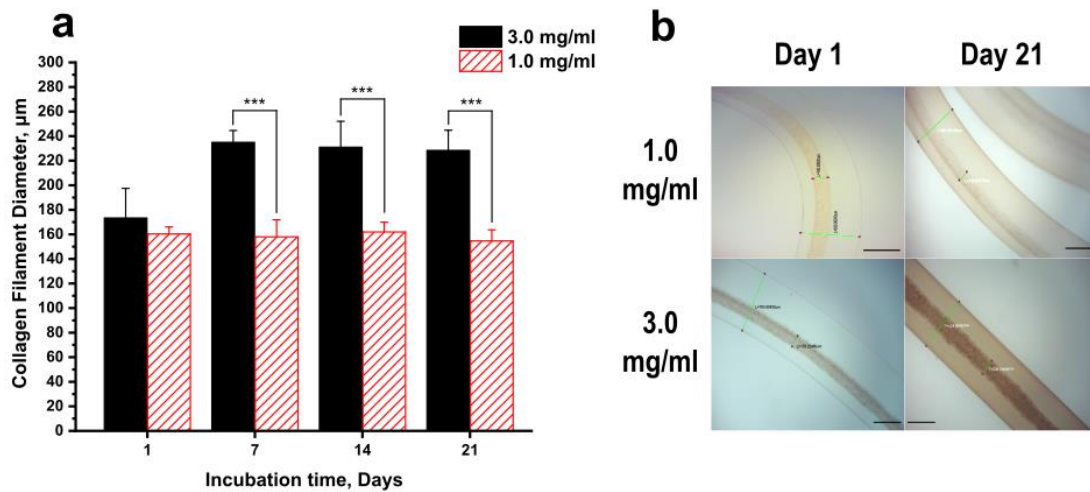


Figure 4-12. Effect of changing core collagen concentration on (a) extruded collagen filament diameter within the alginate shell using $Q_c/Q_s = 0.1/0.4$ ml/min and 3.0 mg/ml. (b) representative light microscopy images of filaments on days 1 and 21 of incubation using both 1.0 and 3.0 mg/ml collagen in the core of the coaxial nozzle. Data points represent mean \pm SD ($n = 3$). Scale bars = 400 μ m.

On analysis of Figure 4-12 (a), it is clear that there is a major effect of collagen concentration on collagen filament diameter from day 7 onwards using $Q_c/Q_s = 0.1/0.4$ ml/min. There was no significance recorded between each collagen concentration at day 1, however, there was major statistical significance found ($p < 0.001$) between the two collagen concentrations used for days 7, 14 and 21, this indicates that the difference in collagen diameter becomes significant between days 1 and 7. The day 7-21 average collagen filament diameter for 3.0 mg/ml collagen was 231.4 ± 14.5 μ m; the 1.0 mg/ml equivalent was 31.6% lower, at 158.2 ± 9.7 μ m. The apparent fact that a lower collagen concentration leads to a finer collagen filament using the given flow rates was used in further experiments, which were aimed at achieving fine diameter collagen and cell filament extrusion experiments.

Furthermore, the apparent significant difference between filament diameters for the 3.0 mg/ml case, between days 1 and 7, is assumed to be the result of using a small sample size ($n = 3$), leading to a poor understanding of the distribution of data. Given that no significant differences were observed for the 1.0 mg/ml case, it is predicted that repeating this work with a larger sample size would lead to no significant differences in collagen filament diameter between each time point for the 3.0 mg/ml case.

4.5.6. Combining flow rate and collagen concentration effects

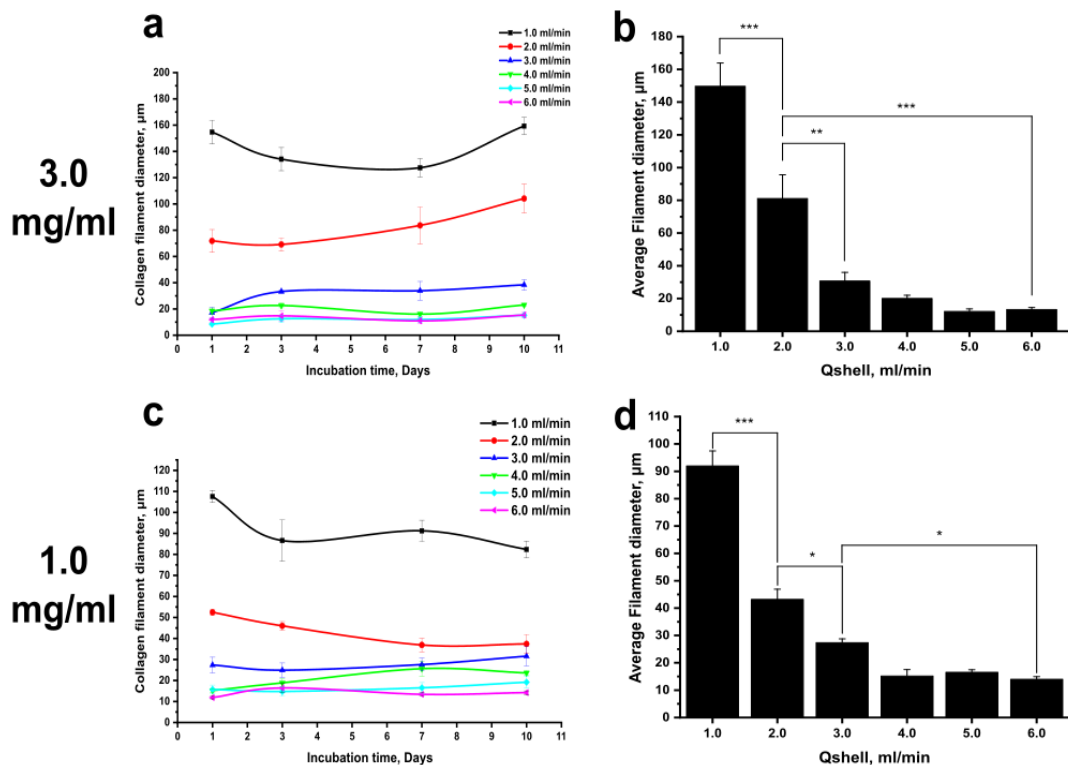
To combine the effect of reducing the core/shell flow rate ratio with the reduction of the collagen concentration, a ten-day experiment was devised whereby the core/shell flow rate ratio and collagen concentrations were manipulated and studied in tandem.

The core collagen flow rate, Q_c , was maintained at 0.1 ml/min whilst Q_s ranged from 1.0 ml/min to 6.0 ml/min, in increments of 1.0 ml/min. Collagen solution concentrations of 1.0 and 3.0 mg/ml were used to allow a comparison between collagen concentrations.

It should be noted that due to issues with media-induced scaffold degradation on long-term incubation in MEM- α (minimum essential medium) culture medium, secondary BaCl₂ cross-linking was employed.

Tabriz et al. [24] utilised 2 minutes of 60 mM BaCl₂ following 10 minutes of 100 mM CaCl₂ cross-linking to extend the stability of 4% (w/v) alginate lattice structures from 3 days to 11 days.

On that basis, the following experiment utilised secondary cross-linking with 50 mM BaCl₂ for 2 minutes following 5 minutes of primary cross-linking using 100 mM CaCl₂. These conditions were implemented in this experiment in order to increase the life of alginate scaffolds prior to media-induced degradation, whereby scaffolds would collapse on attempted pickup using forceps.



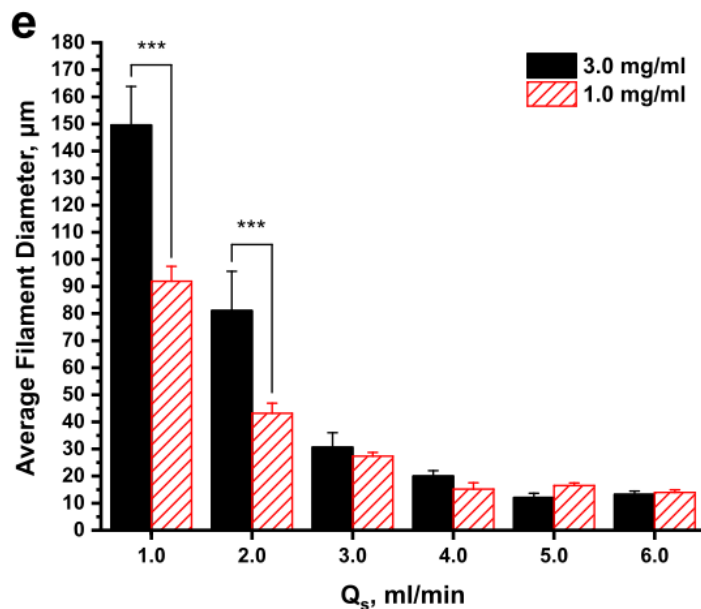


Figure 4-13. Effect of shell flow rate and collagen concentration on coaxially extruded core collagen filament diameter within 2.0 % alginate shell cross-linked using 100 mM CaCl₂ for 5 minutes and subsequently cross-linked using 50 mM BaCl₂ for 2 minutes. Q_c = 0.1 ml/min. Average collagen filament diameter over the ten-day experimental period for each Q_s using (a) 3.0 mg/ml collagen, (c) 1.0 mg/ml. Ten-day average filament diameter for each Q_s using (b) 3.0 mg/ml collagen (d) 1.0 mg/ml. (e) Comparison of average filament diameters at each Q_s using collagen concentrations of 1.0 and 3.0 mg/ml. Data points represent mean ± SE (standard error) (n = 3 for (a), (c) and (e); n = 4 for (b) and (d)).

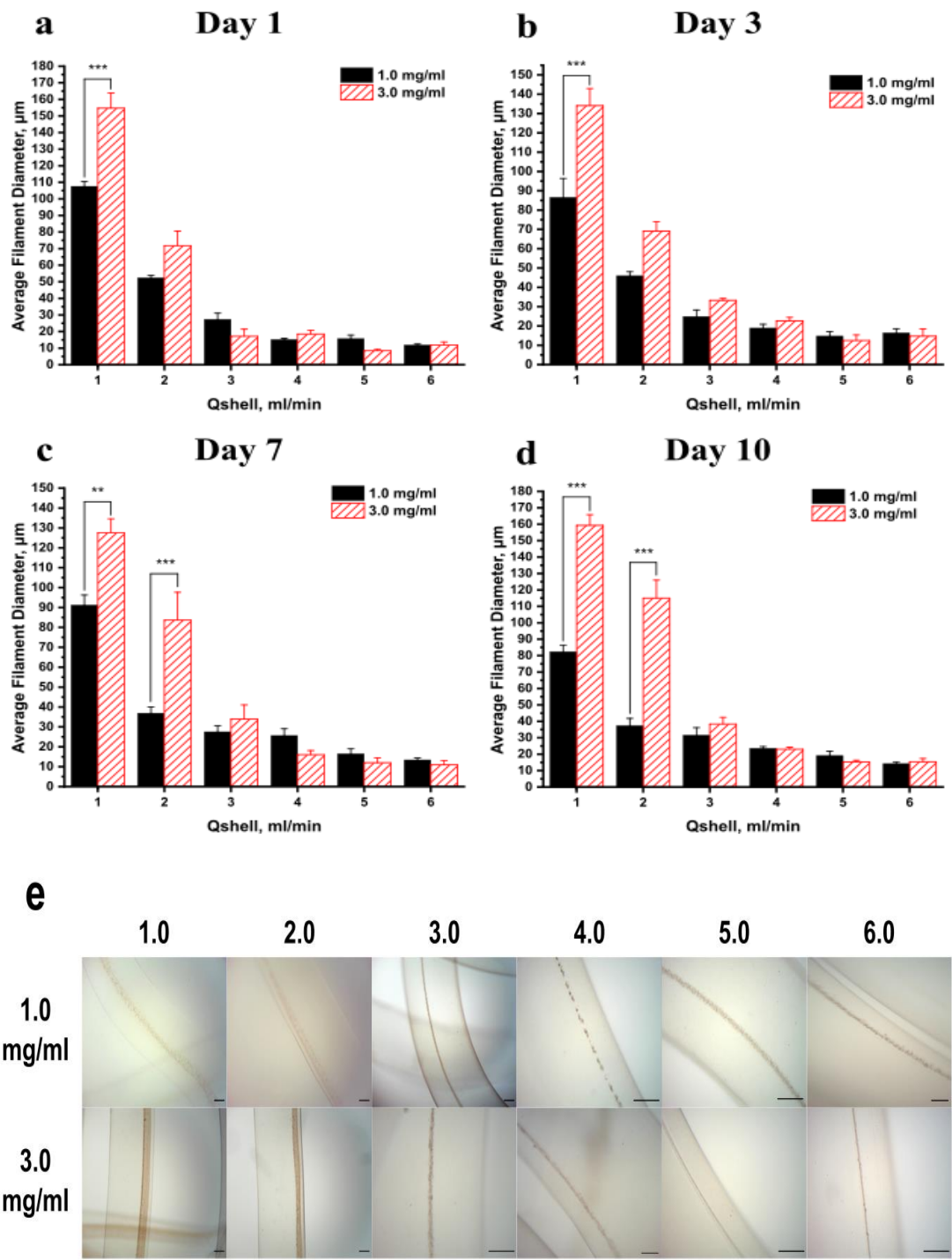
On analysis of Figure 4-13, significant differences in average collagen filament diameter were found on an increase of Q_s from 1.0 to 6.0 ml/min, in increments of 1.0 ml/min, corresponding to a reduction in the core/shell flow rate ratio from 1:10 to 1:60, using both collagen concentrations of 1.0 and 3.0 mg/ml.

With the 3.0 mg/ml case in Figure 4-13 (a), the largest observed filament diameter was 154.7 ± 9.1 µm, recorded on day 1 for the Q_s = 1.0 ml/min case, whilst the smallest observed filament diameter was measured at 8.5 ± 0.7 µm (See Figure 4-14 (f)), using Q_s = 5.0 ml/min on day 1, thus highlighting the significant effect of Q_s on the resulting average collagen filament diameter. In reference to Figure 4-13 (b), it can be seen that there is a statistically significant reduction (p < 0.01, one-way ANOVA with Tukey's post hoc test) in the ten-day average collagen filament diameter when reducing Q_s from 1.0 to 3.0 ml/min, whereby the average filament diameter reduces from 143.9 ± 8.9 µm at Q_s = 1.0 ml/min to 30.7 ± 5.4 µm at Q_s = 3.0 ml/min. In addition, the average diameter reduction effect began to lose statistical significance on the transition of Q_s from 3.0 to 4.0 ml/min, characterised by the plateauing of the 10-day average filament diameter from 4.0 to 6.0 ml/min, where the average filament diameter ranged from 20.0 ± 1.9 µm at 4.0 ml/min to 13.2 ± 1.2 µm with Q_s = 6.0 ml/min.

With regards to the 1.0 mg/ml case, presented in Figure 4-13 (c), the largest filament diameter was again found on day 1 for the 1.0 ml/min experiment, at $91.9 \pm 5.5 \mu\text{m}$, whilst the smallest diameter was found using $Q_s = 6.0 \text{ ml/min}$, at $11.9 \pm 0.6 \mu\text{m}$ on day 1. The plateau effect of the ten-day average filament diameter observed with 3.0 mg/ml was also found with 1.0 mg/ml collagen, as is presented in Figure 4-13 (d), the effect was also observed on the transition from $Q_s = 3.0$ and 4.0 ml/min . The ten-day average collagen filament diameter ranged from $15.2 \pm 2.3 \mu\text{m}$ with $Q_s = 4.0 \text{ ml/min}$ to $14.0 \pm 1.0 \mu\text{m}$ using $Q_s = 6.0 \text{ ml/min}$.

This data suggests that the significant effect of reducing the average collagen filament diameter diminishes once Q_s exceeds 3.0 ml/min , for both collagen concentrations tested here, leading to a plateauing of the resulting average filament diameter. It is predicted that this plateauing effect is a result of the core collagen flow velocity peaking, as a result of the core acceleration effect caused by the transfer of momentum from the shell alginate stream to the core collagen stream.

On comparison of the ten-day average collagen filament diameter between the two utilised collagen concentrations, 1.0 and 3.0 mg/ml, Figure 4-13 (e) highlights that the diameter of the 1.0 mg/ml case was significantly lower than of the 3.0 mg/ml scenario, in a statistical manner ($p < 0.001$), using $Q_s = 1.0$ and 2.0 ml/min . Due to the aforementioned plateau effect, this significant difference was eliminated due to the convergence of the filament diameters when $Q_s \geq 3.0 \text{ ml/min}$.



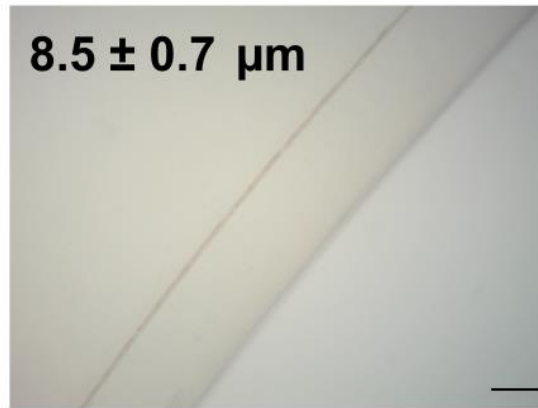
f

Figure 4-14. Effect of collagen concentration (1.0, 3.0 mg/ml) on coaxially extruded core collagen filament diameter on (a) day 1, (b) day 3, (c) day 7, (d) day 10, within 2.0 % alginate shell cross-linked using 100 mM CaCl_2 for 5 minutes and subsequently cross-linked using 50 mM BaCl_2 for 2 minutes. $Q_c = 0.1$ ml/min; $Q_s = 1.0$ to 6.0 ml/min. (e) Representative light microscopy images on day 1 of incubation in culture medium, illustrating narrowing of collagen filaments with increases in Q_s , (f) Light microscopy image showing sub-10 μm collagen filament using 3.0 mg/ml collagen, $Q_c = 0.1$ and $Q_s = 5.0$ ml/min on day 1 of incubation in culture medium. Scale bars = 100 μm . Data points represent mean \pm SE ($n = 3$).

On analysis of the individual time point data displayed in Figure 4-14, comparisons of average filament diameters between each collagen concentration have revealed a constant statistically significant difference ($p < 0.01$) unique to use of the lowest tested Q_s of 1.0 ml/min for all four analysed time intervals (day 1 to day 10). This data indicates that a simple reduction in collagen concentration, from 3.0 to 1.0 mg/ml, results in significantly smaller filament diameters across a ten-day study. A further significant difference was observed for the 2.0 ml/min case, however, this was only observed on days 7 and 10 ($p < 0.001$)

This reduction in filament diameter at lower collagen concentrations may be due to lower collagen concentrations containing lower masses of collagen in an equivalent volume of solution, which allows greater observed filament narrowing as a result of core solution acceleration through transfer of momentum from the faster outer shell solution within the coaxial nozzle setup. In addition, the significant effect of core narrowing may be absent at higher Q_s values due to the shell-to-core solution transfer of momentum effect plateauing. It is predicted that comparatively smaller filament diameters may be observed for collagen concentrations lower than 1.0 mg/ml, however, the concentration must remain sufficient to facilitate filament formation and to prevent filament breakup whilst trying to manipulate filaments, using forceps for example.

In summary, it has been demonstrated that reducing the core/shell flow rate ratio when coaxially extruding collagen filaments in the core of cross-linked alginate shells, leads to the reduction of the average filament diameter until the filament diameter reaches a minimum (at $Q_s = 4.0$ ml/min here) as a result of the limitations of shell-to-core momentum transfer, an effect seen for both collagen concentrations of 1.0 and 3.0 mg/ml. In addition, significant differences were seen between the ten-day average filament diameter on manipulation of the concentration of collagen, between 1.0 and 3.0 mg/ml, until Q_s reached a threshold value of 3.0 ml/min, on the advent of the aforementioned plateauing of filament diameter.

On analysis of the time point filament diameter data, significant differences between collagen concentrations were only observed for $Q_s = 1.0$ ml/min for all time points (day 1, 3, 7, 10), indicating that the significant difference found with the ten-day average diameter of the 2.0 ml/min case was a consequence of significant differences found between collagen concentrations on days 7 and 10, therefore demonstrating a limited application when $Q_s > 2.0$ ml/min.

Therefore, the effect of reducing the collagen concentration from 3.0 to 1.0 mg/ml to significantly reduce the average collagen filament diameter may only be applied in a limited manner, where $Q_s < 2.0$ ml/min for the conditions used here.

4.5.7. Validation of theoretical equation for coaxial diameters

To analyse the validity of the theoretical relationship between the inlet coaxial flow rates and the resulting core and shell filament diameters presented in Equation 4.26, a comparison was made between theoretical and experimental data.

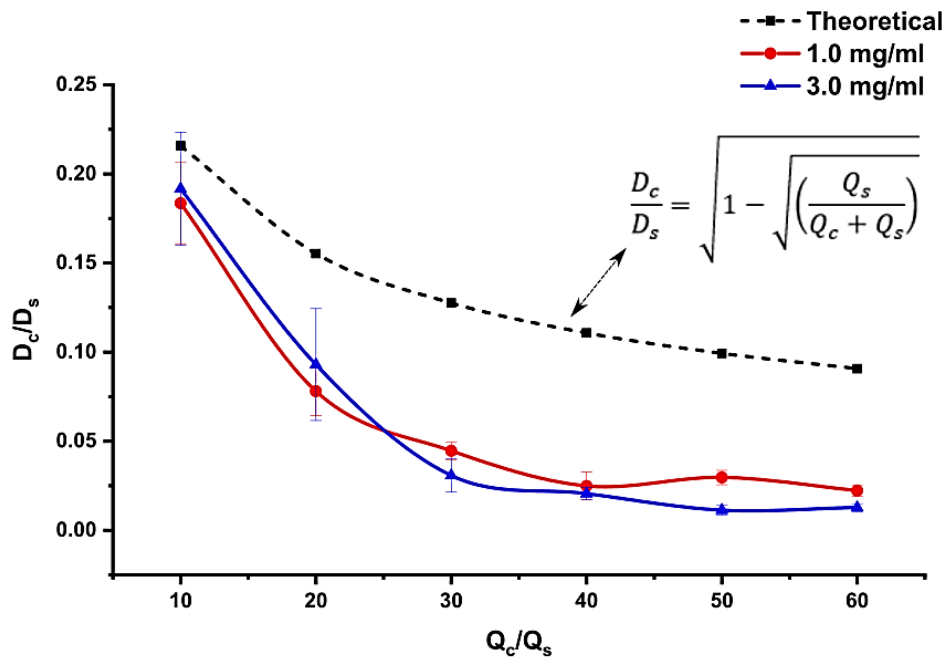


Figure 4-15. Relationship between coaxial diameter ratio (D_c/D_s) and flow rate ratios (Q_c/Q_s), with experimental data for 1.0 and 3.0 mg/ml collagen core solutions plotted alongside theoretical data. Alginate cross-linking was achieved by primary cross-linking using 100 mM CaCl_2 for 5 minutes, followed by secondary cross-linking using 50 mM BaCl_2 for 2 minutes. Data points represent mean \pm SD ($n = 3$).

On study of Figure 4-15, it is clear that the two experimental conditions followed the inverse relationship between the coaxial diameter and flow rate ratios, as is dictated by the theoretical equation. However, the two experimental plots deviated from the idealised theoretical equation, largely due to simplification of the Navier-Stokes equations in order to provide a solvable solution.

Major assumptions which would have resulted in this experimental deviation include the assumption that the fluid is Newtonian (viscosity is independent of shear rate), the fluid is flowing at steady state (flow rate in = flow rate out), the effects of gravity are negligible and there are no radial or angular forces acting on the fluid. In this case, collagen solutions are non-Newtonian fluids and steady state through the nozzle may not have been achieved, however this was not verified. Moreover, gravity, radial and angular forces would have been present and acting on the fluid, thus affecting the nozzle outlet flow rates.

Further inaccuracies may also have presented by assuming negligible fluid viscosity, as the fluid flow rate may be retarded to various degrees by viscosity effects, depending on the chosen material.

Furthermore, alginate cross-linking effects would also have had an effect on alginate flow rate due to the increase in flow-hindering viscosity caused by the cross-linking process and it has been shown in this chapter that cross-linking conditions have an effect on alginate shell diameter, therefore having an effect on D_c/D_s . Finally, the ability of fluids to diffuse at the phase interface in the transverse plain may also have had an effect on resulting coaxial diameters.

As has previously been discussed in section 4.5.6, the two experimental plots, for 1.0 and 3.0 mg/ml collagen filaments, largely stayed statistically similar, this suggests that the differences between these two concentrations of collagen have negligible effects on filament diameter ratios for the given flow rate ratio range. Future investigations on the effect of fluid physical properties, such as density and viscosity, on the resulting extruded filament and shell diameters may allow refinement of the theoretical equation and may provide an informed empirical equation to more accurately predict filament and shell diameters based on the chosen fluid(s) physical properties.

4.6. Alginate shell tuning

This section details the effects of changing various parameters on the resulting extruded alginate shell diameter and wall thickness. The tested parameters include the core/shell flow rate ratio and various cross-linking conditions, namely cation type, concentration and exposure time. A final section provides insight on the requirements for alginate degradation using chelation agents.

The significance of this work lies in the need to limit the alginate shell diameter and wall thickness for tissue engineering applications, as this will have an impact on nutrient and waste diffusion upon seeding collagen extrusion solutions with cells for tissue engineering purposes. It is imperative that shell walls are of an adequate thickness (less than 100 – 200 μm) to facilitate unhindered material transport [33] [34].

4.6.1. Effect of flow rate ratio on alginate shell diameter

The work presented in section 4.5 led to the conclusion that reducing Q_c/Q_s lead to a smaller collagen filament diameter within the cross-linked calcium alginate shell. It is also important to investigate the effect of manipulating this flow rate ratio on both the alginate shell diameter and shell wall thickness for future tissue engineering purposes.

For the following experiment, Q_c was maintained at 0.1 ml/min whilst Q_s ranged from 0.1 to 2.0 ml/min, hence Q_c/Q_s ranged from 1:1 to 1:20.

Extruded filaments were incubated and imaged whilst still in culture media over a seven-day period. The hypothesis, according to the theory, was that as Q_c/Q_s increased (with a corresponding decrease in alginate flow velocity with respect to collagen in the core).

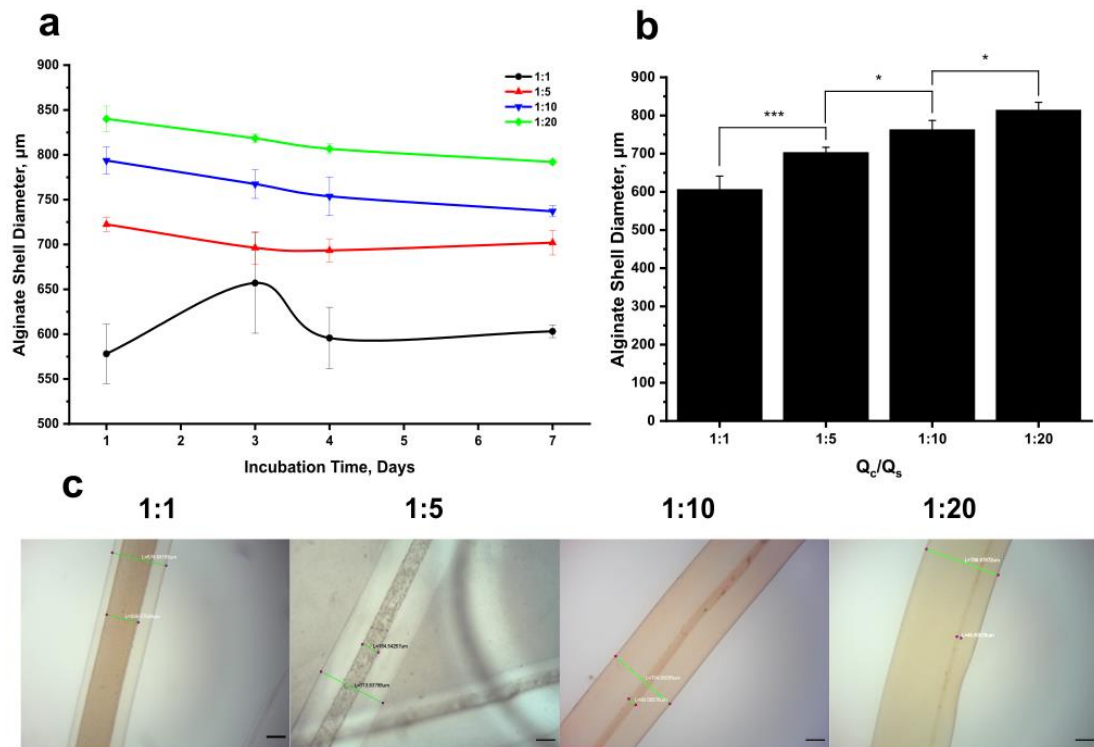


Figure 4-16. (a) Effect of changing Q_c/Q_s on alginate shell outer diameter, (b) seven-day average shell diameter for corresponding Q_c/Q_s values, (c) representative light microscopy images of alginate-shelled scaffolds containing 3.0 mg/ml collagen cores, illustrating the increasing of shell (and collagen filament) diameter with respective decreases in Q_c/Q_s . Data points represent mean \pm SD ($n = 3$). Scale bars = 200 μm .

It can be seen from Figure 4-16 (a) that decreasing Q_c/Q_s does indeed lead to a significantly larger alginate shell outer diameter. With reference to Figure 4-16 (b), there was statistical significance exhibited between the average alginate shell diameter for all data series tested ($p < 0.05$, one-way ANOVA test with Tukey's post hoc test). The average shell diameter ranged from an average of $606.67 \pm 34.6 \mu\text{m}$ at a flow rate ratio of 1:1 to a significantly higher value of $814.25 \pm 20.3 \mu\text{m}$ when Q_c/Q_s was reduced down to 1:20 ($p < 0.001$). Given this evidence, it was concluded that a smaller Q_c/Q_s results in a greater alginate shell diameter for the range provided in Figure 4-16. It is assumed that this trend would continue until a maximum shell diameter is achieved, limited by nozzle diameter and crosslinking-induced swelling.

To find the maximal alginate shell diameter on increasing Q_s further than the previously-tested 1:20 Q_c/Q_s ratio, the range was extended up to 1:60, by fixing Q_c at 0.1 ml/min and testing Q_s between 0.1 ml/min and 6.0 ml/min, with the addition of combined Ca^{2+} and Ba^{2+} cross-linking (5 minutes, 100 mM $CaCl_2$ followed by 2 minutes, 50 mM $BaCl_2$). The effect of shell flow rate on the alginate shell wall thickness was also investigated. It should be noted that there may be an effect of changing Q_c , whereby the maximal shell diameter may be found in a later experiment, using a value other than 0.1 ml/min.

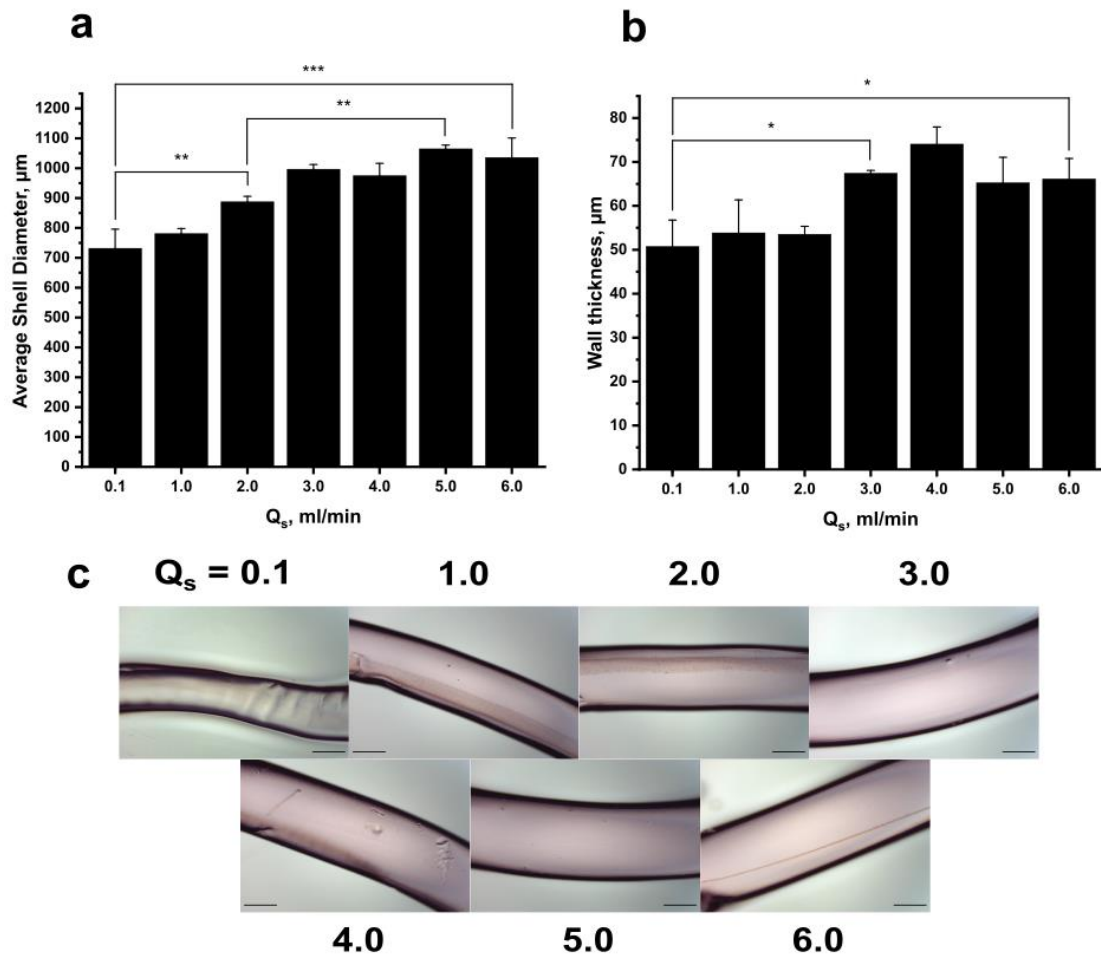


Figure 4-17. Effect of increasing Q_s on coaxial extruded 2% (w/v) alginate shell day 1 (a) outer diameter and (b) wall thickness using a 100 mM $CaCl_2$ cross-linking bath for 5 minutes followed by secondary cross-linking using 50 mM $BaCl_2$ for 2 minutes. $Q_c = 0.1$ ml/min with 3.0 mg/ml collagen solution. (c) representative light microscopy images of alginate shells for each respective Q_s , (shell walls in black). Data points represent mean \pm SD ($n = 3$). Scale bars = 400 μ m.

As can be seen from Figure 4-17 (a), the significant enlarging of the shell outer diameter is again seen on increasing Q_s from 0.1 to 2.0 ml/min ($Q_c/Q_s = 1:1$ to 1:20), whereby the diameter increased from $731.9 \pm 63.9 \mu$ m to $887.4 \pm 18.4 \mu$ m ($p < 0.01$).

A further significant increase in shell diameter can be seen when increasing Q_s from 2.0 to 5.0 ml/min ($p < 0.01$), with the shell diameter reaching $1064.6 \pm 12.9 \mu\text{m}$ at 5.0 ml/min. It is assumed that this increase in diameter is a result of the need to maintain continuity, caused by the higher flow velocity, therefore the shell diameter is consequently larger due to the greater volume of alginate being expelled from the nozzle.

On comparing the diameters between the 3.0 and 6.0 ml/min cases, it is evident that the shell diameter has plateaued, emphasised by the lack of statistical significance between these four groups. At this stage, it is assumed that the shell alginate stream has reached its maximal diameter, limited by the nozzle diameter.

On analysis of Figure 4-17 (b), there is also a significant effect of increasing Q_s on the alginate shell wall thickness. On increasing Q_s from 0.1 to 3.0, there is a corresponding significant increase ($p < 0.05$) of the wall thickness, from $50.8 \pm 6.0 \mu\text{m}$ to $67.5 \pm 0.6 \mu\text{m}$. Again, this significant increase in wall thickness appears to have peaked between 3.0 and 6.0 ml/min, this is due to wall thickness being a further parameter which is intrinsically linked to Q_s and of the need to maintain continuity on flow rate increases. Interestingly, the magnitude of all alginate shell wall thicknesses for all Q_s was $< 80.0 \mu\text{m}$, indicating that diffusion of nutrients and waste should not be limited in future cell seeding experiments.

In summary, it has been demonstrated that there is a significant effect of the shell alginate flow rate on the resulting alginate shell diameter and wall thickness upon coaxial extrusion into a CaCl_2 cross-linking bath (100 mM, 5 min) with further BaCl_2 (50 mM, 2 min) cross-linking. The alginate shell diameter and wall thickness significantly increased on corresponding increases of Q_s from 0.1 to 3.0 ml/min, with further increases to Q_s , up to 6.0 ml/min, not returning further statistically significant increases. It should be noted here that future work could investigate the effect of Q_c on alginate shell diameter and wall thickness by fixing Q_s and modifying Q_c across a similar Q_c/Q_s range as drag or momentum-based interactions between the core and shell fluid may be present.

4.6.2. Effects of cross-linking time

Similar to section 4.5.2, whereby the effect of post-extrusion cross-linking time with 100 mM CaCl_2 on the diameter of extruded collagen filaments in the core of the tubular alginate scaffolds was investigated, this section is focussed on analysing the effect of cross-linking time on the diameter and wall thickness of the alginate shell.

It was suspected that a longer cross-linking time would lead to a reduced alginate shell outer diameter and wall thickness, due to an increase in alginate exposure to Ca^{2+} ions leading to a greater degree of cross-linking, bringing alginate chains in closer proximity, thus leading to a closer-packed structure with a reduced capacity to swell in volume.

Alginate-collagen scaffolds were extruded at a Q_c/Q_s of 1:4 (0.05/0.20 ml/min) into a 100 mM CaCl_2 cross-linking bath and either removed immediately post-extrusion (0 min) or allowed to further crosslink for five or ten minutes. These extrusions were subsequently drained and imaged using light microscopy to record the shell OD and ID. Wall thickness was calculated as half of the difference between OD and ID.

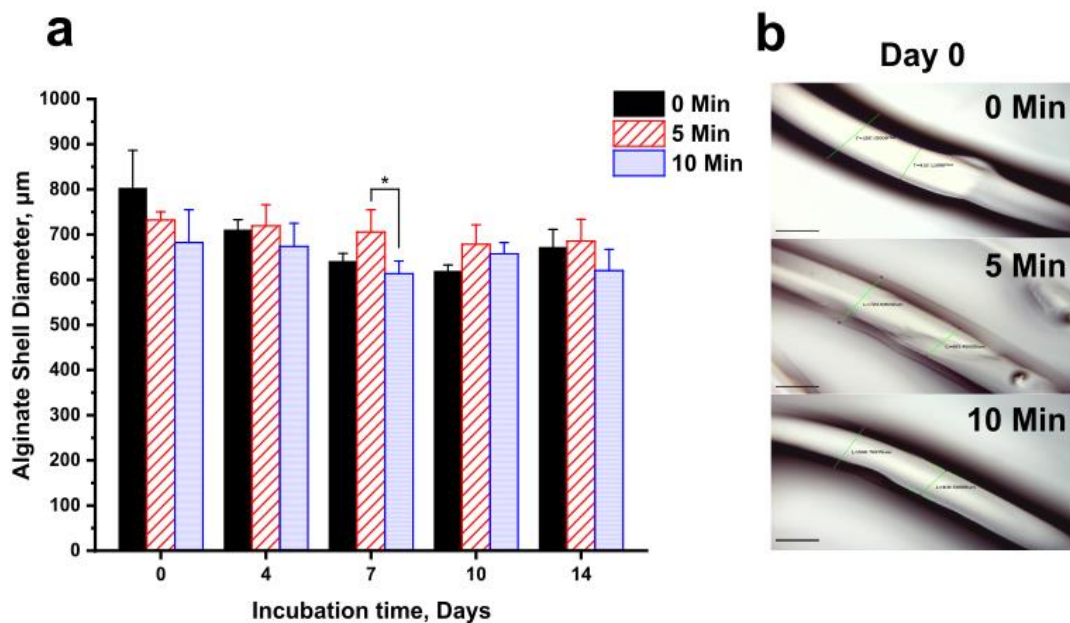


Figure 4-18. (a) Effect of post-extrusion cross-linking time using 100 mM CaCl_2 on alginate shell outer diameter at $Q_c/Q_s = 1:4$ (with 3.0 mg/ml collagen cores). (b) representative day 0 (post-extrusion) light microscopy images showing coaxial alginate scaffold outer and internal diameters for each cross-linking time condition. Data points represent mean \pm SD ($n = 3$). Scale bars = 400 μm .

On analysis of Figure 4-18 (a), the dominant observation was that there was almost no statistically significant contribution of post-extrusion crosslinking time using 100 mM CaCl_2 on alginate shell diameter, with the diameter ranging from $613.33 \pm 28.1 \mu\text{m}$ for day 7 of the 10-min case to $803.0 \pm 28.1 \mu\text{m}$ on day 0 with 0 min post-extrusion cross-linking.

The only statistically significant difference was found at day 7, between 5 and 10 minutes of cross-linking ($p < 0.05$).

However, given that this finding was the only outlier, the overarching conclusion drawn from this experiment was that up to 10 minutes of post-extrusion crosslinking with 100 mM CaCl₂ has no effect on the resulting alginate shell diameter over a 14-day incubation period in culture media. This data emphasises the rapid cross-linking nature of alginate in that the alginate shell diameter appears to be unaffected by cross-linking time and seems to be determined by the flow rate of alginate in the shell nozzle and the initial contact of alginate with the cross-linking bath when initiating extrusion, as has been previously described.

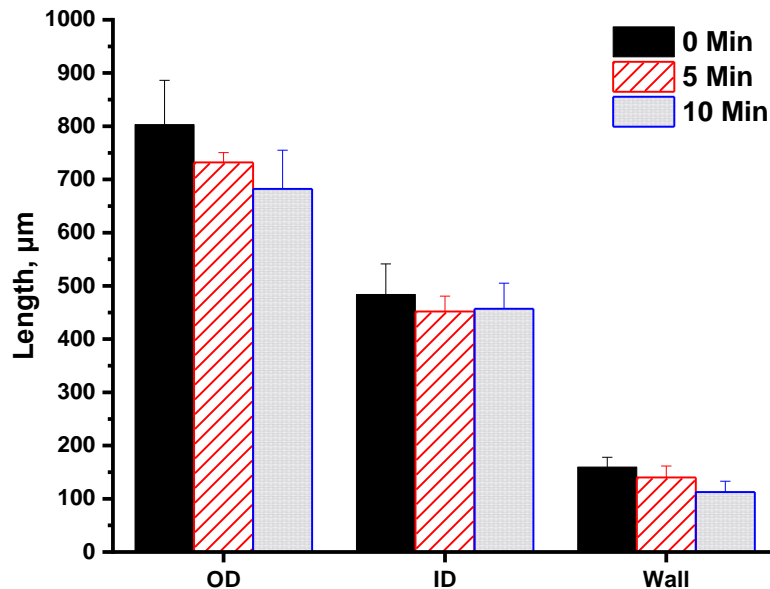


Figure 4-19. Post-extrusion (day 0) alginate shell characteristic lengths when $Q_c/Q_s = 1:4$, including calculated wall thickness for three cross-linking times using 100 mM CaCl₂. Data points represent mean \pm SD (n=3). Note: OD = outer diameter; ID = internal diameter.

Figure 4-19 illustrates the characteristic post-extrusion (day 0) dimensions recorded for each experimental condition and also includes the calculated shell wall thickness. Statistical analysis on calculated wall thicknesses revealed no significant differences between the three cross-linking times used here ($p > 0.05$). This suggests that wall thickness remains unaffected by CaCl₂ concentration due to the alginate shell swelling in an omnidirectional manner, thus whilst the outer and internal diameters change, the wall thickness remains unchanged. However, the mean wall thickness did reduce from $159.5 \pm 18.6 \mu\text{m}$ at 0 min to $112.7 \pm 20.5 \mu\text{m}$ for the 10 min experiment, a reduction of 29.4%.

This preliminary data suggests that cross-linking time with 100 mM CaCl₂ does not have a significant effect on alginate shell wall thickness, however, further experimentation is advised to provide a definite conclusion on this matter, data for following days of incubation in culture media is required to analyse shell reaction to culture media.

4.6.3. Effect of cross-linking bath concentration

The effect of the concentration of the CaCl₂ cross-linking bath on the resulting alginate shell diameter was studied. The aim was to reduce bath concentration from the initial 100 mM CaCl₂ to find the minimal concentration which could extrude alginate tubes with sufficient mechanical strength to be handled without collapsing under their own weight.

Firstly, a study was performed whereby hollow alginate tubes (100 mM CaCl₂ core; 2.0% w/v alginate shell) were extruded at incrementally lower bath concentrations of CaCl₂. The core/shell flow rate ratio (Q_c/Q_s) was set at 1:4 (0.05/0.20 ml/min). This study found that the minimal required concentration was between 25 mM (failed) and 50 mM (succeeded). A subsequent study then extruded tubes at three different concentrations of CaCl₂ (50, 75 and 100 mM, all $\pm 9.0 \mu\text{M}$) and aimed to analyse if there was any significant effect of bath concentration on alginate shell diameter. Extrusion time was maintained at approximately twenty seconds per extrusion in order to control the crosslinking time; no post-extrusion cross-linking was employed. Shell diameter was analysed both immediately post-extrusion, after draining crosslinking CaCl₂ solution and washing with PBS in addition to after one day of incubation in cell culture media.

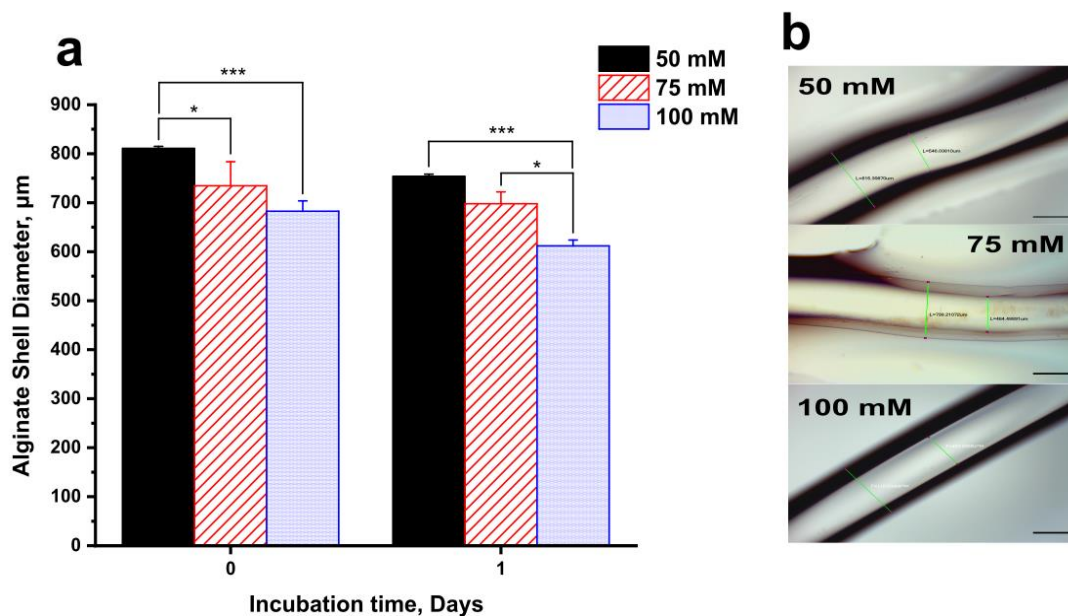


Figure 4-20. Effects of bath CaCl_2 concentration on resulting coaxial extruded alginate (a) shell outer diameter. $Q_c/Q_s = 0.05/0.20$ ml/min. (b) representative day 0 light microscopy images for each tested bath concentration. Data points represent mean \pm SD ($n = 3$). Scale bars = 400 μm .

It can be deduced from Figure 4-20 (a) that reducing the bath concentration results in a larger alginate shell diameter. At day 0, increasing the bath concentration from 50 to 100 mM results in a 15.8% reduction in shell diameter, from 811.0 ± 4.0 μm to 682.7 ± 21.1 μm . Similarly, there is an 18.8% reduction in diameter between the 50 mM and 100 mM cases (753.8 ± 4.5 μm to 612.0 ± 11.8 μm). Although there were some statistical differences observed when changing the bath concentration by 25 mM between the 50 and 75 mM cases on day 0 and also between the 75 and 100 mM cases at day 1 ($p < 0.05$), major differences ($p < 0.001$) were observed both post-extrusion and also on day 1 between the 50 and 100 mM cases.

These results indicate an inverse proportionality relationship between bath concentration and alginate shell outer diameter. When there is a higher concentration of CaCl_2 , there is a proportionally higher concentration of Ca^{2+} ions present, thus facilitating a higher degree of cross-linking between neighbouring alginate chains, resulting in a closer-packed and stiffer cross-linked three-dimensional hydrogel structure. It is known that increasing Ca^{2+} concentration when cross-linking alginate leads to a lower swelling ratio [35], as less water is absorbed to give a lower final alginate volume (or diameter in this case).

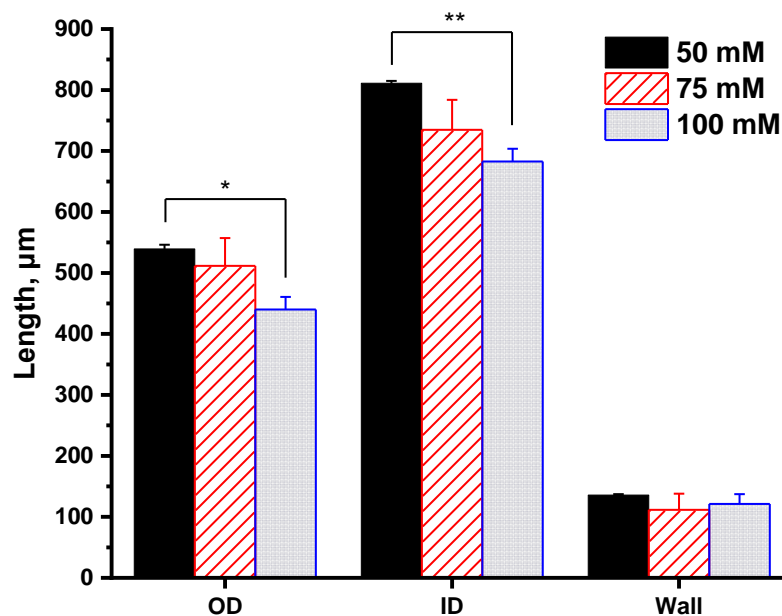


Figure 4-21. Post-extrusion (day 0) alginate shell characteristic lengths including calculated wall thickness for three cross-linking concentrations using CaCl_2 . Data points represent mean \pm SD ($n = 3$). Note: SD error bar for 50 mM wall is too minute to appear visible in image ($135.8 \pm 1.5 \mu\text{m}$).

The day 0 data displayed in Figure 4-20 has been expanded to also display internal diameter and calculated wall thickness for the three cross-linking concentrations utilised, as is shown in Figure 4-21. Besides the aforementioned outer diameter effects, similar expected statistically significant differences ($p < 0.01$) were found between 50 and 100 mM CaCl_2 for the internal diameter, expected as a result of less swelling with the higher concentration. There were no observed statistically significant differences between wall thicknesses, with these ranging from $111.5 \pm 26.6 \mu\text{m}$ with the 75 mM case to $135.8 \pm 1.5 \mu\text{m}$ when using the 50 mM bath. This may again be attributed to equal swelling of the outer and internal diameters, leading to a maintenance of the wall thickness for the given cross-linking concentrations. This leads to a provisional conclusion that crosslinking concentration using CaCl_2 does not affect the resulting alginate shell wall thickness.

4.6.4. Effect of cross-linking cation type

To provide an initial insight into the effect of various cross-linking conditions on the resulting post-extrusion (day 0) alginate shell diameter and wall thickness, an experiment was conducted using six different conditions, employing three different divalent cations (Ca^{2+} , Sr^{2+} and Ba^{2+}) for comparison. Both 5 and 10 minutes of cross-linking was employed using 100 mM CaCl_2 (5/10C) and SrCl_2 (5/10S) in addition to combining 5 minutes of 100 mM CaCl_2 cross-linking with secondary cross-linking using 2 minutes of 50 mM BaCl_2 (5C-2B) or 100 mM SrCl_2 (5C-2S).

It was suspected that the use of Sr^{2+} and Ba^{2+} would lead to comparatively smaller shell diameters and wall thicknesses due to the stronger affinity of alginate for these cations [36], thus having a stronger effect on alginate swelling to provide less water absorption, leading to shrinkage relative to the exclusive use of 100 mM Ca^{2+} .

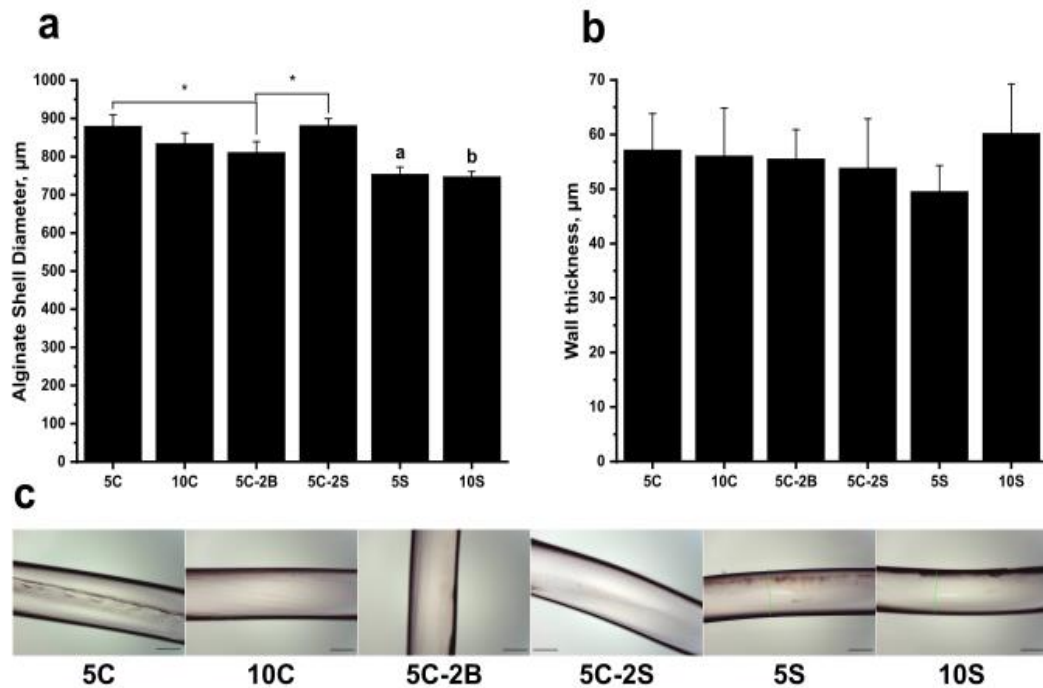


Figure 4-22. Effect of cross-linking conditions on coaxial post-extrusion (day 0) 2% alginate shell (with 3.0 mg/ml collagen cores) (a) diameter and (b) wall thickness. (c) representative light microscopy images for each corresponding cross-linking case. Note: ‘a’ represents statistical significance between 5S and 10C ($p < 0.05$), 5C and 5C-2S ($p < 0.001$); ‘b’ represents statistical significance between 10S and 5C-2B ($p < 0.05$), 10C ($p < 0.01$) and 5C, 5C-2S ($p < 0.001$). Acronyms: 5/10C = 5/10 minutes 100 mM CaCl_2 ; 5C-2B = 5 minutes 100 mM CaCl_2 + 2 minutes 50 mM BaCl_2 ; 5C-2S = 5 minutes 100 mM CaCl_2 + 2 minutes 100 mM SrCl_2 ; 5/10S = 5/10 minutes 100 mM SrCl_2 . Data represents mean \pm SD. Scale bars = 400 μm .

As can be derived from Figure 4-22 (a), there was a significant effect of cross-linking conditions on the resultant alginate shell diameter. The addition of secondary cross-linking using 50 mM BaCl_2 to 5 minutes of 100 mM CaCl_2 provided a significant reduction in shell diameter ($p < 0.05$), from $880.2 \pm 29.4 \mu\text{m}$ to $811.4 \pm 28.3 \mu\text{m}$. Moreover, it appears that using 2 minutes of 100 mM SrCl_2 provided a significantly larger diameter of $881.7 \pm 17.9 \mu\text{m}$ ($p < 0.05$) relative to the 5C-2B case, demonstrating the stronger affinity of Ba^{2+} ions to alginate in comparison to Sr^{2+} ions, even with a halved concentration of 50 mM.

Coaxial extrusion of alginate directly into a 100 mM SrCl_2 cross-linking bath provided the smallest shell diameters for all cases, with multiple statistically significant differences observed (see caption of Figure 4-22).

Interestingly, there was no significant difference between using 5 or 10 minutes of cross-linking time ($p > 0.05$) using the SrCl_2 bath, wherein the shell diameter for the 5S case was $754.7 \pm 17.7 \mu\text{m}$ whilst the 10S case displayed a similar average diameter of $747.9 \pm 13.0 \mu\text{m}$. As was expected, it is apparent that coaxial extrusion of alginate into a bath of SrCl_2 , as opposed to CaCl_2 , leads to a smaller diameter alginate shell due to the stronger ionic attraction between Sr^{2+} and alginate, which, according to theory, should be a more robust structure which may be more resistant to long-term degradation by various ions contained within cell culture media. On this basis, it is predicted that this diameter reduction effect may be further pronounced on the use of a 100 mM BaCl_2 cross-linking bath.

On statistical analysis of post-extrusion alginate shell wall thicknesses, there was no significant effect of cross-linking conditions on the resulting alginate shell wall thickness ($p > 0.05$), with thicknesses ranging from $49.6 \pm 4.7 \mu\text{m}$ for the 5S case to $60.3 \pm 9.0 \mu\text{m}$ with the 10S condition. All cases indicated favourable wall thicknesses for nutrient and waste diffusion for tissue engineering purposes. Given that the alginate shell diameter undergoes significant changes with the manipulation of the cross-linking conditions, this surprising result indicates that the wall thickness appears to be more determined by the coaxial nozzle diameter and flow rate and appears unaffected on post-extrusion analysis under a light microscope. However, further work is required to analyse the long-term effect of incubation on the respective wall thicknesses. It is suspected that alginate shells subjected to relatively weaker cross-linking conditions (5/10C) will degrade quicker when incubated in culture media, resulting in comparably smaller shell wall thicknesses over time when compared to the relatively stronger cross-linking cases using Sr^{2+} and Ba^{2+} .

In summary, it has been demonstrated that the implementation of Sr^{2+} and Ba^{2+} for alginate cross-linking, both exclusively but also in conjunction with primary CaCl_2 cross-linking, results in significant changes to the post-extrusion (day 0) cross-linked alginate shell diameter. As alginate has stronger affinities for Sr^{2+} and Ba^{2+} , in ascending order, these cations appear to have a greater effect on alginate swelling and absorb comparatively less water than CaCl_2 -only cross-linking due to tighter ionic bonding between neighbouring alginate chains. In addition, there was no statistically significant effect of cross-linking conditions on the post-extrusion alginate shell wall thickness. It is assumed that the wall thickness is largely determined by the shell coaxial nozzle diameter and the respective input flow rate.

To conclude, further work is required to analyse the long-term effects of incubation in cell culture media on the alginate shell diameter and wall thickness to inform future tissue engineering studies and associated alginate scaffold degradation studies.

4.6.5. Alginate degradation

A pivotal aspect of extrusion and culturing cell and tissue filaments in the core of hollow tubular hydrogel scaffolds is that of degradability. It is essential that scaffolds can be degraded rapidly and without any adverse toxicity effects caused by the chosen degradation chemical. Degradation can be performed partially or fully in vitro prior to in vivo studies. It is therefore imperative that the kinetics and toxicity of degradation treatments must be elucidated prior to implementation. The most common alginate degradation mechanism involves the cleavage of the ionic bonds between Ca^{2+} (and/or Sr^{2+} and Ba^{2+}) ions and alginate chains using ionic chelation, by means of either EDTA or sodium citrate. A second, less utilised, method is by degradation of glycosidic bonds within the alginate chains by enzymatic means, using the enzyme alginate lyase.

Studies were performed in order to determine suitable concentrations and exposure times of cross-linked alginate (100 mM bath, no post-extrusion cross-linking) to sodium citrate. Extruded collagen/alginate concentric tubular scaffolds were incubated for a specified time, culture media was drained, washed with PBS and subsequently exposed to sodium citrate at varying concentrations and observed for alginate dissolution over time in static conditions. Structures were observed with the naked eye and complete dissolution was determined when collagen structures could be observed adhering to the bottom of culture wells, indicating absence of any alginate shell. A key parameter to be accounted for in these experiments was shell wall thickness. Thicker walls were assumed to require a comparably longer dissolution time for a given concentration of the chosen dissolution chemical. The maximum wall thickness from all experiments never exceeded 200 μm .

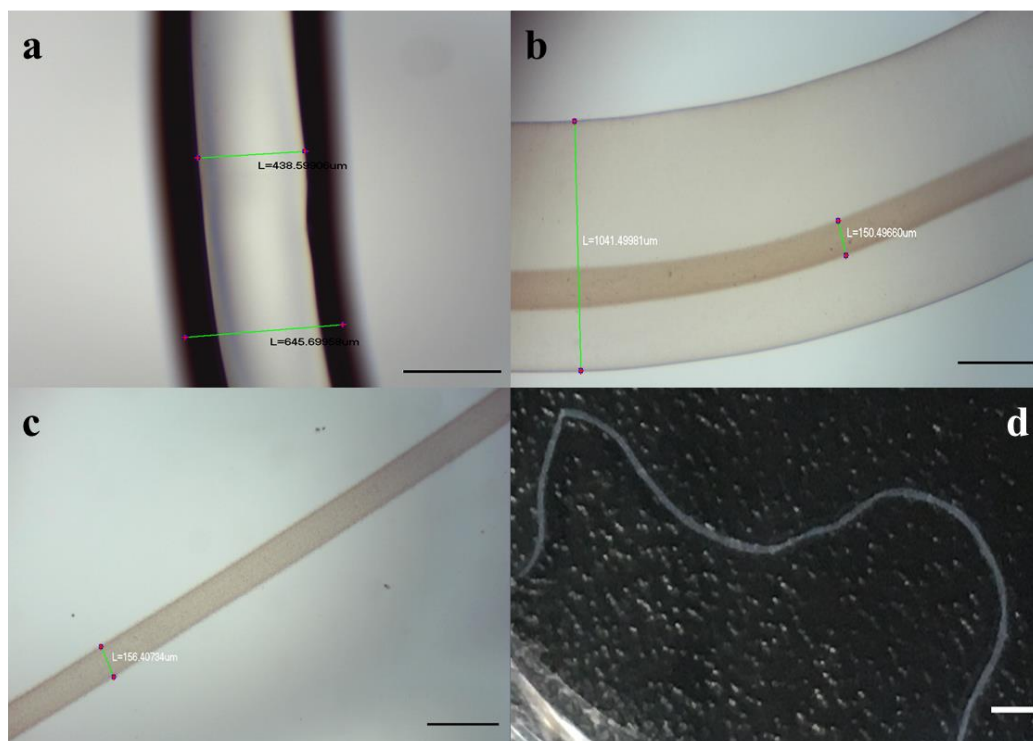


Figure 4-23. Light microscopy images illustrating the culture and degradation of collagen/alginate core/shell scaffolds which were not subjected to post-extrusion cross-linking using 100 mM CaCl₂. Flow ratio = 1:1 (0.1/0.1 ml/min for (a), 0.1/1.2 ml/min for all others). (a) post-extrusion scaffold showing alginate shell walls (collagen is in pre-gel state and thus does not appear under light microscopy). (b) collagen filament contained with alginate shell after one day of incubation in culture media. (c) collagen filament in media after degradation of alginate shell using 55 mM sodium citrate. (d) lone collagen filament pictured in bottom of drained culture well. Scale bars (a - c) = 400 μm; (d) = 1.0 mm.

With the use of sodium citrate to dissolve alginate shells of an average thickness of $159.3 \pm 26.8 \mu\text{m}$, 55 to 110 mM lead to a rapid alginate shell dissolution (<1 min) whilst using 27.5 mM lead to dissolution within two minutes. An example of the transition of collagen/alginate core/shell structures from post-extrusion to scaffold-free collagen filaments is shown in Figure 4-23. The result of dissolving calcium alginate in under one minute with the commonly-used concentration of 55 mM sodium citrate [37] was favourable for further in vitro studies, particularly to aide analyses of fine diameter scaffold-free cell and tissue filaments. A similar result (< 1 min degradation time) was obtained using concentrations in the range of 27.5 to 110 mM EDTA when degrading alginate shells with a comparable wall thickness of $159.5 \pm 18.6 \mu\text{m}$ (0.05/0.20 ml/min).

Both 55 mM sodium citrate and 27.5 mM EDTA are suitable for degrading the calcium alginate shells used here within one minute and the combination of low concentration and rapid exposure time should cause minimal toxicity to the cells used in further experiments (adipose-derived stem cells). A further option which may provide superior to single-chemical alginate degradation is the use of a combination of sodium citrate and EDTA, as has been demonstrated by Gaetani et al. [38] to isolate suspended human cardiac progenitor cells. A solution of 55 mM sodium citrate and 20 mM EDTA was used for 10 minutes to dissolve 5% alginate matrices cross-linked using 102 mM CaCl_2 for 5 to 10 min. No deleterious effects on cell morphology were reported, therefore it is assumed that this combination may be used for the extruded structures detailed here, which should be comparably swifter to degrade due to the lower alginate concentration used here.

It should be noted that alginate structures exposed to further post-extrusion cross-linking using 100 mM CaCl_2 or cross-linking using Sr^{2+} or Ba^{2+} ions may require comparably higher EDTA/sodium citrate concentrations in addition to longer degradation times due to the requirement for the degradation of a comparably higher number of inter-alginate ionic bonds with these cases; further studies are required in this regard.

4.7. Limitations of the coaxial extrusion process

As alginate is bio-inert, there is no capacity for cellular adhesion when solely using alginate as a scaffold material. In such cases where a bioactive shell is desired, there is scope to use RGD (Arginine-Glycine-Aspartic acid) modified alginate [39] [40] or to blend alginate with an additional bioactive material, such as GelMA [41] or fibrinogen [42] [43].

The concentrations of collagen used here (1.0 to 3.0 mg/ml) lead to mechanically-weak, non-physiologically-comparable extruded filaments [44]. These filaments fragment on manipulation using forceps and therefore will need to be mechanically-modified for transplantation purposes. Otherwise, higher collagen concentrations, which are more clinically-relevant, may be tested [45].

With respect to flow rate manipulation, further increase of the shell flow rate will lead to the failure to produce continuous collagen filaments, due to the acceleration of the core collagen stream causing excessive core velocities. Data from previous experiments were analysed to find the collagen/shell core/shell flow rate ratio which would show filament discontinuities using 1.0 and 3.0 mg/ml. The cross-linking parameters consisted of 5 minutes of 100 mM CaCl_2 followed by 2 minutes within 50 mM BaCl_2 .

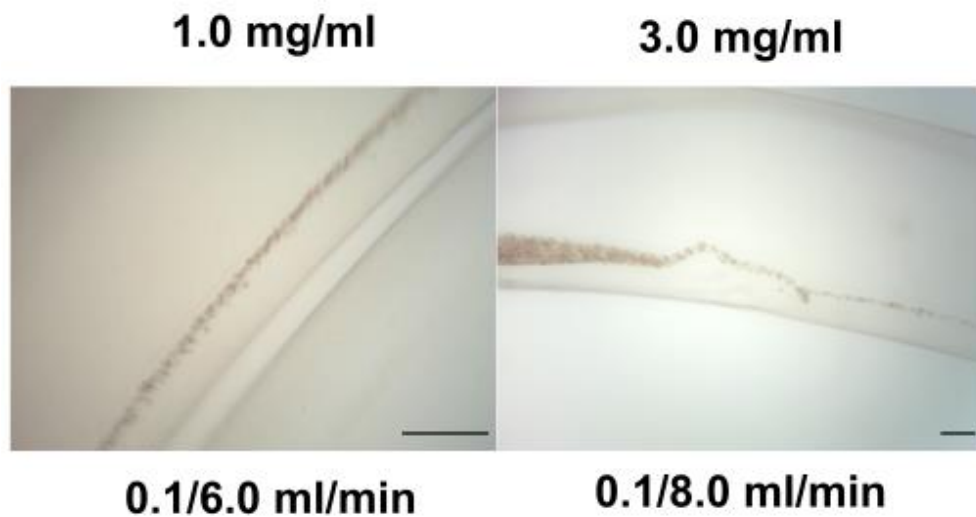


Figure 4-24. Representative light microscopy images showing discontinuous collagen filaments. Using (a) 1.0 mg/ml and (b) 3.0 mg/ml, displaying convergence and subsequent formation of discontinuous filament (containing 3×10^6 HepaRG cells) caused by excessive acceleration of core collagen stream by 2.0% (w/v) alginate shell streams. Scale bars = (a) 200 μm , (b) 100 μm .

With reference to Figure 4-24, it can be seen that using a 1:60 flow rate ratio resulted in discontinuities using 1.0 mg/ml collagen whilst using a 1:80 core/shell flow rate ratio resulted in the fracturing of the collagen stream using 3.0 mg/ml, caused by shell flow rate-induced acceleration by momentum transfer. It can be seen that this fracturing effect is observed using a comparatively lower flow rate ratio using the lower collagen concentration. This is assumed to be due to the comparatively lower mass of collagen being present, leading to a reduced propensity for continuous filament formation. The presence of cells within the 3.0 mg/ml case may also have had an effect, however, this image still serves to show that there is an upper limit to the shell flow rate in which core filaments will fail to form continuous filaments due to excessive induced velocities.

On the other hand, the use of core collagen flow rates lower than 0.1 ml/min within a 100 mM CaCl_2 cross-linking bath resulted in the failure of collagen to flow and be narrowed by the fast alginate stream. Similarly, the reduction (or cessation) of the alginate shell stream flow rate resulted in nozzle blockage, with the formation of cross-linked alginate lumps. This effect was first observed at $Q_s < 0.2$ ml/min using 2.0% alginate and a 100 mM CaCl_2 cross-linking bath. The formation of alginate lumps on flow reduction or halting of flow is assumed to be due to the fact that alginate flowing within a CaCl_2 cross-linking bath must maintain a certain level of momentum to prevent nozzle blockage due to the rapid cross-linking ability of Ca^{2+} ions within a 100 mM CaCl_2 bath.

Furthermore, a coaxial extrusion setup is inherently limited to the use of two input nozzles, however, this system may be adapted to accommodate further nozzles, thus allowing high-precision fabrication of diameter-controlled, multi-layer cylindrical scaffold structures. In addition, the coaxial nozzle used for every experiment within this chapter was fabricated using stainless steel. Future nozzles may be designed using computer-aided drawing (CAD) and 3D-printed using resin polymers. This provides a cheaper nozzle system which provides complete control of nozzle internal anatomy and orifice geometry, facilitating the experimentation of various flow channel geometries in addition to the implementation of multi-channel nozzles [46].

Moreover, control of flow rates may also have an influence on resulting filament and shell dimensions. On using stepper motors, any transient fluctuations in the power supply to a stepper motor (or the corresponding stepper motor driver) could result in changes to motor speed, directly affecting material flow rates. As has been demonstrated in this chapter, any changes to core/shell material flow rates can impact extruded core/shell diameters. Therefore, it is important to control motor power supply as much as possible over the course of the extrusion process. Similarly, the control of temperature may also affect extruded material diameters due to temperature affecting viscosity and density. As viscosity is defined as the resistance of a material to flow, modifications to viscosity may affect flow rates and resulting diameters upon extrusion. In a similar manner, changes in density may lead to changes in filament or shell volume, therefore affecting apparent diameters. It is therefore imperative to control room and nozzle temperature as much as possible.

4.8. Conclusion

By taking the findings and conclusions from the experiments given in this chapter, a summary to guide the tuning of the alginate shell and collagen core filament diameters is shown in Tables 5-1 and 5-2 below, listing the relevant coaxial extrusion parameters and their effects on the aforementioned diameters.

Table 4-1. Effect of various coaxial extrusion parameters on extruded alginate shell diameter.

Parameter	Effect on alginate shell diameter	Notes
Flow rate ratio (Q_c/Q_s)	Smaller Q_c/Q_s leads to larger shell outer diameter (and wall thickness)	Valid for $Q_c < 3.0$ ml/min
Cross-linking time (100 mM $CaCl_2$)	Apparently no effect.	Tested between 0 and 10 min with 100 mM $CaCl_2$, no results for before day 4
Bath $CaCl_2$ concentration	Higher bath $CaCl_2$ conc. results in significantly smaller shell diameter	50, 75, 100 mM $CaCl_2$ tested
Divalent cation type	Use of Sr^{2+} and Ba^{2+} modify day 0 shell diameter (but not wall thickness)	Only tested on day 0, using 5/10min 100 mM $CaCl_2$, 100 mM $SrCl_2$ and 100 mM $CaCl_2$ with 2 min 50 mM $BaCl_2$ / 100 mM $SrCl_2$

Table 4-2. Effect of various coaxial extrusion parameters on extruded collagen filament diameter.

Parameter	Effect on collagen filament diameter	Notes
Flow rate ratio (Q_c/Q_s)	Lower Q_c/Q_s leads to smaller filament diameter	Confirmed from 1:1 to 1:30 using 1.0 and 3.0 mg/ml collagen
Flow rate magnitude at equal flow rate ratio	Higher magnitude leads to larger filament diameter	Tested at Q_c and $Q_s = 0.1, 0.5, 1.0$ ml/min
Collagen concentration	Lower collagen concentration leads to smaller filament diameter	Concentration tested between 1.0 and 3.0 mg/ml collagen solution, valid for $Q_c < 2.0$ ml/min.

These tables were used to inform the tuning of alginate shell and core collagen filament diameters during coaxial extrusion experiments in the following chapter, which involves the use of adipose-derived stem cells to provide a proof-of-concept for the extrusion of fine diameter, continuous cell-collagen filaments contained in porous, cross-linked tubular alginate scaffolds.

4.9. References

- [1] K. Y. Lee and D. J. Mooney, “Alginate: Properties and biomedical applications,” *Prog. Polym. Sci.*, vol. 37, no. 1, pp. 106–126, Jan. 2012.
- [2] O. Smidsrød and G. Skjåk-Bræk, “Alginate as immobilization matrix for cells,” *Trends Biotechnol.*, vol. 8, no. C, pp. 71–78, Jan. 1990.
- [3] N. C. Hunt, A. M. Smith, U. Gbureck, R. M. Shelton, and L. M. Grover, “Encapsulation of fibroblasts causes accelerated alginate hydrogel degradation,” *Acta Biomater.*, vol. 6, no. 9, pp. 3649–3656, Sep. 2010.
- [4] Y. S. Zhang *et al.*, “Bioprinting 3D microfibrinous scaffolds for engineering endothelialized myocardium and heart-on-a-chip,” *Biomaterials*, vol. 110, pp. 45–59, 2016.
- [5] Z. Wu, X. Su, Y. Xu, B. Kong, W. Sun, and S. Mi, “Bioprinting three-dimensional cell-laden tissue constructs with controllable degradation,” *Sci. Rep.*, vol. 6, no. 1, p. 24474, 2016.
- [6] B. Zhu and H. Yin, “Alginate lyase: Review of major sources and classification, properties, structure-function analysis and applications,” *Bioengineered*, vol. 6, no. 3. Taylor and Francis Inc., pp. 125–131, 2015.
- [7] N. Rajan, J. Habermehl, M.-F. Côté, C. J. Doillon, and D. Mantovani, “Preparation of ready-to-use, storable and reconstituted type I collagen from rat tail tendon for tissue engineering applications,” *Nat. Protoc.*, vol. 1, no. 6, pp. 2753–2758, Jan. 2007.
- [8] F. H. Silver, J. W. Freeman, and G. P. Seehra, “Collagen self-assembly and the development of tendon mechanical properties,” *J. Biomech.*, vol. 36, no. 10, pp. 1529–1553, Oct. 2003.
- [9] M. Achilli and D. Mantovani, “Tailoring mechanical properties of collagen-based scaffolds for vascular tissue engineering: The effects of pH, temperature and ionic strength on gelation,” *Polymers (Basel)*, vol. 2, no. 4, pp. 664–680, Dec. 2010.
- [10] T. L. Jenkins and D. Little, “Synthetic scaffolds for musculoskeletal tissue engineering: cellular responses to fiber parameters,” *npj Regen. Med.*, vol. 4, no. 1, pp. 1–14, Dec. 2019.
- [11] G. S. Lazarus, R. S. Brown, J. R. Daniels, and H. M. Fullmer, “Human granulocyte collagenase,” *Science (80-.)*, vol. 159, no. 3822, pp. 1483–1485, Mar. 1968.

- [12] T. L. Willett, R. S. Labow, N. C. Avery, and J. M. Lee, "Increased proteolysis of collagen in an in vitro tensile overload tendon model," *Ann. Biomed. Eng.*, vol. 35, no. 11, pp. 1961–1972, Nov. 2007.
- [13] C. Bonnans, J. Chou, and Z. Werb, "Remodelling the extracellular matrix in development and disease," *Nat. Rev. Mol. Cell Biol.*, vol. 15, no. 12, pp. 786–801, Dec. 2014.
- [14] A. Blaeser, D. F. Duarte Campos, U. Puster, W. Richtering, M. M. Stevens, and H. Fischer, "Controlling Shear Stress in 3D Bioprinting is a Key Factor to Balance Printing Resolution and Stem Cell Integrity," *Adv. Healthc. Mater.*, vol. 5, no. 3, pp. 326–333, Feb. 2016.
- [15] Y. Nakayama, *Introduction to Fluid Mechanics*. Butterworth-Heinemann, 2000.
- [16] P. Xu, R. Xie, Y. Liu, G. Luo, M. Ding, and Q. Liang, "Bioinspired Microfibers with Embedded Perfusible Helical Channels," *Adv. Mater.*, vol. 29, no. 34, p. 1701664, Sep. 2017.
- [17] M. Hu *et al.*, "Hydrodynamic spinning of hydrogel fibers," *Biomaterials*, vol. 31, no. 5, pp. 863–869, Feb. 2010.
- [18] L. Shao *et al.*, "Fiber-Based Mini Tissue with Morphology-Controllable GelMA Microfibers," *Small*, vol. 14, no. 44, 2018.
- [19] K. Yue, G. Trujillo-de Santiago, M. M. Alvarez, A. Tamayol, N. Annabi, and A. Khademhosseini, "Synthesis, properties, and biomedical applications of gelatin methacryloyl (GelMA) hydrogels," *Biomaterials*, vol. 73, pp. 254–271, 2015.
- [20] H. Williams, M. McPhail, S. Mondal, and A. Münch, "Modeling Gel Fiber Formation in an Emerging Coaxial Flow from a Nozzle," *J. Fluids Eng. Trans. ASME*, vol. 141, no. 1, 2018.
- [21] S. J. Shin *et al.*, "'On the fly' continuous generation of alginate fibers using a microfluidic device," *Langmuir*, vol. 23, no. 17, pp. 9104–9108, Aug. 2007.
- [22] S. Sugiura, T. Oda, Y. Aoyagi, M. Satake, N. Ohkohchi, and M. Nakajima, "Tubular gel fabrication and cell encapsulation in laminar flow stream formed by microfabricated nozzle array," *Lab Chip*, vol. 8, no. 8, pp. 1255–1257, Jul. 2008.

- [23] Ý. A. Mørch, I. Donati, B. L. Strand, and G. Skjåk-Bræk, “Effect of Ca²⁺, Ba²⁺, and Sr²⁺ on alginate microbeads,” *Biomacromolecules*, vol. 7, no. 5, pp. 1471–1480, May 2006.
- [24] A. G. Tabriz, M. A. Hermida, N. R. Leslie, and W. Shu, “Three-dimensional bioprinting of complex cell laden alginate hydrogel structures,” *Biofabrication*, vol. 7, no. 4, Dec. 2015.
- [25] H. Onoe *et al.*, “Metre-long cell-laden microfibres exhibit tissue morphologies and functions,” *Nat. Mater.*, vol. 12, no. 6, pp. 584–590, 2013.
- [26] F. E. Freeman and D. J. Kelly, “Tuning alginate bioink stiffness and composition for controlled growth factor delivery and to spatially direct MSC Fate within bioprinted tissues,” *Sci. Rep.*, vol. 7, no. 1, pp. 1–12, 2017.
- [27] Q. Gao, B. S. Kim, and G. Gao, “Advanced Strategies for 3D Bioprinting of Tissue and Organs Analogs Using Alginate Hydrogel Bioinks,” *Mar. Drugs*, vol. 19, no. 708, Dec. 2021.
- [28] Y. Zhang, S. T. Ellison, S. Duraivel, C. D. Morley, C. R. Taylor, and T. E. Angelini, “3D printed collagen structures at low concentrations supported by jammed microgels,” *Bioprinting*, vol. 21, p. e00121, Mar. 2021.
- [29] S. Rhee, J. L. Puetzer, B. N. Mason, C. A. Reinhart-King, and L. J. Bonassar, “3D Bioprinting of Spatially Heterogeneous Collagen Constructs for Cartilage Tissue Engineering,” *ACS Biomater. Sci. Eng.*, vol. 2, no. 10, pp. 1800–1805, Oct. 2016.
- [30] J. Li, Y. Wu, J. He, and Y. Huang, “A new insight to the effect of calcium concentration on gelation process and physical properties of alginate films,” *J. Mater. Sci.*, vol. 51, no. 12, pp. 5791–5801, Jun. 2016.
- [31] J. Hazur *et al.*, “Improving alginate printability for biofabrication: establishment of a universal and homogeneous pre-crosslinking technique,” *Biofabrication*, vol. 12, no. 4, p. 045004, Jul. 2020.
- [32] H. F. Chieh *et al.*, “Effects of cell concentration and collagen concentration on contraction kinetics and mechanical properties in a bone marrow stromal cell-collagen construct,” *J. Biomed. Mater. Res. - Part A*, vol. 93, no. 3, pp. 1132–1139, 2010.
- [33] F. J. O’Brien, “Biomaterials & scaffolds for tissue engineering,” *Materials Today*, vol. 14, no. 3. Elsevier B.V., pp. 88–95, 01-Mar-2011.

- [34] E. C. Novosel, C. Kleinhans, and P. J. Kluger, "Vascularization is the key challenge in tissue engineering," *Adv. Drug Deliv. Rev.*, vol. 63, no. 4, pp. 300–311, Apr. 2011.
- [35] H. J. Kong, K. Y. Lee, and D. J. Mooney, "Nondestructively probing the cross-linking density of polymeric hydrogels," *Macromolecules*, vol. 36, no. 20, pp. 7887–7890, Oct. 2003.
- [36] A. Haug, "The Affinity of Some Divalent Metals to Different Types of Alginates," *Acta Chem. Scand.*, vol. 15, pp. 1794–1795, 1961.
- [37] M. D. Darrabie, W. F. Kendall, and E. C. Opara, "Characteristics of Poly-L-Ornithine-coated alginate microcapsules," *Biomaterials*, vol. 26, no. 34, pp. 6846–6852, 2005.
- [38] R. Gaetani *et al.*, "Cardiac tissue engineering using tissue printing technology and human cardiac progenitor cells," *Biomaterials*, vol. 33, no. 6, pp. 1782–1790, Feb. 2012.
- [39] N. C. Hunt *et al.*, "3D culture of human pluripotent stem cells in RGD-alginate hydrogel improves retinal tissue development," *Acta Biomater.*, vol. 49, pp. 329–343, Feb. 2017.
- [40] G. Choe, J. Park, H. Jo, Y. S. Kim, Y. Ahn, and J. Y. Lee, "Studies on the effects of microencapsulated human mesenchymal stem cells in RGD-modified alginate on cardiomyocytes under oxidative stress conditions using in vitro biomimetic co-culture system," *Int. J. Biol. Macromol.*, vol. 123, pp. 512–520, Feb. 2019.
- [41] W. Jia *et al.*, "Direct 3D bioprinting of perfusable vascular constructs using a blend bioink," *Biomaterials*, vol. 106, pp. 58–68, 2016.
- [42] E. V. Solovieva, A. Y. Fedotov, V. E. Mamonov, V. S. Komlev, and A. A. Panteleyev, "Fibrinogen-modified sodium alginate as a scaffold material for skin tissue engineering," *Biomed. Mater.*, vol. 13, no. 2, p. 25007, Jan. 2018.
- [43] L. Ning *et al.*, "3D bioprinting of scaffolds with living Schwann cells for potential nerve tissue engineering applications," *Biofabrication*, vol. 10, no. 3, p. 35014, 2018.
- [44] S. Ramanujan, A. Pluen, T. D. McKee, E. B. Brown, Y. Boucher, and R. K. Jain, "Diffusion and convection in collagen gels: Implications for transport in the tumor interstitium," *Biophys. J.*, vol. 83, no. 3, pp. 1650–1660, Sep. 2002.

- [45] V. L. Cross *et al.*, “Dense type I collagen matrices that support cellular remodeling and microfabrication for studies of tumor angiogenesis and vasculogenesis in vitro,” *Biomaterials*, vol. 31, no. 33, pp. 8596–8607, Nov. 2010.
- [46] Y. Morimoto, M. Kiyosawa, and S. Takeuchi, “Three-dimensional printed microfluidic modules for design changeable coaxial microfluidic devices,” *Sensors Actuators, B Chem.*, vol. 274, pp. 491–500, Nov. 2018.

5. Coaxial Extrusion of Fine Diameter Cell-laden Filaments

5.1. Introduction

This chapter builds on the foundational work presented in Chapter 2 by adding cells to the core collagen solution within a coaxial nozzle. In doing so, an in vitro extracellular matrix (ECM)-mimicking environment is created, facilitating the seeding, aggregation and proliferation of dispersed cells along the self-assembled collagen fibrils. This provides a valid platform for the in vitro study of cells in a three-dimensional native-like environment, with the goal of engineering aligned, transplantable tissue filaments.

5.1.1. Challenges of adding cells

On the addition of cells to collagen core filaments during coaxial extrusion and further incubation in culture media, alginate shell porosity and wall thickness must be controlled in order to facilitate nutrient delivery and waste metabolite removal [1]. As has been previously stated, hydrogel shell wall thickness must be $< 100 - 200 \mu\text{m}$ to prevent limitations in diffusion-based mass transport in the absence of perfusion culture [2].

The work in Chapter 2 demonstrated that by controlling cross-linking conditions and the flow rate of alginate in the shell of a coaxial nozzle, the post-extrusion wall thickness can be controlled to satisfy these requirements for the given coaxial nozzle system diameters (203/690 μm core/shell).

5.2. Process description

The previously-described coaxial process (see Chapter 2) was utilised with the addition of adipose-derived stem cells (ADSCs) to the core collagen solution prior to extrusion. Upon incubation in culture media, collagen self-assembled to form a gelled filament, thus providing a backbone for dispersed cells to attach through integrin receptor binding to RGD (Arginine-Glycine-Aspartic acid) motifs located on the collagen polymer alpha chains. Over time, viable cells may spread and aggregate with nearby cells to form tissue filaments.

5.2.1. Experimental aims

The aim of the work presented in this chapter was analyse the effect of extrusion parameters on the resulting minimal filament diameter, viability and aggregation ability of ADSCs added in the collagen core of coaxial extruded hollow alginate shells, with the aim of producing fine diameter, high-viability, continuous cell-collagen filaments capable of further cell differentiation to produce transplantable tissue filaments.

Early experiments focussed on the control of parameters to observe cellular aggregation and alignment into tissue filaments whereas later experiments were concerned with the reduction of alginate scaffold and cell filament diameters to ensure adequate porosity for mass transport. An additional study investigated the viability of differentiated ADSCs, with a Schwann cell-like phenotype, to assess the potential of this platform for neural repair applications.

Efforts were then directed at achieving fine diameter cell filaments through the manipulation of input flow rates. On achieving sub-100 μm filaments, it then became important to increase the lifespan of viable and continuous filaments prior to in vitro degradation. This was achieved through the increase of alginate shell porosity through the manipulation of cross-linking parameters. On achieving suitable porosity and cell filament diameter, more attempts at fine diameter filaments were made through the manipulation of collagen concentration and cell seeding density

The cells of choice were ADSCs. All culture media was changed every 3 to 4 days (twice per week). Day 0 images refer to approximately three hours post-extrusion. Experimentally, extruded filaments were primarily analysed using live/dead and brightfield imaging, to assess filament diameter and continuity in addition to cell viability over time.

5.3.Extrusion of ADSCs at high-viability

With all cell-seeding coaxial extrusion experiments, there were many key observations to assess for successful cellular integration and survival within the extruded alginate constructs. Firstly, it was necessary to assess post-extrusion cellular viability, as nozzle shear stresses were identified as a major barrier to successful cell extrusion. On observation of successful extrusion and maintenance of viability, spreading and aggregation of cells into fibres was the next key step. This was crucial as it essential for cells to successfully form tissue junctions to adjacent cells in order to form a tissue filament along an aligned collagen backbone and to maintain overall tissue viability through adequate nutrition and intercellular signalling [3].

Early experiments were concerned with the extrusion of ADSCs at high viability and to investigate the ability of the cells to spread and aggregate. On progressing from the collagen-only coaxial experiments there were additional considerations to make. The cell seeding density had to be sufficient such that dispersed cells within the collagen filament could spread to find neighbouring cells to facilitate aggregation. The cross-linking time had to be sufficient to achieve collagen and alginate mechanical stabilisation in addition to achieving sufficient porosity to facilitate unhindered nutrient and waste diffusion whilst containing cells and collagen within the scaffold core.

The aim of this first experiment was to analyse the viability of ADSCs encapsulated within the collagen core of alginate shell scaffolds, with the hope of observing high viability and cellular aggregation into filaments. The cell seeding density used here was 4.0×10^6 cells/ml collagen solution. A 1:1 core/shell flow rate ratio (Q_c/Q_s) was used, with both Q_c and Q_s equalling 1.0 ml/min.

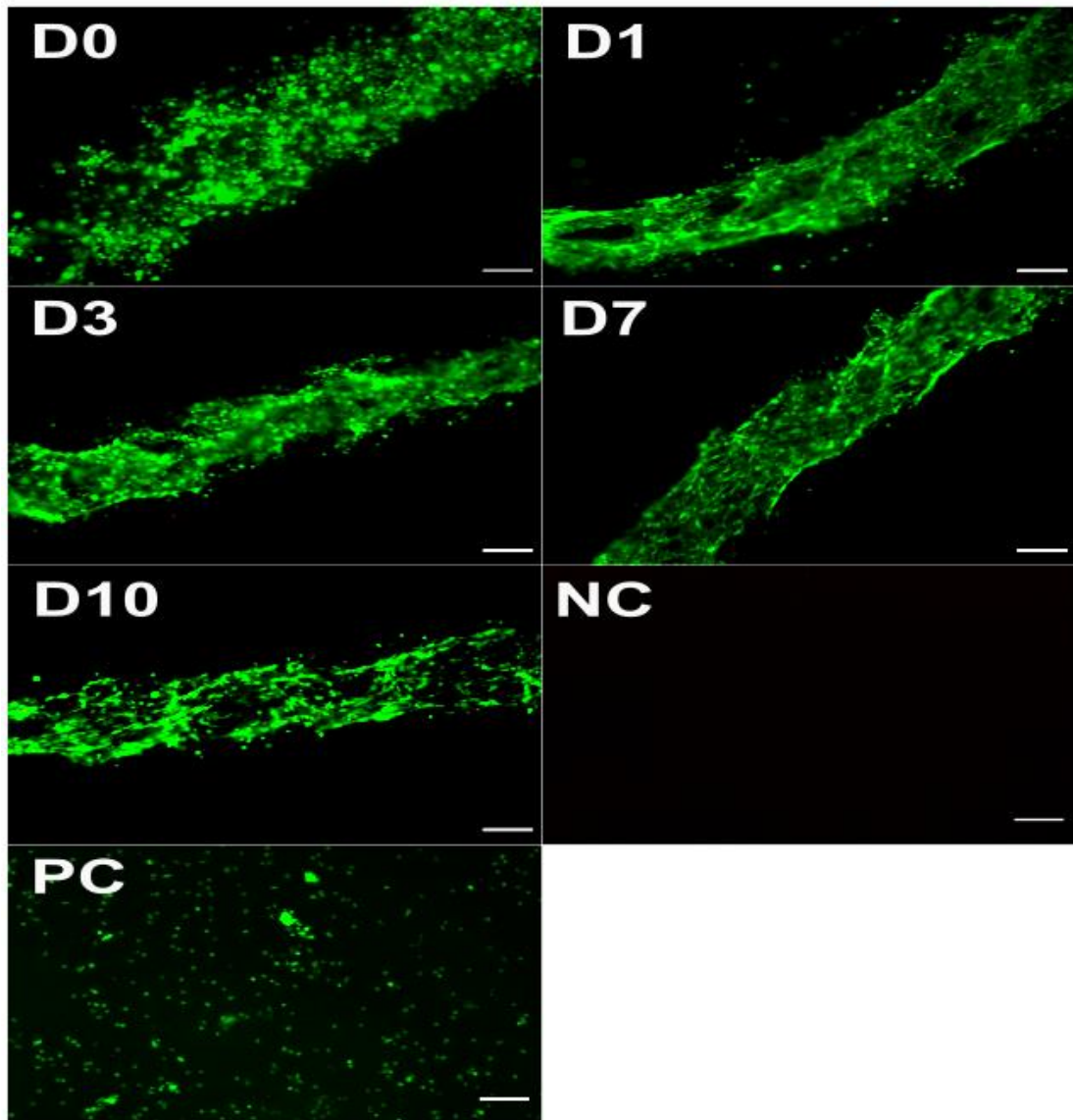


Figure 5-1. Representative live/dead images of ADSCs encapsulated within the gelled 3.0 mg/ml collagen core of 2.0% (w/v) alginate scaffolds cross-linked in a 100 mM CaCl_2 bath for 10 minutes at a cell seeding density of 4.0×10^6 cells/ml and core/shell flow rates of 1.0/1.0 ml/min. NC = negative control (hollow alginate shell cross-linked by 100 mM CaCl_2 core solution); PC = positive control (4.0×10^6 cells/ml in 75% / 25% (v/v) collagen/media solution in bottom of culture well). Scale bars = 200 μm .

With reference to Figure 5-1, the day 0 live/dead image shows ADSCs dispersed within the collagen core, requiring more time to spread and aggregate. Between days 0 and 1, the cells appear to contract the collagen filament, as evidenced by the apparent reduction in filament diameter. From days 1 to 7, cells remained aggregated and elongated at high viability, indicating that, as expected, the ADSCs are in an ECM-like environment conducive to cell survival and proliferation. However, the ADSCs do not appear to form a continuous filament with cells aggregating to form a tissue-like filament, as is shown by the apparent holes throughout the structures, this was attributed to a low cell seeding density and it was concluded that further work should use relatively higher concentrations of cells within the collagen core solution to observe cellular aggregation.

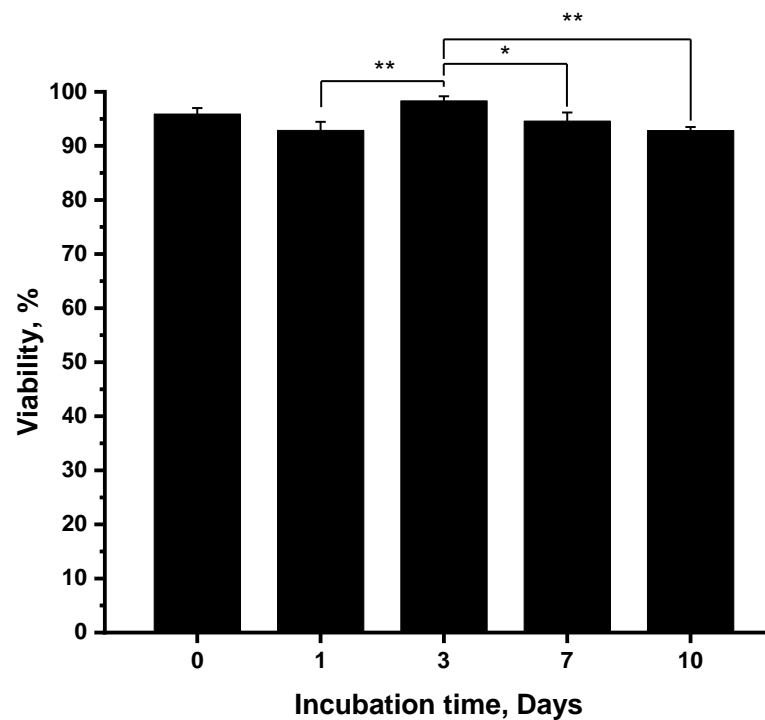


Figure 5-2. Viability of ADSCs encapsulated within the gelled 3.0 mg/ml collagen core of 2.0% (w/v) alginate scaffolds cross-linked in a 100 mM CaCl₂ bath for 10 minutes at a cell seeding density of 4.0 x 10⁶ cells/ml and core/shell flow rates of 1.0/1.0 ml/min. Data represents mean ± SD (n = 3). Statistical analysis performed using a one-way ANOVA test with Tukey's post hoc test. (* indicates p < 0.05; ** indicates p < 0.01. *** indicates p < 0.001).

Cellular viability analysis, shown in Figure 5-2, revealed that cell viability was > 92.0% throughout the experiment, with a significant increase from day 1 to day 3 (p < 0.01), to a maximum of 98.3 ± 0.84% on day 3. Viability then declined in a statistically-significant manner (p < 0.05) to a minimum of 92.8 ± 0.64% on day 10.

It should be noted here that the absence of dead cells in all live/dead images presented in this chapter may be attributed to the washing of constructs prior to imaging, using phosphate-buffered saline (PBS), leading to the removal of non-adhered dead cells. Therefore, viability may only be determined for adhered cells.

The day 10 image appears largely fragmented and discontinuous, signalling the breakdown of the collagen structure, which may have attributed to the fact that the collagen filament diameter is $> 200 \mu\text{m}$, consequently leading to nutrient diffusion being limited and causing the formation of necrotic regions and subsequent collagen filament fragmentation.

Moreover, the increased fragmentation of the cell-collagen structures may be a consequence of cellular remodelling of the collagen by release of MMPs (matrix metalloproteinases) [4]. The absence of cell filaments was suspected to be a result of low cell-seeding density, subsequent experiments were therefore performed at higher cell-seeding densities

5.4. High cell density study for tissue filament culture

Upon successful high-viability ADSC seeding within coaxial extruded collagen filaments, the next step was to observe aggregation into cell filaments. To achieve this, the cell seeding density was increased from 4.0×10^6 cells/ml to 10.0×10^6 cells/ml and further to 15.0×10^6 cells/ml with further live/dead analyses used to compare results. These density values were chosen in reference to similar coaxial extrusion filament-forming work, where Dai et al. [5] formed heterogeneous tumour fibres using 10.0×10^7 cells/ml. The higher value of 15.0×10^7 cells/ml was also trialled to investigate any effects of using a higher concentration.

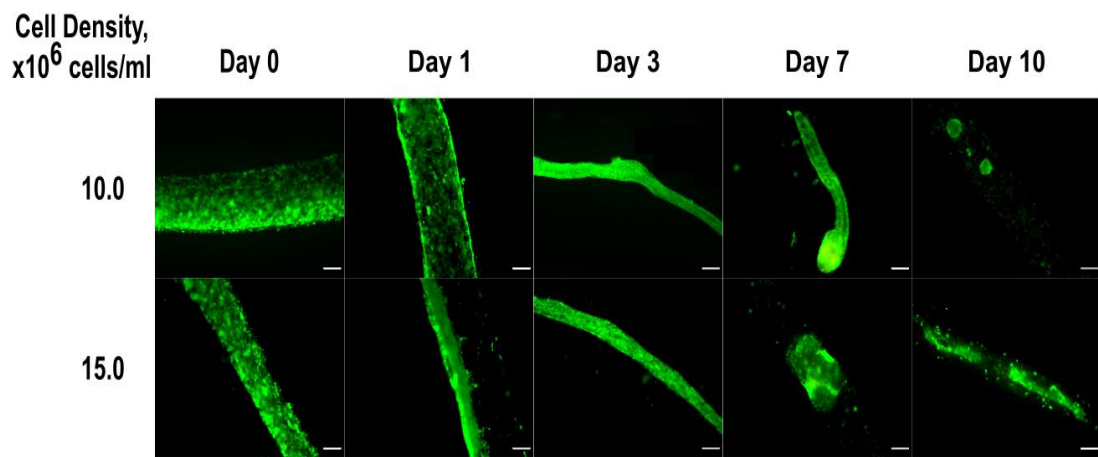


Figure 5-3. Representative live/dead imaging of ADSCs encapsulated within the gelled 3.0 mg/ml collagen core of 2.0% (w/v) alginate scaffolds cross-linked in a 100 mM CaCl_2 bath for 10 minutes at a cell seeding density of 10.0×10^6 and 15.0×10^6 cells/ml and core/shell flow rates of 1.0/1.0 ml/min. Scale bar = 200 μm .

On analysis of the results presented in Figure 5-3, the aim of the experiment was achieved through the successful culture of ADSC filaments on day 3 for both tested cell densities. The general observation for both cases is that the cells begin culture in the dispersed state prior to spreading and aggregation into a cell-contracted filament. The major difference between the lower cell density of 4.0×10^6 cells/ml used in the previous experiment (section 5.2.1) and using $\geq 10.0 \times 10^6$ cells/ml is that the initial aggregation phase results in the formation of a cell-collagen filament as opposed to the previously-observed fragmented aggregates. The day 3 filament diameters measured $136 \pm 15.6 \mu\text{m}$ and $139.8 \pm 14.7 \mu\text{m}$ respectively (mean \pm SD), in line with the sub-200 μm diameter diffusion requirements discussed in section 5.1.1.

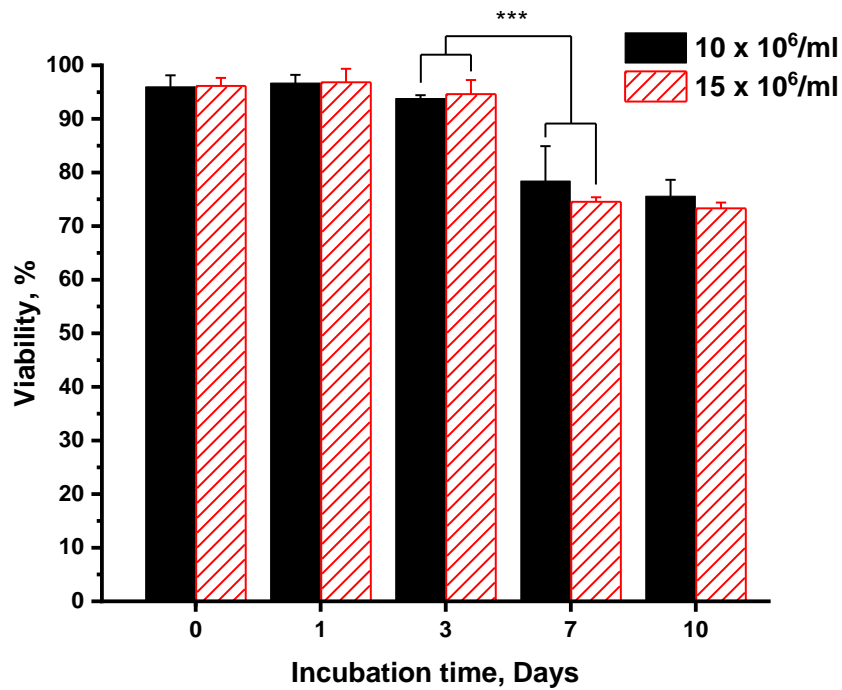


Figure 5-4. Viability of ADSCs encapsulated within the gelled 3.0 mg/ml collagen core of 2.0% (w/v) alginate scaffolds cross-linked in a 100 mM CaCl₂ bath for 10 minutes at cell seeding densities of 10.0 x 10⁶ and 15.0 x 10⁶ cells/ml and core/shell flow rates of 1.0/1.0 ml/min. Data represents mean ± SD (n = 3). Statistical analysis performed using a one-way ANOVA test with Tukey's post hoc test.

On comparison of day 1 viability data between the two experimental cases, it can be seen that the ADSCs are still in a dispersed state at the lower cell seeding density, however, a filament is clearly observed for the higher density of 15.0 x 10⁶ cells/ml, meanwhile, Figure 5-4 shows that cell viability can be considered high (> 90%) for both cases (> 96.7%). It can therefore be inferred that with the flow rates and nozzle diameters used here, the cell seeding density must be > 10.0 x 10⁶ cells/ml to increase the rate of filament formation. Using a higher cell seeding density reduces the requirement of cells to spread to facilitate aggregation due to the closer proximity of neighbouring cells. Consequently, it can be expected that a higher cell seeding density results in a swifter filament formation under controlled experimental conditions. However, it should be noted that there were no observed statistically significant differences in viability between the two cell seeding densities used here.

Between days 3 and 7, these filaments degraded into smaller aggregates until day 10. This degradation was suspected to be caused by limited nutrient diffusion due to a combination of day 1 collagen filament diameter measuring a mean of 517.0 ± 9.5 μm in addition to an alginate shell outer diameter of 851 ± 40.7 μm.

As a consequence, many cells which were adhered to the collagen filament appear to have died between days 3 and 7 due to a lack of sufficient nutrition caused by a large diffusion distance from the outer shell to the core of the collagen filaments. This is reflected in the statistically-significant reduction ($p < 0.001$) in cell viability for both cell seeding densities used between days 3 and 7, from $> 93.8 \pm 0.63\%$ on day 3 to $> 74.5 \pm 0.85\%$ on day 7, with a further reduction to $> 73.3 \pm 1.08\%$ observed on day 10.

Furthermore, cellular MMP remodelling of collagen and alginate degradation may have also contributed to cell-collagen filament degradation, however, further experiments first focussed on the effect of a smaller collagen filament diameter on cellular filament formation and degradation times.

5.5. Extrusion of Schwann cell-like filaments

With the successful extrusion and culture of ADSC filaments, the viability and filament-forming ability of differentiated ADSCs to a Schwann cell-like phenotype (dADSCs) within coaxially extruded alginate scaffolds was tested. The core/shell flow rate ratio was maintained at 1:1 and the flow rates were halved, from 1.0 ml/min to 0.5 ml/min, as a result of collagen-only experiments indicating that a reduced flow rate magnitude would result in a lower collagen filament diameter.

With the use of growth factors to maintain the differentiated state of the dADSCs, there were economic concerns regarding the cell-seeding density in addition to permeability concerns with the molecular weight of the growth factors, listed in Table 5-1.

Table 5-1. Growth factors used in Schwann-like dADSC culture.

Growth factor	Molecular weight	Concentration in media
Glial growth factor (GGF)	8.0 kDa	250 ng/ml
Human basic fibroblastic growth factor (hBFGF)	18.0 kDa	10 ng/ml
Platelet-derived growth factor (PDGF)	24.0 kDa	5 ng/ml
Forskolin	410.5 Da	5.8 mg/ml

The initial work here used a cell-seeding density of 15.0×10^6 cells/ml, chosen to provide a high probability of cell filament formation whilst providing a baseline to inform future experiments. Firstly, a quantitative analysis of viability across the culture period is presented in Figure 5-5 below.

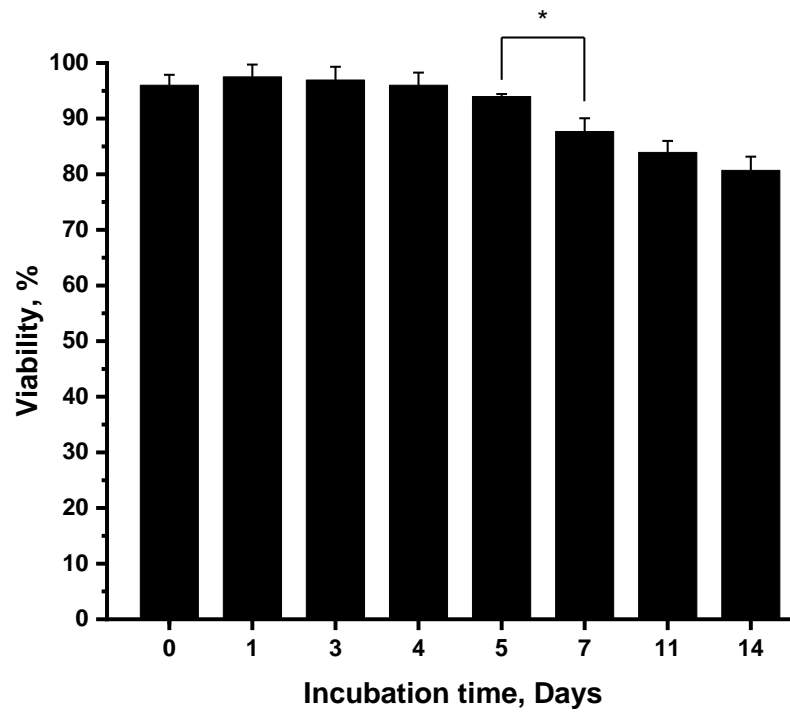


Figure 5-5. Viability of dADSCs encapsulated within the gelled 3.0 mg/ml collagen core of 2.0% (w/v) alginate scaffolds cross-linked in a 100 mM CaCl₂ bath for 10 minutes at a cell seeding density of 15.0 x 10⁶ cells/ml and core/shell flow rates of 0.5/0.5 ml/min. Data represents mean ± SD (n = 3), Statistical analysis performed using a one-way ANOVA test with Tukey's post hoc test.

In addition to live/dead images, brightfield images were also taken here. This would provide further information on the morphology of formed filaments and to investigate cell spreading across extruded collagen filaments.

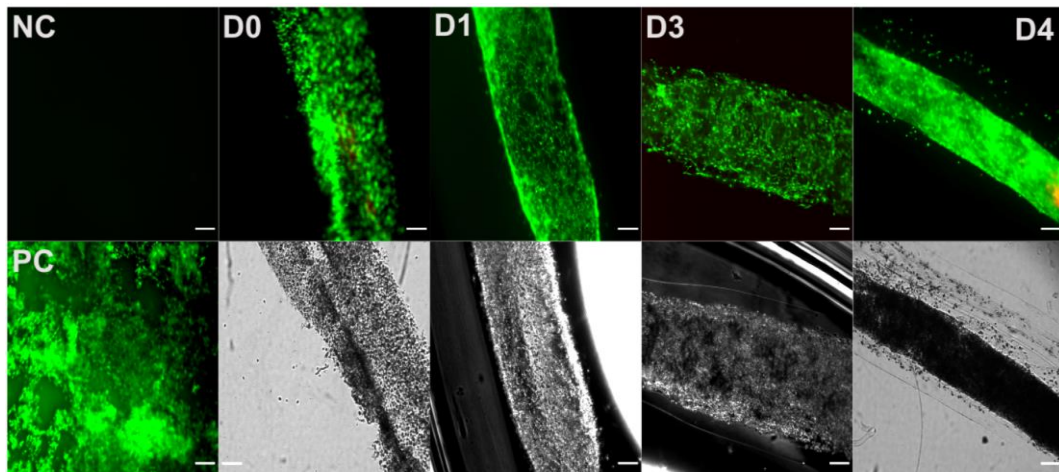


Figure 5-6. Representative day 0 to 4 live/dead and brightfield imaging of dADSCs encapsulated within the gelled 3.0 mg/ml collagen core of 2.0% (w/v) alginate scaffolds cross-linked in a 100 mM CaCl₂ bath for 10 minutes at a cell seeding density of 15.0 x 10⁶ cells/ml and core/shell flow rates of 0.5/0.5 ml/min. Scale bar = 200 μm.

On analysis of Figure 5-6, cells are firstly in a dispersed phase at high-viability ($96.0 \pm 1.85\%$) at day 0 and begin to aggregate from days 1 to 4. From days 1 to 3, cells have spread and aggregated with nearby cells across the collagen filament, with viability remaining above 96.9%, however, a complete cell-collagen filament had not yet formed. Cells at the periphery of the collagen filament aligned parallel to the alginate shell inner walls. At day 4, continuous, uniform, apparently contracted cell-collagen filaments have formed at high-viability. In addition, the mean filament diameter reduced to approximately 44.9% of day 1 diameter ($757.2 \pm 41.5 \mu\text{m}$ to $340.3 \pm 5.2 \mu\text{m}$) as a result of the filament-forming process. This contraction was expected, as cellular collagen contraction by cells is a transient process [6].

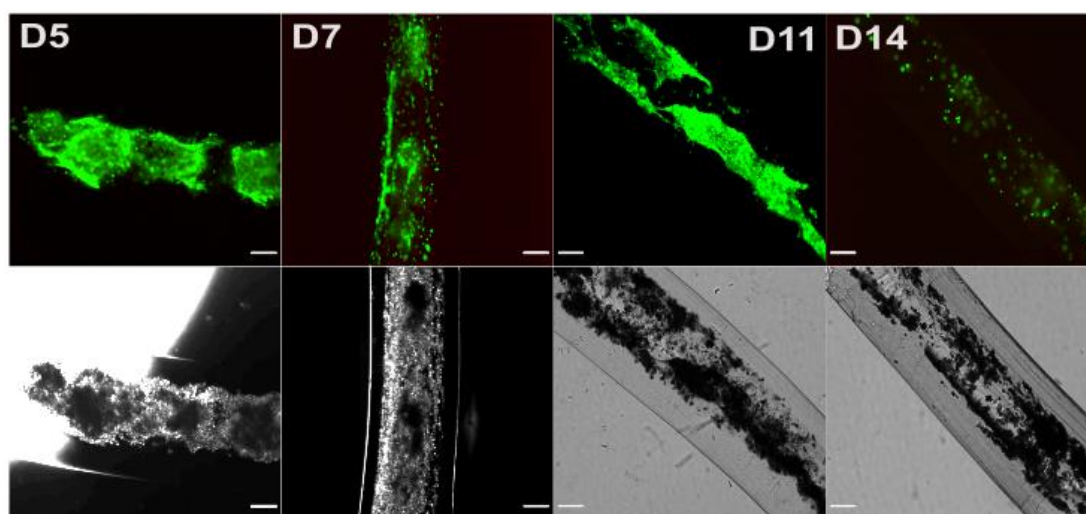


Figure 5-7. Representative day 5 to 14 live/dead and brightfield imaging of dADSCs encapsulated within the gelled 3.0 mg/ml collagen core of 2.0% (w/v) alginate scaffolds cross-linked in a 100 mM CaCl_2 bath for 10 minutes at a cell seeding density of 15.0×10^6 cells/ml and core/shell flow rates of 0.5/0.5 ml/min. Scale bar = 200 μm .

As is evidenced in Figure 5-7, the cell-collagen filament present on day 4 significantly degraded within 24 hours, from day 5 onwards. Viability remained at $94.0 \pm 0.5\%$ on day 5, however, no continuous collagen filaments were observed and only fragments of filaments were observed. Viability then dropped in a statistically-significant manner to $87.7 \pm 2.4\%$ on day 7 ($p < 0.05$) and this continued to decline to a minimum of $80.7 \pm 2.5\%$ on day 14. This drop in viability appears related to the fragmented appearance of filaments from days 5 to 11, indicating nutrient diffusion limitations as a result of the contracted collagen filament diameter being $> 200 \mu\text{m}$ ($412.6 \pm 11.0 \mu\text{m}$), cellular remodelling of collagen may also be a contributor to this degradation and drop in viability. A further issue may have been the limitation in the transport of growth factors across the alginate shell walls.

Further experimentation on alginate permeability to large molecules, in the 4.4 to 40.0 kDa range, as mentioned in section 5.1.1, is required for further work using Schwann-like dADSCs to confirm this. Additionally, a lower filament diameter is also required to eliminate the necrotic effects on cells caused by any limitations to nutrient diffusion.

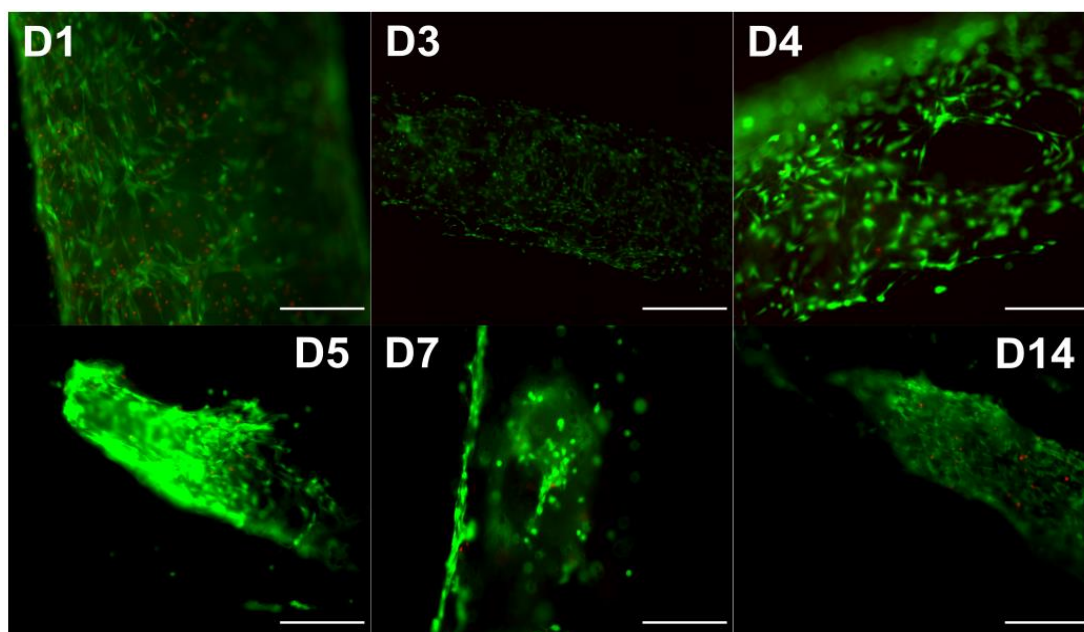


Figure 5-8. Representative day 1 to 14 live/dead imaging of dADSCs encapsulated within the gelled 3.0 mg/ml collagen core of 2.0% (w/v) alginate scaffolds cross-linked in a 100 mM CaCl_2 bath for 10 minutes at a cell seeding density of 15.0×10^6 cells/ml and core/shell flow rates of 0.5/0.5 ml/min. Scale bar = 200 μm .

Figure 5-8 provides higher magnification images to inform the assessment of cellular alignment within the collagen filaments during the aggregation and degradation phases. During the aggregation phases (days 1 to 3) cells can be seen to aggregate and align to neighbouring cells, however many cells were not aligned parallel to the filament walls, suggesting that the collagen fibres within the collagen filament were misaligned and that these cells appear unsuitable to be used in any future in vivo work. This cellular misalignment continued from the filament phase (day 4) to the degradation phase (day 5 to day 14). Interestingly, the day 7 image shows another case where a number of cells aligned parallel to the alginate shell, indicating that the alginate shell wall acts as a guide for peripherally-located cells.

To summarise, this experiment has shown successful high-viability coaxial extrusion and culture of Schwann cell-like dADSC-collagen filaments at day 4 of culture, with alignment of cells at the periphery of filaments parallel to the alginate shell walls but with misaligned cells across the cross section of the collagen filament.

Further work is required to investigate the filament formation kinetics and long-term viability for a collagen filament diameter of $< 200 \mu\text{m}$, to eliminate any deleterious effects of limited nutrient diffusion, in addition to cell-collagen alignment studies in order to minimise the presence of misaligned collagen fibres.

5.6. Modification of cross-linking parameters for increased stability

5.6.1. Tuning of alginate exposure time to calcium chloride

From earlier ADSC-collagen experiments, it was evident that collagen filaments would quickly degrade in vitro, usually within 24 hours. This was suspected primarily due to collagen filaments being too large in diameter to facilitate unhindered nutrient and waste diffusion in addition to cellular collagen remodelling and alginate degradation by divalent cations in media. In response, further ADSC-collagen filaments were extruded at a lower flow rate magnitude, at 0.1 ml/min , whilst maintaining the 1:1 Q_c/Q_s ratio to provide lower diameter cell-collagen filaments to aid nutrient diffusion. In addition, the cross-linking time in a CaCl_2 bath (100 mM) was increased, from 10 to 20 minutes, to improve the stability of alginate shells in media. These scaffolds were extruded at a cell seeding density of $10.0 \times 10^6 \text{ cells/ml}$.

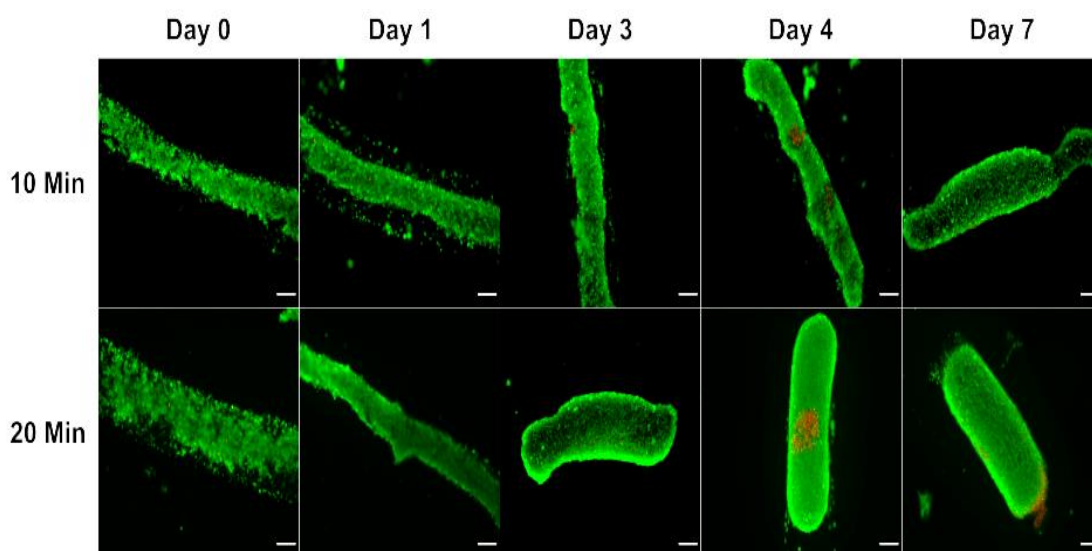


Figure 5-9. Representative day 0 to 7 live/dead imaging of ADSCs encapsulated within the gelled 3.0 mg/ml collagen core of $2.0\% \text{ (w/v)}$ alginate scaffolds cross-linked in a 100 mM CaCl_2 bath for 10 and 20 minutes at a cell seeding density of $10.0 \times 10^6 \text{ cells/ml}$ and core/shell flow rates of $0.1/0.1 \text{ ml/min}$. Scale bar = $200 \mu\text{m}$.

In addition to the live/dead images, a quantitative summary of cell viability for this experiment is presented in Figure 5-10, showing a comparison between the two experimental conditions.

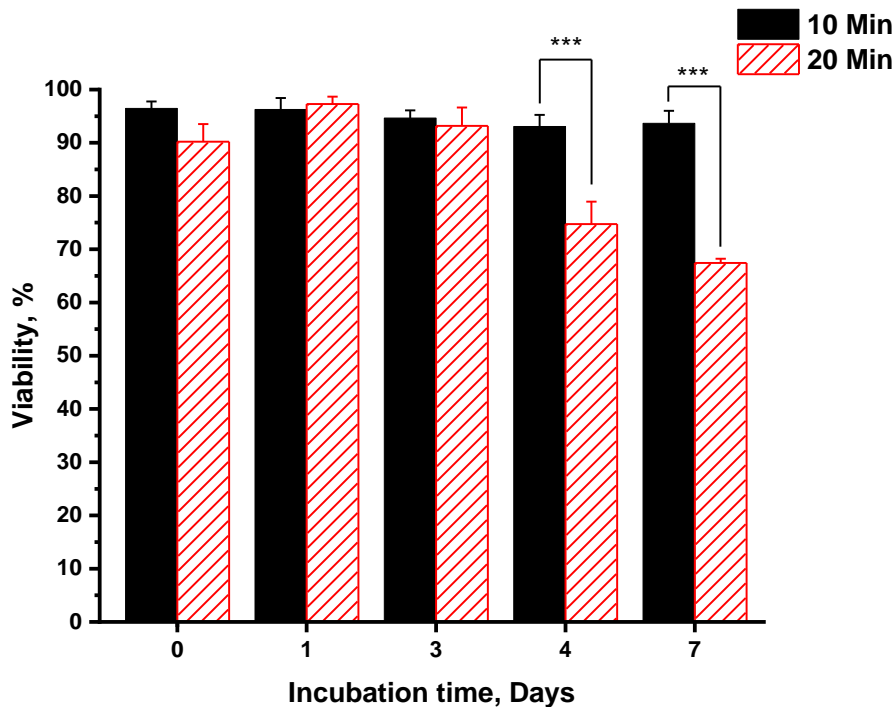


Figure 5-10. Viability of ADSCs encapsulated within the 3.0 mg/ml collagen core of 2.0% (w/v) alginate scaffolds cross-linked in a 100 mM CaCl₂ bath for 10 and 20 minutes at a cell seeding density of 10.0 x 10⁶ cells/ml and core/shell flow rates of 0.1/0.1 ml/min. Data represents mean ± SD (n = 3), Statistical analysis performed using a one-way ANOVA test with Tukey's post hoc test.

With reference to Figure 5-9, high-viability (> 96.3%), continuous filaments were apparent at day 1 for both cases after being in a dispersed state on day 0 (3 hours post-extrusion). The mean contracted filament diameter of the 10-minute case measured approximately 211.2 ± 11.0 μm and approximately 206.3 ± 15.8 μm for the 20-minute experiment. As both diameters were > 200 μm, this suggested that nutrient diffusion may have been hindered.

The structures which were cross-linked for 10 minutes also facilitated the support of filaments on day 3 at high viability, indicating that cell filaments can be maintained for at least 48 hours prior to degradation from day 4 onwards. Conversely, filaments are shown to be in a state of degradation from days 3 to 7 for the 20-minute case, with an associated statistically significant drop in viability from 93.1 ± 2.18% on day 3 to a minimum of 67.4 ± 0.79% on day 7 (p < 0.001). This indicates that the alginate scaffold porosity or cell-collagen filament diameter may be restricting nutrient and waste diffusion, leading to necrosis in the filament core, as is exemplified for the day 4 image with a cluster of dead cells in the core of the remaining filament structure.

These results suggest that the post-extrusion cross-linking time for scaffolds in 100 mM CaCl₂ should be restricted to < 20 minutes to support filament viability as it appears that the excess exposure to CaCl₂ may be leading to cell death and filament degradation, from day 3 onwards. Nutrient diffusion using these lower smaller diameters may also be aided by reducing the cross-linking time to < 10 minutes in addition to the further reduction of collagen filament diameter by further core/shell flow rate manipulation.

Furthermore, cell leakage was observed with both experimental conditions, from days 0 to 4. This indicates that cells were leaking through pores in the alginate shells therefore future experiments were concerned with further manipulation of cross-linking parameters to balance porosity, scaffold media stability and cell-collagen filament viability.

5.6.2. Implementation of secondary alginate cross-linking using barium

As cell-collagen filament degradation and cellular leakage from scaffolds was observed, this was suspected to be the consequence of alginate scaffold degradation from divalent cations in culture media. Work from Tabriz et al. [7] showed that the addition of 60 mM barium chloride (BaCl₂) for 2 minutes extended the stability of 4% (w/v) alginate cross-linked with 100 mM CaCl₂ for 10 minutes from 3 days to 11 days with no significant deleterious effects on the viability of U87-MG cells.

Secondary barium cross-linking was therefore employed to improve scaffold stability and viability. After initial post-extrusion alginate cross-linking within a 100 mM CaCl₂ bath for 10 minutes, extruded structures were subsequently placed in a 50 mM BaCl₂ bath for 1 or 2 minutes. This provided secondary cross-linking to add further stability to the alginate shell, with the aim of reducing porosity to contain the ADSCs within the scaffold core in addition to providing further mechanical stability to collagen filaments.

A concern with the addition of BaCl₂ was that nutrient diffusion may have been limited as a result of a further reduction of porosity; therefore, live/dead imaging was used to investigate the viability of these structures over a seven-day period. The core and shell flow rates were maintained at 0.1 ml/min and cell seeding density remained at 10.0 x10⁶ cells/ml.

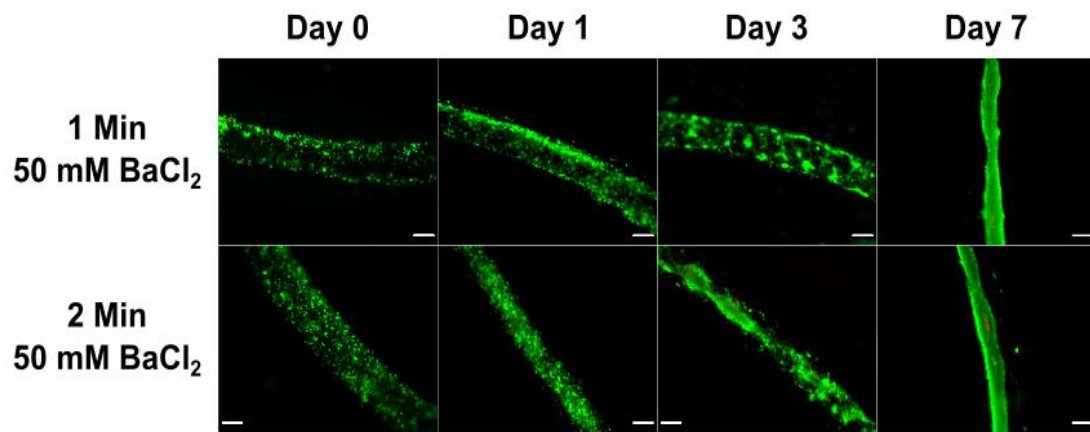


Figure 5-11. Representative day 0 to 7 live/dead imaging of ADSCs encapsulated within the 3.0 mg/ml collagen core of 2.0% (w/v) alginate scaffolds cross-linked in a 100 mM CaCl_2 bath for 10 minutes with secondary cross-linking using 50 mM BaCl_2 for 1 or 2 minutes at a cell seeding density of 10.0×10^6 cells/ml and core/shell flow rates of 0.1/0.1 ml/min. Scale bar = 200 μm . Note: experiment terminated at day 7 due to undesirably slow filament formation rate.

On inspection of Figure 5-11, it is clear that the addition of 50 mM BaCl_2 for 1 to 2 minutes has resulted in a reduction in the rate of cell-collagen filament formation. For both experimental cases, cells were extruded in a dispersed configuration on day 0 and subsequently commenced spreading and aggregation until filaments were formed on day 7.

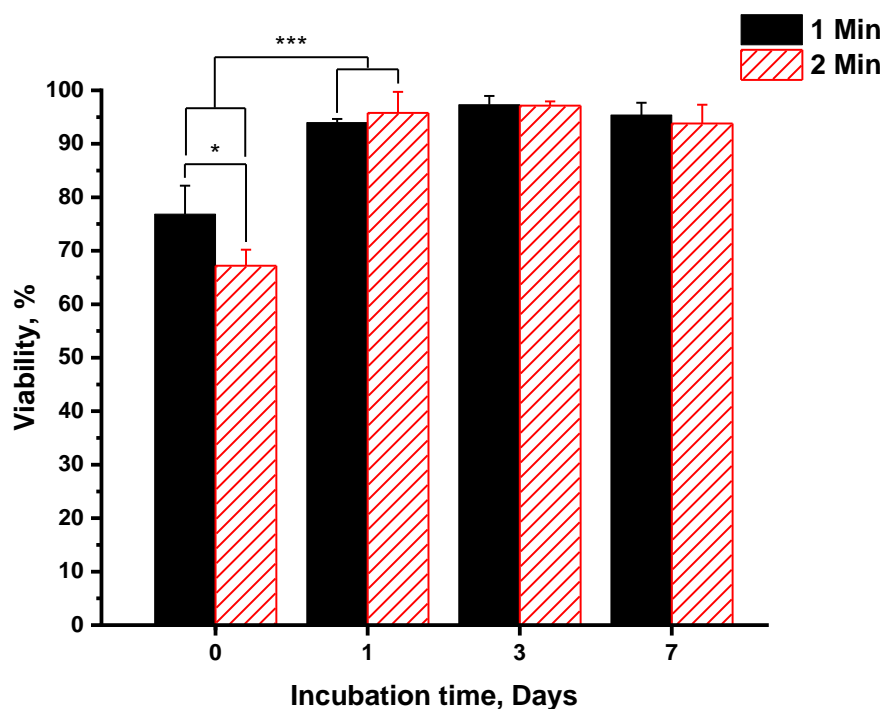


Figure 5-12. Viability of ADSCs encapsulated within the 3.0 mg/ml collagen core of 2.0% (w/v) alginate scaffolds cross-linked in a 100 mM CaCl₂ bath for 10 minutes with secondary cross-linking using 50 mM BaCl₂ for 1 or 2 minutes at a cell seeding density of 10.0 x 10⁶ cells/ml and core/shell flow rates of 0.1/0.1 ml/min. Data represents mean ± SD (n = 3). Statistical analysis performed using a one-way ANOVA test with Tukey's post hoc test.

On analysis of the experimental cell viabilities presented in Figure 5-12, it is clear that post-extrusion viability is undesirably low (< 90%). Day 0 viability for the 1-minute case was 76.8 ± 5.3%; meanwhile viability for the 2-minute case was significantly lower, at 67.2 ± 3.0% (p < 0.05). Viability significantly recovered on day 1, up to 94.0 ± 0.69% and 95.8 ± 3.92% respectively (p < 0.001). This high-viability state was maintained for both cases until termination of the experiment, on day 7. In addition, many cells appeared rounded in morphology between days 0 and 3 for both cases. This indicates that the addition of BaCl₂ may have stifled the ability of cells and collagen to interact to facilitate cellular elongation, spreading and subsequent aggregation.

Mean day 7 filament diameters were 170.7 ± 8.4 μm and 155.8 ± 12.6 μm for the 1 and 2-minute cases respectively, indicating that nutrient and waste diffusion should not have been significantly hindered from the collagen perspective. However, due to the slow filament formation process, it was suspected that the exposure of alginate scaffolds to Ba²⁺ ions at 50 mM for 1 to 2 minutes following primary cross-linking with 100 mM CaCl₂ for 10 minutes was sufficient to significantly reduce scaffold porosity such that material exchange across the scaffold walls appeared limited.

This limitation may account for the slow rate of filament formation in addition to the appearance of dead cells in the core of the day 7 filaments for both cases.

In response to these results, it appeared that secondary cross-linking of alginate using 50 mM BaCl₂ for 1 to 2 minutes resulted in significant reduction of the porosity and rate of filament formation of CaCl₂-crosslinked (10 min, 100 mM) alginate scaffolds whilst avoiding deleterious effects on cell viability. These effects, whilst positively containing cells within the core of extruded scaffolds at finer diameter and viability, also resulted in an undesirably slow rate of filament formation with limited cellular elongation. Future experiments may benefit from the stability and porosity reduction offered by secondary cross-linking using BaCl₂, however, the overall cross-linking conditions used in this experiment appeared too harsh on the rate of filament formation and appear to require a reduction in severity to rectify these issues.

5.7. Further experimentation for small diameter filaments

5.7.1. Extrusion for fine filaments with secondary barium cross-linking

To improve nutrient diffusion, finer-diameter cell-collagen fibres were extruded, by reducing the core/shell flow rate ratio. The core/shell flow rate ratio was reduced to 1:4 and further to 1:8 by increasing the shell flow rate to 0.4 ml/min and subsequently to 0.8 ml/min whilst maintaining the core flow rate at 0.1 ml/min. In addition, there was also an additional revision to the cross-linking conditions, in response to earlier experiments, by reducing the post-extrusion cross-linking time using 100 mM CaCl₂ from 10 minutes to 5 minutes with secondary cross-linking using 50 mM BaCl₂ for 2 minutes. Live/Dead analyses were used to analyse resulting filament viability and diameter.

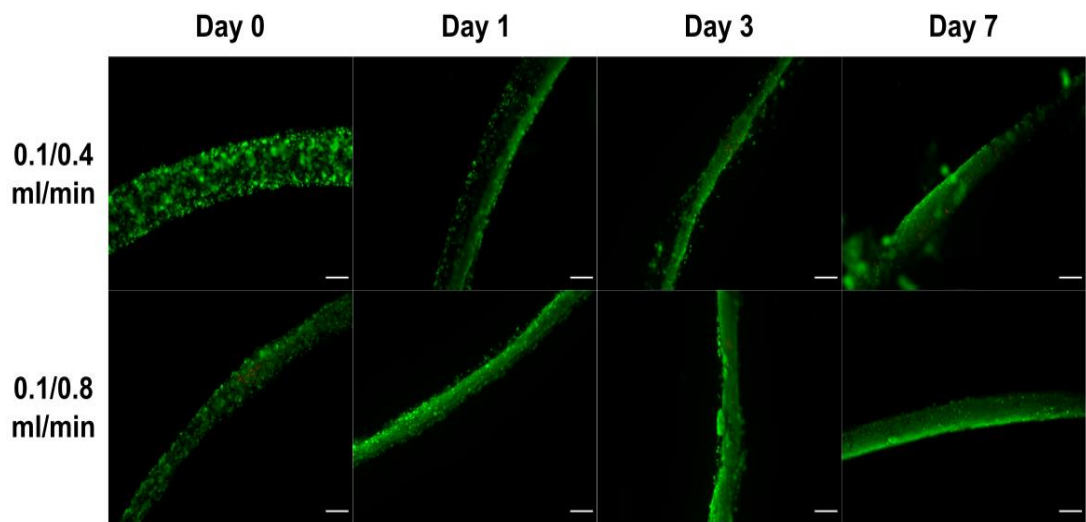


Figure 5-13. Representative day 0 to 7 live/dead imaging of ADSCs encapsulated within the 3.0 mg/ml collagen core of 2.0% (w/v) alginate scaffolds cross-linked in a 100 mM CaCl_2 bath for 5 minutes with secondary cross-linking using 50 mM BaCl_2 for 2 minutes at a cell seeding density of 10.0×10^6 cells/ml and core/shell flow rates of 0.1/0.4 and 0.1/0.8 ml/min. Scale bar = 200 μm .

On analysis of Figure 5-13, it can be seen that the increase in shell flow rate resulted in an expected reduction in the cell-collagen filament diameter on day 1, from $98.5 \pm 5.2 \mu\text{m}$ for a shell flow rate of 0.4 ml/min to $86.5 \pm 3.6 \mu\text{m}$ for the 0.8 ml/min case. The 0.1/0.4 ml/min case produced filaments which retained integrity for at least 48 hours, between days 1 and 3 prior to degradation between days 3 and 7. Meanwhile, the 0.1/0.8 ml/min case produced filaments which successfully retained morphology and viability for 6 days, between days 1 and 7.

On comparison of the day 7 images, the filaments extruded at the lower shell flow rate of 0.4 ml/min were in a degraded form; meanwhile, the higher flow rate case of 0.8 ml/min remained in a continuous filament state and may retain this fibrous state for > 7 days. It was assumed, according to theory, that the reduction in diameter provided by the increase in the shell flow rate was sufficient to facilitate unrestricted nutrient and waste diffusion to support filament viability. It was expected that smaller diameter filaments may be extruded with further increases to the shell flow rate.

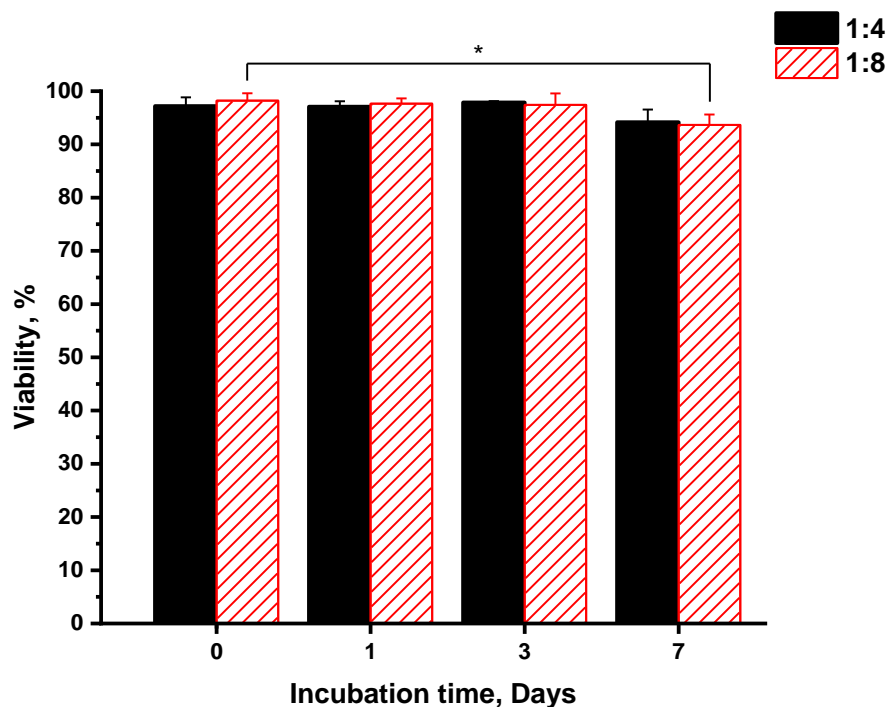


Figure 5-14. Viability of ADSCs encapsulated within the 3.0 mg/ml collagen core of 2.0% (w/v) alginate scaffolds cross-linked in a 100 mM CaCl_2 bath for 5 minutes with secondary cross-linking using 50 mM BaCl_2 for 2 minutes at a cell seeding density of 10.0×10^6 cells/ml and $Q_c/Q_s = 1:4, 1:8$. Data represents mean \pm SD ($n = 3$), Statistical analysis performed using a one-way ANOVA test with Tukey's post hoc test.

On quantitative analysis of cell viability for the two cases, displayed in Figure 5-14, post-extrusion viability for both cases was very high ($> 97.2\%$). Viability remained high throughout the course of the seven-day experiment, reaching minima on day 7 ($> 93.7\%$), with a statistically significant difference between the day 0 and day 7 viabilities for the 1:8 case ($p < 0.05$) indicating a slight decline in viability which requires further study with a longer-term experiment. In summary, cell viability for both cases across the seven-day experiment was acceptably high, demonstrating that the combination of flow rates and cross-linking conditions led to high-viability, fine diameter ADSC-collagen filaments. Filaments with lower average diameters produced as a result of the increase in shell flow rate appeared to have greater life spans, a characteristic which was studied further.

5.7.2. Combining flow effects with collagen concentration effects

With reference to previous work in this chapter and in Chapter 2, as it has been demonstrated that separately reducing the core/shell flow rate ratio and reducing the concentration of collagen apparently lead to a reduction in the coaxial extruded collagen filament diameter. It was assumed that these two effects could be combined and studied with the addition of cells in the collagen core.

Nirmalanandhan et al. [8] seeded collagen constructs with mesenchymal stem cells (MSCs) and studied the effect of the cell-to-collagen ratio on collagen contraction over a 168h period. The collagen concentration ranged from 1.3 to 2.6 mg/ml whilst the cell seeding density ranged from 0.1 to 1.0×10^6 cells/ml. The major finding was that the higher the cell-to-collagen ratios led to significantly greater contraction in comparison to the lower ratios.

Similarly, Chieh et al [9] performed a 14-day study using bone marrow stromal cells seeded within collagen constructs to study collagen contraction kinetics. By manipulating the collagen concentration between 0.5 and 2.0 mg/ml and using cell seeding densities between 0.1×10^6 and 1.0×10^6 cells/ml, their findings positively correlated with the findings of Nirmalanandhan et al. in that the highest cell density and lowest collagen concentration produced the most rapid construct contractions. Interestingly, all constructs contracted to similar final sizes (around 5% of initial area).

5.7.2.1. Effect of flow rate on filament diameter with changing collagen concentration

Given these results, it was assumed that significantly smaller coaxial extruded cell-collagen filaments could be cultured using comparatively lower collagen concentrations whilst maintaining the cell seeding density. To analyse the diameter and lifespan of these filaments over a 21-day culture period, collagen solutions at concentrations of 0.3 ($\pm 0.13\%$), 1.0 and 3.0 mg/ml were seeded and coaxially extruded with 1.0×10^6 ADSC/ml. The shell flow rate was tested at flow rates between 1.0 ml/min and 6.0 ml/min, in increments of 1.0 ml/min to provide an analysis of the combined effect of flow rate ratio and collagen concentration manipulation. The core flow rate was maintained at 0.1 ml/min. Live/Dead analyses and brightfield microscopy were used to analyse resulting filament viability and diameter over a 21-day culture period.

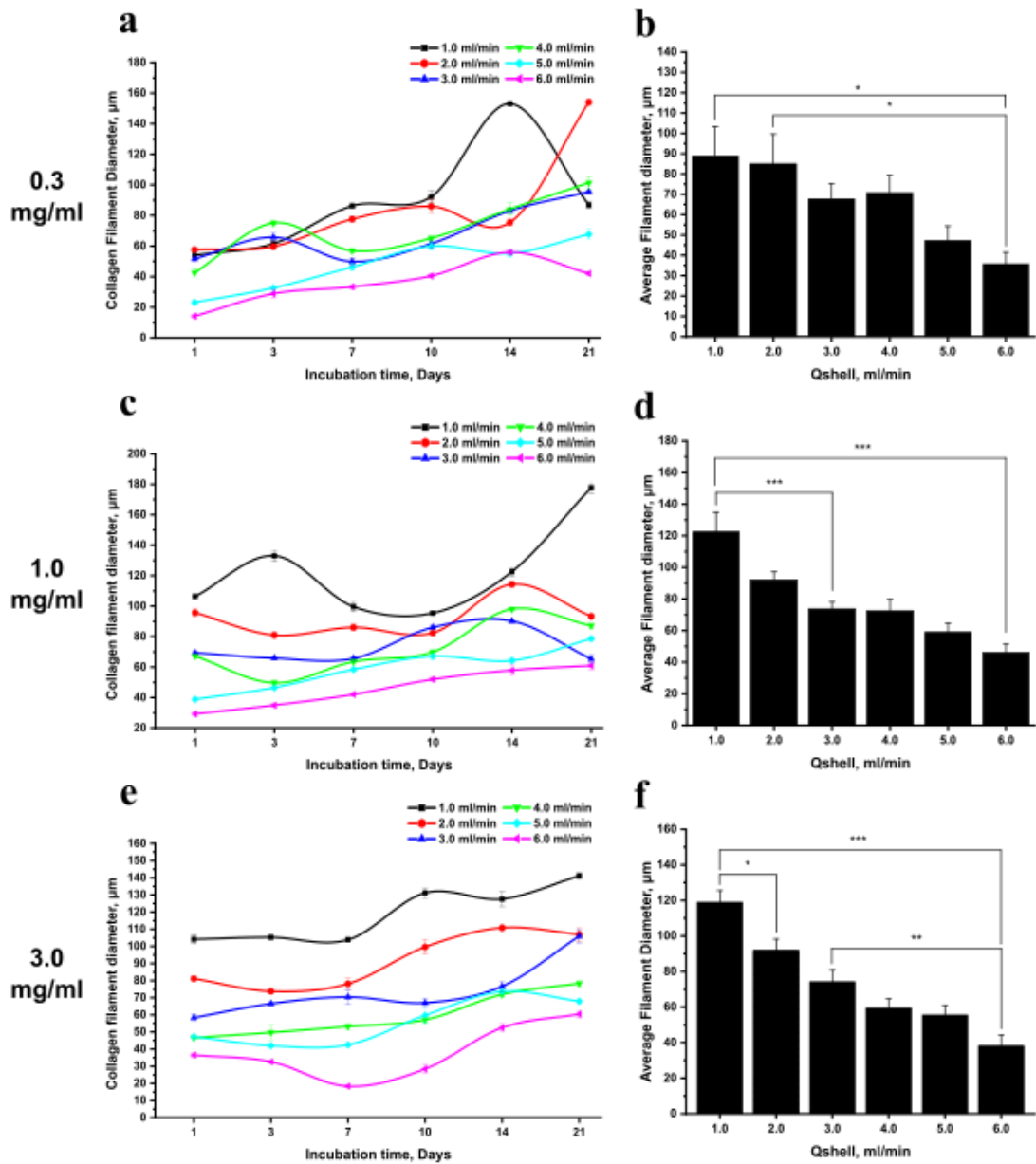


Figure 5-15. Effect of changing shell alginate flow rate on collagen filament diameter seeded with 1.0×10^6 cells/ml within 2.0% w/v alginate shell cross-linked in a 100 mM CaCl_2 bath for 5 minutes with secondary cross-linking using 50 mM BaCl_2 for 2 minutes, $Q_c = 0.1$ ml/min. Cell-collagen filament diameter over 21-day incubation period using (a) 0.3 mg/ml, (c) 1.0 mg/ml, (e) 3.0 mg/ml. (b) 21-day average cell-collagen filament diameter using 0.3 mg/ml, (d) 1.0 mg/ml, (f) 3.0 mg/ml. Data points represent mean \pm standard error (SE) ((a), (c), (e) $n = 3$; (b), (d), (f) $n = 6$). Statistical analysis performed using a one-way ANOVA test with Tukey's post hoc test.

Figure 5-15 (a), (c) and (e) track the average cell filament diameter over the 21-day incubation period for each tested shell flow rate using the respective collagen core concentrations. Additionally, Figure 5-15 (b), (d) and (f) present the corresponding 21-day average filament diameter as a function of shell flow rate for each tested collagen concentration.

This section serves to provide observations on the highest and lowest filament diameters for each collagen concentration used, in addition to analysing and comparing the statistical effect of Q_s variations on filament diameter. Later sections will seek to analyse the effect of collagen concentration on filament diameter and viability.

Firstly, it should be noted that continuous filaments were not observed at every time interval, in this case the recorded diameter was that of the average diameter of any aligned cell aggregates present (see Figure 5-16 (d)). On general observation of Figure 5-15, it was found that, in accordance with the collagen-only filament results in the previous chapter (see Figure 4-13), it was also observed that increasing Q_s led to a significant reduction in cell-seeded filament diameter, for all tested collagen concentrations on increasing the shell flow rate in increments of 1.0 ml/min ($p < 0.05$).

On analysis of Figure 5-15 (a), using 0.3 mg/ml collagen, the largest recorded filament diameter was found on day 21 for $Q_s = 2.0$ ml/min, at 154.1 ± 2.0 μm . It was expected that the smallest Q_s (1.0 ml/min) would return the lowest diameter; however, this configuration returned a similar diameter of 153.0 ± 0.4 μm seven days prior, on day 14. These two values appear as outliers; an explanation for these values may be that the samples may have been extruded before the core collagen filament experienced acceleration and narrowing due to transfer of momentum from the faster shell alginate flow. However, these values may not be outliers and may simply be part of the distribution when repeating this work using a higher sample number. The overall smallest diameter found was 14.1 ± 1.2 μm for $Q_s = 6.0$ ml/min on day 1, however, a continuous filament was not observed here (see Figure 5-16 (c) for corresponding image). It should be noted that continuous filaments were only observed using $Q_s = 1.0$ to 3.0 ml/min, from days 7 to 21.

On studying the 21-day average for each Q_s , Figure 5-15 (b) illustrates the statistically-significant effect of increasing Q_s on the cell-collagen filament diameter for the 0.3 mg/ml case, whereby significant reductions ($p < 0.05$, one-way ANOVA with Tukey's post hoc test) were observed between the 1.0, 2.0 and the 6.0 ml/min cases. The smallest average filament diameter, found for the $Q_s = 6.0$ ml/min case, measured 35.8 ± 5.7 μm . Further, the highest average filament diameter for cases where continuous filaments were observed using 0.3 mg/ml collagen was 67.9 ± 7.4 μm ($Q_s = 3.0$ ml/min, day 10 to 21).

Studying Figure 5-15 (c), it can be seen that on utilisation of 1.0 mg/ml collagen in the core of the coaxial nozzle, the smallest diameter filament channel found was 29.2 ± 1.2 μm , found again on day 1 for $Q_s = 6.0$ ml/min.

Conversely, the largest filament diameter was recorded for the lowest Q_s of 1.0 ml/min on day 21, at $177.8 \pm 3.8 \mu\text{m}$, an expected outcome given previous findings. However, this value appears as another outlier in comparison to all other filament diameters using the same flow rate. Another suspected case whereby the measured samples may have been an initial filament segment yet to experience momentum-induced narrowing which is a transient process or a result of a low sample number.

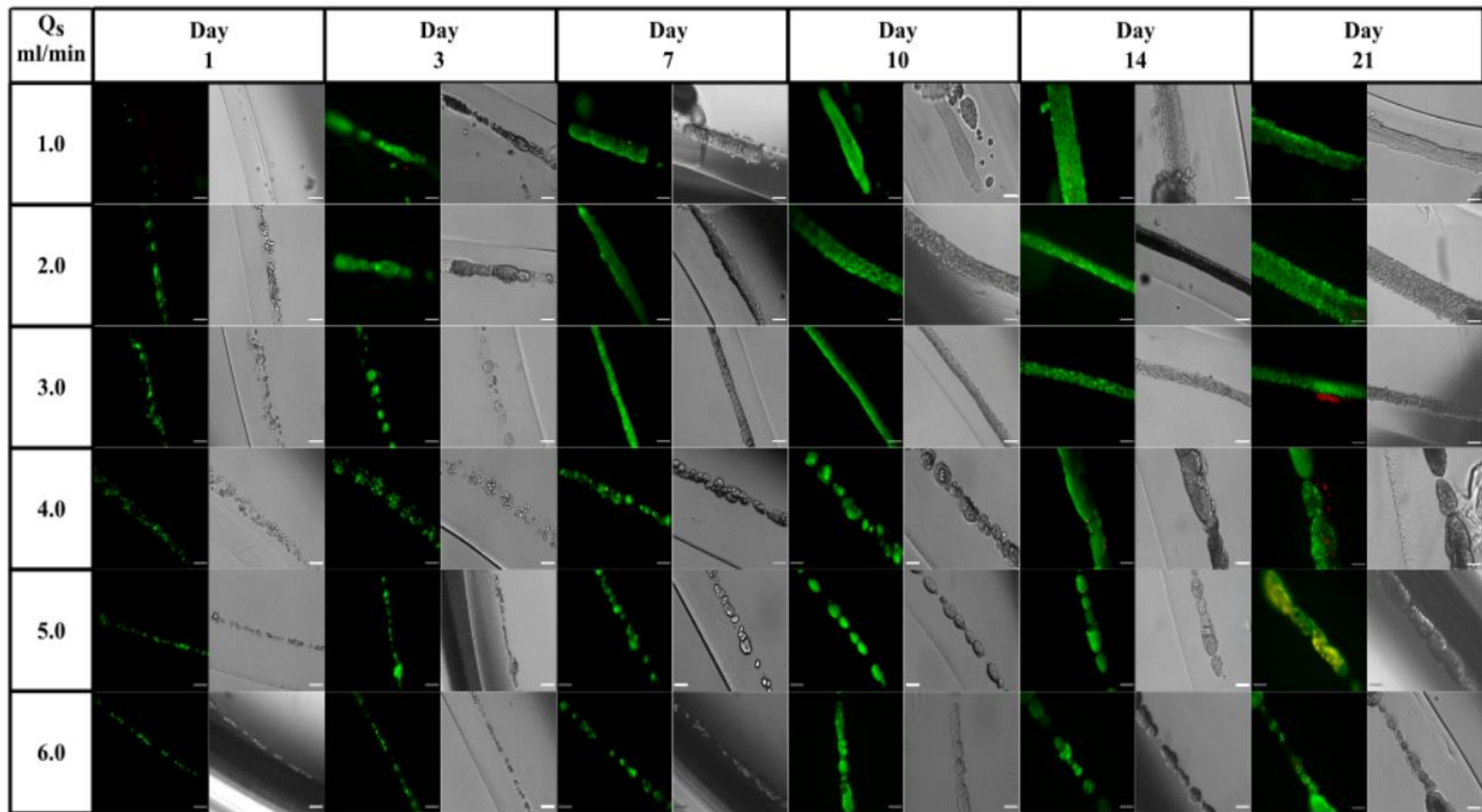
Figure 5-15 (d) provides the 21-day average cell-collagen filament diameters across the Q_s range of 1.0 to 6.0 ml/min, using 1.0 mg/ml collagen in the core stream. Significant differences were found between the 1.0 and 3.0 ml/min cases ($p < 0.001$), in addition to a significant statistical difference found between the highest (6.0 ml/min) and lowest (1.0 ml/min) shell flow rates ($p < 0.001$). The largest average filament diameter, using the lowest Q_s (1.0 ml/min) was $122.5 \pm 12.5 \mu\text{m}$ whilst the smallest filament diameter was found with the highest Q_s (6.0 ml/min), equalling $46.1 \pm 5.2 \mu\text{m}$.

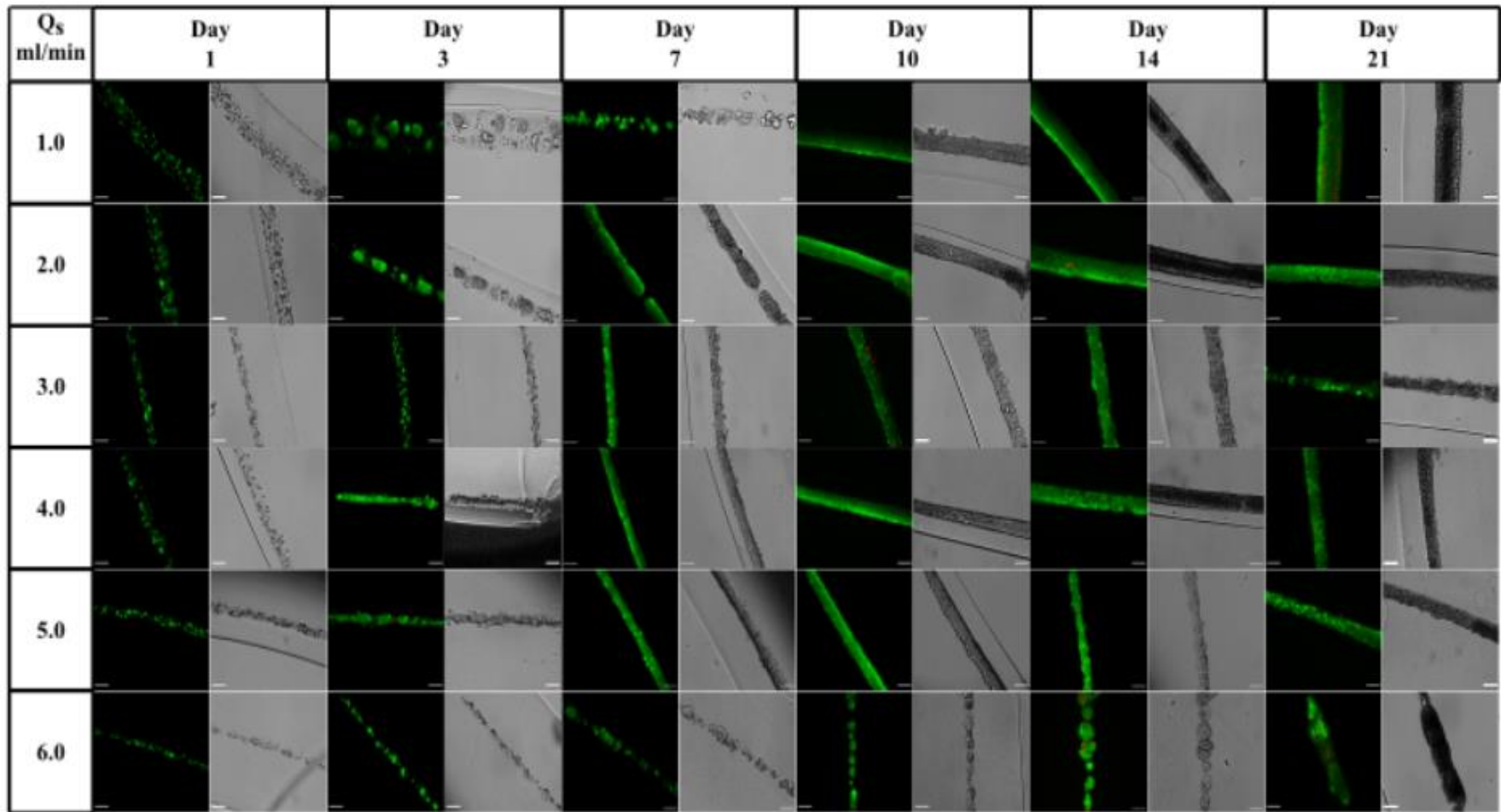
Figure 5-15 (e) tracks the average cell filament diameter over the 21-day incubation period using a 3.0 mg/ml collagen core for each tested shell flow rate. The filament diameter for the 1.0 ml/min case progressively increased from day 1 to day 21, peaking at a diameter of $141.1 \pm 2.1 \mu\text{m}$ on day 21. Meanwhile, the 6.0 ml/min case reached a minimum diameter of $18.3 \pm 0.4 \mu\text{m}$ on day 7 of culture, representing the smallest continuous filament diameter found for this collagen concentration experiment.

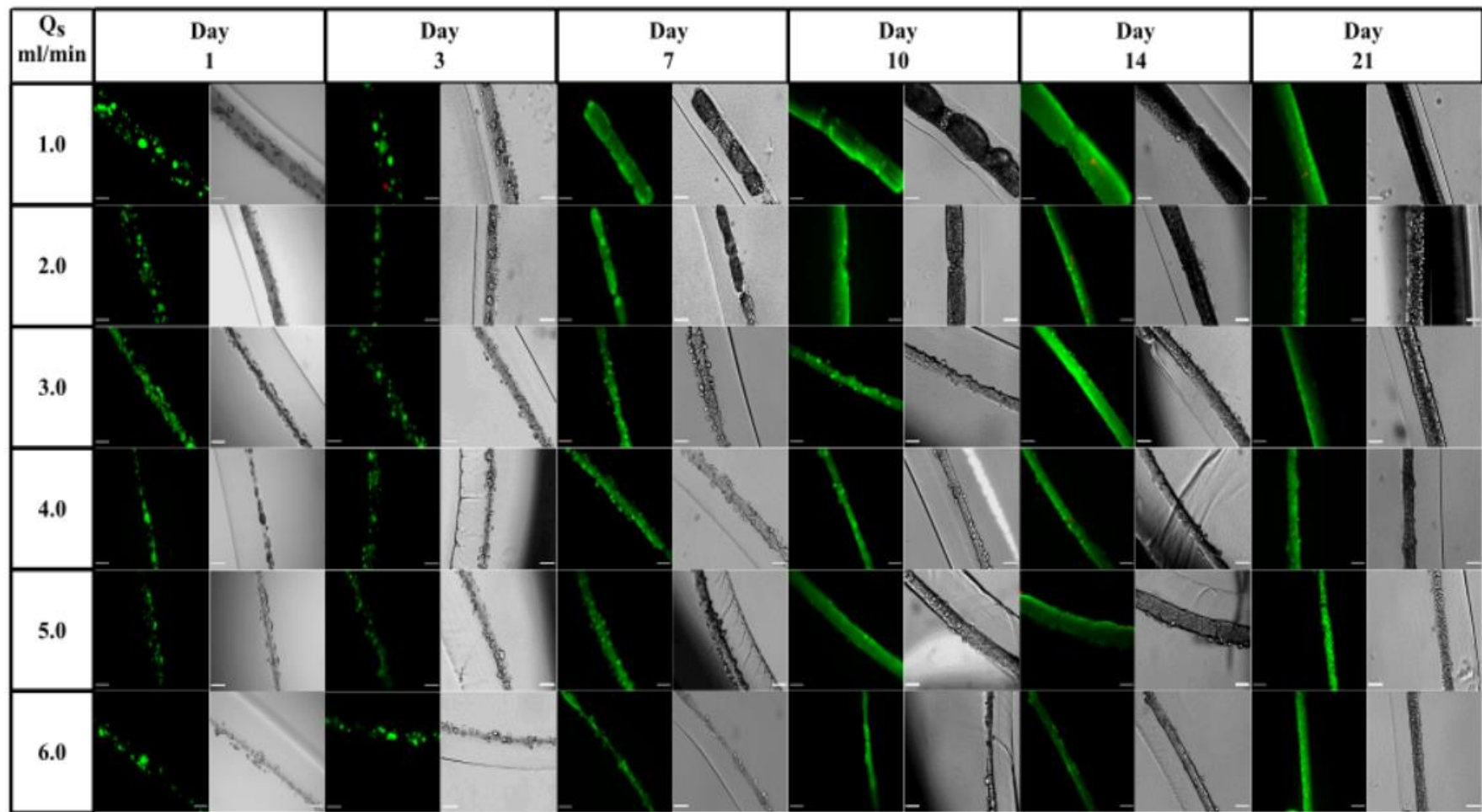
Addressing Figure 5-15 (f), the highest 21-day average filament diameter, using $Q_s = 1.0$ ml/min, measured $118.8 \pm 6.7 \mu\text{m}$. Meanwhile, this reduced, in a statistically-significant manner ($p < 0.001$), to $38.1 \pm 6.4 \mu\text{m}$ with $Q_s = 6.0$ ml/min. Significant differences were also found between the 1.0 and 2.0 ml/min cases ($p < 0.05$) and on a further increase of Q_s from 3.0 and 6.0 ml/min ($p < 0.01$). Collectively, the data in Figure 5-15 has clearly demonstrated the significant effect of reducing Q_c/Q_s on the resulting cell-collagen filament diameter.

5.7.2.2. Live/dead and brightfield imaging for three collagen concentrations

Figure 5-16 (a) – (c) presents the representative live/dead and brightfield images across the 21-day experimental period for all three tested collagen concentrations, thus providing a clear visual demonstration of the transition from dispersed cells into cell filaments.

a**0.3 mg/ml**

b**1.0 mg/ml**

C**3.0 mg/ml**

d

Q _s	0.3 mg/ml						1.0 mg/ml						3.0 mg/ml					
	Day 1	Day 3	Day 7	Day 10	Day 14	Day 21	Day 1	Day 3	Day 7	Day 10	Day 14	Day 21	Day 1	Day 3	Day 7	Day 10	Day 14	Day 21
1.0	-	-	-	-	+	+	-	-	-	+	+	+	-	-	+	+	+	+
2.0	-	-	+	+	+	+	-	-	+	+	+	+	-	-	+	+	+	+
3.0	-	-	+	+	+	+	-	-	+	+	+	+	-	-	+	+	+	+
4.0	-	-	-	-	-	-	-	-	+	+	+	+	-	-	+	+	+	+
5.0	-	-	-	-	-	-	-	-	+	+	+	+	-	-	+	+	+	+
6.0	-	-	-	-	-	-	-	-	-	-	-	-	-	-	+	+	+	+

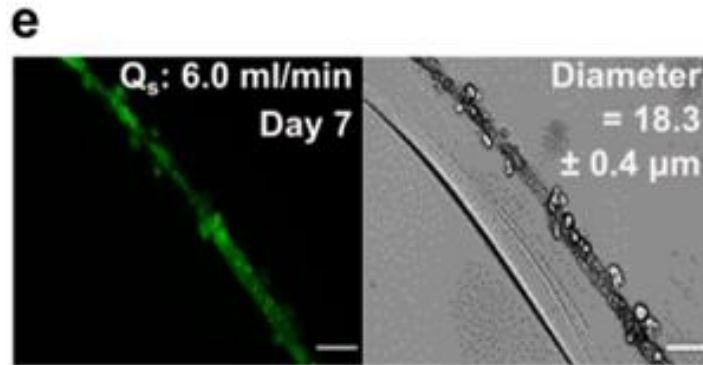


Figure 5-16. Representative live/dead and brightfield images over the 21-day experimental timeline for $Q_s = 1.0$ to 6.0 ml/min, in 1.0 ml/min increments, using (a) 0.3 mg/ml, (b) 1.0 mg/ml (c) 3.0 mg/ml collagen. Internal scale bars (white) = 100 μ m, External scale bar (black) = 1.0 mm. (d) Success (+) or failure (-) to produce aggregated cell filaments for the corresponding incubation time (day 1 - 21) and shell flowrate ($1.0 - 6.0$ ml/min) using 0.3 , 1.0 and 3.0 mg/ml collagen, (e) Live/dead and brightfield images showing the smallest extruded ADSC-collagen filament diameter, achieved on day 7 using 3.0 mg/ml collagen and $Q_s = 6.0$ ml/min. Scale bars = 100 μ m.

Figure 5-16 (d) provides information on the ability of filaments to form continuous cell filaments for each Q_s and corresponding collagen concentration. This allowed a comparison between shell flow rates and collagen concentrations on the success to form continuous filaments and their corresponding lifespans. For all cases, the earliest continuous filament appearance was day 7, indicating that 7 days are required for dispersed cells to aggregate and form a filament for the given cell seeding density. It is assumed that a higher cell-seeding density would lead to a more rapid filament formation time. The 3.0 mg/ml case was the only collagen concentration which facilitated the production of continuous filaments for all six tested shell flow rates. Moreover, filaments which successfully formed on day 7 remained continuous on day 21, proving a minimum filament lifespan of 14 days. The smallest diameter achieved for a single continuous filament measured 18.3 ± 0.4 μ m, as is presented in Figure 5-16 (e), found using 3.0 mg/ml collagen, recorded on day 7 of culture where $Q_s = 6.0$ ml/min.

5.7.2.3. Comparison between collagen and cell-seeded filaments

Using the data presented in Figure 5-15, a comparison was made between the ten-day average diameter of collagen-only and cell-seeded filaments, using 1.0 and 3.0 mg/ml collagen. This allowed an analysis of the effect of cells on the average filament diameter using brightfield microscopy.

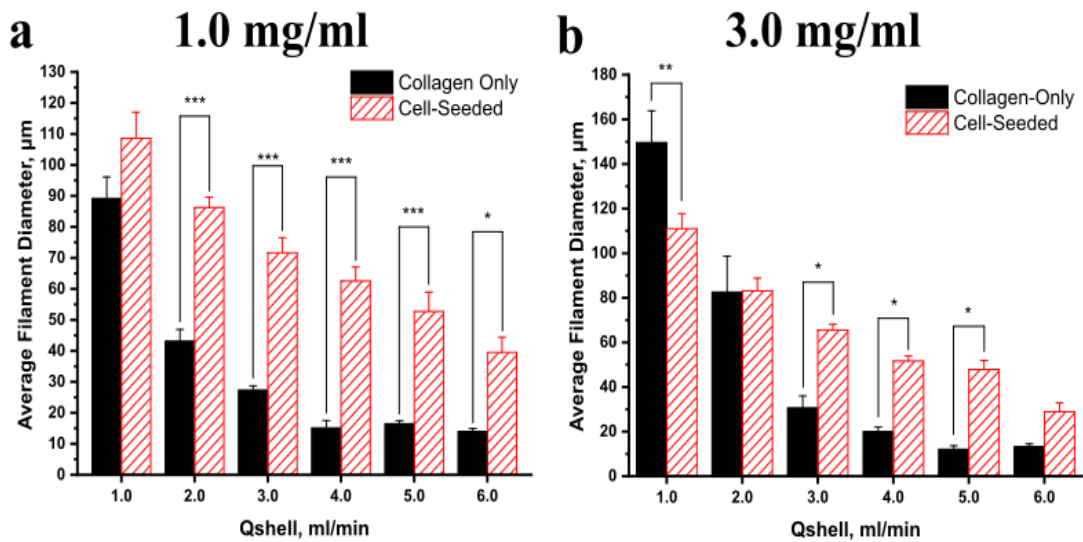


Figure 5-17. Comparison of ten-day average collagen-only and cell-seeded filament diameters using (a) 1.0 and (b) 3.0 mg/ml collagen within 2.0 % (w/v) alginate shell. $Q_c = 0.1$ ml/min. Cell seeding density = 1.0×10^6 ADSC/ml. Data points represent mean \pm SE (n = 4).

Figure 5-17 compares the collagen-only and cell-seeded filament diameter over a ten-day incubation period, using 1.0 and 3.0 mg/ml collagen respectively. It is clear that the addition of cells leads to a significant increase in the average filament diameter ($p < 0.05$) within the tested shell flow rate range. For the 1.0 mg/ml case, significant differences were found between the collagen-only and cell-seeded filament diameters for all Q_s save the lowest flow rate of 1.0 ml/min ($p < 0.05$). Further statistically significant differences were observed with the 3.0 mg/ml experiment ($p < 0.05$), with the 2.0 and 6.0 ml/min cases as exceptions.

This difference in average filament diameter between collagen-only and cell-seeded scaffolds was assumed to largely be a consequence of cell attachment and proliferation on collagen fibrils, leading to a larger cross-sectional filament area when cells are seeded and extruded within collagen solutions. It is assumed that the increase in filament diameter is proportional to cell-seeding density and this increase may continue up to a maximal value, whereby all cell-collagen binding sites are occupied.

5.7.2.4. Analysing the effect of collagen concentration on filament diameter

To investigate the effect of collagen concentration on cell filament diameter, the collagen concentration data was compared at three time intervals: days 1, 7 and 21. This allowed an analysis of the effect of collagen concentration and of the rate of cell-mediated collagen contraction and subsequent remodelling.

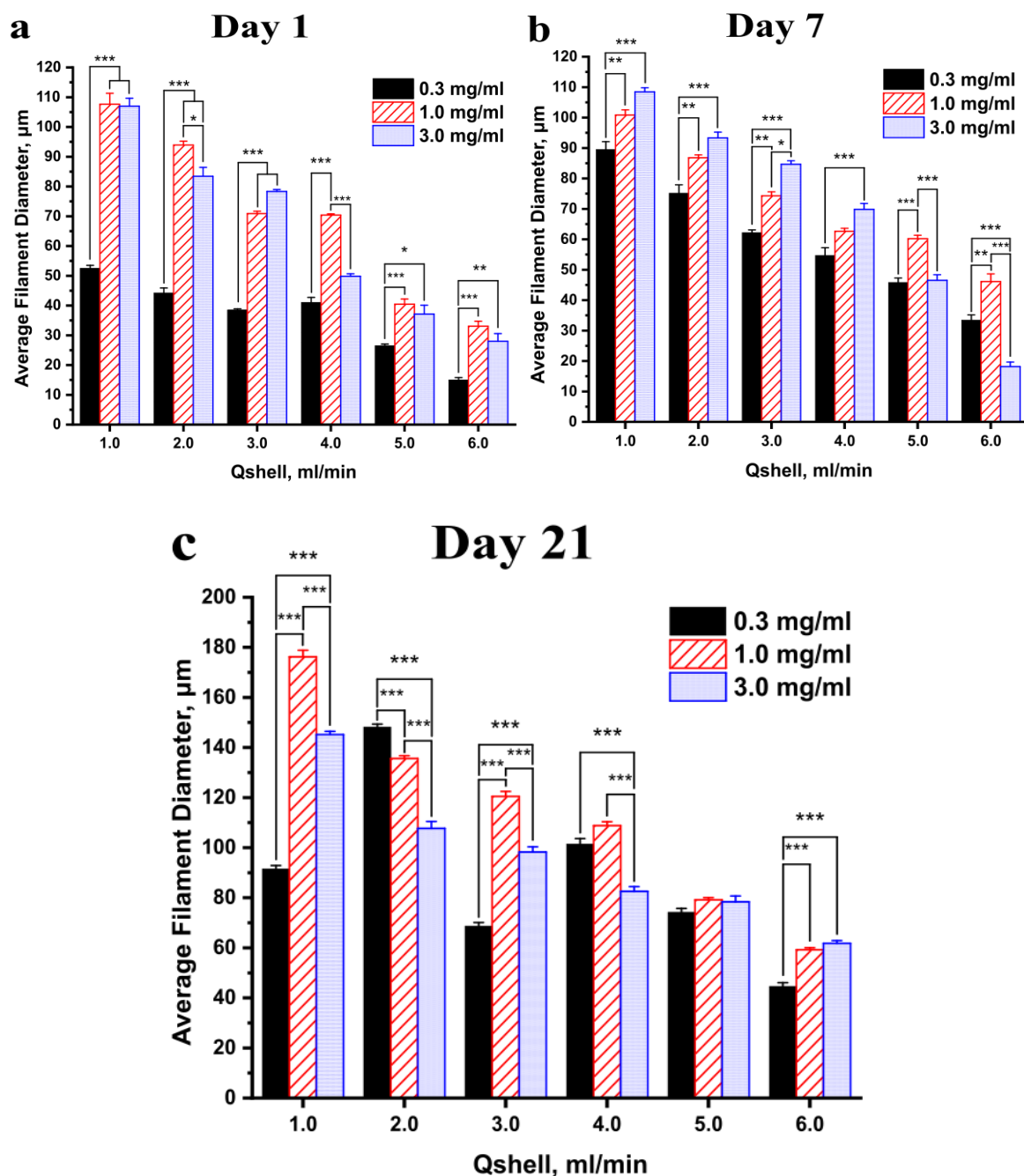
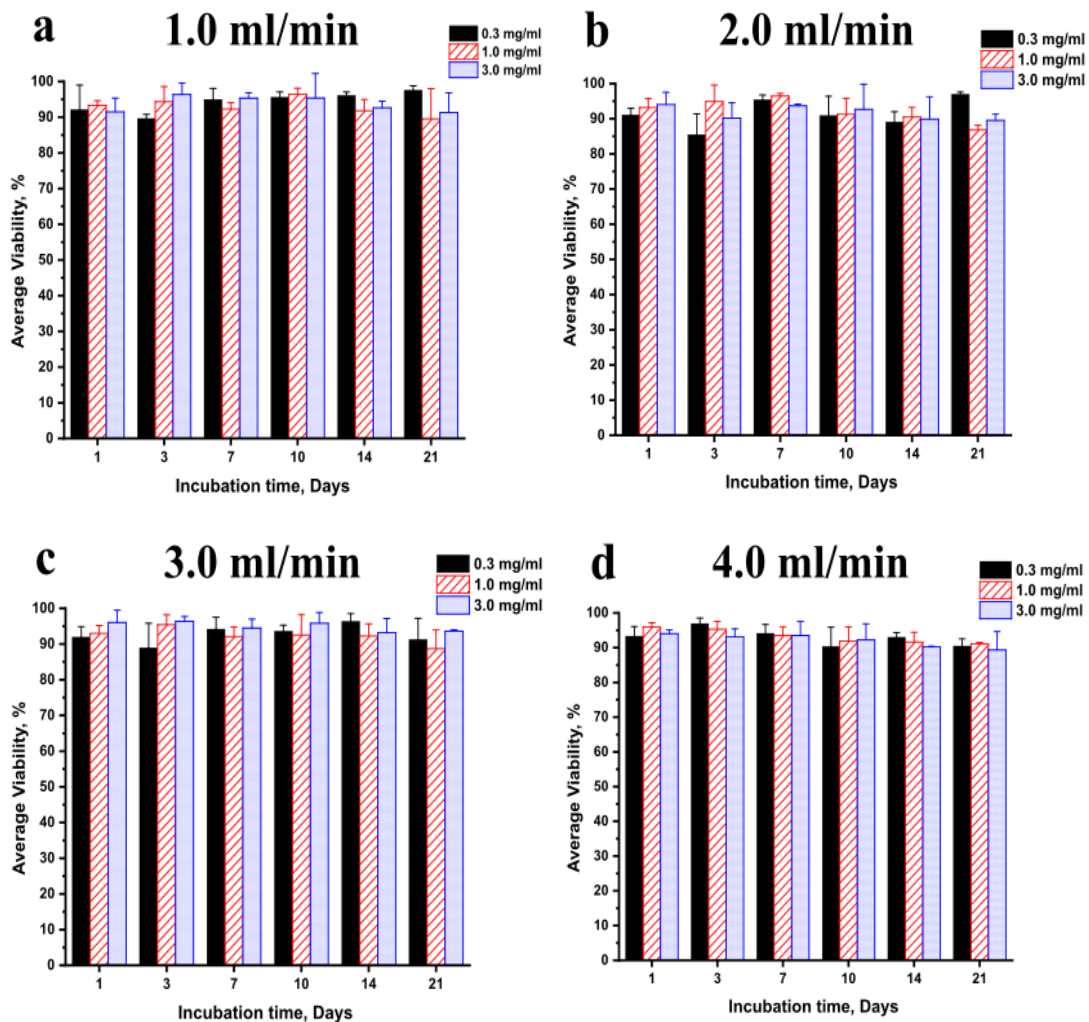


Figure 5-18. Effect of collagen concentration on average cell-seeded filament diameter within 2.0 % (w/v) alginate shell. Cell seeding density = 1.0×10^6 ml/min, $Q_c = 0.1$ ml/min. (a) day 1; (b) day 7; (c) day 21. Data points represent mean \pm SE (n = 3).

Figure 5-18 provides a comparison of the day 1, day 7 and day 21 average cell filament diameters using the three tested collagen concentrations (0.3, 1.0 and 3.0 mg/ml). On day 1, the 0.3 mg/ml case provided the lowest average filament diameter for all Q_s values ($p < 0.05$), indicating that the highest cell seeding density/collagen concentration ratio provided the most rapid collagen contraction compared to the 1.0 and 3.0 mg/ml collagen. The 0.3 mg/ml filaments were significantly smaller ($p < 0.05$) than the 3.0 mg/ml filaments on day 1. This difference was also observed on day 7 and day 21 for every Q_s case but the 4.0 ml/min case on day 1 and the 5.0 ml/min case on days 7 and 21.

However, as this significant difference was additionally observed for the higher Q_s value of 6.0 ml/min, these findings appeared as outliers.

Overall, given this evidence, the conclusion is that using 0.3 mg/ml collagen leads to significantly smaller filaments in comparison to using 3.0 mg/ml collagen; however, there were no persistent statistical differences between the filament diameters of 0.3 mg/ml case and the 1.0 mg/ml. Furthermore, there were also no constant statistical differences between the 1.0 and 3.0 mg/ml cases over the 21-day incubation period. This leads to a further conclusion that there is no significant difference in filament diameter between using 1.0 and 3.0 mg/ml over the course of the 21-day experiment.



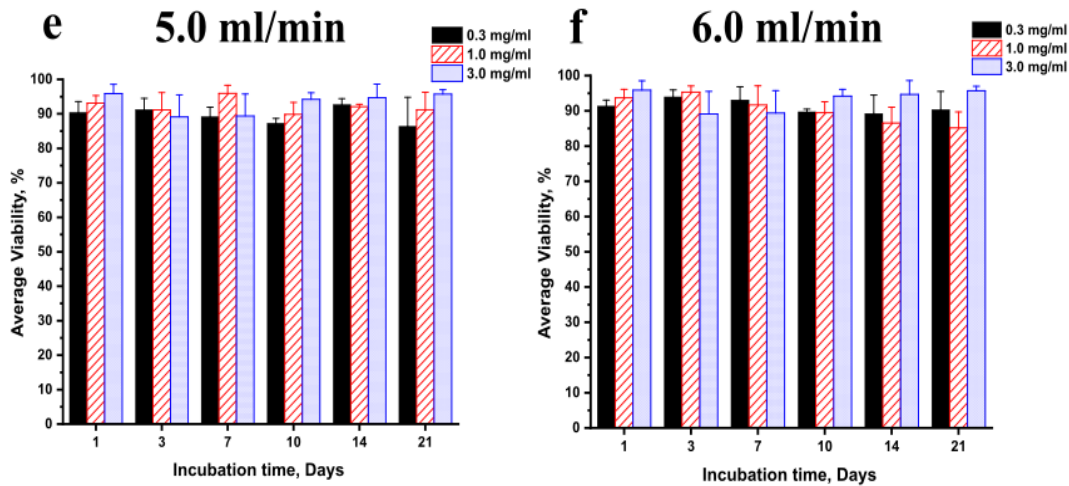


Figure 5-19. Average cell viability over a 21-day incubation period for $Q_s = 1.0 - 6.0$ ml/min in 1.0 ml/min increments. (a) 1.0 ml/min, (b) 2.0 ml/min, (c) 3.0 ml/min, (d) 4.0 ml/min, (e) 5.0 ml/min, (f) 6.0 ml/min. Data points represent mean \pm SD ($n = 3$).

Figure 5-19 displays the average cell viability over the 21-day experiment for each tested Q_s , comparing each of the three collagen concentrations used at each selected interval. On statistical analysis, when comparing both the effect of shell flow rate and collagen concentration on cell viability at each time point, there were no statistically significant differences found ($p > 0.05$, one-way ANOVA).

Furthermore, day 1 viability for all experiments was $\geq 90.4\%$, indicating that the chosen shell flow rate and collagen concentrations do not significantly compromise cell survival and thus facilitate proliferation over the course of the 21-day experiment. The average cell viability over the course of all experiments ranged from a high of $97.5 \pm 1.3\%$ (1.0 ml/min, 0.3 mg/ml collagen, day 21) to a minimum of $85.2 \pm 4.5\%$ (6.0 ml/min, 1.0 mg/ml, day 21), indicating favourable culture conditions.

On addition of ADSCs to the core collagen solution at 1.0×10^6 cells/ml and utilising 3.0 mg/ml collagen, fine diameter, high-viability cell-seeded filaments were cultured over a 21-day period. Again, there was an incremental decrease in filament diameter with corresponding increases in Q_s . The finest continuous cell-seeded filament, observed whilst using 3.0 mg/ml collagen, measured $18.3 \pm 0.4 \mu\text{m}$ in diameter, using $Q_s = 6.0$ ml/min (day 7). Thus, the theoretical relationship of decreasing the core/shell flow rate ratio leading to a finer filament diameter has been demonstrated for both collagen-only and cell-seeded collagen filaments using the coaxial extrusion platform described here.

It was observed that using the chosen cell-seeding density of 1.0×10^6 cells/ml, continuous cell filaments were not formed until day 7 of culture for all three studied concentrations of collagen, with the highest concentration of 3.0 mg/ml providing the greatest degree of success for filament formation relative to the Q_s values used, in that all six cases produced continuous, viable filaments on day 7.

An explanation may be that as higher concentrations of collagen provide greater mechanical strength, largely through hydrogen bonding between amino acid groups located along the collagen molecular backbone, there is a greater probability that filaments retain integrity prior to mechanical failure. Furthermore, all day 7 filaments retained continuity over a 14-day period, from day 7 to day 21, for all three studied collagen concentrations, indicating that formed continuous filaments retained integrity and resisted significant breakdown caused by ECM remodelling by cell-secreted MMPs.

On comparison of cell filament diameters whilst manipulating the collagen concentration, it was observed that the lowest concentration of 0.3 mg/ml produced the greatest apparent contraction of collagen and thus led to the lowest filament channel diameter on day 1 of culture. The contraction effect was at its most significant on day 1 of culture, with comparatively smaller filaments using 0.3 mg/ml in contrast to both 1.0 mg/ml and 3.0 mg/ml. In addition to the effect of reducing the core/shell flow rate ratio, this combined effect led to the production of fine diameter cell-seeded collagen filaments on day 7. However, due to the aforementioned mechanical weakness, the smallest diameter continuous filaments of the 0.3 mg/ml case measured $62.2 \pm 0.9 \mu\text{m}$ ($Q_s = 3.0 \text{ ml/min}$, day 7), comparatively larger than the $18.3 \pm 0.4 \mu\text{m}$ filaments ($Q_s = 6.0 \text{ ml/min}$, day 7) produced using 3.0 mg/ml. This significant difference between the 0.3 mg/ml and 3.0 mg/ml filament diameters remained until day 21; however, there was no persistent significant difference between the intermediate 1.0 mg/ml case and the 0.3 and 3.0 mg/ml tests.

These results suggest that there is an effect of collagen concentration on the rate of collagen contraction and filament diameter, particularly on day 1 and, to a lesser extent, across the entirety of the 21-day experiment. However, this effect is only significant between a very low, difficult-to-use concentration of 0.3 mg/ml and the commonly used concentration of 3.0 mg/ml across the 21-day experimentation period. Further studies may benefit from the combined application of a low core/shell flow rate ratio and low collagen concentration to provide reductions in filament diameter in addition to potential cross-linking of low concentration collagen filaments to produce more mechanically-stable filaments. Further work will investigate the effect of the manipulation of cell seeding density on filament diameter and viability.

5.7.3. Effect of cell seeding density on filament diameter

In order to elucidate the effect of cell seeding density on cell-collagen filament diameter, morphology and viability, filaments were extruded at a range of cell seeding densities, achieved by manipulating the number of cells embedded within neutralised collagen solutions based on cell counting results using a haemocytometer. It was hypothesised that an increase of cell seeding density would lead to both a greater likelihood for filaments to form and result in a more rapid rate of filament formation and smaller filament diameters due to the ability of cells to contract ECM materials as part of the cell-mediated remodelling effect.

As part of this hypothesis, it was suspected that this diameter reduction effect would be limited in application and further increases in cell density would firstly result in an increase of filament diameter, as a result of cellular overcrowding and the contractile ability consequently plateauing. Further increases in cell seeding density would ultimately lead to nozzle blockage due to insurmountable resistances to material flow caused by cell sedimentation and increases in solution viscosity.

The five chosen seeding densities were 0.1, 0.3, 0.5, 1.0 and 3.0 (all $\times 10^6$) cells/ml collagen, chosen due to limitations in resources in comparison to earlier experiments, where comparably higher cell seeding densities were used. This provided a 30-fold increase between the lowest and highest cell seeding density, thus providing a large range of study to provide informed conclusions based on the results of the study. The collagen solution concentration was fixed at 3.0 mg/ml whilst $Q_c = 0.1$ ml/min and $Q_s = 4.0$ ml/min. Extruded structures were cross-linked for 5 minutes using 100 mM CaCl_2 with further cross-linking using 50 mM BaCl_2 for 2 minutes. Test filaments were cultured over a 14-day period and analysed on days 1 (24h post-extrusion), 7 and 14 of culture, wherein live/dead and brightfield imaging were used to provide quantitative data on cell viability and filament diameter respectively.

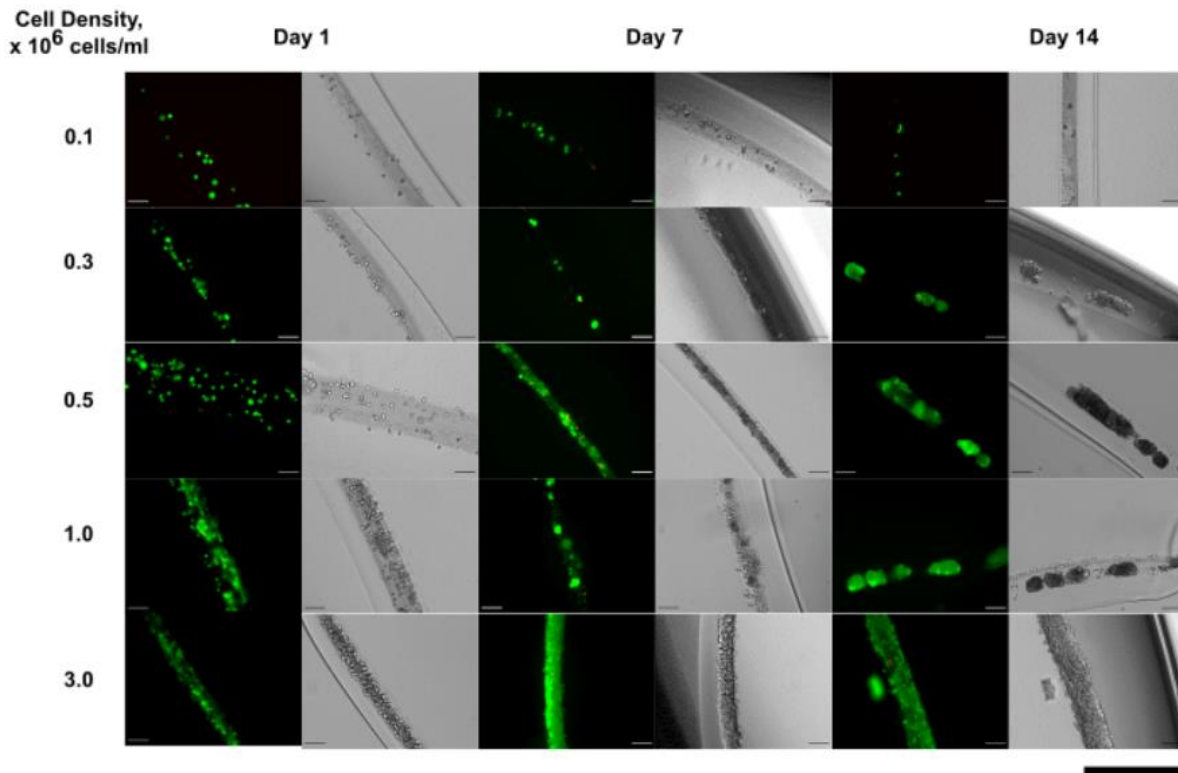
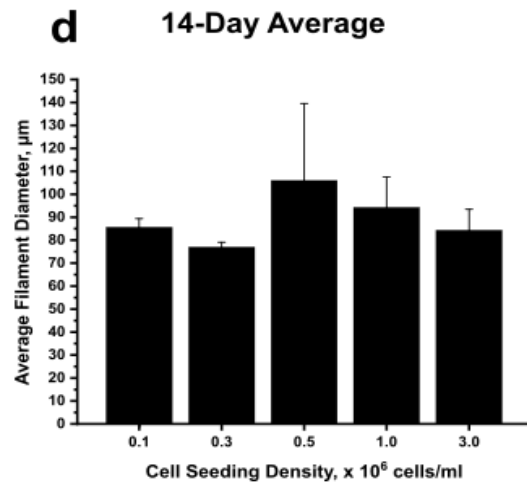
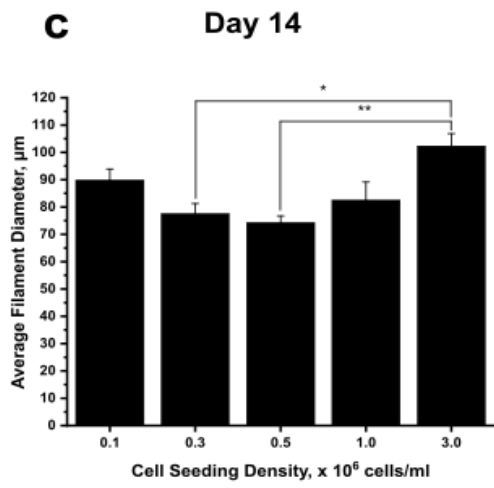
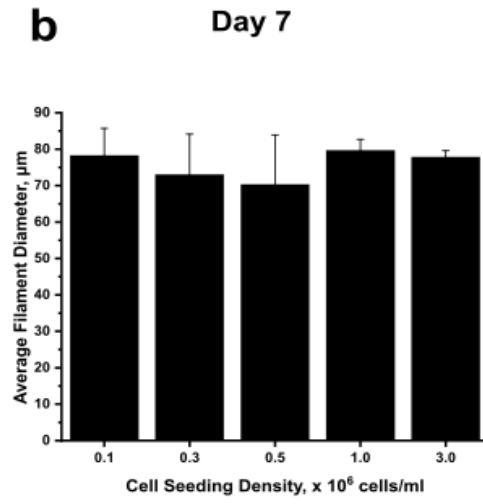
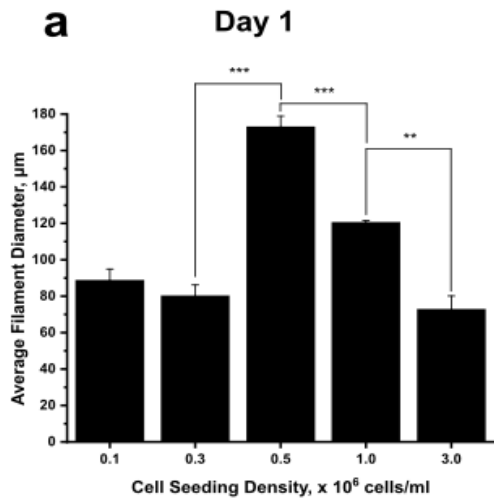


Figure 5-20. Representative live/dead and brightfield imaging across the 14-day experimental period, illustrating the effect of cell seeding density on coaxial extruded filament morphology and diameter using 0.1, 0.3, 0.5, 1.0 and 3.0 (all $\times 10^6$) cells/ml collagen. Collagen concentration = 3.0 mg/ml, shell = 2.0% w/v alginate cross-linked in a 100 mM CaCl_2 bath for 5 minutes with secondary cross-linking using 50 mM BaCl_2 for 2 minutes. $Q_c = 0.1$ ml/min, $C_s = 4.0$ ml/min. Internal scale bars = 100 μm , external scale bar = 500 μm .

On analysis of the live/dead and brightfield images presented in Figure 5-20, the common observation for all cases is that cells appear in a dispersed state on day 1, with proportionately more cells present with higher cell seeding densities. In addition, cells aggregated into either dispersed aggregates or, as is the case with the 3.0×10^6 cells/ml experiment, formed aggregated cell-collagen filaments on day 7 and remained in their relative states on day 14. It is clearly illustrated that when the cell seeding density is between 0.1 and 1.0×10^6 cells/ml the constructs lacked the ability to form continuous filaments, with an apparent transition between dispersed and aggregated states observed on days 7 and 14 for the 0.5 and 1.0×10^6 cells/ml case. On the basis of the evidence provided, it is recommended that the cell seeding density be set at $\geq 3.0 \times 10^6$ cells/ml to achieve the aggregation of cells along the collagen filament backbone to produce continuous cell-collagen filaments, using the provided extrusion and cross-linking parameters.



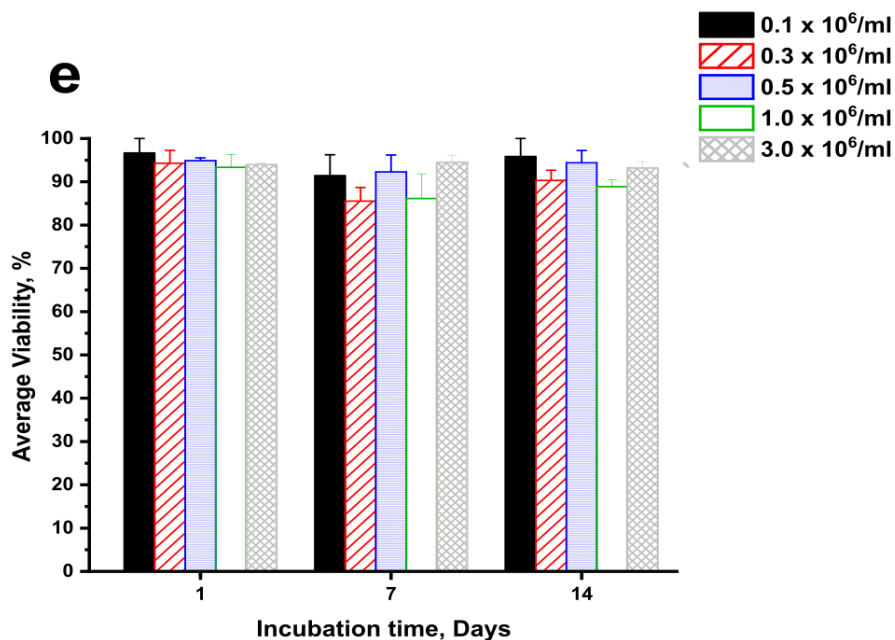


Figure 5-21. Effect of changing cell seeding density within 3.0 mg/ml collagen core on coaxial extruded collagen filament diameter using 2.0% w/v alginate shell cross-linked in a 100 mM CaCl₂ bath for 5 minutes with secondary cross-linking using 50 mM BaCl₂ for 2 minutes. $Q_c = 0.1$ ml/min, $C_s = 4.0$ ml/min. Average cell-collagen filament diameter on (a) Day 1, (b) Day 7, (c) Day 14 and (d) 14-Day average. (e) Effect of cell seeding density on cell filament viability. Data points represent mean \pm standard error (SE) ($n = 3$). Statistical analysis performed using a one-way ANOVA test with Tukey's post hoc test.

On the effect of cell density on cell-collagen filament diameter, it appears that there is minimal effect, from a statistical perspective. On analysis of Figure 5-21 (a), the diameter for the 0.5×10^6 cells/ml presents as statistically larger than all other cases ($p < 0.001$), with further significant decreases in diameter on increasing the cell density from 1.0×10^6 cell/ml and further to 3.0×10^6 cells/ml. Given this day 1 data, it seems that when using 0.5×10^6 cells/ml cells, these cells simply spread over the collagen filament and radially stretch the collagen filament, thus the filament diameter appearing relatively larger than lower seeding densities. However, given the day 7, day 14 and 14-day average diameter data, this data point seems more likely to be an anomaly, perhaps as a result of experimental error.

There was no apparent statistical effect of cell seeding density on filament diameter on day 7. On day 14, there was a significant increase ($p < 0.05$) in filament diameter on increasing the seeding density from 0.3 and 0.5×10^6 cells/ml to 3.0×10^6 cells/ml. This indicates that potential cellular overcrowding with the highest seeding density appears to have plateaued with regards to cellular contraction and remodelling of the collagen filament. Furthermore, there were no statistically significant differences in the 14-day average filament diameter.

In summary, it appears conclusive from the presented data in Figure 5-21 (a) – (d) that there is no clear statistically significant effect of cell seeding density on cell-collagen filament diameter, within the $0.1 - 3.0 \times 10^6$ cells/ml range whilst using ADSCs and 3.0 mg/ml collagen in the core of the coaxial nozzle. This indicates that changes to the collagen solution viscosity had negligible effect on the resulting filament diameters.

Finally, in reference to Figure 5-21 (e), cell viability remained high across the 14-day experimental period, with a minimum of $85.5 \pm 3.2\%$ recorded on day 7 for the 0.3×10^6 cells/ml case. Moreover, there was no statistically significant effect of cell seeding density on filament diameter within the tested density range. The maximal viability across the experiment of $96.7 \pm 3.3\%$ was recorded on day 14 for the 0.1×10^6 cells/ml case. Given this data, it was concluded that there is no statistically significant effect of changing cell seeding density, within the $0.1 - 3.0 \times 10^6$ cells/ml range, on the viability of ADSCs adhered to collagen filaments located with a cross-linked alginate shell.

5.8. Summary

To summarise, this chapter began with the demonstration of high viability coaxial extrusion of ADSCs within the collagen core of cross-linked alginate-shelled scaffolds with filament diameters measuring in excess of 400 μm . On the discovery of these alginate shells being degraded by ions contained within culture medium (phosphate, sodium, potassium etc.) within days, the alginate cross-linking parameters were modified, from 10 minutes in a 100 mM CaCl_2 bath to 5 minutes with the addition of secondary 50 mM BaCl_2 cross-linking for 2 minutes. In doing so, alginate shells retained integrity to facilitate the culture of collagen cores for > 21 days.

By reducing the core/shell flow rate ratio, from 1:10 to 1:60, whilst using 3.0 mg/ml, high viability, fine diameter cell-collagen filaments (< 30 μm) were cultured over a 21-day period, with filaments retaining continuity and viability for 14 days, from day 7 to 21 on the use of 1.0×10^6 cells/ml. Furthermore, it has also been presented that the manipulation of collagen concentration, from 3.0 to 0.3 mg/ml resulted in significantly smaller cell-collagen filaments ($p < 0.05$) across the 21-day period of study. However, this application is limited due to the low mechanical strength of the lower concentration of collagen. Future work may capitalise on this finding by utilising collagen cross-linking to increase the mechanical strength of these inherently weak filaments.

Finally, it has also been demonstrated that there was no significant effect of manipulating the cell seeding density, from 0.1 to 3.0×10^6 cells/ml, on the diameter or viability of the resulting extruded cell-collagen filaments, across a 14-day period.

The work presented in this chapter provides a valuable baseline to understand the various parameter effects on the diameter, continuity, and viability of ADSC-collagen filaments contained within tuneable porous cross-linked alginate shell scaffolds. Further work may focus on the use of other cell types and ECM materials within the core nozzle. Collagen alignment studies may be used to demonstrate the applicability of this work for the engineering of fibrous tissues and an investigation on the effect of leached cross-linking cations on in vivo applicability would also be very beneficial, in addition to many other valuable areas of study. The following chapter focuses on another aspect, namely the validity of this coaxial extrusion platform for drug testing applications.

5.9. References

- [1] F. J. O'Brien, "Biomaterials & scaffolds for tissue engineering," *Materials Today*, vol. 14, no. 3. Elsevier B.V., pp. 88–95, 01-Mar-2011.
- [2] E. C. Novosel, C. Kleinhans, and P. J. Kluger, "Vascularization is the key challenge in tissue engineering," *Adv. Drug Deliv. Rev.*, vol. 63, no. 4, pp. 300–311, Apr. 2011.
- [3] Q. Wei, V. Hariharan, and H. Huang, "Cell-cell contact preserves cell viability via plakoglobin," *PLoS One*, vol. 6, no. 10, p. 27064, 2011.
- [4] P. E. Van Den Steen, B. Dubois, I. Nelissen, P. M. Rudd, R. A. Dwek, and G. Opdenakker, "Biochemistry and molecular biology of gelatinase B or matrix metalloproteinase-9 (MMP-9)," *Critical Reviews in Biochemistry and Molecular Biology*, vol. 37, no. 6. pp. 375–536, 2002.
- [5] X. Dai *et al.*, "Coaxial 3D bioprinting of self-assembled multicellular heterogeneous tumor fibers," *Sci. Rep.*, vol. 7, no. 1, pp. 1–12, 2017.
- [6] N. Kakudo *et al.*, "Effects of transforming growth factor-beta1 on cell motility, collagen gel contraction, myofibroblastic differentiation, and extracellular matrix expression of human adipose-derived stem cell," *Hum. Cell*, vol. 25, no. 4, pp. 87–95, Dec. 2012.
- [7] A. G. Tabriz, M. A. Hermida, N. R. Leslie, and W. Shu, "Three-dimensional bioprinting of complex cell laden alginate hydrogel structures," *Biofabrication*, vol. 7, no. 4, Dec. 2015.
- [8] V. S. Nirmalanandhan, M. S. Levy, A. J. Huth, and D. L. Butler, "Effects of cell seeding density and collagen concentration on contraction kinetics of mesenchymal stem cell-seeded collagen constructs," *Tissue Eng.*, vol. 12, no. 7, pp. 1865–1872, 2006.
- [9] H. F. Chieh *et al.*, "Effects of cell concentration and collagen concentration on contraction kinetics and mechanical properties in a bone marrow stromal cell-collagen construct," *J. Biomed. Mater. Res. - Part A*, vol. 93, no. 3, pp. 1132–1139, 2010.
- [10] Y. Li, C. Qiao, L. Shi, Q. Jiang, and T. Li, "Viscosity of collagen solutions: Influence of concentration, temperature, adsorption, and role of intermolecular interactions," *J. Macromol. Sci. Part B Phys.*, vol. 53, no. 5, pp. 893–901, May 2014.

6. Extruded Tissue Filaments as a Mini Organ Platform for Drug Toxicity Testing

6.1. Introduction

On successful coaxial extrusion of fine diameter, high-viability ADSC-seeded collagen filaments within fine-tuned cross-linked alginate shells, it was hypothesised that this methodology could also serve as the basis for a high-throughput organ-on-a-chip drug testing platform, by testing collagen filaments seeded with primary hepatocytes or hepatocyte-like cells, using various hepatotoxic compounds at a range of concentrations. There are a few different approaches to drug testing methodologies, of which are highlighted in Figure 6-1 below.

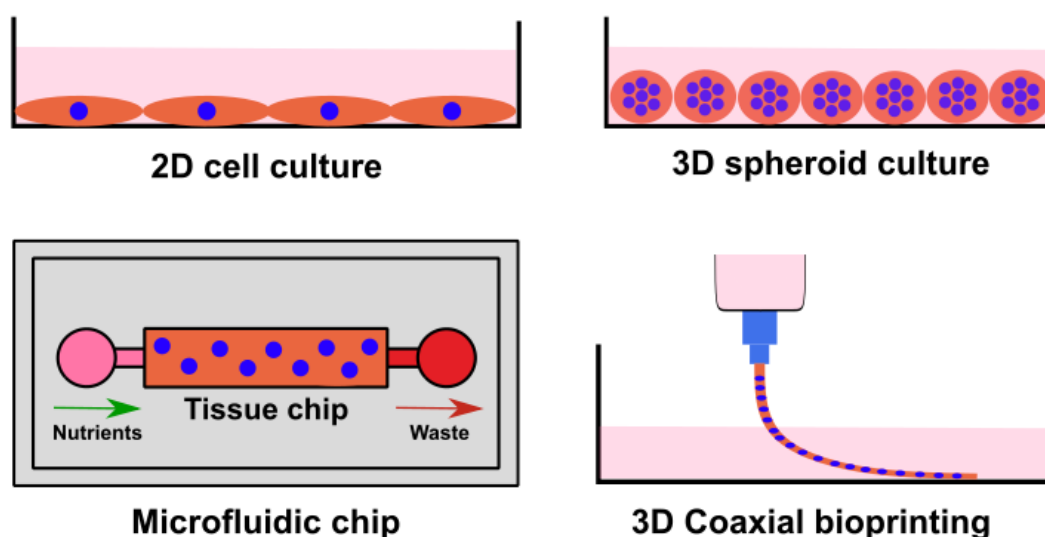


Figure 6-1. Illustration showing different cell-based drug testing methodologies, ranging from traditional 2D culture to 3D spheroids, microfluidic chips and coaxial extrusion.

Tissue engineering and bio-extrusion approaches to drug testing provide a substantial advantage over traditional 2D cellular models for testing due to the ability to provide cells with a more natural, biomimetic in vivo-like 3D environment with limited contact to synthetic materials such as tissue culture plastics. Bio-extrusion particularly provides the advantage of automation, stability and predictability and can permit the fabrication of multi-material, highly-biomimetic tissue models [1]

6.1.1. Aims

By analysing coaxial extruded tissue filament cell viability response to various drugs and comparing the acquired LC_{50} values (lethal concentration which reduces population viability to 50% of negative control value) with available published data; this would provide preliminary data to demonstrate the validity of this platform for drug testing. A further analysis of cytochrome P450 (CYP450) enzyme activity was also performed to provide further insight into the effects of tested drugs on cellular metabolic function.

The chosen cell line for the studies presented within this chapter was HepaRG, a bipotent human hepatoma cell line originally derived from a hepatocellular carcinoma (cholangiocarcinoma) capable of terminal differentiation towards either biliary-like or hepatocyte-like phenotype [2]. HepaRG cells are capable of expressing most liver-specific functions, such as MRP-2, albumin and phase I, II and III enzymes and can be cultivated for several weeks with stable phenotype [3]. Moreover, in contrast to other human hepatoma cell lines, including HepG2, HepaRG cells also express many CYP450 enzymes [4]. Furthermore, HepaRG cells have successfully been used for experimentation involving a wide range of compounds for toxicity studies since their introduction via a first publication in 2002 [5] across an array of academic journals [6] [7] [8], thus demonstrating their reliability for application in this work.

The aim of this work was to analyse the viability of the coaxial extrusion platform, using HepaRG-seeded collagen core filaments within alginate shells, for use in drug testing applications involving HepaRG cells by performing cellular viability testing using various drugs to compare LC₅₀ values with those of the literature, with 3D culture values being more desirable due to expected differences between 3D and 2D culture. The tested drugs were selected based on their published relative hepatotoxicity, ranging from prednisolone (non-toxic) [9], to acetaminophen (toxic) [10] and azathioprine (toxic) [11] and finally to amiodarone (severely toxic) [12]. The chemical structure of each tested drug is shown in Figure 6-2.

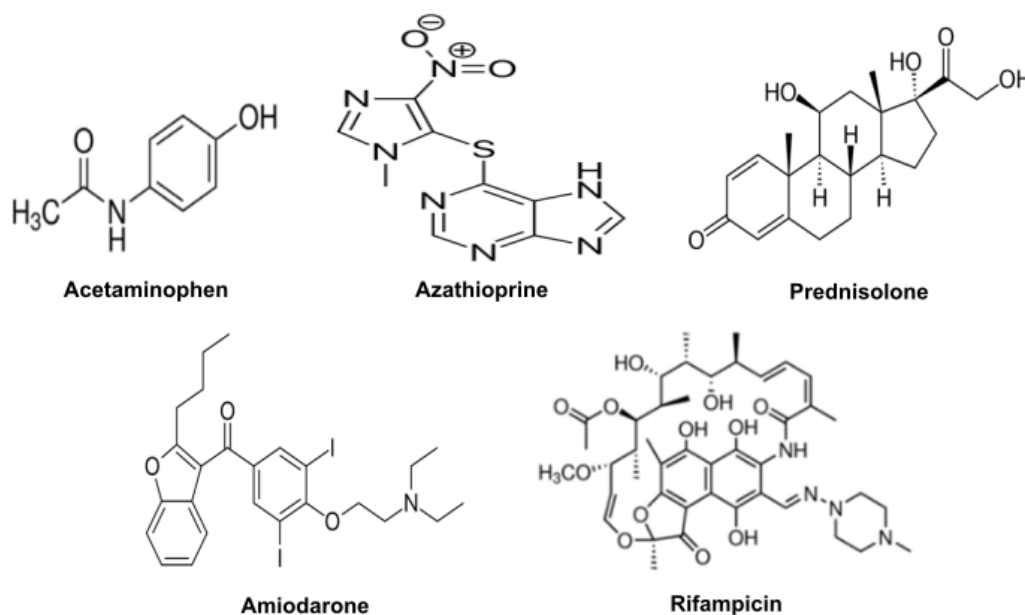


Figure 6-2. Chemical structures of compounds used as test drugs within the work presented in this chapter.

In addition, a CYP450 enzyme activity assay was also performed to analyse cellular metabolic function in response to dosing with a well-known CYP450-inducing drug, rifampicin.

6.2. Drug testing viability analysis

HepaRG cells were added to a collagen solution (3.0 mg/ml) and drawn into a 1.0 ml syringe and subsequently placed into the core inlet of the extrusion nozzle (see sections 3.1.4 and 3.1.5 for collagen preparation protocol). The cell seeding density utilised here was 3.0×10^6 cells/ml, Q_c (core nozzle flow rate) was 0.1 ml/min; 2.0% (w/v) alginate was used as the shell solution and Q_s (shell nozzle flow rate) was set at 3.0 ml/min. Extruded structures were cross-linked in 100 mM CaCl_2 for 5 minutes, followed by secondary cross-linking using 50 mM BaCl_2 for 2 minutes. For drug testing, cells were exposed to test compounds for 48 hours, between days 5 and 7 of culture, prior to viability analysis on day 7. Viability analysis was performed by live/dead assay, using solutions of FDA (Fluorescein diacetate) and PI (propidium iodide). Whilst acetaminophen was dissolved directly in warmed media (37 °C), azathioprine, amiodarone, prednisolone and rifampicin were firstly dissolved in DMSO (dimethyl sulfoxide) prior to dilution to the desired concentration in media, whereby the final concentration of DMSO in media was fixed at 0.1% (v/v) in all cases, sufficient to avoid HepaRG differentiation (See section 3.2 for further information on drug solution preparation) [13]. Data are presented in the form: mean \pm SD (standard deviation).

6.2.1. Drug-free HepaRG extrusion

Firstly, to understand the ability of HepaRG cells to survive the extrusion process and subsequent culture, a 14-day experiment was conducted, in which HepaRGs were combined with collagen in the core coaxial nozzle and extruded, where extruded constructs were suspended and incubated in culture medium at 37 °C, in the absence of test drugs.

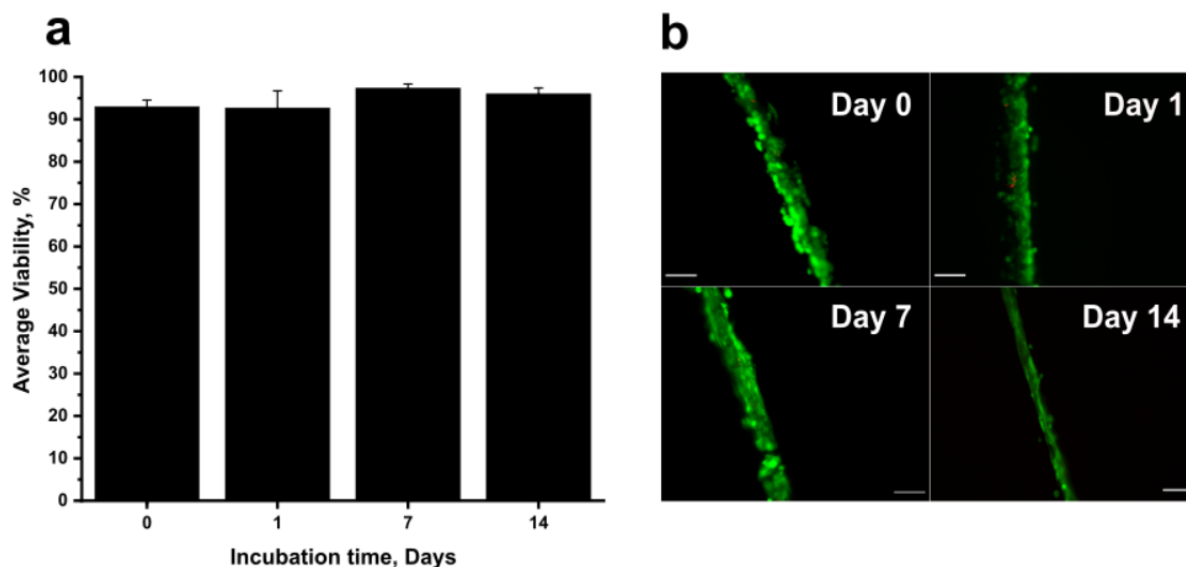


Figure 6-3. Live/dead analysis of coaxial extruded HepaRG cell-collagen filaments contained within alginate shells. Collagen concentration = 3.0 mg/ml, cell seeding density = 3.0×10^6 cells/ml, alginate shells were cross-linked using 100 mM CaCl_2 for 5 min with secondary cross-linking using 50 mM BaCl_2 for 2 min. (a) Cell viability at days 0, 1, 7 and 14 of culture. Data points represent mean \pm SD ($n = 3$), (b) representative live/dead images for each corresponding day of culture. Scale bars = 200 μm .

In reference to Figure 6-3 (a), it can be seen that viability remained acceptably high ($> 90\%$) throughout the 14-day culture period, with viability at a minimum of $92.7 \pm 4.0\%$ on day 1 and reaching a maximum of $97.4 \pm 0.9\%$ on day 7. Interestingly, filament diameter (D_c) ranged from $68.9 \pm 5.0 \mu\text{m}$ on day 0 to $24.4 \pm 1.2 \mu\text{m}$ on day 14, thus demonstrating the findings in previous chapters, which utilised ADSCs also hold true for HepaRGs, in that using a low core/shell flow rate ratio provides fine diameter core collagen filaments within cross-linked alginate shells. The combination of the high 14-day cell viability and sub-100 μm filament minimal filament diameter indicate that, on addition of drugs for testing, observed cell death would solely be from these drugs and unaffected by nutrient or waste diffusion limitations.

6.2.2. Acetaminophen

As a widely-used over-the-counter analgesic drug, acetaminophen (APAP), or paracetamol, is the leading cause of acute liver failure in Europe and the US [14]. In patients with chronic liver disease (CLD), APAP is considered a frontline analgesic, mainly due to concerns with side effects caused by non-steroidal anti-inflammatory drugs (NSAIDs), such as ibuprofen (renal dysfunction), and opioid-derived substances (dependence and over-sedation) [15] [16].

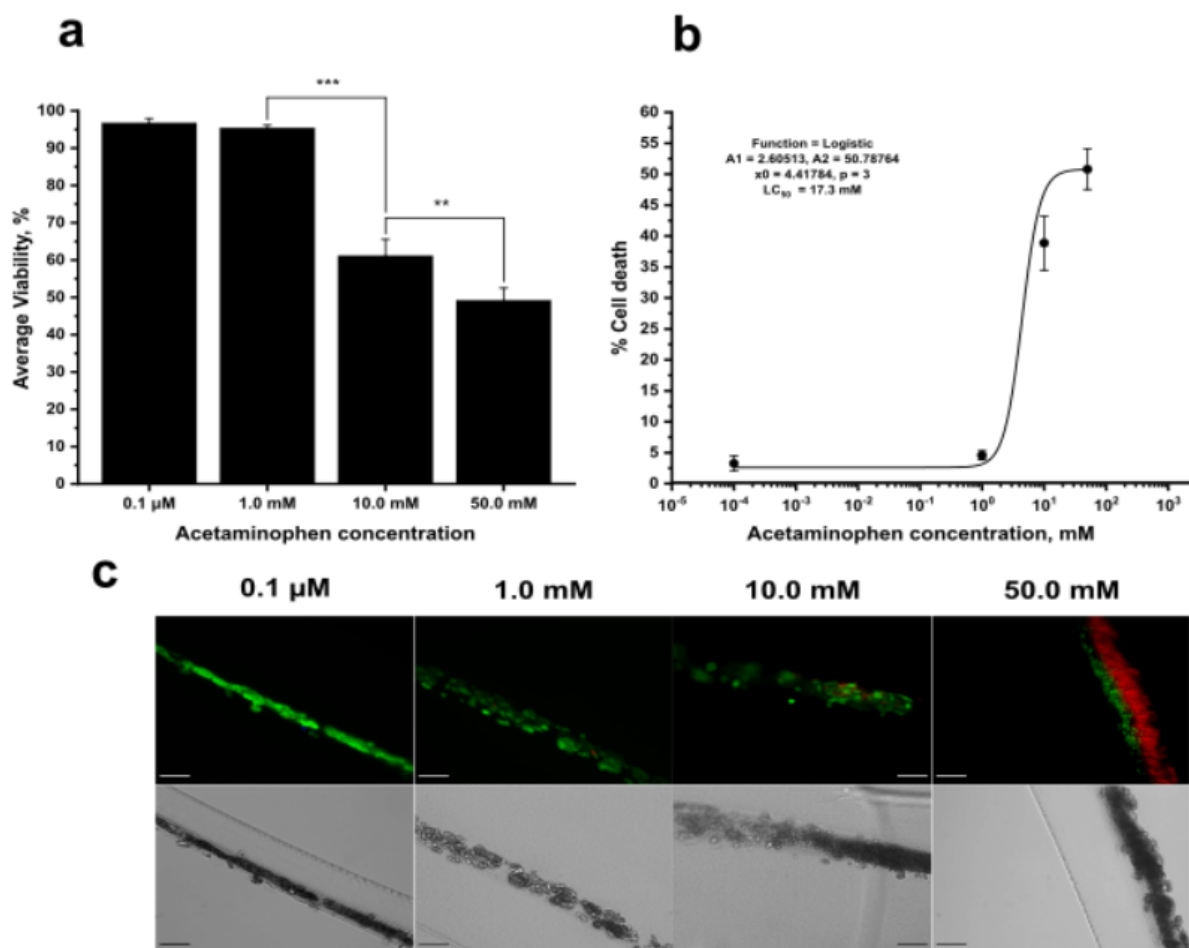


Figure 6-4. Day 7 HepaRG toxicity data on 48h exposure to 0.1 μ M, 1.0 mM, 10.0 mM and 50.0 mM acetaminophen (APAP). (a) Cell viability results for corresponding APAP concentrations, (b) LC_{50} graph with sigmoidal dose-response curve fit displaying corresponding equation parameters and LC_{50} value. Data points represent mean \pm SD ($n = 3$). (c) Representative day 7 live/dead and brightfield images showing decreasing cellular viability with increasing APAP concentration. Scale bars = 200 μ m. Statistical analysis performed using a one-way ANOVA test with Tukey's post hoc test. (* indicates $p < 0.05$; ** indicates $p < 0.01$. *** indicates $p < 0.001$). Note: dead cells in (c) for 50.0 mM case may be on one side due to drift of sample in well during image capture.

On analysis of many publications, Fey et al. reported that the LC_{50} of APAP on human hepatocytes ranged from 0.21 to 28.2 mM, with drug incubation times usually within the 24h – 72h window. On application of HepaRGs, Zhang et al. published data suggesting an LC_{50} of 20.0 mM on dosing 3D-cultured HepaRG cells with APAP for 24h [17]. In addition, Minsart et al. [18] presented viability data suggesting that the LC_{50} was in the range of 2.0 – 10.0 mM on dosing HepaRG cells with APAP for 24h. In consideration of these three sources, it was predicted that if the LC_{50} of the coaxial extruded HepaRGs fell within the general 0.21 – 28.2 mM range, that given by Fey et al. but also including those of Zhang et al. and Minsart et al., that there would be preliminary validity of these results, worthy of further experimentation.

On analysis of Figure 6-4 (a), it can be seen that increasing the APAP concentration from 1.0 mM to 10.0 mM (absolute error in concentration is $\pm 2.52\%$) resulted in a significant decrease in cell viability ($p < 0.001$), from $95.4 \pm 0.7\%$ to $61.1 \pm 4.4\%$, on incubation of HepaRGs with APAP for 48h. On increasing APAP concentration from 10.0 mM, viability declined further ($p < 0.01$) and dropped below 50% on dosing cells with $50.0 \text{ mM} \pm 0.52\%$ APAP.

On fitting the acquired data to a sigmoidal fit curve, shown in Figure 6-4, the LC_{50} was calculated as 17.1 mM, well within the predicated range, based on available published data, indicating the validity of the model for drug testing (see section 3.2.1 for information on curve fitting). The major drop in cell viability between the 10.0 and 50.0 mM cases is illustrated in the live/dead images presented in Figure 6-4 (c).

6.2.3. Azathioprine

Azathioprine (AZA) is used as an anticancer drug and as an immunosuppressant in addition to being used for the treatment of many inflammatory disorders, such as inflammatory bowel disease (IBD) and autoimmune diseases [19]. However, AZA has documented hepatotoxicity, whereby hepatotoxicity has occurred in patients using AZA for immunosuppressive treatment of IBD [20] and has also occurred in rheumatoid arthritis patients [21], amongst many other cases [22].

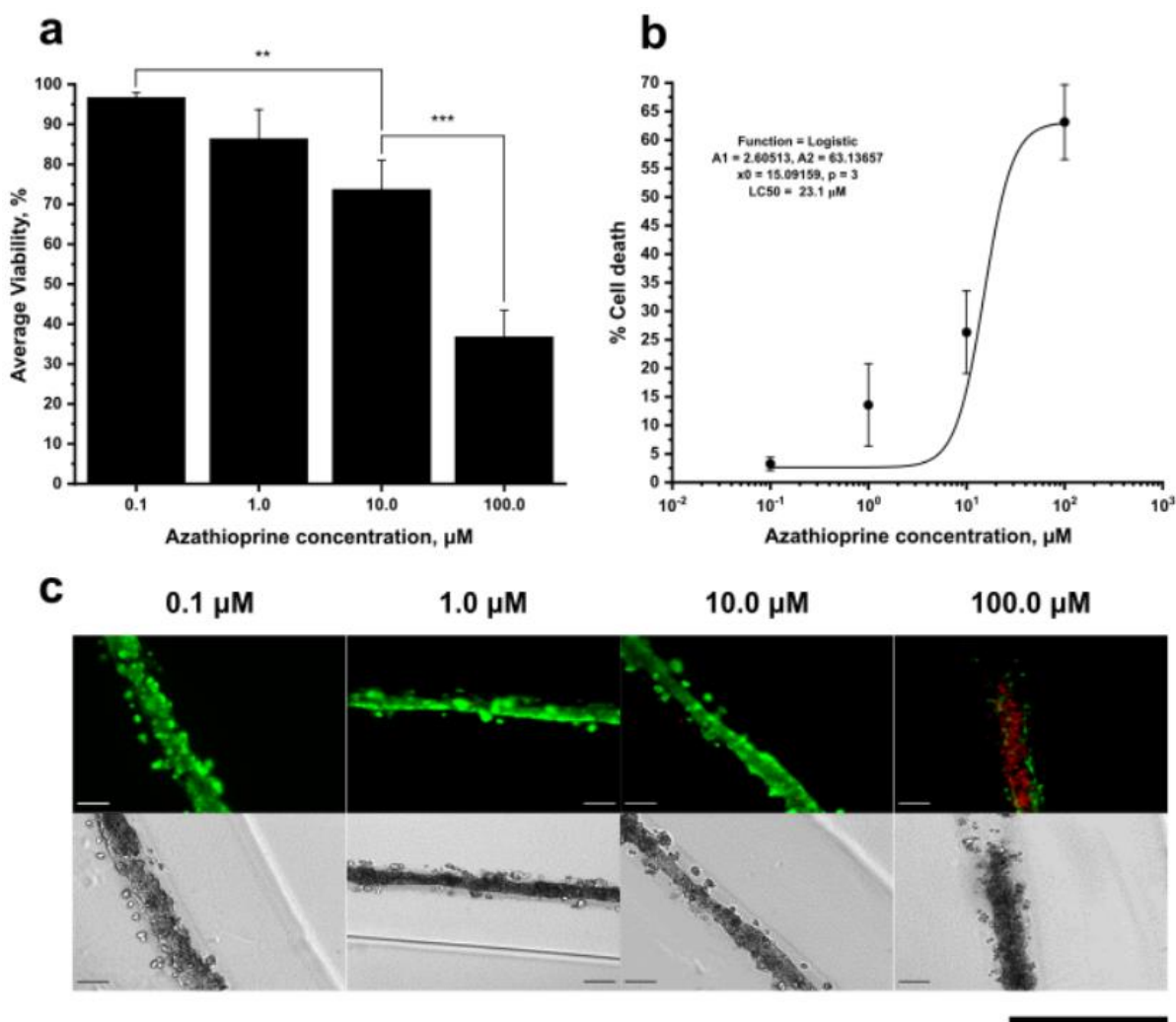


Figure 6-5. Day 7 HepaRG toxicity data on 48h exposure to 0.1, 1.0, 10.0 and 100.0 (all μM) azathioprine (AZA). (a) Cell viability results for corresponding AZA concentrations, (b) LC_{50} graph with sigmoidal dose-response curve fit displaying corresponding equation parameters and LC_{50} value. Data points represent mean \pm SD ($n = 3$), (c) representative day 7 live/dead and brightfield images showing decreasing cellular viability with increasing AZA concentration. Internal scale bars = 200 μm , External scale bar = 1.0 mm.

On culturing rat-derived hepatocytes with AZA for 48h, Tapner et al. [23] presented cellular viability data suggesting an LC_{50} in the range of 2.0 – 5.0 μM . Furthermore, Wu et al. [24] exposed primary rat hepatocytes to AZA for 48h and presented an LC_{50} in the range of 0.5 – 5.0 μM .

Interestingly, on dosing human hepatocytes with 1.0 – 25.0 μM AZA for 48h, Petit et al. [25] found that cellular viability remained above 70%. However, on exposing HepaRG cells to a supra-pharmacological concentration of 25 μM for 48h, they recorded a decline in viability to approximately 50% cell viability, hence providing the LC_{50} . Given that there are radical differences between the published LC_{50} values for rat and human hepatocytes with HepaRG cells and that there appears to be only one published source for AZA-induced HepaRG toxicity, it was assumed that the best benchmark for the results of this study would be the 25 μM presented by Petit et al.

With progressive ten-fold increases in AZA concentration added to HepaRG cells, it can be inferred from Figure 6-5 (a) that there was a significant effect on viability. On increasing the AZA concentration from 0.1 to 10.0 μM (absolute error of concentration is $\pm 0.20\%$), viability significantly decreased ($p < 0.01$) from $96.8 \pm 1.1\%$ to $73.7 \pm 7.2\%$. With a further ten-fold increase in AZA concentration, from 10.0 to 100.0 μM , viability declined further ($p < 0.001$) to a minimum of $36.9 \pm 6.6\%$. On fitting this data to a sigmoidal dose-response curve, presented in Figure 6-5 (b), the resulting LC_{50} was calculated as 23.1 μM , which was within 7.6% of the benchmark value of 25.0 μM , an acceptable difference given the usually wide range of LC_{50} values for various drugs during toxicity testing and the 3D cell culture nature of this study. However, given that the equation fit only intersected two data points, it is recommended to revise this work with more data points to provide a greater degree of accuracy.

6.2.4. Amiodarone

Amiodarone (AM) is a class III antiarrhythmic drug used to treat a wide array of cardiac arrhythmias [26]. The therapeutic use of AM is limited due to the range of side-effects associated with its severe toxicity, including pulmonary, thyroidal and hepatotoxicity [27] [28].

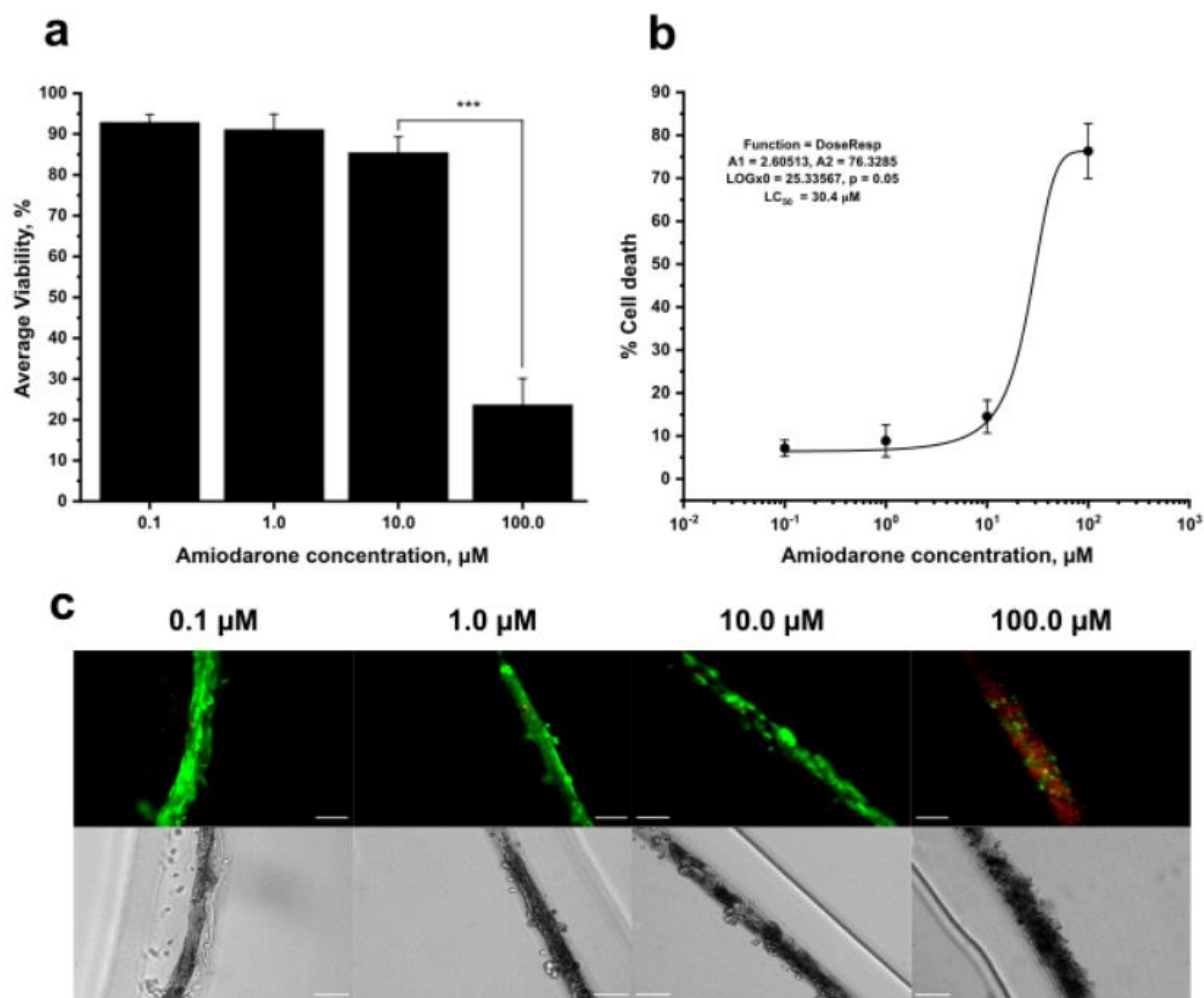


Figure 6-6. Day 7 HepaRG toxicity data on 48h exposure to 0.1, 1.0, 10.0 and 100.0 (all μM) amiodarone (AM). (a) Day 7 cell viability results for corresponding AM concentrations, (b) LC_{50} graph with sigmoidal dose-response curve fit displaying corresponding equation parameters and LC_{50} value. Data points represent mean \pm SD ($n = 3$), (c) Representative day 7 live/dead and brightfield images showing decreasing cellular viability with increasing AM concentration. Scale bars = 200 μm .

On cytotoxicity testing of AM, Gerets et al. [29] published an average LC_{50} of 56.0 μM ($n = 2$) on exposing cultured HepaRG cells to amiodarone for 48h. Additionally, Ferreira et al. [30] published viability data for HepaRG cells to AM for 72h, with the LC_{50} falling in the range of 15.0 – 30.0 μM ; it was expected that the 48-hour LC_{50} range would be higher, given that a higher concentration would be required to induce similar toxicity with a reduced exposure time. In response to these published results, it was predicted that if the LC_{50} was found to be within the 15.0 – 56.0 μM range, the results would possess provisional validity, with further, more robust testing being required due to the small number of data points presented here.

The data presented in Figure 6-6 (a) shows a significant fall in cellular viability ($p < 0.001$) on increasing the concentration of AM from 10.0 to 100.0 μM (absolute error of concentration is $\pm 0.82\%$), whereby viability was reduced from $85.5 \pm 3.8\%$ to $23.7 \pm 6.4\%$, with the LC_{50} evidently falling within this range.

On fitting the data to a dose-response curve, the LC₅₀ value was found to be 30.4 μM , well within the predicted range based on available published data. However, given that this result was obtained with 3D culture of HepaRG cells, a direct comparison to the published data for 2D (two-dimensional) culture should be taken with caution.

6.2.5. Prednisolone

Prednisolone (PRD) is a synthetic glucocorticoid (corticosteroid) which is utilised for its anti-inflammatory and immunosuppressive properties, including for the treatment of chronic obstructive pulmonary disease (COPD) [31]. PRD is used in cell culture applications to mimic the effect of hydrocortisone on liver function and is also used to alleviate hepatotoxicity in some cases [32] [33]. Moreover, PRD is also the current optimal treatment for severe alcoholic hepatitis [34]. Therefore, it was assumed that there would be no effect on the viability of the coaxial extruded HepaRG cells on adding 0.1 – 100.0 μM to the HepaRG culture medium with subsequent incubation for 48h.

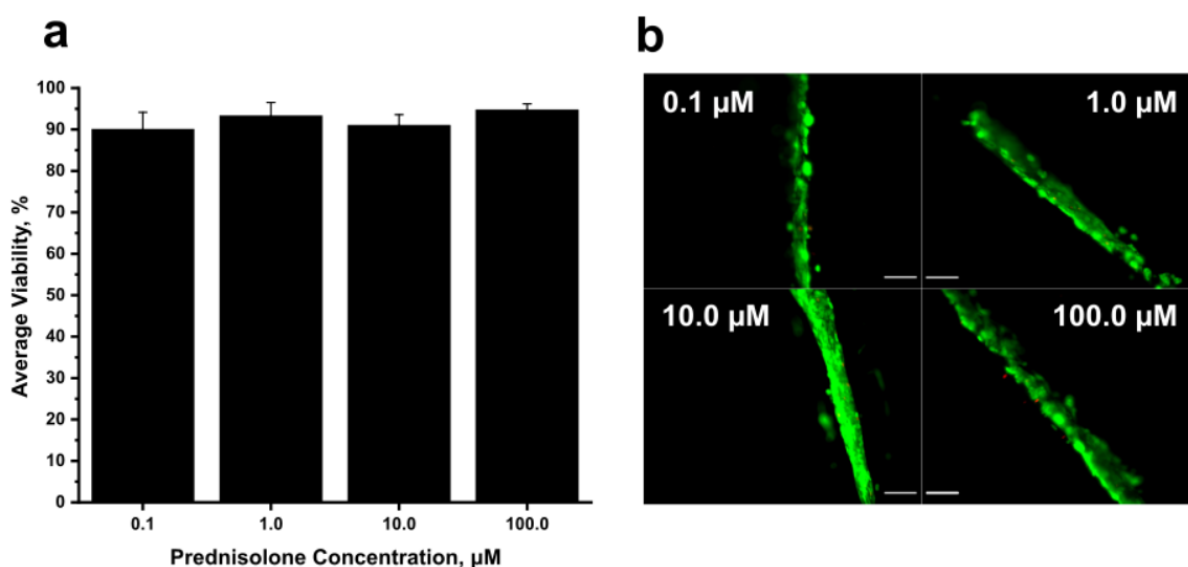


Figure 6-7. Day 7 HepaRG viability data on 48h exposure to 0.1, 1.0, 10.0 and 100.0 (all μM) prednisolone (PRD), (a) day 7 cell viability results for corresponding PRD concentrations. Data represents mean \pm SD (n = 3). (b) Representative day 7 live/dead images showing no effect on cellular viability with increasing PRD concentration. Scale bars = 200 μm .

As was expected, Figure 6-7 (a) confirms that there were no statistically significant effects of adding 0.1 – 100.0 μM PRD on cell viability, with viability ranging from 90.1 \pm 4.4% with 0.1 μM to 94.8 \pm 1.4% on using 100.0 μM (absolute error of concentration is \pm 0.71%). This data therefore confirmed the hypothesis in that PRD does not have any effect on cell viability within the tested concentration range and again adds further validity to the application of the coaxial extrusion platform to be used for drug testing applications.

6.2.6. Summary of toxicity data

In summary, all three of the hepatotoxic drugs which were tested using coaxial extruded filaments containing HepaRG cells, APAP, AZA and AM, achieved LC₅₀ values which fell within ranges, which were comparable with values reported in the literature, as is presented in Table 6-1.

Table 6-1. Summary of literature and achieved LC₅₀ values for known hepatotoxic compounds. Note: multiple cell types used for literature values for APAP and AZA.

Compound	Literature LC ₅₀	Cell types	Achieved LC ₅₀ (HepaRG)
Acetaminophen (APAP)	0.21 – 28.2 mM	Human hepatocytes, HepaRG	17.3 mM
Azathioprine (AZA)	0.5 – 25 µM	Rat hepatocytes, HepaRG	23.1 µM
Amiodarone (AM)	15.0 – 56.0 µM	HepaRG	30.4 µM

Given that all cited literature LC₅₀ values were recorded using 2D cell culture protocols and also with some sources using cell types other than HepaRG cells, there is a degree of uncertainty in the achieved LC₅₀ recorded here. However, given that the LC₅₀ found for all three drugs was within the expected range, these results do provide an indication that there is merit in further study and validation of the coaxial extrusion methodology for drug testing, as a potential alternative to traditional 2D cell culture models, given the aforementioned benefits of the 3D coaxial extrusion platform (automation, enhanced biomimicry, customisation etc.). Future work could involve a parallel study to compare between 2D and 3D culture experiments to give greater understanding between their differences.

6.3. CYP assay using rifampicin

To provide further data on HepaRG function within the coaxial extruded collagen filaments, a test on cellular metabolic function was performed by analysis of the cytochrome P450 (CYP450) activity of HepaRG cells in response to a CYP-inducing drug. Of the range of CYP450 isozymes responsible for the metabolism of most substances within the liver, CYP3A4 provides the largest contribution towards the metabolism of marketed drugs [35]. Therefore, a commercial assay kit to analyse the CYP3A4 activity of HepaRG cells in response to a common CYP3A4-inducing drug, rifampicin, was utilised. It should be noted that each sample measured approximately 10 mm in length, in order to ensure an equal volume of cell-collagen filaments per well as it was not possible to normalise CYP activity to the mass of cell-only protein due to the presence of collagen.

The assay involved the use of a pro-luciferin substrate, which is converted from a non-reactive derivative of luciferin into luciferin by action of CYP3A4. Luciferin then reacts with luciferase within a subsequently added detection reagent solution in a reaction, which is luminescent. As luminescent activity is directly proportional to CYP3A4 activity, this provides a measure of the CYP activity of each tested sample (see Figure 3-6).

It should be noted that cell culture media was used to suspend filaments prior to gathering luminescence data (as opposed to using cell lysate). It was assumed that the provided 24 hours was sufficient to permit CYP3A4 diffusion from cells and into the cell culture media.

Rifampicin, or rifampin, (RIF) is an antibiotic commonly used to treat tuberculosis [36] [37] but also has a powerful induction effect of CYP3A4. The RIF induction concentration used in published CYP studies is usually in the 5.0 – 50.0 μM range [38] [39] [40]. The chosen RIF concentrations for the following CYP3A4 assay were 10.0, 25.0 and 50.0 μM and were compared to a baseline negative control with no RIF added to allow an analysis of RIF concentration on CYP activity.

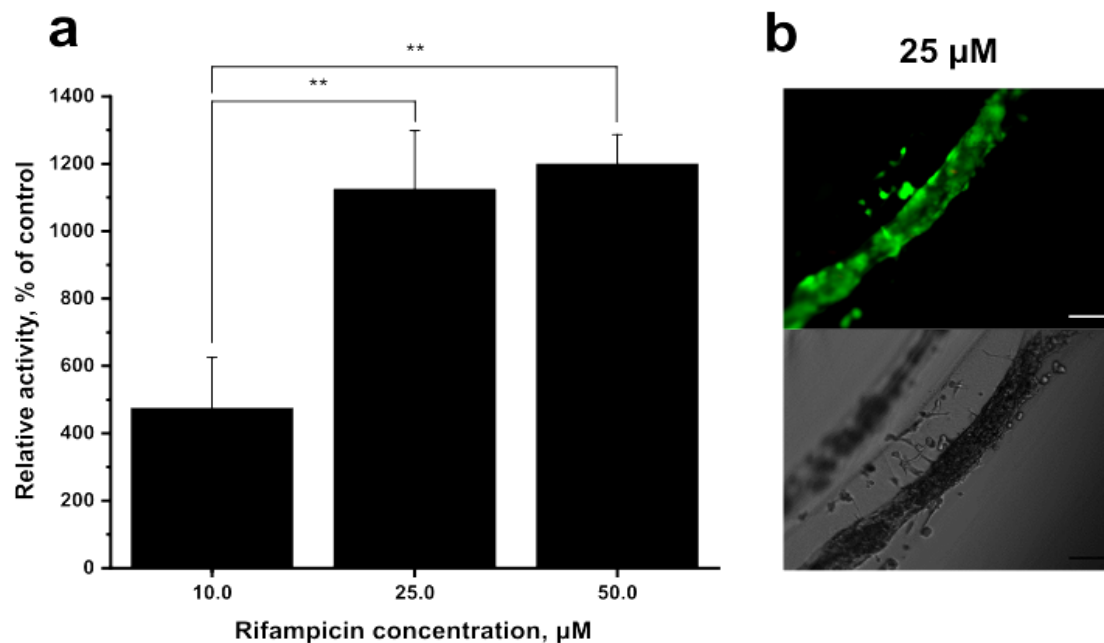


Figure 6-8, Day 7 CYP 3A4 assay results on dosing HepaRG cells with 10.0, 25.0 and 50.0 (all μM) rifampicin (RIF) for 48h with live/dead and brightfield images for 25.0 μM case. (a) Effect of RIF concentration on CYP 3A4 activity on dosing HepaRG cells for 48h. Data represents mean \pm SD (n = 3). (b) Representative day 7 live/dead and brightfield images on dosing HepaRG cells with 25.0 μM rifampicin for 48h. Scale bars = 200 μm .

Firstly, as is displayed in Figure 6-8, it can be seen that HepaRG CYP3A4 activity was induced by all three tested RIF concentrations (absolute error of concentration is \pm 3.29%). The lowest tested concentration of 10.0 μM provided an increase in CYP activity of $475.0 \pm 150\%$ relative to the negative control case. Activity significantly increased ($p < 0.01$) to $1125.0 \pm 173.2\%$ on use of 25.0 μM . On application of 50.0 μM , there was no further significant increase in relative CYP3A4 activity, calculated at $1200.0 \pm 86.6\%$, therefore indicating that 10.0 – 25.0 μM is a suitable concentration range for future CYP-induction studies involving coaxial extruded HepaRG cells. In summary, as CYP induction of HepaRG cells contained within coaxial extruded collagen filaments has been demonstrated using concentrations of rifampicin within the published range, this provides a further indication that the extrusion methodology may provisionally be suitable as a drug testing platform.

6.4. Conclusion

In summary, this chapter aimed to provide data on the suitability of the coaxial extrusion platform for use in drug testing applications. It has firstly been demonstrated that HepaRG cells can survive for a 14-day period post extrusion at high viability and fine diameter, thus facilitating the subsequent drug testing experiments, whereby the aim was to perform cytotoxicity assays and compare LC₅₀ values with available published values. Three hepatotoxic agents were tested, acetaminophen, azathioprine and amiodarone, whilst prednisolone was chosen as the positive control substance.

LC₅₀ values were found for all three agents (APAP: 17.3 mM; AZA: 23.1 µM; AM: 30.4 µM) and all three were within the expected ranges, given available published data, in 2D cell culture studies. However direct comparisons to published data were difficult due to variations in cell type, drug incubation time and culture conditions (2D vs 3D). The positive control case also performed as expected, with up to 100.0 µM prednisolone having no effect on cellular viability.

Finally, a test of HepaRG cytochrome P450 metabolic activity produced results indicating that the HepaRG cells were capable of CYP3A4 induction and provided a $1125.0 \pm 173.2\%$ increase relative to the negative control case on use of a commonly used concentration of 25.0 µM rifampicin.

To conclude, it has been demonstrated that the coaxial extrusion platform holds initial viability for drug testing applications. However, additional work is required to give a more robust evaluation, in which this could include testing of secretion rates of various hepatocyte-specific compounds such as albumin, the most abundant plasma protein which is an important carrier molecule of endogenous and exogenous chemicals [41] [42], transferrin, an iron-carrying glycoprotein [43], and ceruloplasmin, a copper-carrying ferroxidase enzyme [44].

In addition, immunostaining may also be performed, to detect the presence of various hepatocyte markers, such as cytokeratin 18, a cytoplasmic filament protein found in human hepatocytes, MRP2 (multi-drug resistance protein 2), a biliary canalicular transporter protein, and ZO-1 (zona occludens-1), a tight junction protein which permits intercellular communication between hepatocytes [45] [46] [47]. Additional studies may also analyse known hepatotoxic effects such as glutathione depletion and lactate dehydrogenase release [48].

6.5. References

- [1] W. Peng, P. Datta, B. Ayan, V. Ozbolat, D. Sosnoski, and I. T. Ozbolat, “3D bioprinting for drug discovery and development in pharmaceuticals,” *Acta Biomater.*, vol. 57, pp. 26–46, Jul. 2017.
- [2] M. J. Marion, O. Hantz, and D. Durantel, “The HepaRG cell line: biological properties and relevance as a tool for cell biology, drug metabolism, and virology studies.,” in *Hepatocytes. Methods in Molecular Biology (Methods and Protocols)*, vol. 640, Humana Press, 2010, pp. 261–272.
- [3] P. Gunness, D. Mueller, V. Shevchenko, E. Heinzle, M. Ingelman-Sundberg, and F. Noor, “3D organotypic cultures of human heparg cells: A tool for in vitro toxicity studies,” *Toxicol. Sci.*, vol. 133, no. 1, pp. 67–78, May 2013.
- [4] K. P. Kanebratt and T. B. Andersson, “Evaluation of HepaRG cells as an in vitro model for human drug metabolism studies,” *Drug Metab. Dispos.*, vol. 36, no. 7, pp. 1444–1452, 2008.
- [5] P. Gripon *et al.*, “Infection of a human hepatoma cell line by hepatitis B virus,” *Proc. Natl. Acad. Sci. U. S. A.*, vol. 99, no. 24, pp. 15655–15660, Nov. 2002.
- [6] S. B. Leite *et al.*, “Three-dimensional HepaRG model as an attractive tool for toxicity testing,” *Toxicol. Sci.*, vol. 130, no. 1, pp. 106–116, Nov. 2012.
- [7] L. J. Nelson *et al.*, “Human hepatic HepaRG cells maintain high intrinsic CYP450 activity/metabolism and significantly outperform standard HepG2/C3A cells used in drug pharmacology applications,” *J. Hepatol.*, vol. 60, no. 1, pp. S176–S177, Apr. 2014.
- [8] R. Sonoi, T. Yamakawa, N. Nakatani, M. Kokubo, and Y. Hagihara, “Noninvasive Evaluation of HepaRG Aggregates during Drug-Induced Intrahepatic Cholestasis Using Optical Coherence Tomography,” *Adv. Biol.*, vol. 5, no. 2, p. 2000198, Feb. 2021.
- [9] R. F. Speck, C. Schranz, and B. H. Lauterburg, “Prednisolone stimulates hepatic glutathione synthesis in mice. Protection by prednisolone against acetaminophen hepatotoxicity in vivo,” *J. Hepatol.*, vol. 18, no. 1, pp. 62–67, Jan. 1993.
- [10] S. Anthérieu, C. Chesné, R. Li, C. Guguen-Guillouzo, and A. Guillouzo, “Optimization of the HepaRG cell model for drug metabolism and toxicity studies,” *Toxicol. Vitro.*, vol. 26, no. 8, pp. 1278–1285, Dec. 2012.
- [11] G. P. Aithal, “Hepatotoxicity related to antirheumatic drugs,” *Nature Reviews Rheumatology*, vol. 7. Nature Publishing Group, pp. 139–150, 25-Mar-2011.

- [12] F. Wandrer *et al.*, “Autophagy alleviates amiodarone-induced hepatotoxicity,” *Arch. Toxicol.*, vol. 94, no. 10, pp. 3527–3539, Oct. 2020.
- [13] S. P. Rebelo, R. Costa, M. Estrada, V. Shevchenko, C. Brito, and P. M. Alves, “HepaRG microencapsulated spheroids in DMSO-free culture: novel culturing approaches for enhanced xenobiotic and biosynthetic metabolism,” *Arch. Toxicol.*, vol. 89, pp. 1347–1358, Aug. 2015.
- [14] Z. Oaks *et al.*, “Transaldolase haploinsufficiency in subjects with acetaminophen-induced liver failure,” *J. Inherit. Metab. Dis.*, vol. 43, no. 3, pp. 496–506, May 2020.
- [15] K. L. Hayward, E. E. Powell, K. M. Irvine, and J. H. Martin, “Can paracetamol (acetaminophen) be administered to patients with liver impairment?,” *Br. J. Clin. Pharmacol.*, vol. 81, no. 2, pp. 210–222, Feb. 2016.
- [16] J. P. Dwyer, C. Jayasekera, and A. Nicoll, “Analgesia for the cirrhotic patient: A literature review and recommendations,” *J. Gastroenterol. Hepatol.*, vol. 29, no. 7, pp. 1356–1360, Jul. 2014.
- [17] C. Zhang *et al.*, “Integration of in vitro data from three dimensionally cultured HepaRG cells and physiologically based pharmacokinetic modeling for assessment of acetaminophen hepatotoxicity,” *Regul. Toxicol. Pharmacol.*, vol. 114, p. 104661, Jul. 2020.
- [18] C. Minsart *et al.*, “New insights in acetaminophen toxicity: HMGB1 contributes by itself to amplify hepatocyte necrosis in vitro through the TLR4-TRIF-RIPK3 axis,” *Sci. Rep.*, vol. 10, p. 5557, Dec. 2020.
- [19] Y. E. Cho, P. G. Moon, and M. C. Baek, “An integrated proteomic and transcriptomic approach to understanding azathioprine-induced hepatotoxicity in rat primary hepatocytes,” *Electrophoresis*, vol. 35, no. 6, pp. 911–922, Mar. 2014.
- [20] S. Ramirez-Rubio *et al.*, “Molecular Mechanisms Involved in Azathioprine-induced Hepatotoxicity,” in *Journal of Hepatology*, 2008, vol. 48, p. S72.
- [21] M. E. C. Jeurissen, A. M. T. Boerbooms, L. B. A. Van De Putte, and M. W. M. Kruijsen, “Azathioprine induced fever, chills, rash, and hepatotoxicity in rheumatoid arthritis,” *Ann. Rheum. Dis.*, vol. 49, no. 1, pp. 25–27, 1990.
- [22] A. U. Lee and G. C. Farrell, “Mechanism of azathioprine-induced injury to hepatocytes: Roles of glutathione depletion and mitochondrial injury,” *J. Hepatol.*, vol. 35, no. 6, pp. 756–764, Dec. 2001.

- [23] M. J. Tapner, B. E. Jones, W. M. Wu, and G. C. Farrell, "Toxicity of low dose azathioprine and 6-mercaptopurine in rat hepatocytes. Roles of xanthine oxidase and mitochondrial injury," *J. Hepatol.*, vol. 40, no. 3, pp. 454–463, Mar. 2004.
- [24] Y. T. Wu, C. Shen, J. Yin, J. P. Yu, and Q. Meng, "Azathioprine hepatotoxicity and the protective effect of liquorice and glycyrrhizic acid," *Phyther. Res.*, vol. 20, no. 8, pp. 640–645, Aug. 2006.
- [25] E. Petit, S. Langouet, H. Akhdar, C. Nicolas-Nicolaz, A. Guillouzo, and F. Morel, "Differential toxic effects of azathioprine, 6-mercaptopurine and 6-thioguanine on human hepatocytes," *Toxicol. Vitro.*, vol. 22, no. 3, pp. 632–642, Apr. 2008.
- [26] A. Zahno *et al.*, "The role of CYP3A4 in amiodarone-associated toxicity on HepG2 cells," *Biochem. Pharmacol.*, vol. 81, no. 3, pp. 432–441, Feb. 2011.
- [27] H. L. Greene *et al.*, "Toxic and therapeutic effects of amiodarone in the treatment of cardiac arrhythmias," *J. Am. Coll. Cardiol.*, vol. 2, no. 6, pp. 1114–1128, Dec. 1983.
- [28] G. Pomponio *et al.*, "In vitro kinetics of amiodarone and its major metabolite in two human liver cell models after acute and repeated treatments," *Toxicol. Vitro.*, vol. 30, no. 1, pp. 36–51, Dec. 2015.
- [29] H. H. J. Gerets *et al.*, "Characterization of primary human hepatocytes, HepG2 cells, and HepaRG cells at the mRNA level and CYP activity in response to inducers and their predictivity for the detection of human hepatotoxins," *Cell Biol. Toxicol.*, vol. 28, pp. 69–87, 2012.
- [30] A. Ferreira, M. Rodrigues, S. Silvestre, A. Falcão, and G. Alves, "HepaRG cell line as an in vitro model for screening drug-drug interactions mediated by metabolic induction: Amiodarone used as a model substance," *Toxicol. Vitro.*, vol. 28, no. 8, pp. 1531–1535, Dec. 2014.
- [31] S. Fernandes and G. McKay, "Prednisolone," *Pract. Diabetes*, vol. 30, no. 6, pp. 251–252a, Jul. 2013.
- [32] A. J. Akindele, G. O. Oludadebo, K. I. Amagon, D. Singh, and D. D. Osiagwu, "Protective effect of carvedilol alone and coadministered with diltiazem and prednisolone on doxorubicin and 5-fluorouracil-induced hepatotoxicity and nephrotoxicity in rats," *Pharmacol. Res. Perspect.*, vol. 6, no. 1, p. e00381, Feb. 2018.
- [33] C. W. Kim *et al.*, "Drug-induced liver injury caused by iodine-131," *Clin. Mol. Hepatol.*, vol. 22, no. 2, pp. 272–275, Jun. 2016.
- [34] M. Thursz and T. R. Morgan, "Treatment of Severe Alcoholic Hepatitis," *Gastroenterology*, vol. 150, no. 8, pp. 1823–1834, Jun. 2016.

- [35] F. P. Guengerich, "Cytochrome P450 and chemical toxicology," *Chem. Res. Toxicol.*, vol. 21, no. 1, pp. 70–83, Jan. 2008.
- [36] M. Niemi, J. T. Backman, M. F. Fromm, P. J. Neuvonen, and K. T. Kivistö, "Pharmacokinetic interactions with rifampicin: Clinical relevance," *Clin. Pharmacokinet.*, vol. 42, no. 9, pp. 819–850, Sep. 2003.
- [37] L. Binkhorst *et al.*, "Effects of CYP induction by rifampicin on tamoxifen exposure," *Clin. Pharmacol. Ther.*, vol. 92, no. 1, pp. 62–67, Jul. 2012.
- [38] N. Hariparsad, S. C. Nallani, R. S. Sane, D. J. Buckley, A. R. Buckley, and P. B. Desai, "Induction of CYP3A4 by efavirenz in primary human hepatocytes: Comparison with rifampin and phenobarbital," *J. Clin. Pharmacol.*, vol. 44, no. 11, pp. 1273–1281, Nov. 2004.
- [39] A. P. Li *et al.*, "Primary human hepatocytes as a tool for the evaluation of structure-activity relationship in cytochrome P450 induction potential of xenobiotics: evaluation of rifampin, rifapentine and rifabutin," *Chem. Biol. Interact.*, vol. 107, pp. 17–30, 1997.
- [40] L. J. Nelson *et al.*, "Human Hepatic HepaRG Cells Maintain an Organotypic Phenotype with High Intrinsic CYP450 Activity/Metabolism and Significantly Outperform Standard HepG2/C3A Cells for Pharmaceutical and Therapeutic Applications," *Basic Clin. Pharmacol. Toxicol.*, vol. 120, pp. 30–37, Jan. 2017.
- [41] K. Oettl *et al.*, "Oxidative albumin damage in chronic liver failure: Relation to albumin binding capacity, liver dysfunction and survival," *J. Hepatol.*, vol. 59, no. 5, pp. 978–983, Nov. 2013.
- [42] Y. suke Torisawa, A. Takagi, Y. Nashimoto, T. Yasukawa, H. Shiku, and T. Matsue, "A multicellular spheroid array to realize spheroid formation, culture, and viability assay on a chip," *Biomaterials*, vol. 28, no. 3, pp. 559–566, Jan. 2007.
- [43] Y. Matsumoto *et al.*, "In situ visualization of a glycoform of transferrin: Localization of α 2,6-sialylated transferrin in the liver," *J. Biochem.*, vol. 157, no. 4, pp. 211–216, Apr. 2015.
- [44] K. Strzelak, J. Głowacka, and R. Koncki, "Towards mechanized biparametric ceruloplasmin assay," *Talanta*, vol. 214, p. 120881, Jul. 2020.
- [45] N. S. Bhise *et al.*, "A liver-on-a-chip platform with bioprinted hepatic spheroids," *Biofabrication*, vol. 8, no. 1, p. 014101, 2016.
- [46] V. L. Tsang *et al.*, "Fabrication of 3D hepatic tissues by additive photopatterning of cellular hydrogels," *FASEB J.*, vol. 21, no. 3, pp. 790–801, Mar. 2007.
- [47] C. Decaens, M. Durand, B. Grosse, and D. Cassio, "Which in vitro models could be best used to study hepatocyte polarity?," *Biol. Cell*, vol. 100, no. 7, pp. 387–398, Jul. 2008.

- [48] M. R. McGill, H. M. Yan, A. Ramachandran, G. J. Murray, D. E. Rollins, and H. Jaeschke, “HepaRG cells: A human model to study mechanisms of acetaminophen hepatotoxicity,” *Hepatology*, vol. 53, no. 3, pp. 974–982, Mar. 2011.

7. Research Assessment and Recommendations for Future Work

7.1. Research Summary

Provided the aim of this research was to develop a 3D coaxial extrusion platform for the production of high viability, fine diameter tissue filaments capable of survival for multiple weeks, there have been various advances presented within this work. Multiple approaches to tune alginate hydrogel shells have been explored to balance stability and porosity and have resulted in successful long-term (> 20 days) culture of ADSC and HepaRG cells embedded within extruded collagen tissue filaments, up to sub-25 μm minimal filament diameter, whilst maintaining high viability (> 90%). In addition, preliminary nozzle tip and printing bed temperature control modules have been developed, with PID control employed for nozzle temperature control. Finally, the potential of coaxial extruded collagen filaments for drug testing has been demonstrated, by cytotoxicity testing of various known hepatotoxic compounds using HepaRG cells with a further demonstration of expected metabolic function using a CYP enzyme assay.

Given these advances, there were many issues encountered, hindering progress at various stages of the work. These include the fact that 3D coaxial printing was not achieved (as only extrusion was employed here), due to difficulties in coding of the popular Marlin firmware. Furthermore, as has been previously stated, the use of collagen as the sole extracellular matrix (ECM) material contained within the core of extruded core/shell filaments was significantly hindered by its inherent low mechanical strength. Therefore, testing of other attractive ECM materials such as hyaluronic acid, fibrin and GelMA could have addressed this issue.

On developing the nozzle temperature control system, despite progress with the technology and array coding, due to the issue of heat leakage and insufficient heat transfer to the nozzle tip when utilising disposable plastic syringes, low-cost, repeatable deposition of liquid agarose was not achieved. It is suspected that the use of an all-in-one high thermal conductivity syringe-nozzle system would achieve this goal, albeit at a significantly greater cost.

Despite the progress in fine diameter extrusion of ADSC-collagen, and subsequently HepaRG-collagen, filaments, much of the earlier, higher filament diameter experiments presented in Chapter 5 would have benefitted from the developments of the collagen-only extrusion work displayed in Chapter 2. This disparity is due to these tests running simultaneously, however, in hindsight; it may have been optimal to perform all collagen-only work prior to any cell seeding attempts, due to the additional porosity and fine filament diameter requirements (sub-200 μm) associated with the use of cells and tissues.

On assessing the provisional viability of the coaxial extrusion platform for drug testing, the presented cytotoxicity tests would have benefitted with many more data points to provide a more accurate dose-response curve to compare to available literature.

Moreover, although the performed CYP450 enzyme assay provided a high CYP response on rifampicin induction of HepaRG cells, further tests with normalisation to the cell protein content would have provided a greater degree of accuracy and validity.

The overall aim of this research was to use 3D coaxial extrusion to fabricate high-viability, fine diameter tissue filaments capable of long-term survival within robust, porous alginate hydrogel scaffolds. This objective has successfully been achieved and summaries of the key findings are presented below.

- The theoretical prediction which dictated that the core/shell flow diameter ratio would change on changes to the corresponding coaxial nozzle core/shell flow rate ratio has been proven for collagen filament extrusion using alginate shells. Deviations from the idealised plot were due to various assumptions, such as treating the fluids as Newtonian, neglecting the effects of viscosity and gravity to solve the Navier-Stokes equations
- Key extrusion parameters such as flow rate magnitude, core/shell flow rate and collagen concentration have been manipulated in order to tune core collagen filament diameter in order to aid nutrient diffusion and long-term cell survival.
- Fine diameter ADSC-collagen filaments have been extruded and cultured with maintenance of high viability over a 21-day period on modification of alginate core/shell flow rate ratio and collagen concentration, with combined calcium barium cross-linking to maintain scaffold integrity.
- The finest average filament diameter achieved during the culture of acellular collagen filaments measured approximately $8.5 \pm 0.7 \mu\text{m}$ whilst the smallest diameter of cell-seeded collagen filaments was approximately $18.3 \pm 0.4 \mu\text{m}$, achieved using adipose-derived stem cells at a seeding density of 1.0×10^6 cells/ml. In both cases, 3.0 mg/ml collagen was used as the core fluid.
- The application of the coaxial extrusion platform to extrude and culture different cell types whilst maintaining fine diameter and high viability for 14 days has been demonstrated on the use of human hepatoma HepaRG cells.
- The viability of the coaxial extrusion platform as a drug testing platform has been initially assessed by performing hepatotoxicity testing of HepaRG cells using various known toxic agents and obtaining LC_{50} values similar to available published data. An additional assay of CYP450 enzyme activity further validated this platform by demonstrating strong CYP3A4 activity on induction with rifampicin, a known CYP3A4 inducer.

To conclude, a coaxial extrusion platform was created, wherein fine diameter (sub-20 μm) collagen filaments containing adipose-derived stem cells were fabricated and cultured, retaining high viability (> 90%) over multiple days (> 21 days). This achievement was aided by the tuning of material flow rates, alginate shell cross-linking parameters and collagen concentration. Finally, fine diameter collagen filaments containing human hepatoma HepaRG cells (sub-25 μm) were also extruded and cultured at high viability for 14 days. These HepaRG-containing filaments were also exposed to different hepatotoxic compounds at varying concentrations to obtain LC_{50} values comparable to literature, thus providing preliminary validation of the coaxial extrusion system to be used as a drug testing platform.

7.2. Future Work Recommendations

Given the research assessment, there are various aspects of this work which may be further explored in order to address the issues and concerns raised. Firstly, on the issue of extrusion hardware, upgrading the operating firmware to facilitate 3D coaxial printing (as opposed to simple extrusion) is a major issue to address, due to the need for the extruder to move in order to facilitate the deposition of filaments onto a print bed or at the point of care, to create desired geometries,

On the subject of core/shell flow rate tuning for fine filament diameters, it would be desirable to investigate the effect of different nozzle diameters on extruded filament diameter. It is predicted that it may be possible to print finer filaments using smaller diameter nozzles than those used within this work. Similarly, using different concentrations, molecular weights and viscosities of alginate in the shell may also lead to finer filament and alginate shell diameters, as would the blending of collagen and alginate with other materials. These modifications would affect the rheological properties of extruded materials, which may result in reduced filament diameter through the transfer of momentum experienced during the coaxial extrusion process.

Given the many presented approaches to alginate tuning, further work to quantify porosity and long-term alginate degradation and associated cation leakage would be highly valuable to balance alginate stability and porosity with cell-mediated degradation and any resulting deleterious effects on cell and tissue function.

Due to the aforementioned limitations of using collagen as the only ECM material, this work may benefit from experimentation using blends of collagen and bioactive hydrogel to combine the natural biocompatibility of collagen with the desirable mechanical properties of synthetic hydrogel; collagen cross-linking may also provide a synergistic effect in these studies. In addition, bioactive hydrogels may also aide in this pursuit, with materials such as RGD-alginate and methacrylated hyaluronic acid showing promise. These blends may be extruded using multi-nozzle and multiple input extrusion hardware, which may provide further opportunities in the creation of bioinks with desirable properties. It is also imperative that cells can remain at high viability when placed within engineered constructs.

Moreover, this work may be built upon by studies using differentiated stem cells, in situ differentiation of stem cells or co-culture using multiple cell types. In doing so, further progress towards extrusion and culture of transplantable tissue filaments will be made, especially in the case of neural tissue fibres where neurons and glial support cells are interdependent. Such studies may also benefit from the addition of growth factors to ECM core or hydrogel shell materials in order to induce or maintain desired phenotype. Studies on the alignment of cells along ECM filaments will also be essential to ensure desired tissue function.

On further investigating the potential of the coaxial extrusion platform for drug testing purposes, in addition to testing more hepatotoxic compounds with additional data points, further work will be required to test hepatocyte-specific function, ranging from albumin, glucose and transferrin secretion to immunohistochemical analyses to assess markers such as cytokeratin 18, MRP2 and ZO-1. Moreover, further hepatotoxic effects which may be studied include lactate dehydrogenase release and glutathione depletion. These common tests have been identified as it is important that the functionality of extruded hepatocytes or hepatocyte-like cells is not impaired as a result of the extrusion process, in order to validate the use of coaxial extrusion (or 3D coaxial bioprinting) for drug studies, over traditional tissue engineering methodologies. It should be noted that in vitro tests are currently considered simpler to perform than using 3D tissue models, largely due to the lack of understanding on 3D cell culture and difficulties in achieving sufficient vascularisation in engineered tissue constructs.

In the long-term future, given that the aforementioned technical challenges can be solved, the coaxial extrusion platform may be employed in a clinical manner to provide bespoke, on-demand tissues and organs to patients in need, using their own cells as feedstock. This demonstrates the potential to save many lives, such as in cases where donor tissues are not readily available (perhaps due to donor mismatches), in cases where bespoke tissues are required due to complex geometries or with immunocompromised patients, where tissue rejection can be fatal.

The coaxial extrusion platform could be developed into a medical device by developing the technology in adherence to international standards, such as ISO 13485 and 14971, and gain approval for commercialisation by the MHRA in the UK and/or the FDA in the USA, amongst other regulatory agencies in the world. Part of this approval process would require strict control of the sterility and endotoxin control of implants, amongst other tests designed to prevent or minimise potential harm to patients. On successful approval, there is an option to open-source or subsidise the technology across the world, to provide access to underprivileged communities, whereby the hardware and associated computer code could be easily reproduced by health boards with prohibitively low budgets. This could be accomplished by using readily available technologies such as 3D printers and using off-the-shelf parts, such as sensors, microcontrollers and other electrical components in addition to stock materials such as metals and plastics, in forms such as sheet and bar.